Doctoral Dissertation
Doctoral Program in Physics (30^{th}cycle)

Non-local orders in Hubbard-like low dimensional systems

By

Serena Fazzini
******

Supervisor:
Prof. Arianna Montorsi

Doctoral Examination Committee:
Prof. George Japaridze , Referee, Ilia State University
Prof. Elisa Ercolessi, Referee, University of Bologna
Prof. Vittorio Penna, Politecnico di Torino
Prof. Giovanni Ummarino, Politecnico di Torino
Prof. Maria Benedetta Barbaro, University of Turin

Politecnico di Torino
February 2018

Declaration

I hereby declare that, the contents and organization of this dissertation constitute my own original work and does not compromise in any way the rights of third parties, including those relating to the security of personal data.

<div align="right">
Serena Fazzini

February 2018
</div>

* This dissertation is presented in partial fulfillment of the requirements for **Ph.D. degree** in the Graduate School of Politecnico di Torino (ScuDo).

Acknowledgements

First of all, I would like to sincerely thank my supervisor Prof. Arianna Montorsi for having introduced me to the fascinating research topics of my PhD, and for her guidance and support during my studies.

I would also like to acknowledge Dr. Federico Becca, for his precious advices and teachings, Dr. Marco Roncaglia, Dr. Luca F. Tocchio and Dr. Luca Barbiero, for the inspiring conversations.

Finally, I thanks my family and Fabio, for always encouraging and supporting me.

Abstract

This PhD thesis is devoted to explore non-local orders in low-dimensional Hubbard-like systems. This kind of systems plays a crucial role in condensed matter physics. They were originally introduced to model solid state materials and, indeed, they successfully describe many observed physical phenomena. Additionally, in last decades, their scientific interest has exponentially increased thanks to the experiments with cold atoms, which have opened the opportunity to simulate and manipulate this type of lattice models. Trapping ultracold atomic gases into an optical lattice potential provides the purest realization of Hubbard Hamiltonians. Most important, the high control on the parameters involved allows to achieve even new fascinating regimes, among them exotic phases occurring in one and two spatial dimensions. These investigations are extremely interesting, since they unveil a totally novel physics, with many potential applications. On the other hand, from the theoretical point of view, Landau developed a theory that classifies possible phases of matter according to their symmetry. These are called spontaneous symmetry breaking phases and are typically identified by a local order parameter. Nevertheless, recent researches have proven that many more phases may exist in quantum systems. These are often called non-symmetry-breaking, hidden, exotic or topological phases. Hidden phases can be revealed by non-local order parameters. Given their central task in this attractive scenario, here we undertake to provide an overview on the capability of non-local order parameters to detect fully or partly gapped quantum phases and capture their essential microscopic features. To this end, we study their behavior, both analytically and numerically, in different systems. First of all we show that they can probe a large variety of one-dimensional quantum phases, actually all of them in the kind of Hamiltonians we will consider. Then, we will use them to uncover possible new phases and, finally, we will successfully attempt a generalization to the two dimensional case. Our results supply a step forward in the comprehension of this valuable tool and its range of applicability, in addition to the information we managed to disclose about the physical systems we studied, thanks to their employment.

Contents

List of Figures

List of Tables

Introduction

One of the main goals of condensed matter and quantum many-body physics is the understanding of strongly correlated systems. Thanks to the interplay between different kinds of degrees of freedom, they manifest very rich phase diagrams, which often embody hidden orders beyond the spontaneous symmetry breaking phases. In the wideness of possible scenarios appearing in the states of such materials, many fascinating phenomena may emerge, such as high-temperature superconductivity, fractional quantum Hall effect and topological ordering. That makes them particularly interesting for the potential impact on future technologies. An attractive subclass of strongly interacting systems is formed by the low-dimensional materials, in which collective quantum effects are expected to play a major role.

The fervid activity in this research field, has been stimulated in last decades by the development of extremely efficient numerical techniques. Among them, the density matrix renormalization group is the dominant method to handle one-dimensional systems; while the quantum Monte Carlo algorithm enables to explore higher dimensions, especially when dealing with bosonic systems.

On the other hand, the theoretical research is supported and motivated by the development of quantum simulators with ultracold gases of atoms trapped in optical lattices. The fast advancement of experimental techniques in this area has allowed to get high control and tunability of many kinds of interactions among the atoms, thus mimicking a huge variety of quantum systems, notably Heisenberg- or Hubbard-type model Hamiltonians.

In this PhD thesis, we address the second type of models. Our interest is focused on the unveiling of non-symmetry-breaking phases in such kind of systems, in one and two spatial dimensions. To this purpose, we devote our efforts to the study of non-local order parameters, which should be able to detect and characterize all the fully and partly gapped quantum phases. In particular, we will consider two kinds of

non-local string-like operators: the parity and the Haldane string. They can reveal the presence of hidden regimes, which may manifest a trivial or non-trivial topological behavior. In fact, they also disclose meaningful information about the topological order and the microscopic arrangement of particles in a given state. Furthermore, the spin-charge separation occurring for fermionic systems in low dimensionality provides independent observables in the two channels. That equips us with four different non-local order parameters for the discovery of different quantum regimes. Among them, also the symmetry breaking phases can be captured, since in one dimension they are found to appear by the coexistence of two non-local orders. Therefore, non-local order parameters supply an extremely powerful tool to explore the emergent low-dimensional quantum world. In this thesis, on one hand we will frame them in the context of bosonization, which is the convenient environment to build up a solid theoretical explanation of their action as quantum probes and give predictions in the weak coupling regime. On the other hand, we will perform accurate numerical simulations, based both on density matrix renormalization group and Green's function quantum Monte Carlo techniques to yield a complete picture of the physical problems we will consider. Most of our work is concerned with fermionic systems. In particular, our main goals are

1. prove that the non-local order parameters are able to detect all the phase transitions occurring in Hubbard-like systems: to this end we examine the rich phase diagram of the one-dimensional extended Hubbard model;

2. use non-local order parameters to unveil possible new phases: in this regard, we determine the zero temperature phase diagram of a one-dimensional bond-charge Hubbard model with dipolar interaction, which may eventually be generated by a Floquet mapping from a time-periodic model;

3. generalize the non-local order parameters to two dimensions: to this last purpose, we focus on one of them, the charge parity, and test its behavior in the two-dimensional Bose-Hubbard model.

The thesis is organized in two main parts: the first one (Chs. 1-5) is devoted to the introduction of the required physical, mathematical and numerical tools, while the second one (Chs. 6-8) contains the author's original contribution. The content of the single chapters is outlined in the following:

- Chapter 1 is an introduction to the Hubbard model and its symmetries. Particularly important for the development of the following results are the spin and pseudo-spin operators which generate the continuous symmetry of the model. This chapter also includes some results from the previous literature on various generalizations of the model.

- Chapter 2 is devoted to the discussion of phase transitions and the classification of one dimensional quantum phases. Here the fundamental concepts of non-local order and non-local order parameters are provided.

- In Chapter 3 we present a derivation of the bosonization formalism, which is the primary analytical technique used for our studies. Then, it is applied to derive an effective model for interacting fermions in the weak coupling limit and, in the last section, the non-local order parameters and the classification of phases are framed into this picture, where they find a deeper explanation.

- Chapter 4 provides an introduction to the numerical techniques employed to perform our analysis, i.e., the density matrix renormalization group and the quantum Monte Carlo.

- Chapter 5 is an overview on the experimental achievements in simulating and probing the Hubbard-like systems.

- In Chapter 6 we numerically compute the non-local order parameters through the ground state phase transitions of the one dimensional extended Hubbard model in order to check their validity as probes to detect both symmetry breaking and hidden phases.

- In Chapter 7 we investigate the effect of both long-range dipolar interaction and density-dependent hopping on the one-dimensional Hubbard model. We first calculate the two-particle scattering matrix to identify the integrability points. Then we tackle the many-body problem with both bosonization and density matrix renormalization group techniques, tracing the transition lines in the ground state phase diagram based on non-local order parameters. Moreover we use the Floquet analysis to demonstrate that the Hamiltonian under examination can be treated as an effective model for a time-periodic system.

- Finally Chapter 8 contains a generalization of the non-local order parameter for the Mott insulator to the two dimensional case. We check the validity of

our guess on the Bose-Hubbard model by employing the Green's function quantum Monte Carlo technique.

Part I

Literature review and theoretical framework

Chapter 1

Hubbard Model and its extensions

1.1 A brief introduction: from real materials to cold atom systems

Describing the microscopic phenomena related to the physics of solids is one of the most challenging objectives of condensed matter physics. Indeed, real materials possess many complex properties, which turn out to be the result of several mixing effects. Moreover, they are affected by the presence of defects and impurities, which need to be accounted for, in order to get a correct description of the system.

Many simplified models have been developed and analyzed, depending on the phenomena that were requested to be captured. Among them, the simplest model beyond the free electron theory is the Hubbard model. It was introduced in 1963 in two independent papers by Martin C. Gutzwiller [1] and John Hubbard [2] to describe correlation phenomena of transition and rare-earth metals due to their partly filled d- or f- bands. Later J. Hubbard developed the model in five subsequent papers [3–7].

Thenceforth, the Hubbard model has been intensively studied. In fact, it is capable to capture many features of real materials, ranging from itinerant magnetism and metal-insulator (Mott) transition to high-T_c superconductivity.

Its relevance has been further increased by the implementation of experiments with cold atoms, which not only allow to simulate existing materials with high control of the interaction parameters, but also make it possible to faithfully realize new Hamiltonian systems. In particular, they provide a toolbox to investigate the very

rich physics of low dimensional Hubbard-like systems, where new exotic phenomena can be observed. That justifies the prolific theoretical activity around this model. For all the clarifications about cold atom systems, we refer the reader to Chapter 5.

1.2 The Hubbard Model

This section is devoted to illustrate the origins, the properties and the main results concerning the Hubbard model, in its simplest form. After having derived the Hamiltonian for the generic three dimensional case, we will focus on the low dimensional models.

1.2.1 Origin of the model

Here we derive the Hubbard Hamiltonian, starting from the picture of a solid as a three-dimensional static lattice where electrons can move under the effect of the ionic potential and the mutual Coulomb repulsion [8]. Within this approximation, the system can be modeled by the following Hamiltonian

$$H = \sum_{i=1}^{N} \left(\frac{\vec{p}_i^2}{2m} + V_I(\vec{x}_i) \right) + \sum_{1 \leq i < j \leq N} V_C(\vec{x}_i - \vec{x}_j) \tag{1.1}$$

where N is the number of electrons, $V_I(\vec{x})$ is the ionic potential and $V_C(\vec{x}) = e^2/|\vec{x}|$ is the Coulomb repulsion among the electrons. This Hamiltonian is still too complicated to be solved. A further simplification consists in subtracting part of the Coulomb interaction and reinsert it in the one-body term as a mean field contribution, in such a way that the remaining two-body interaction has small matrix elements when computed between the eigenstates of the one-particle Hamiltonian. The aim of this procedure is to neglect most of these matrix elements. In fact, we will retain only the main contribution which turns out to be a contact interaction. After having transfered part of the interaction among electrons into the one-body term, the Hamiltonian can be regarded as having a new single particle potential $V(\vec{x})$ and an effective two-body interaction $U(\vec{x}, \vec{y})$. By using the following notation for the single-particle Hamiltonian

$$h_1(\vec{x}, \vec{p}) = \frac{\vec{p}^2}{2m} + V(\vec{x}) \quad , \tag{1.2}$$

the full Hamiltonian has the form

$$H = \sum_{i=1}^{N} h_1(\vec{x}_i, \vec{p}_i) + \sum_{1 \leq i < j \leq N} U(\vec{x}_i, \vec{x}_j) \,. \tag{1.3}$$

We now introduce the second quantization formalism, which will be used hereinafter. We may construct a suitable basis starting from the eigenfunctions $\varphi_{\alpha\vec{k}}$ of h_1, meaning those satisfying the eigenvalue equation

$$h_1 \varphi_{\alpha\vec{k}}(\vec{x}) = \varepsilon_{\alpha\vec{k}} \varphi_{\alpha\vec{k}}(\vec{x}) \,, \tag{1.4}$$

which constitute a basis for the one-particle states. Here α is the band index and $\vec{k}$ is the quasi-momentum, which runs over the first Brillouin zone. Since h_1 only contains the kinetic term and a periodic potential, its eigenfunctions are Bloch functions. Hence they can be written as

$$\varphi_{\alpha\vec{k}}(\vec{x}) = e^{i\vec{k}\cdot\vec{x}} u_{\alpha\vec{k}}(\vec{x}) \tag{1.5}$$

where $u_{\alpha\vec{k}}$ has the same periodicity of the lattice. These states are localized in the reciprocal space. Another suitable basis is provided by the Wannier wave functions $\tilde{\varphi}_\alpha$, which are localized in the real space. They are related to the Bloch wave functions by a Fourier transform

$$\tilde{\varphi}_\alpha(\vec{x}) = \frac{1}{\sqrt{L}} \sum_{\vec{k}} \varphi_{\alpha\vec{k}}(\vec{x}) = \frac{1}{\sqrt{L}} \sum_{\vec{k}} e^{i\vec{k}\cdot\vec{R}_i} \varphi_{\alpha\vec{k}}(\vec{x} - \vec{R}_i) \tag{1.6}$$

$$\varphi_{\alpha\vec{k}}(\vec{x}) = \frac{1}{\sqrt{L}} \sum_{i} e^{i\vec{k}\cdot\vec{R}_i} \tilde{\varphi}_\alpha(\vec{x} - \vec{R}_i) \tag{1.7}$$

where L is the number of lattice sites. Now we can introduce the creation operator $c^\dagger_{\alpha\vec{k},\sigma}$ for an electron with spin σ in a Bloch state $\varphi_{\alpha\vec{k}}$, and its Fourier transform

$$c^\dagger_{\alpha i,\sigma} = \frac{1}{\sqrt{L}} \sum_{\vec{k}} e^{-i\vec{k}\cdot\vec{R}_i} c^\dagger_{\alpha\vec{k},\sigma} \,. \tag{1.8}$$

Finally, the field operator, which creates an electron of spin σ at position $\vec{x}$ is

$$\Psi^\dagger_\sigma(\vec{x}) = \sum_{\alpha\vec{k}} \varphi^*_{\alpha\vec{k}}(\vec{x}) c^\dagger_{\alpha\vec{k},\sigma} = \sum_{\alpha i} \tilde{\varphi}^*_\alpha(\vec{x} - \vec{R}_i) c^\dagger_{\alpha i,\sigma} \tag{1.9}$$

where the asterisk denotes complex conjugation. Hence the Hamiltonian (1.3) can be written as

$$
\begin{aligned}
H = &\sum_{\sigma=\uparrow,\downarrow} \int dx^3 \Psi_\sigma^\dagger(\vec{x}) h_1 \Psi_\sigma(\vec{x}) \\
&+ \frac{1}{2} \sum_{\sigma,\sigma'=\uparrow,\downarrow} \int dx^3 \int dy^3 \Psi_\sigma^\dagger(\vec{x}) \Psi_{\sigma'}^\dagger(\vec{y}) U(\vec{x},\vec{y}) \Psi_{\sigma'}(\vec{y}) \Psi_\sigma(\vec{x}) \,.
\end{aligned}
\tag{1.10}
$$

This formula relates the first and second quantized formalisms. By using the expressions (1.9) for the field operators, we get the Hamiltonian in second quantization. In the Wannier basis, it reads

$$
H = -\sum_\alpha \sum_{i,j} \sum_\sigma t_{i,j}^\alpha c_{\alpha i,\sigma}^\dagger c_{\alpha j,\sigma} + \frac{1}{2} \sum_{\alpha,\beta,\gamma,\delta} \sum_{i,j,k,l} \sum_{\sigma,\sigma'} U_{i,j,k,l}^{\alpha,\beta,\gamma,\delta} c_{\alpha i,\sigma}^\dagger c_{\beta j,\sigma'}^\dagger c_{\gamma k,\sigma'} c_{\delta l,\sigma} \,.
\tag{1.11}
$$

Here, the amplitudes of the hopping term and the interaction parameters are given by

$$
t_{i,j}^\alpha = -\langle i|h_1|j\rangle = -\int dx^3 \tilde{\varphi}_\alpha^*(\vec{x}-\vec{R}_i) h_1 \tilde{\varphi}_\alpha(\vec{x}-\vec{R}_j) = -\frac{1}{L} \sum_{\vec{k}} e^{i\vec{k}\cdot(\vec{R}_i-\vec{R}_j)} \varepsilon_{\alpha\vec{k}}
\tag{1.12}
$$

and

$$
U_{i,j,k,l}^{\alpha,\beta,\gamma,\delta} = \langle ij|U|kl\rangle = \int dx^3 dy^3 \tilde{\varphi}_\alpha^*(\vec{x}-\vec{R}_i) \tilde{\varphi}_\beta^*(\vec{y}-\vec{R}_j) U(\vec{x},\vec{y}) \tilde{\varphi}_\gamma(\vec{y}-\vec{R}_k) \tilde{\varphi}_\delta(\vec{x}-\vec{R}_l) \,,
\tag{1.13}
$$

respectively. We notice that this Hamiltonian is still equivalent to (1.1). The influence of the mutual Coulomb interaction, enclosed into the range and magnitude of $U_{i,j,k,l}^{\alpha,\beta,\gamma,\delta}$, can be minimized by an optimal choice of Wannier states (through an optimal choice of the mean field potential which contribution is transfered from the two-body term into the one-body term of the Hamiltonian). When the matrix elements $U_{i,j,k,l}^{\alpha,\beta,\gamma,\delta}$ are small compared to the hopping amplitudes, they can be set equal to zero in a first approximation, and can later be taken into account by perturbation theory (band theory). In the approximation of the Hubbard model the interaction parameters are no longer considered as negligible. However their range is still very small: in the sum only the intra-atomic contribution $U_{i,i,i,i}^{\alpha,\beta,\gamma,\delta}$ is retained. A further simplification occurs when the Fermi surface lies within a single conduction band. In this case, we can ignore the matrix elements that involve other bands. Thus, we

get the so-called one-band Hubbard model

$$H = \sum_{i,j} \sum_{\sigma} t_{i,j} c_{i,\sigma}^{\dagger} c_{j,\sigma} + \frac{U}{2} \sum_{i} \sum_{\sigma,\sigma'} c_{i,\sigma}^{\dagger} c_{i,\sigma'}^{\dagger} c_{i,\sigma'} c_{i,\sigma} , \qquad (1.14)$$

where we have omitted the band index and have set $U_{i,i,i,i} = U$. A further simplification is possible when the tight binding approximation can be assumed. In this case, the only relevant hopping processes are those occurring between neighboring sites. Then, if we assume isotropic hopping, the Hamiltonian reduces to

$$H = -t \sum_{\langle i,j \rangle} \sum_{\sigma} c_{i,\sigma}^{\dagger} c_{j,\sigma} + U \sum_{i} n_{i,\uparrow} n_{i,\downarrow} \qquad (1.15)$$

where the symbol $\langle i,j \rangle$ denotes summation over ordered pairs of nearest neighbors and $n_{i,\sigma} = c_{i,\sigma}^{\dagger} c_{i,\sigma}$ is the local occupation number operator. This is the Hamiltonian will be referred to as the Hubbard Hamiltonian hereinafter.

1.2.2   Symmetries of the model

The role of the symmetries is very fundamental in determining the physical properties of a system. Here we analyze the symmetries possessed by the Hubbard model. Even though we will reduce our discussion to the one dimensional case, the results generalize to (bipartite) lattices of arbitrary dimension. The Hubbard Hamiltonian (1.15) in 1D is

$$H = -t \sum_{j=1}^{L} \sum_{\sigma=\uparrow,\downarrow} \left(c_{j,\sigma}^{\dagger} c_{j+1,\sigma} + c_{j+1,\sigma}^{\dagger} c_{j,\sigma} \right) + U \sum_{j=1}^{L} n_{j,\uparrow} n_{j,\downarrow} \qquad (1.16)$$

where we have assumed periodic boundary conditions (PBC): $c_{L+1,\sigma} \equiv c_{1,\sigma}$.
Hilbert space. The fermionic operators involved in the Hamiltonian satisfy the following anticommutation rules

$$\left\{ c_{i,\sigma}, c_{j,\sigma'} \right\} = \left\{ c_{i,\sigma}^{\dagger}, c_{j,\sigma'}^{\dagger} \right\} = 0 \qquad (1.17)$$

$$\left\{ c_{i,\sigma}, c_{j,\sigma'}^{\dagger} \right\} = \delta_{i,j} \delta_{\sigma,\sigma'} . \qquad (1.18)$$

As a consequence of the previous relations, we get

$$[c_{i,\sigma}, c_{i,\sigma}^\dagger] = 1 - 2n_{i,\sigma} \tag{1.19}$$

$$[n_{i,\sigma}, c_{i,\sigma}] = -c_{i,\sigma} \tag{1.20}$$

$$[n_{i,\sigma}, c_{i,\sigma}^\dagger] = c_{i,\sigma}^\dagger . \tag{1.21}$$

The Hilbert space can be constructed by applying the creation operators to the vacuum state. In particular, the local Hilbert space on each site is given by the four states

$$\begin{aligned}
\mathbb{I}_j |0\rangle_j &= |0\rangle_j \equiv |00\rangle_j \\
c_{j,\uparrow}^\dagger |0\rangle_j &= |\uparrow\rangle_j \equiv |10\rangle_j \\
c_{j,\downarrow}^\dagger |0\rangle_j &= |\downarrow\rangle_j \equiv |01\rangle_j \\
c_{j,\uparrow}^\dagger c_{j,\downarrow}^\dagger |0\rangle_j &= |\uparrow\downarrow\rangle_j \equiv |11\rangle_j
\end{aligned} \tag{1.22}$$

where we have introduced two equivalent notations. Another possibility is to use the matrix formalism. This is described in Appendix A, together with the formalism of Hubbard operators.

Then, if we write a generic local state as $|n_\uparrow \ n_\downarrow\rangle_j \equiv |n_{j,\uparrow}, n_{j,\downarrow}\rangle$, a basis for the total Hilbert space can be identified with the 4^L states given by

$$\left\{ \prod_{j=1}^L |n_\uparrow \ n_\downarrow\rangle_j \quad \text{with } n_\sigma = 0, 1 \right\} . \tag{1.23}$$

Thus, a generic state turns out to be a linear combinations of the states (1.23). We notice that the latters can also be constructed starting from the so-called Wannier states $c_{x_N,\sigma_N}^\dagger...c_{x_1,\sigma_1}^\dagger |0\rangle$ and ordering the Fermi operators. Here, each operator $c_{x_n,\sigma_n}^\dagger$ creates a fermion with spin $\sigma_n \in \{\uparrow,\downarrow\}$ in the position $x_n \in \{1,..,L\}$, and $|0\rangle \equiv \prod_j |0\rangle_j$. The Wannier state contains a fixed number N of fermions; however, in order to build a basis, N is allowed to range in the interval $[0, 2L]$. The basis (1.23) is called the Wannier basis.

Another possible basis is the Bloch basis, which is built by ordering the operators in $c_{k_N,\sigma_N}^\dagger...c_{k_1,\sigma_1}^\dagger |0\rangle$, with $N \in \{0,...,2L\}$. This is obtained through the Fourier transformation, which is a canonical transformation since it leaves the anticommutation

rules invariant.

Now one can verify that the hopping term $\hat{T}$ of the Hubbard Hamiltonian (1.16) is diagonal in the Bloch basis; whereas the double occupancy operator $\hat{D} = \sum_{j=1}^{L} n_{j,\uparrow} n_{j,\downarrow}$, which represents the interaction term in the Hubbard Hamiltonian, is diagonal in the Wannier basis. It follows that, since $[\hat{T}, \hat{D}] \neq 0$, the Hubbard Hamiltonian cannot be diagonal neither in the Bloch basis nor in the Wannier basis.

The physics of the model is determined by the competition between $\hat{T}$, which tends to delocalize the fermions on the lattice, and $\hat{D}$, which favors the localization.

The Hilbert space spanned by the set (1.23) has dimension 4^L. However, one can exploit the symmetries of the Hamiltonian in order to work in a smaller subspace.

Conserved quantities. Two very important conserved quantities are the total particle number and the total magnetization, defined respectively as

$$
\begin{aligned}
\hat{N} &= \hat{N}_\uparrow + \hat{N}_\downarrow = \sum_{j=1}^{L} (n_{j,\uparrow} + n_{j,\downarrow}) \\
\mathrm{S}^{(s),z} &= \frac{1}{2} \left(\hat{N}_\uparrow - \hat{N}_\downarrow \right) = \frac{1}{2} \sum_{j=1}^{L} (n_{j,\uparrow} - n_{j,\downarrow})
\end{aligned}
\tag{1.24}
$$

where $\hat{N}_\sigma = \sum_{j=1}^{L} n_{j,\sigma}$ is the total number operator for the species σ. It can be verified that $N_\uparrow$ and $N_\downarrow$ are separately conserved by the Hamiltonian: $[H, \hat{N}_\uparrow] = [H, \hat{N}_\downarrow] = 0$. This implies that both the total number of particles and the total magnetization are conserved quantities: $[H, \hat{N}] = [H, \mathrm{S}^{(s),z}] = 0$. Thus, hereinafter we will assume to deal with systems with fixed filling $n = N/L$ and magnetization, if not otherwise specified. Sometimes, instead of the number operator, the so-called total charge operator is introduced

$$
\mathrm{S}^{(c),z} = \frac{1}{2} \left[\hat{N} - L \right] = \frac{1}{2} \sum_{j=1}^{L} (n_j - 1).
\tag{1.25}
$$

We notice that at half-filling the local operator $n_j - 1$ measures the deviation of the particle number at site j with respect to its mean value, namely it coincides with the normal ordered form of the local particle number operator $: n_j :$. Hence, in this case,

the spin and charge operators previously introduced can be regarded as

$$S^{(s),z} = \frac{1}{2} \sum_{j=1}^{L} (: n_{j,\uparrow} : - : n_{j,\downarrow} :)$$

$$S^{(c),z} = \frac{1}{2} \sum_{j=1}^{L} (: n_{j,\uparrow} : + : n_{j,\downarrow} :) \,.$$

(1.26)

Because of the particle number conservation, we can add a term proportional to $\hat{N}$ to the Hamiltonian, without affecting its spectrum. Then, the Hamiltonian can be written as

$$H = -t \sum_{j=1}^{L} \sum_{\sigma=\uparrow,\downarrow} \left(c_{j,\sigma}^{\dagger} c_{j+1,\sigma} + c_{j+1,\sigma}^{\dagger} c_{j,\sigma} \right) + U \sum_{j=1}^{L} \left(n_{j,\uparrow} - \frac{1}{2} \right) \left(n_{j,\downarrow} - \frac{1}{2} \right) \,,$$

(1.27)

which turns out to be of higher symmetry, if L is even.

Continuous symmetry. The Hamiltonian (1.27) has many symmetries. In particular, it has two U(1) symmetries related to the conservation of $S^{(c),z}$ and $S^{(s),z}$. Indeed both operators generate U(1) transformations. In particular, $S^{(s),z}$ is the z-component of the total spin. The Hubbard Hamiltonian also commutes with the other two components, $S^{(s),x}$ and $S^{(s),y}$. Since the three components combined together form a representation of the Lie algebra su(2) that generates the group SU(2) of rotations in spin space, our Hamiltonian is fully rotationally invariant. The components of the spin operator are written in terms of the fermionic creation and annihilation operators as

$$S^{(s),\alpha} = \sum_{j=1}^{L} S_j^{(s),\alpha} = \frac{1}{2} \sum_{j=1}^{L} \sum_{\sigma,\sigma'} c_{j,\sigma}^{\dagger} (\sigma^{\alpha})_{\sigma\sigma'} c_{j,\sigma'}$$

$$= \frac{1}{2} \sum_{j=1}^{L} \left(\begin{array}{cc} c_{j,\uparrow}^{\dagger} & c_{j,\downarrow}^{\dagger} \end{array} \right) \left(\begin{array}{cc} (\sigma^{\alpha})_{\uparrow\uparrow} & (\sigma^{\alpha})_{\uparrow\downarrow} \\ (\sigma^{\alpha})_{\downarrow\uparrow} & (\sigma^{\alpha})_{\downarrow\downarrow} \end{array} \right) \left(\begin{array}{c} c_{j,\uparrow} \\ c_{j,\downarrow} \end{array} \right)$$

(1.28)

where $\alpha = x, y, z$ and σ^{α} are the Pauli matrices

$$\sigma^x = \left(\begin{array}{cc} 0 & 1 \\ 1 & 0 \end{array} \right), \qquad \sigma^y = \left(\begin{array}{cc} 0 & -\iota \\ \iota & 0 \end{array} \right), \qquad \sigma^z = \left(\begin{array}{cc} 1 & 0 \\ 0 & -1 \end{array} \right), \qquad (1.29)$$

which elements have been labeled through the two fermionic species: the first element of each row or column is labeled by the up spin species ($\uparrow$) and the second

element by the down spin species ($\downarrow$). Hence, the components of the local spin at each site are

$$
\begin{aligned}
S_j^{(s),x} &= \frac{1}{2}\left(c_{j,\uparrow}^\dagger c_{j,\downarrow} + c_{j,\downarrow}^\dagger c_{j,\uparrow}\right) \\
S_j^{(s),y} &= \frac{1}{2\imath}\left(c_{j,\uparrow}^\dagger c_{j,\downarrow} - c_{j,\downarrow}^\dagger c_{j,\uparrow}\right) \\
S_j^{(s),z} &= \frac{1}{2}\left(c_{j,\uparrow}^\dagger c_{j,\uparrow} - c_{j,\downarrow}^\dagger c_{j,\downarrow}\right) = \frac{1}{2}\left(n_{j,\uparrow} - n_{j,\downarrow}\right).
\end{aligned}
\tag{1.30}
$$

Instead of the x and y components, one can also use the following combinations

$$
S^{(s),\pm} = S^{(s),x} \pm \imath S^{(s),y}
\tag{1.31}
$$

defined, respectively, as

$$
\begin{aligned}
S^{(s),+} &= \sum_{j=1}^{L} c_{j,\uparrow}^\dagger c_{j,\downarrow} \\
S^{(s),-} &= \sum_{j=1}^{L} c_{j,\downarrow}^\dagger c_{j,\uparrow}.
\end{aligned}
\tag{1.32}
$$

The spin operators obey the following commutation rules

$$
\begin{aligned}
[S^{(s),\alpha}, S^{(s),\beta}] &= \imath \varepsilon_{\alpha\beta\gamma} S^{(s),\gamma} \\
[S^{(s),z}, S^{(s),\pm}] &= \pm S^{(s),\pm} \\
[S^{(s),+}, S^{(s),-}] &= 2 S^{(s),z}.
\end{aligned}
\tag{1.33}
$$

where the greek indexes in the first line can be x, y, z and $\varepsilon_{\alpha\beta\gamma}$ is the totally antisymmetric tensor. In the relations (1.33) we can recognize the commutator relationships of the su(2) algebra. They are valid for the local spin operators as well as for the total spin operators. However, in general the Hubbard Hamiltonian does not commute with the local spin components

$$
[H, S_j^{(s),\alpha}] \neq 0
\tag{1.34}
$$

but it commutes with each component of the total spin:

$$
[H, S^{(s),\alpha}] \equiv \sum_j [H, S_j^{(s),\alpha}] = 0
\tag{1.35}
$$

and thus is fully rotationally invariant, as claimed before.

Another $SU(2)$ symmetry is generated by the components of the charge operator. They are also called pseudo-spin or η-pairing operators and can be obtained from the spin operators by applying a particle-hole transformation solely on the fermion species with down spin, accompanied by a change of sign on the sub-lattice formed by the even sites:

$$c_{j,\uparrow} \to c_{j,\uparrow} \quad , \quad c_{j,\downarrow} \to (-)^j c_{j,\downarrow}^\dagger . \tag{1.36}$$

If we apply (1.36) to (1.30) and (1.32), we get

$$\begin{aligned}
S_j^{(c),x} &= \frac{(-)^j}{2} \left(c_{j,\uparrow}^\dagger c_{j,\downarrow}^\dagger + c_{j,\downarrow} c_{j,\uparrow} \right) \\
S_j^{(c),y} &= \frac{(-)^j}{2\imath} \left(c_{j,\uparrow}^\dagger c_{j,\downarrow}^\dagger - c_{j,\downarrow} c_{j,\uparrow} \right) \\
S_j^{(c),z} &= \frac{1}{2} \left(c_{j,\uparrow}^\dagger c_{j,\uparrow} - c_{j,\downarrow} c_{j,\downarrow}^\dagger \right) = \frac{1}{2} \left(n_{j,\uparrow} + n_{j,\downarrow} - 1 \right) \\
S_j^{(c),+} &= (-)^j c_{j,\uparrow}^\dagger c_{j,\downarrow}^\dagger \\
S_j^{(c),-} &= (-)^j c_{j,\downarrow} c_{j,\uparrow} .
\end{aligned} \tag{1.37}$$

These can also be obtained applying the transformation directly to the local operators in eq. (1.28). In this case, we get the compact form

$$S_j^{(c),\alpha} = \frac{1}{2} \begin{pmatrix} c_{j,\uparrow}^\dagger & (-)^j c_{j,\downarrow} \end{pmatrix} \begin{pmatrix} (\sigma^\alpha)_{\uparrow\uparrow} & (\sigma^\alpha)_{\uparrow\downarrow} \\ (\sigma^\alpha)_{\downarrow\uparrow} & (\sigma^\alpha)_{\downarrow\downarrow} \end{pmatrix} \begin{pmatrix} c_{j,\uparrow} \\ (-)^j c_{j,\downarrow}^\dagger \end{pmatrix} . \tag{1.38}$$

The total operators obtained by summing each equation in (1.37) over j obey the same commutation rules (1.33) and commute with the Hubbard Hamiltonian

$$[H, S^{(c),\alpha}] = 0 . \tag{1.39}$$

However we notice that this relations hold only for lattices with an even number of sites. That imposes some restrictions on joint irreducible representations of spin and charge realized on eigenstates of the Hubbard Hamiltonian. In fact $S^{(s),z} + S^{(c),z} = \hat{N}_\uparrow - \frac{L}{2}$ is an integer when L is even, implying that not all representations of $SU(2) \times SU(2)$ are present. Thus the complete continuous symmetry of Hamiltonian (1.27) is given by

$$SU(2) \times SU(2)/\mathbb{Z}_2 = SO(4) . \tag{1.40}$$

Further clarifications about the role of the two SU(2) symmetries are given in Appendix A. However, here we still want to mention that the transformation (1.36) not only maps the spin sector into the charge sector, but also maps the repulsive U regime into the attractive U regime, when applied to Hamiltonian (1.27). Indeed the latter transforms as

$$H(t,U) \to H(t,-U) \tag{1.41}$$

under (1.36), thus being invariant modulo sign of the coupling.

We observe that the presence of a magnetic field term (meaning a term proportional to $S^{(s),z}$) in the Hamiltonian would break the rotational invariance, whereas a chemical potential term (meaning a term proportional to $\hat{N}$ or equivalently $S^{(c),z}$) would break the η-symmetry. Then the symmetry, in the sector involved, is reduced from full SU(2) (corresponding to the conservation of $(S^{(v)})^2$, $v = s,c$) to U(1) (corresponding to the conservation of $S^{(v),z}$). In fact the conservation of the particle number, for each species, is related to the U(1) gauge symmetry $c_{j,\sigma} \to e^{-\imath\alpha}c_{j,\sigma}$, as we already said.

Discrete symmetries. Finally, we would like to mention that, in addition to the SO(4) continuous symmetry, the Hubbard Hamiltonian has many discrete symmetries. Among them, the most common are

1. the lattice translations on a ring of L sites $c_{j,\sigma} \to c_{j+r,\sigma}$ (if we assume PBC);

2. the symmetry under reflection $c_{j,\sigma} \to c_{L-j+1,\sigma}$;

3. the already mentioned particle-hole symmetry for bipartite lattices $c_{j,\sigma} \to (-)^j c_{j,\sigma}^\dagger$;

4. the symmetry under spin-flips $c_{j,\sigma} \to c_{j,\bar{\sigma}}$;

5. the time-reversal symmetry $c_{j,\sigma} \to \sigma c_{j,\bar{\sigma}}$ (where we associate a plus sign to the species $\sigma = \uparrow$ and a minus sign to the species $\sigma = \downarrow$).

We observe that only the Hamiltonian (1.27) is invariant under the particle-hole symmetry and not the Hamiltonian (1.16). In fact the particle number operator $n_{j,\sigma}$ under this symmetry transforms into $1 - n_{j,\sigma}$ so that the interaction term counts the number of empty sites instead of that of doubly occupations. This is equivalent to say that a term proportional to $L - \hat{N}$ is added to the Hamiltonian. However it disappears in case of filling $n = 1$. In this case the particle-hole transformation turns out to be a symmetry also for the Hamiltonian (1.16).

1.2.3 Physical properties

Apart form the physical parameters t and U, the behavior of the system is determined by the dimension D of the lattice, the temperature T and the filling n. Hereinafter we will restrict our discussion to the case of zero temperature and half-filling balanced ($N_\uparrow = N_\downarrow = L/2$) systems , and we will mainly focus on low dimensional lattices ($D = 1, 2$).

Except for the two limiting cases $t = 0$ and $U = 0$, the Hubbard model is exactly solvable only in $1D$, by means of the Bethe Ansatz approach. The system turns out to be insulating in its ground state (GS) at any $U > 0$. The nature of this insulator is different from that of the usual band insulators. In fact, here the charge gap is produced by the interaction among the electrons. This kind of phase is called Mott insulator (MI). In the attractive case, the role of charge and spin degrees of freedom are exchanged; thus the ground state is formed by a spin gapped metallic phase. The spin gap is the energy paid to reverse one spin, thus to pass from the subspace $S^{(s),z} = 0$ to the subspace $S^{(s),z} = 1$.

Also for $D = 2, 3$, the entire repulsive U regime is characterized by an insulating behavior. Besides that, it shows long-range antiferromagnetic correlations [9, 10]. We observe that this cannot occur in $1D$, since it would break the continuous spin rotational $SU(2)$ symmetry, thus violating the Mermin-Wagner theorem. Instead, at $U < 0$, the system shows superconducting properties. In fact, by applying the partial particle-hole transformation (1.36), one can verify that the existence of long-range magnetic order in the repulsive case implies the existence of long-range superconducting order in the attractive case.

The main features of these phases can be derived in the strong coupling limit. In particular, in the repulsive regime the Hubbard Hamiltonian (1.15) can be mapped into an effective t-J model by using a perturbation theory which includes projection onto the restricted Hilbert space with no doubly occupied sites. At half-filling the distribution of fermions on the lattice corresponds to exactly one particle per site and the t-J Hamiltonian reduces to an isotropic antiferromagnetic spin-$1/2$ Heisenberg Hamiltonian

$$H_{Heis.} = J \sum_j \left(\vec{S}_j^{(s)} \cdot \vec{S}_{j+1}^{(s)} - \frac{1}{4} \right) \tag{1.42}$$

with exchange coupling $J = 4t^2/U$.

Most features and results about the Hubbard model can be found in [8, 11, 12].

1.2.4   Mapping to spin models

To conclude this section, we would like to do some considerations about the relation
between fermion systems and spin systems.

In eq. (1.28) we have introduced the spin-1/2 operators and expressed them in
terms of fermions. This is known as the Schwinger representation and was first
introduced to relate the spin operators to the boson operators. Then it was generalized
to fermions.

We want to mention that there exist other ways to represent the spin $su(2)$ algebra in
terms of fermions. These are the Jordan-Wigner and the Majorana representations.
Here we describe just the first one and refer the interested reader to Refs. [13, 14].
The local Hilbert space for fermion systems is formed by the four states (1.22).
Since the dimension of the local Hilbert space for a spin-S system is $(2S+1)$, one
can write a fermionic Hamiltonian as a two-spin-1/2 Hamiltonian. Let's start by
recalling the Jordan-Wigner mapping for spinless fermions.

$$
\begin{aligned}
\tilde{S}_j^z &= n_j - 1/2 \\
\tilde{S}_j^+ &= e^{\imath \pi \Sigma_{l<j} n_l} c_j^\dagger \\
\tilde{S}_j^- &= e^{-\imath \pi \Sigma_{l<j} n_l} c_j \, .
\end{aligned}
\tag{1.43}
$$

Here the $\tilde{S}$ operators are spin-1/2 Pauli operators. This transformation could also
be applied to spinfull fermions. However, in this case one gets that the fermions of
different species obey commuting relations instead of the usual anticommuting rules.
In order to fulfill the latters, we need to modify the transformation for just one of the
two species. Thus the correct mapping turns out to be

$$
\begin{aligned}
\tilde{S}_{j,1}^z &= n_{j,\uparrow} - 1/2 & \tilde{S}_{j,2}^z &= n_{j,\downarrow} - 1/2 \\
\tilde{S}_{j,1}^+ &= K_{j,\uparrow} c_{j,\uparrow}^\dagger & \tilde{S}_{j,2}^+ &= K_\uparrow K_{j,\downarrow} c_{j,\downarrow}^\dagger \\
\tilde{S}_{j,1}^- &= K_{j,\uparrow}^\dagger c_{j,\uparrow} & \tilde{S}_{j,2}^- &= K_\uparrow^\dagger K_{j,\downarrow}^\dagger c_{j,\downarrow}
\end{aligned}
\tag{1.44}
$$

where we have introduced the non-local operators Ks, defined as

$$
K_{j,\sigma} = e^{\imath \pi \Sigma_{l<j} n_{l,\sigma}} = \prod_{l<j}(1 - 2n_{l,\sigma})
$$

$$
\bar{K}_{j\sigma} = e^{\imath \pi \Sigma_{l>j} n_{l,\sigma}} = \prod_{l>j}(1 - 2n_{l,\sigma})
$$

$$
K_\sigma = e^{\imath \pi \Sigma_l n_{l,\sigma}} = \prod_l (1 - 2n_{l,\sigma}) \, .
$$

We observe that each of the local exponential operators forming the non-local operators commute with annihilation and creation operators when they do not act on the same lattice site

$$[e^{\iota\pi n_{j,\sigma}}, c_{i,\sigma}] = 0 \qquad \text{if} \quad j \neq i. \tag{1.45}$$

Meanwhile, when acting on the same site, the following useful identities hold

$$
\begin{aligned}
c_{j,\sigma}^{\dagger} e^{\iota\pi n_{j,\sigma}} &= c_{j,\sigma}^{\dagger}(1 - 2n_{j,\sigma}) = c_{j,\sigma}^{\dagger} \\
e^{\iota\pi n_{j,\sigma}} c_{j,\sigma} &= (1 - 2n_{j,\sigma})c_{j,\sigma} = c_{j,\sigma} \\
e^{\iota\pi n_{j,\sigma}} c_{j,\sigma}^{\dagger} &= (1 - 2n_{j,\sigma})c_{j,\sigma}^{\dagger} = -c_{j,\sigma}^{\dagger} \\
c_{j,\sigma} e^{\iota\pi n_{j,\sigma}} &= c_{j,\sigma}(1 - 2n_{j,\sigma}) = -c_{j,\sigma} \, .
\end{aligned}
\tag{1.46}
$$

Thus their effect consists, at most, in a change of sign.

1.3   The 1D extended Hubbard model

A natural generalization of the Hubbard model consists in adding the nearest-neighbor interaction deriving from the Coulomb repulsion to the Hamiltonian. This is the so-called extended Hubbard model. The Hamiltonian reads

$$H = -t\sum_{j=1}^{L}\sum_{\sigma=\uparrow,\downarrow}\left(c_{j,\sigma}^{\dagger}c_{j+1,\sigma} + h.c.\right) + U\sum_{j=1}^{L}n_{j,\uparrow}n_{j,\downarrow} + V\sum_{j=1}^{L}n_j n_{j+1}, \tag{1.47}$$

where *h.c.* denotes the hermitian conjugate. It shares the same symmetries of the Hubbard model, except for the SU(2) η-symmetry, which is reduced to U(1). This model has been intensively studied [15–24]. In fact, it presents a much richer phase diagram then the simple Hubbard model. In particular, in the repulsive regime, although the system is always insulating, three different orders can be distinguished. Around the line $U \approx 2V$ the Mott phase is replaced by a small bond ordered wave (BOW) phase, while below it a charge density wave (CDW) phase appears. These emerge as a result of the competition between the *U* and *V* interactions. Indeed the interaction among nearest-neighbor sites contrasts the tendency of uniformly distributing the fermions on the lattice due to the on-site repulsion and favors the alternation of holons (empty sites) and doublons (doubly occupied sites). In fact, for large enough *V*, this is the picture of the ground state with CDW order. Instead, the BOW phase is characterized by pairs of both holons/doublons and up/down spins

on near sites. For negative V, the system shows some phase transitions to several metallic phases, i.e. the phase separated (PS) phase and two phases with dominant singlet superconducting (SS) or triplet superconducting (TS) correlations. The PS is induced by a strong attractive V, which produces a separate condensation of holons and doublons with a non-zero spin gap. This remains finite at the transition with the SS region, making it a Luther Emery (LE) phase, and vanishes in the TS region, which is, therefore, a gapless Luttinger Liquid (LL) phase. Figure 1.1a shows the phase diagram of the model. The phases here introduced will be better characterized in the following chapters.
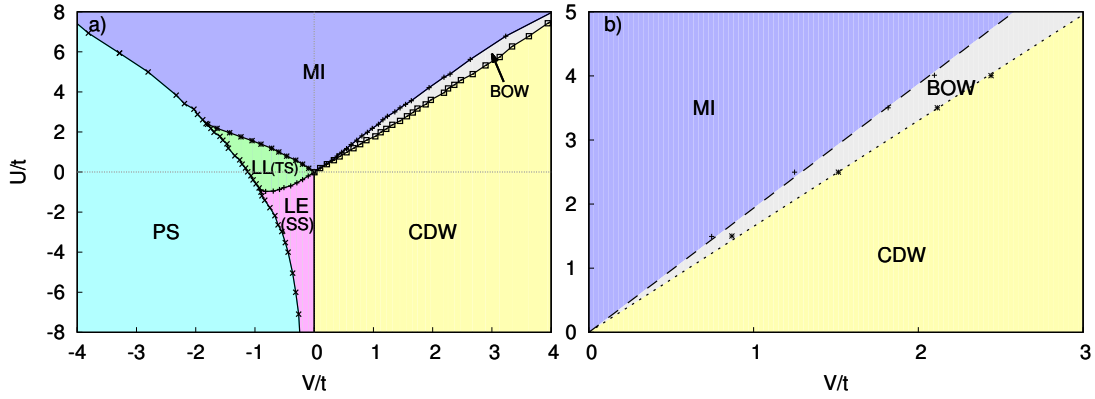
Fig. 1.1 a) Phase diagram of the extended Hubbard model. The figure has been reproduced by extrapolating data from ref. [25]. b)Phase diagram of the extended Hubbard model with long-range dipolar interaction in the repulsive regime. The figure has been reproduced by extrapolating data from ref. [26].

The effect of long-range dipolar interaction $V \sum_{i \neq j} \frac{n_i n_j}{|i-j|^3}$ on the ground state of the extended Hubbard model has also been studied [26] in the repulsive regime. The results show a stabilization of the BOW phase. In Figure 1.1b), we present the phase diagram.

1.4 The 1D bond-charge Hubbard model

Another well known generalization of the Hubbard Hamiltonian is the bond-charge Hubbard model, in which the hopping term incorporates a density-dependent two-

body contribution

$$H = -t \sum_{j=1}^{L} \sum_{\sigma=\uparrow,\downarrow} \left(c_{j,\sigma}^{\dagger} c_{j+1,\sigma} + h.c. \right) \left[1 - \frac{X}{t} \left(n_{j,\bar{\sigma}} + n_{j+1,\bar{\sigma}} \right) \right] + U \sum_{j=1}^{L} n_{j,\uparrow} n_{j,\downarrow} . \tag{1.48}$$

This is also called correlated hopping, since the amplitude of the hopping processes varies according to the occupation of the sites involved. In fact, the bond-charge interaction X naturally arises in systems with extended orbitals, where the charge in the bond affects the screening and therefore the effective potential acting on valence electrons. This model can be usefully rewritten in terms of Hubbard operators (see Appendix A):

$$H = -t \sum_{j=1}^{L} \sum_{\sigma=\uparrow,\downarrow} \left[X_j^{\sigma 0} X_{j+1}^{0\sigma} + \left(1 - \frac{X}{t} \right) \sigma \left(X_j^{\sigma 0} X_{j+1}^{\bar{\sigma} 2} + X_j^{2\bar{\sigma}} X_{j+1}^{0\sigma} \right) + \right. $$
$$\left. \left(1 - \frac{2X}{t} \right) X_j^{2\bar{\sigma}} X_{j+1}^{\bar{\sigma} 2} \right] + h.c. + U \sum_{j=1}^{L} X_j^{22} . \tag{1.49}$$

We observe that for $X = t$, this reduces to the following particle-hole symmetric model

$$H = -t \sum_{j=1}^{L} \sum_{\sigma=\uparrow,\downarrow} \left[X_j^{\sigma 0} X_{j+1}^{0\sigma} + X_j^{2\bar{\sigma}} X_{j+1}^{\bar{\sigma} 2} \right] + h.c. + U \sum_{j=1}^{L} X_j^{22} \tag{1.50}$$

which is exactly solvable [27, 28]. The exact solution is facilitated by the symmetries. In particular, $[\hat{T}, \hat{U}] = 0$ in (1.50) implies that the number of doublons is conserved. At half filling, it is characterized by a Mott insulator for $U \geq 4$ and by a superconducting phase which contains both singly and doubly occupied sites for $U < 4$. This phase extends into the region of negative U, until $U = -4$. Below this point, the state is still superconducting but does not contain singly occupied sites. Figure 1.2a) shows the phase diagram as a function of the filling. The region above the curve is characterized by the maximum number of singly occupied sites. However, only at half filling it shows an insulating behavior.
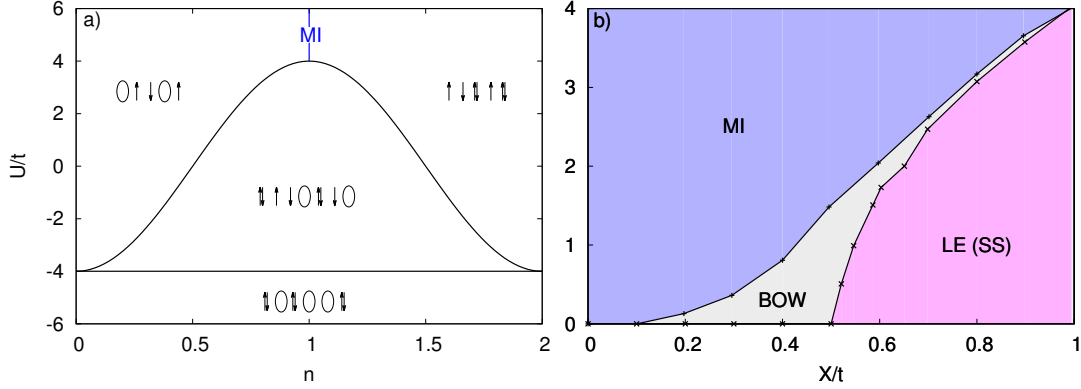
Fig. 1.2 a) Phase diagram of the bond-charge Hubbard Hamiltonian at $X/t = 1$ (eq. 1.50) as a function of the filling n. b) Phase diagram of the bond-charge Hamiltonian (1.48). The figure has been reproduced by extracting data from ref. [29].

For a generic X the ground state (at half filling) shows three different phases in the repulsive regime: MI, BOW and LE with dominant SS correlations [29]. The phase diagram is depicted in Figure 1.2b).

We observe that, while the Hamiltonian (1.48) in general breaks the continuous η-symmetry and the particle-hole symmetry, these are restored[1] in the integrable case $X/t = 1$. For arbitrary X, both symmetries can be rebuilt by modifying the correlated hopping term in the following way

$$
H = -t \sum_{j=1}^{L} \sum_{\sigma=\uparrow,\downarrow} \left(c_{j,\sigma}^{\dagger} c_{j+1,\sigma} + h.c. \right) \left[1 - \frac{X}{t} \left(n_{j,\bar{\sigma}} - n_{j+1,\bar{\sigma}} \right)^2 \right] + U \sum_{j=1}^{L} n_{j,\uparrow} n_{j,\downarrow} .
$$
(1.51)

At $X/t = 1$ this system shows the same ground state of Hamiltonian (1.50) (Fig. 1.2a) [27]. Hamiltonian (1.51) is a particular case of the more general Hamiltonian

$$
H = -t \sum_{j=1}^{L} \sum_{\sigma=\uparrow,\downarrow} \left(c_{j,\sigma}^{\dagger} c_{j+1,\sigma} + h.c. \right) \left[1 - \frac{X}{t} \left(n_{j,\bar{\sigma}} + n_{j+1,\bar{\sigma}} \right) + \frac{\tilde{X}}{t} n_{j,\bar{\sigma}} n_{j+1,\bar{\sigma}} \right] + \hat{U} ,
$$
(1.52)

obtained by setting $\tilde{X} = 2X$. Here $\hat{U} = U\hat{D}$ is the usual on-site interaction. The three-body term is not obtained from the Coulomb interaction, but can be derived from a three band model. In fact, (1.52) was derived from the three band model as an effective one-band Hamiltonian for the description of cuprate superconductors [30]. Here, its presence can be justified by the fact that it can be implemented in cold

---

[1]Note that in order to fully restore the η-symmetry the on-site interaction should be written as $(n_{j,\uparrow} - 1/2)(n_{j,\downarrow} - 1/2)$.

atom systems. In terms of Hubbard operators, it reads

$$
H = -t \sum_{j=1}^{L} \sum_{\sigma=\uparrow,\downarrow} \left[X_j^{\sigma 0} X_{j+1}^{0\sigma} + \left(1 - \frac{X}{t}\right) \sigma \left(X_j^{\sigma 0} X_{j+1}^{\bar{\sigma} 2} + X_j^{2\bar{\sigma}} X_{j+1}^{0\sigma} \right) + \\
\left(1 - \frac{2X}{t} + \frac{\tilde{X}}{t}\right) X_j^{2\bar{\sigma}} X_{j+1}^{\bar{\sigma} 2} \right] + h.c. + U \sum_{j=1}^{L} X_j^{22} .
$$

(1.53)

Some results about this model will be given in the next section.

1.5 Other extensions

The Hamiltonian (1.52) has also been studied in the presence of the nearest-neighbor interaction

$$
H = -t \sum_{j=1}^{L} \sum_{\sigma=\uparrow,\downarrow} \left(c_{j,\sigma}^\dagger c_{j+1,\sigma} + h.c. \right) \left[1 - \frac{X}{t} \left(n_{j,\bar{\sigma}} + n_{j+1,\bar{\sigma}} \right) + \frac{\tilde{X}}{t} n_{j,\bar{\sigma}} n_{j+1,\bar{\sigma}} \right] \\
+ U \sum_{j=1}^{L} n_{j,\uparrow} n_{j,\downarrow} + V \sum_{j=1}^{L} n_j n_{j+1} .
$$

(1.54)

This model is symmetric under the continuous SU(2) symmetry[2] in the charge sector only for $V = 2X - \tilde{X} = 0$, while in the general case the η-symmetry is reduced to U(1). Moreover, it is not invariant under the particle-hole symmetry, which holds only for $\tilde{X} = 2X$.

However, as (1.48), the model (1.54) has an integrable point at $X/t = 1$. In this case, three phases are found [31] in the repulsive V regime: a MI for large and positive values of U, a CDW in the strong repulsive V regime and a metallic phase, not better characterized, in an extended region around the origin U=V=0. The phase diagram is shown in Figure 1.3.

---

[2]Note that in order to have the full η-symmetry the on-site interaction should be written as $(n_{j,\uparrow} - 1/2)(n_{j,\downarrow} - 1/2)$, and $V = 2X - \tilde{X} = 0$.
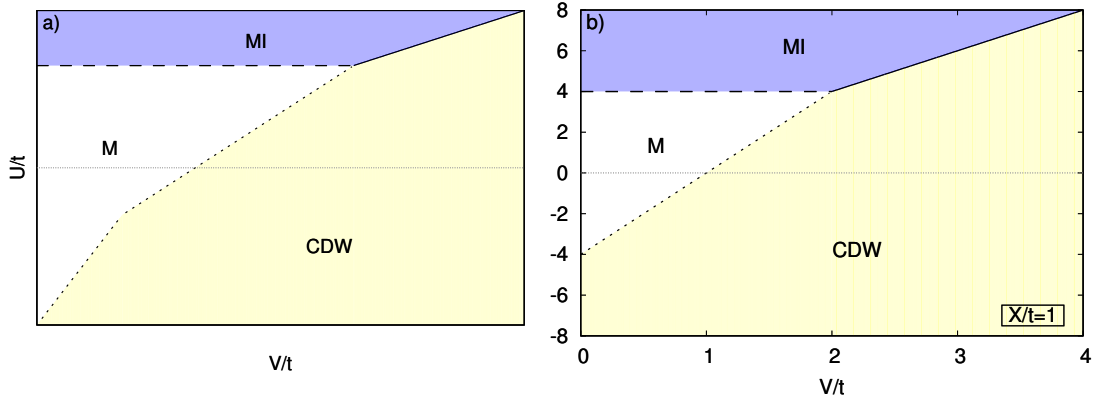
Fig. 1.3 a) Phase diagram of Hamiltonian (1.54) at $X/t = 1$. It is identified by the following lines: $U = 2V$, $U = 4V - 2(1 + |1 - \tilde{X}|)$, $U = 8V - 4\max(1, |1 - \tilde{X}|)$, $U = 2(1 + |1 - \tilde{X}|)$, where we have set $t = 1$ [31]. b) Phase diagram of Hamiltonian (1.54) at $X/t = 1$ and $\tilde{X} = 2X$.
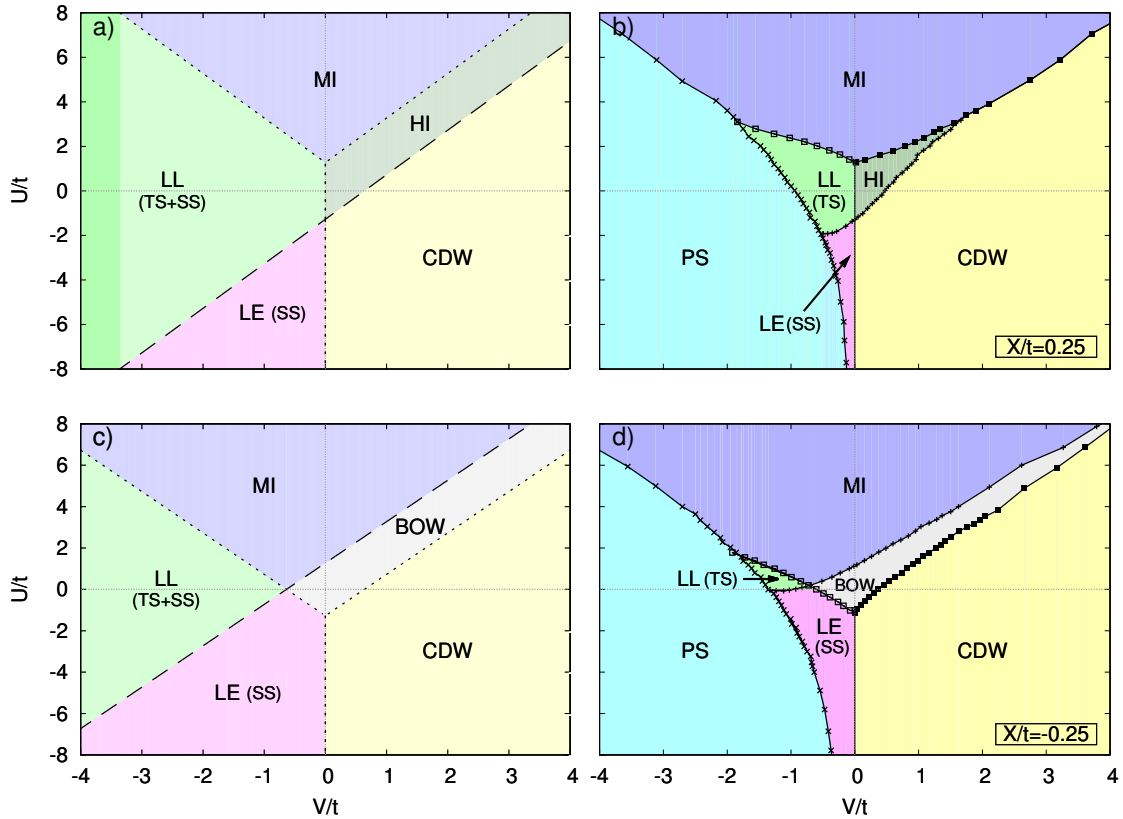
Fig. 1.4 Phase diagram of Hamiltonian (1.54) at $\tilde{X} = 2X$ and $|X/t| = 0.25$ as obtained from bosonization (left column) and numerical simulations (right column). Figures a),b) refer to the case $X/t = 0.25$, while Figures c),d) refer to the case $X/t = -0.25$. The bosonization transition lines have been obtained for a generic $\tilde{X}$ [32]. They are given by: $U - 2|V| + 8|\tilde{X}|/\pi$ and $U - 2V - 8|\tilde{X}|/\pi$. Along the dotted (dashed) lines the charge (spin) gap is zero. Figures b),d) have been reproduced by extracting data from ref. [25].

The general case has been studied in the weak coupling regime by means of bosonization [32]. In this limit, the X-term leads only to a renormalization of the hopping amplitude t [33]. Instead the three-body term plays an important role. Indeed, the metallic phase is replaced by an Haldane insulator (HI) for $\tilde{X} > 0$ and by a BOW phase for $\tilde{X} < 0$ [32]. These results have been confirmed numerically in the particle-hole symmetric case $\tilde{X} = 2X$ [25]. Moreover, in the attractive (U,V) regime, the bosonization predicts the existence of phases with dominant superconducting correlations, while in the particle-hole symmetric strong coupling limit numerical simulations show the occurrence of a phase separation. Finally, at $V = 0$ the ground state is described by a MI for $U > 8|\tilde{X}|/\pi$, by a LE phase for $U < -8|\tilde{X}|/\pi$, and by a Luttinger liquid (if $\tilde{X} > 0$) or a BOW (if $\tilde{X}<0$) in the middle region delimited by the two critical points. These results are summarized in Fig. 1.4.

1.6 The Bose-Hubbard model

Thanks to the possibility to realize condensed matter systems in cold atom experiments, great attention has been devoted also to the Hubbard model with bosonic particles. This is called the Bose-Hubbard model and is described by the following Hamiltonian

$$H = -t \sum_{\langle i,j \rangle} \left(b_i^\dagger b_j + h.c. \right) + \frac{U}{2} \sum_i n_i(n_i - 1) \tag{1.55}$$

where $b_i^\dagger$ (b_i) creates (destroys) a boson on the site i and $n_i = b_i^\dagger b_i$. This Hamiltonian is invariant under a global $U(1)$ transformation. It is obtained by applying the operator $e^{\iota \phi n_i}$ (with $\phi \in [0, 2\pi]$) at each site, and corresponds to the conservation of the total particle number.

As usual, we focus on the case $n = 1$. In the weak coupling regime, the phase diagram presents a superfluid (SF) region. As the strength of the interaction is increased, the system undergoes a transition to a MI phase (see Fig. 1.5). This behavior is observed in one, two and three spatial dimensions. The respective critical values at which the transition occurs are $U_c/t \approx 3.3$ in $D = 1$ [34], $U_c/t \approx 18$ in $D = 2$ [35, 36], and

Fig. 1.5 Phase diagram of the Bose-Hubbard model (1.55).

$U_c/t \approx 29.3$ in $D = 3$ [37]. In the limiting case $U = 0$, the ground state is given by

$$|\Phi\rangle_{U=0} \propto \left(\sum_i b_i^\dagger\right)^N |0\rangle, \qquad (1.56)$$

which shows Bose-Einstein condensation in the zero-momentum Bloch state. Indeed the creation operator associated to the zero-momentum Bloch state is proportional to $\sum_i b_i^\dagger$. Thus, each particle is delocalized over the entire lattice, and the superfluid state is described by a macroscopic wave function. In the opposite limit $t = 0$, the ground state has the form

$$|\Phi\rangle_{t=0} \propto \prod_i (b_i^\dagger)^{n_i} |0\rangle = \prod_i |n_i\rangle. \qquad (1.57)$$

Thus it consists of localized wave functions with a fixed number of bosons in each lattice site that minimizes the interaction energy.

Chapter 2

Phase transitions and classification of quantum phases of matter

A phase transition is a change of the equilibrium state of a system - which implies a sudden change of one or more physical properties - due to a small variation of some externally controllable parameters. In the case of classical phase transitions (CPTs), this role is played by a thermodynamic variable, typically the temperature. Instead, quantum phase transitions (QPTs) occurring at zero temperature are driven by a physical parameter, such as magnetic field. The CPTs arise from the thermal fluctuations, which vanish at zero temperature and therefore no phase transition can occur at $T = 0$. However quantum fluctuations, arising from Heisenberg's uncertainty principle, are present and are responsible for QPTs. These occur at the quantum critical point (QCP), where quantum fluctuations diverge and become scale invariant in space and time. Although absolute zero is not physically realizable, characteristics of the transition can be detected in the low-temperature behavior of the system near the critical point. Indeed, at non-zero temperatures, quantum fluctuations compete with classical fluctuations and dominate the system behavior until their energy scale is larger than $k_B T$ (where k_B is the Boltzmann constant). This condition marks the so-called quantum critical region (see Fig. 2.1).

At each side of the transition, the order of the system changes. Thus, the transition can be described by an order parameter, which behavior is different in the two phases. Typically, it is non-zero in the ordered phase and vanishes in the disordered one. Phase transitions can be classified according to the behavior of the order parameter near the critical point. If it is discontinuous, the transition is first-order. If instead it
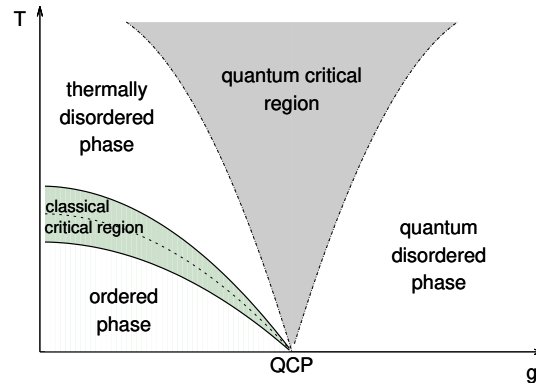
Fig. 2.1 Phase diagram of classical and quantum phase transitions. Here T is the temperature and g is the quantum tuning parameter.

changes from zero to a non-zero value in a continuous way, the transition is second-order (or continuous). In the latter case, the correlation length diverges, giving rise to the so-called critical phenomena. Indeed the infinite correlation length implies that fluctuations are present at each length scale, since they extend over the whole many-body system. Thus the system is scale invariant, meaning that it looks similar at every length scale and the renormalization group method [38, 39] can be applied. The above classification of phase transitions has been developed for CPTs. When these concepts are applied to QPTs, great attention should be paid. In fact the physics underlying QPTs is quite complex and not completely understood yet. In the following sections we will first remind the theory of CPTs and then we will discuss QPTs. After that we will introduce some useful tools to study several new phases that have been discovered in the last decades and that cannot be included in the Landau symmetry breaking (SB) scheme [40–43].

2.1   Classical Phase Transitions

As mentioned before, phase transitions are traditionally classified into first order and continuous or second-order transitions. This classification was firstly introduced by Paul Ehrenfest basing on the singularities of the free energy derivatives. In particular, a transition is said to be first order if a first derivative of the free energy (e.g. the magnetization) is discontinuous at the transition point. Often this discontinuity is accompanied by a jump in the entropy, thus involving a latent heat $Q = T\Delta S$ (being

$\Delta S = S_2 - S_1$ the difference between the entropies of the two phases). This is also related with the possible coexistence of two phases at the critical point. Indeed the presence of latent heat implies an absorption or release of energy, which cannot occur instantaneously. If, instead, all the first derivatives of the free energy are continuous but a second derivative (e.g. the susceptibility or the specific heat) has a discontinuity, the transition is classified as continuous or second order. In this case the latent heat is not involved and the different phases do not coexist. Although the nomenclature of the Ehrenfest classification is still used, very often the literature disagrees on the precise definition of these concepts. In fact the Ehrenfest classification does not take into account the case in which a derivative of the free energy diverges. In the modern classification it is often referred to first order phase transitions as those involving a latent heat and phase coexistence (such as ice and water at $T = 273.15$ K or water and steam at $T = 373.15$ K). Whereas second order phase transitions are defined in terms of a diverging susceptibility, an infinite correlation length, and a power-law decay of correlations near criticality.

Phase transitions can be accompanied by symmetry breaking, meaning that the state of the system is driven from a highly symmetric phase to a lower symmetric one. An example of first order phase transition with symmetry breaking is the liquid-solid transition, where the continuous translational symmetry is broken. Instead the liquid-vapor transition does not break any symmetry. Second order phase transitions typically involve change of symmetry. In fact they continuously drive the system from a state with higher symmetry to a state with reduced symmetry. The more symmetrical phase is commonly identified as the disordered phase and the less symmetrical one as the ordered phase. Typically the disordered phase dominates the behavior of the system at high temperature, where thermal fluctuations allow the system to access states in a broader range of energies. As the temperature decreases, the thermal agitation does not provide enough energy to let the constituent microscopic particles to arrange themselves in many different configurations. The number of accessible configurations is reduced and an order is established according to the Hamiltonian terms, which overcome the entropy driven term. That results in a reduced symmetry. The symmetry can be spontaneously or explicitly broken. Typically the first case occurs when the Hamiltonian exhibits all the possible symmetries of a system, whereas the ordered state lacks some of them. The symmetry is explicitly broken when some terms in the Hamiltonian do not respect the symmetry of the theory. Usually this is referred to situations in which the symmetry breaking

is small and hence the symmetry is approximately respected. To better clarify these concepts, let's consider an example. One of the most illustrative phase transitions is that occurring in the Ising model between paramagnetic and ferromagnetic states. The Hamiltonian reads

$$H = -\sum_{\langle i,j \rangle} J_{i,j} \sigma_i \sigma_j - \sum_j B_j \sigma_j \tag{2.1}$$

where σ_j are discrete variables taking the values ± 1 and the coupling coefficients are often chosen to be constant: $J_{i,j} = J$ and $B_j = B \; \forall i,j$. Moreover we assume $J > 0$. At zero applied magnetic field, the magnetization varies continuously from zero (in the paramagnetic phase) to finite values (in the ferromagnetic phase) as a function of the temperature. Thus the transition is classified as second-order. At low temperature, where the thermal fluctuations are not sufficient to destroy the order wanted by the Hamiltonian, all the spins are aligned in the same direction, meaning that the system spontaneously chooses one of the two possible degenerate ground states ($\sigma_i = +1 \, \forall i$ or $\sigma_i = -1 \, \forall i$). The ground state breaks the $\mathbb{Z}_2$ symmetry owned by the Hamiltonian[1]. Hence this is a spontaneous symmetry breaking. When the symmetry is spontaneously broken, the ground state is chosen arbitrarily and changing this choice should have zero energy cost. The presence of the magnetic field in the Ising Hamiltonian breaks itself the symmetry (the Hamiltonian is no more $\mathbb{Z}_2$ invariant) and for each value of T induces the state to assume one of the two ferromagnetic configurations, depending on the sign of B. In this case the symmetry is explicitly broken.

Beyond first and second order phase transitions, other kinds of phase transitions can be found. In particular, infinite order phase transitions have the characteristic to be continuous without breaking any symmetry. Among them the most known is the Berezinskii–Kosterlitz–Thouless (BKT) transition, that was first designed to indicate the transition from bound vortex-antivortex pairs at low temperatures to unpaired vortices and anti-vortices at some critical temperature in the two-dimensional XY-model. It involves the presence of topological order and will be discussed later.

---

[1]The original symmetry group is $\mathbb{Z}_2$, containing the trivial identity transformation $\sigma_i \rightarrow \sigma_i$ and the reflection symmetry $\sigma_i \rightarrow -\sigma_i$. As a result of the transition, the $\mathbb{Z}_2$ symmetry group is reduced to the identity transformation, since the ferromagnetic ground state breaks the reflection symmetry. A similar phenomenon occurs in the Heisenberg ferromagnet, which is similar to the Ising model but the spins are allowed to point in a continuum of directions. In this case the parent symmetry is the three dimensional rotation group O(3), which breaks to O(2) as the system is cooled down at low temperature, where it spontaneously magnetizes along a random direction.

For the moment, we focus on the second order phase transitions, which have been well studied in the past century and for which a well known theory exists.

2.1.1   Critical exponents in second order phase transitions

Continuous phase transitions have an associated order parameter. It is a thermodynamic quantity that characterizes the ordered phase, where it is non-zero, and vanishes at the critical point, where the disordered phase takes place. Although the thermodynamic average of the order parameter is zero for $T > T_c$, its fluctuations are non-zero. The spatial correlations of these fluctuations increase as the system is driven towards the transition and become long-ranged as the critical point is approached. A typical behavior is the exponential decay

$$C(i,j) \propto e^{-|\vec{x}_i - \vec{x}_j|/\xi} \qquad (2.2)$$

where ξ is the correlation length. Close to T_c it diverges as

$$\xi \sim |\varepsilon_T|^{-\nu} \qquad (2.3)$$

where

$$\varepsilon_T = \frac{|T - T_c|}{T_c} \qquad (2.4)$$

is a dimensionless parameter estimating the distance from the critical point, and ν is a critical exponent. In general, a critical exponent defines the scaling behavior of a given quantity very close to the critical point of a continuous phase transition. Contrary to the high temperature behavior, for $T < T_c$ the correlation function at large distance is finite; however, the relation (2.3) for the correlation length remains true when approaching the critical point from below. In addition to a diverging correlation length, we also observe a diverging correlation time as $\varepsilon_T \to 0$

$$\tau_c \sim \xi^z \sim |\varepsilon_T|^{-\nu z}. \qquad (2.5)$$

Here z is the dynamic critical exponent. These two divergences are responsible for the so-called critical phenomena. Indeed, close to the transition, the correlation length is the only relevant length scale. Therefore, rescaling all lengths by a common factor leaves the physical properties unchanged and the system is said scale-invariant. In

Table 2.1 Commonly used critical exponents for magnetic systems. D is the space dimensionality. These exponents are related to each other and to the exponent ν.

	definition	conditions
specific heat	$c \sim |\varepsilon_T|^{-\alpha}$	$\varepsilon_T \to 0, B = 0$
magnetization	$m \sim (-\varepsilon_T)^{\beta}$	$\varepsilon_T \to 0^-, B = 0$
susceptibility	$\chi \sim |\varepsilon_T|^{-\gamma}$	$\varepsilon_T \to 0, B = 0$
magnetization	$m \sim \text{sign}(B)|B|^{-\delta}$	$\varepsilon_T = 0, B \to 0$
correlation function	$C(r) \sim \frac{1}{r^{D-2+\eta}}$	$\varepsilon_T = 0, B = 0$

addition to the critical exponents defined above, other critical exponents are usually introduced. The most common for magnetic systems are reported in Table 2.1.

2.1.2   Landau theory for symmetry breaking phases

Landau theory of phase transitions was developed by Landau in 1937 and later generalized to the so-called Ginzburg-Landau theory to study superconductivity. It is a phenomenological theory; hence it is not concerned with the microscopic details of the interactions. Meanwhile it is strictly related to symmetry. In fact, different systems, described by different microscopic theories, which share the same symmetry, may look very similar within the Landau theory. As we will see, this is at the very basis of the idea of universality. The Landau theory applies to symmetry breaking transitions, and in particular to second order phase transitions. Indeed, it relies on the idea that the order parameter is small close to the phase transition. This observation led Landau to suggest that a Taylor expansion of the free energy with respect to the order parameter would provide information about the behavior of the system near the phase transition. Thus the first step of the theory is to identify an order parameter which is non-zero only in the ordered (symmetry breaking) phase. Then, one can proceed to construct the Landau free energy $\mathscr{F}$ as a function of the external parameters (e.g. temperature, pressure, magnetic field) and the order parameter m. It has the following form

$$\mathscr{F} = \mathscr{F}_0 + \sum_n \mathscr{F}_n m^n \ . \tag{2.6}$$

The first term represents the free energy of the highly symmetric phase, where the order parameter is zero. The number of terms in the series can be restricted by

symmetry considerations: it must only contain terms which respect the symmetry of the Hamiltonian (for example, a magnetic system in zero applied magnetic field has the symmetry $m \to -m$, which excludes any odd power of m in (2.6)). Moreover the series is truncated as soon as the physics is captured. For a given set of external parameters, the stable state of the system is obtained by minimizing the free energy with respect to m

$$\frac{\partial \mathscr{F}}{\partial m} = 0 \,. \tag{2.7}$$

Finally, one can compute the critical exponents.

We would like to mention that the critical exponents derived from the Landau theory are not exact in low dimension, since it is based on mean field approximation and neglects fluctuations: the order parameter is treated as being completely uniform in space. Typically the upper critical dimension, above which the approximation is valid, is $D = 4$. For example, this is the case of the Ising model. The upper critical dimension can be obtained from the Ginzburg criterion. In fact, Ginzburg understood how to see what goes wrong with Landau theory. It fails in $D = 1$ and gives only qualitative results in $D = 2, 3$. The issue was solved some decades later by Wilson and others through the renormalization group method [38, 39].

2.1.3   Universality

The concept of universality is related to the behavior of the system near the critical point. As we have discussed in Section 2.1.1, the physical properties close to a second order phase transition are described by the critical exponents. As argued by Landau, those depend only on the symmetry of the system and the dimension of the space. This phenomenon is known as universality and systems which share the same critical exponents are said to belong to the same universality class. In fact, near criticality the microscopic details of the Hamiltonian become unimportant and different Hamiltonians with the same symmetries show a similar behavior.

2.2   Quantum Phase Transitions

A quantum phase transition is the transformation of a system from one phase of matter to another at zero temperature. It implies an abrupt change in the ground
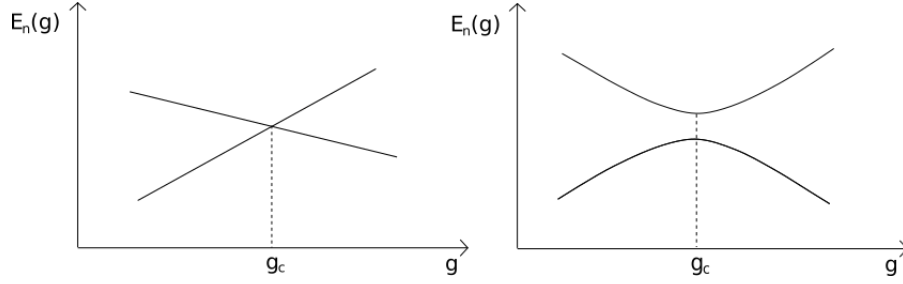
Fig. 2.2 Low eigenvalues E of an Hamiltonian $H(g)$ as a function of g. *Left:* Actual level crossing. It can occur in the case $H(g) = H_0 + gH_1$ and $[H_0, H_1] = 0$. *Right:* Avoided level crossing. It occurs in most cases.

state due to quantum fluctuations. In fact, at finite temperature quantum fluctuations compete with thermal fluctuations. At high enough temperatures, the quantum fluctuations are completely destroyed and a purely classical theory is applicable. In order to establish the range of validity of the classical picture, one has to compare the typical energy scales of long-distance order parameter fluctuations. The typical energy of quantum fluctuations is $\hbar\omega_{typ}$ (ω_{typ} being the typical frequency at which the important degrees of freedom at long distance fluctuate), whereas the thermal energy is $k_B T$. The behavior of the order parameter fluctuations crosses over from classical to quantum when $k_B T < \hbar\omega_{typ}$.

At $T = 0$, the transition is driven by a parameter g appearing in the Hamiltonian $H(g)$ as a dimensionless coupling. By varying g, one can follow the evolution of the ground state energy $E_{GS}(g)$. In general, for a finite lattice, it will be an analytic function of g. An exception is obtained when the Hamiltonian has the form

$$H(g) = H_0 + gH_1 \qquad \text{with } [H_0, H_1] = 0. \tag{2.8}$$

Indeed, in this case H_0 and H_1 can be simultaneously diagonalized, meaning that there exist a common set of eigenfunctions $\{|\psi_n\rangle\}$ for H_0, H_1 and $H(g)$, with eigenvalues $\{E_n^{(0)}\}$, $\{E_n^{(1)}\}$ and $\{E_n(g) = E_n^{(0)} + gE_n^{(1)}\}$, respectively. Thus, although the eigenvalues of $H(g)$ depend on g, its eigenfunctions are independent of g. That entails the possibility of a level crossing between the ground state $E_0(g)$ and an excited state $E_1(g)$ at some critical point $g = g_c$ (see Fig. 2.2, *left panel*). To better explain this concept, let's fix the value of the coupling constant $g = \bar{g}$. For this value, the ground state of the system is found in a given phase A and its energy is $E_{GS}^A(\bar{g}) = \min_n \{E_n(\bar{g})\}$. Suppose the minimum of the energy in this phase is obtained for $n = 0$: $E_{GS}^A(\bar{g}) \equiv E_0(\bar{g})$. Then let's start to tune g with continuity. The energy of

the ground state $E_{GS}^A(g) \equiv E_0(g)$ varies with continuity as a function of g, until it reaches a critical point $g = g_c$. Here the energy of the first excited state equals that of the ground state:

$$E_1(g_c) = E_0(g_c) \,, \tag{2.9}$$

and for $g > g_c$ it becomes smaller. Then the ground state energy switches to $E_{GS}^B(g) \equiv E_1(g)$. The system has passed from the phase A to the phase B through the critical point $g = g_c$ identified as a point of non-analyticity in $E_{GS}(g)$. In fact a phase transition is defined as a point of non-analyticity in the ground state energy of the system in the limit of an infinite lattice. This can emerge from a level crossing in the finite size system as well as the limiting case of an avoided level crossing (see Fig. 2.2, *right panel*). Indeed, in the latter case the gap between the energy of the first excited state and that of the ground state could become smaller and smaller as the size L of the system is increased and reduces to zero in the limit $L \to \infty$.

Similarly to CPTs, also QPTs can be classified as first or second order phase transitions. Different definitions can be found in the literature. In Ref. [44], a first order phase transition is associated with a singularity arising from a simple level crossing, which could occur also in a finite lattice system. In this case one does not observe diverging correlations. By contrast, second order phase transitions are associated with an avoided level crossing. In Ref [45], second order phase transitions are related to the fact that the characteristic energy scale of fluctuations above the ground state (i.e., the energy gap Δ, if this is non-zero) vanishes when $g \to g_c$, and the characteristic length scale (i.e., the correlation length) diverges. We agree that second order phase transitions show a diverging correlation length, in analogy with the classical case[2]. On the other hand, the behavior of the energy gap near the critical point could reveal the nature of the phase transition. In fact, in most first order phase transitions, it closes exponentially fast, contrary to the polynomial decay typically observed in second order phase transitions[3]. Here

$$\Delta \sim |g - g_c|^{z\nu} \,. \tag{2.10}$$

This behavior holds for both $g > g_c$ and $g < g_c$, with the same critical exponent $z\nu$, which value is universal, but with different constants of proportionality. The

---

[2]In analogy with CPTs, we will also recognize first order phase transitions as showing a jump in the order parameter (see Chapter 6).

[3]We observe that the behavior described above is typical of most phase transitions, but some exceptions have been found (see, for instance, [46]).

correlation length diverges as

$$\xi^{-1} \sim \Lambda |g - g_c|^{\nu}, \qquad (2.11)$$

hinting that $\Delta \sim \xi^{-z}$.

Strictly speaking, QPTs occur only at $T = 0$. However, all experiments are carried out at some finite temperature. For small enough temperatures, around the critical point $g = g_c$, we observe the interplay between quantum and thermal fluctuations. Thus, a central task is to understand the effects of the singularity at $T = 0$ on the $T > 0$ regime. Two cases can be distinguished. In the first one, the singularity occurs only at $T = 0$ and all properties are analytic functions of g at $T > 0$[4]. The second possibility occurs when the singularity at $T = 0$ is the end point of a line describing a classical second order phase transition, along which the thermodynamic free energy is not analytic. Along this line, $\hbar \omega_{typ} << k_B T$ and a purely classical description can be applied. Consequently, the singularity at $T = 0$ can be inferred by the classical theory. In both cases, several regions can be identified (see Fig. 2.1). In the thermally disordered region, the long-range order is mainly destroyed by thermal fluctuations of the order parameter, whereas in the quantum disordered region the physics is controlled by the quantum fluctuations and the ground state looks similar to that observed at $T = 0$ and $g > g_c$. In the quantum critical region ($k_B T \sim \hbar \omega_{typ} \sim |g - g_c|^{z\nu}$), both types of fluctuations are relevant. We finally highlight the fact that universality is characteristic of the neighborhood of the quantum critical point, therefore it is not observed at high temperatures.

A last consideration is deserved by the possibility to map quantum models into classical models. In fact, QPTs in D dimensions are related to CPTs in $D + z$ dimensions.The mapping between D-dimensional quantum models and $D + z$-dimensional classical models becomes exact in the scaling limit (i.e., when the lattice spacing goes to zero). This mapping entails that the critical dimensions are reduced by z in the theory of quantum phase transitions. Therefore, most QPTs (with $z = 1$) show mean field behavior in $D = 3$ [45, 44].

---

[4]This is the case of $2D$ spin systems with SU(2) symmetry, where long-range order at $T > 0$ is forbidden by the Mermin-Wagner theorem.

2.3   The KT transition

In the last decades, many new phases of matter have been found, that cannot be identified by their pattern of symmetry breaking. These usually involve topological order and their phase transitions are not described by the Landau theory, since there is not a change of symmetry and an associated local real order parameter. A completely new kind of phase transition was discovered in 1972 by J. Michael Kosterlitz and David J. Thouless. The Kosterlitz-Thouless (KT) transition (sometimes also called Berezinskii-Kosterlitz-Thouless (BKT) transition) was firstly studied in the two dimensional (classical) XY-model[5], which is an effective theory for both planar magnets and superfluid systems. In fact, they can be both described by a complex order parameter that depends by a single angle θ and therefore belong to the same universality class. The two-point correlations of the order parameter are usually finite in the ordered phase (typically at low temperature) and decay exponentially with the distance in the disordered (high temperature) phase

$$\lim_{r \to \infty} C(r) = \begin{cases} c_1 & T < T_c \\ c_2 e^{-r/\xi} & T > T_c \, , \end{cases} \tag{2.12}$$

where c_1 and c_2 are constants. Exactly at the transition point $T = T_c$, the correlation falls as a power law

$$\lim_{r \to \infty} C(r) \sim r^{-(1+\eta)} \, , \tag{2.13}$$

signaling a critical behavior. That happens, for example, in three dimensions. Instead, in the KT transition, the correlations decay exponentially at high temperature, but their behavior follows a power law in the low temperature regime:

$$C(r) \sim r^{-aT} \qquad \text{for } T < T_{KT} \, . \tag{2.14}$$

This is know as quasi-long-range order. In the superfluid system, this is generated by the formation of vortex-antivortex pairs, which creation requires small energy and can be thermally excited also at low temperature. At a certain critical temperature, the pairs will break up into individual vortices, which have high energy. The KT transition does not break any symmetry and does not present a singularity

---

[5]This is equivalent to a one dimensional quantum model.

in any derivative of the thermodynamic potential, thus constituting an infinite-order transition.

2.4   Mermin-Wagner theorem

After having introduced the possible types of phase transitions, here we would like to mention that some of them are not permitted in low dimensions, as established by the Mermin-Wagner theorem [47]. It states that, in $D \leq 2$, classical systems with sufficiently short-range interactions cannot show ordered phases that spontaneously break a continuous symmetry. It exemplifies the fact that fluctuations become more important in low dimension, and below $D = 2$, they destroy potential ordering. On the other hand, the quantum-classical mapping allows to map a zero-temperature $1D$ quantum problem into a $2D$ classical problem and a zero-temperature $2D$ quantum problem into a $3D$ classical problem. Therefore, we conclude that the Mermin-Wagner theorem prevents the appearance of ordered phases that break a continuous symmetry in $1D$ systems already at $T = 0$ and in $2D$ systems at $T > 0$.

Nevertheless, some phase transitions that do not break any continuous symmetry of the system can occur. Actually, in last decades it has been found that also several zero-temperature one-dimensional phases that respect all the symmetries of the Hamiltonian may exist. These phases do not fall into the classification of symmetry breaking phases derived from the Landau theory. That brings us to ask whether and how the system is ordered at this type of phase transitions. As we will see in the following section, the answer relies on the appearance of non-local ordering.

2.5   Hidden orders and non-local order parameters

In this section, we focus on the one dimensional quantum phases at zero temperature that do not break any symmetry of the Hamiltonian and consequently are not predicted by the Landau theory, although they are allowed by the Mermin-Wagner theorem. In fact, in recent years they have been observed in many one dimensional lattice systems. Since these quantum phases are not depicted inside the Landau scheme, they cannot be characterized by a local order parameter. Nevertheless, it is reasonable to inquire whether they manifest any different kind of ordering.

Indeed, the appearance of such new phases in many cases can be revealed by proper non-local string-like operators. Different string-like operators have been proposed in both bosonic and fermionic systems, as well as for spin systems. The first findings concerned the Haldane phase in quantum spin chains [48]. Here, it was shown that this non-symmetry-breaking regime can be captured by a proper non-local order parameter (NLOP), called Haldane string [49]. Subsequently, the same type of order was found in the extended Bose-Hubbard model [50], and few years later also the Mott insulating phase was characterized in terms of a non-local order, called parity [51]. Finally, similar non-local order parameters were introduced in the context of fermionic systems, in both the charge and spin degrees of freedom [52]. Furthermore, subsequent numerical studies on the extended Hubbard model proved that non-local orders are hidden also in local gapped phases [53].

Here, we concentrate on 1D fermionic systems, where the presence of non-local hidden order is strictly related to the spin-charge separation. As argued, in the context of Hubbard-like systems, two kinds of string operators have been introduced, which are able to capture the presence of some hidden order. These are called parity (P) and Haldane string (S) operators, respectively, and are defined by the following expressions:

$$O_P^{(v)}(j) = \prod_{k=0}^{j-1} e^{\imath 2\pi S_k^{(v),z}} \tag{2.15}$$

$$O_S^{(v)}(j) = 2S_j^{(v),z} \prod_{k=0}^{j-1} e^{\imath 2\pi S_k^{(v),z}} \tag{2.16}$$

where $v = s,c$ indicate the spin and charge degrees of freedom and $S_j^{(v),z}$ are the spin and pseudo-spin operators defined in eqs. (1.30) and (1.37), i.e.

$$S_j^{(s),z} = \frac{1}{2}(n_{j,\uparrow} - n_{j,\downarrow}) \quad ; \quad S_j^{(c),z} = \frac{1}{2}(n_{j,\uparrow} + n_{j,\downarrow} - 1). \tag{2.17}$$

The corresponding correlators $C_A^{(v)}(r) = \langle O_A^{(v)\dagger}(j)O_A^{(v)}(j+r) \rangle$ (with $A = P,S$) have the form

$$C_P^{(v)}(r) = \langle \prod_{k=j}^{j+r-1} e^{\imath 2\pi S_k^{(v),z}} \rangle \tag{2.18}$$

$$C_S^{(v)}(r) = \langle 2S_j^{(v),z} \prod_{k=j}^{j+r-1} e^{\imath 2\pi S_k^{(v),z}} 2S_{j+r}^{(v),z} \rangle. \tag{2.19}$$

In the asymptotic limit $r \to \infty$, the correlators themselves play the role of order parameters, since they are non-zero only in the ordered phase. In particular, a non-vanishing correlator in the charge sector signals the presence of an insulating phase with a finite charge gap

$$\Delta_c = \frac{E(L+2,0) + E(L-2,0) - 2E(L,0)}{2} \, , \qquad (2.20)$$

where $E(N, \mathrm{S}^{(s),z})$ is the energy of the system with N particles and total magnetization $\mathrm{S}^{(s),z}$. Instead, a non-zero correlator in the spin channel entails a finite spin gap, defined as the energy necessary to reverse one spin:

$$\Delta_s = E(L,1) - E(L,0) \, . \qquad (2.21)$$

The non-local operators find a systematic description in the context of field theory, which mathematical framework can be used to study the low energy behavior of lattice systems. That is achieved by means of an analytical technique, called bosonization, which details can be found in Chapter 3. In particular, in Section 3.13, we will revisit the non-local order parameters in this picture.

2.5.1   Classification of different phases

In the literature, non-local order parameters have been used to characterize different gapped phases. In particular, each parameter can in principle identify one hidden phase, when it is non-zero while the others vanish: $C_A^{(v)} \neq 0$ only for a specific combination of A and v. Therefore, we think that NLOPs should allow to recognize four distinct partly gapped phases. However, up to now only three of them have been observed in Hubbard-like systems [54, 53]. In the strong coupling limit, each partly gapped phase is described by a parent state with the corresponding correlator equal to its maximum value: $C_A^{(v)} = 1$. In presence of fluctuations, the value of the non-local correlator decreases ($C_A^{(v)} < 1$) but still remains non-zero, while it vanishes in the other partly gapped phases. Fluctuations in the parity order consist in the formation of holon/doublon pairs in a background of singly occupied sites or up/down spin pairs in a background of holons and doublons depending on whether the ordering occurs in the charge or in the spin sector. These partly gapped phases are called Mott insulator (MI) and Luther Emery (LE), respectively. Instead, the Haldane string order

Table 2.2 *Left:*Classification of 1*D* fermionic quantum phases based on string orders. *Right:*Schematic representation of string orders.
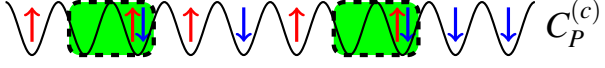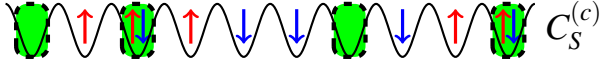
	Δ_c	Δ_s	NLOP
LL	0	0	none
MI	$\neq 0$	0	$C_P^{(c)}$
LE	0	$\neq 0$	$C_P^{(s)}$
HI	$\neq 0$	0	$C_S^{(c)}$
CDW	$\neq 0$	$\neq 0$	$C_S^{(c)}, C_P^{(s)}$
BOW	$\neq 0$	$\neq 0$	$C_P^{(c)}, C_P^{(s)}$

signals the presence of alternated and diluted holons and doublons or up and down spins. The first kind of order characterizes the Haldane insulator (HI), while the second one has not been observed yet. Besides the partly gapped phases, non-local order parameters capture also the fully gapped phases, identified by the coexistence of two simultaneous non-local orders, such as the charge density wave (CDW) and the bond ordered wave (BOW). The observed phases are summarized in Table 2.2 and characterized in terms of non-local order parameters, while in the right panel we illustrate a schematic picture of non-local orders.

The classification of Table 2.2 finds a complete description in the bosonization context, as will be clarified in Section 3.13.

2.6   Symmetry protected topological phases

Over the last decades, the discovery of phase transitions that occur without spontaneous symmetry breaking has stimulated the development of the concept of topological quantum phases, besides that of the already discussed non-local order. Actually, the two concepts are closely related to each other. In particular, the Haldane string order is linked to non-trivial topological properties.

Two kinds of topological phases are commonly recognized, a first one characterized by an "intrinsic" topological order, and a second one that is strictly connected to the presence of a certain symmetry. Here we are concerned about the latter, usually referred to as symmetry protected topological (SPT) order. As opposed to the topological phases, SPT phases can be distinguished from each other unless the symmetry is broken. Therefore, they can be smoothly deformed into the same trivial product

state if the deformation does not preserve the symmetry. Different SPT phases are typically identified by means of the projective representations of the symmetry group of the Hamiltonian and can be classified according to group cohomology theory (in case of bosonic SPT phases) [55, 56] and group supercohomology theory (in case of fermionic SPT phases) [57]. The first examples of non-trivial SPT phases are given by the Haldane phase of spin-1 chain [58, 59], which is protected by $SO(3)$ spin rotation symmetry, and the topological insulators [60–65], which are protected by $U(1)$ and time reversal symmetries. The early results in the attempt of classifying SPT phases were obtained for free fermion systems, in the development of a periodic table for topological insulators and superconductors [66–69]. Focusing on the one-dimensional case, the next breakthrough was the complete classification of all the $1D$ gapped bosonic quantum phases [55, 56]. In fact, $1D$ bosonic systems cannot manifest long-range entanglement [70] and their states belong to the category of either SB states or SPT states. Instead, the situation is more complicated when dealing with interacting fermionic systems. Nevertheless, in Refs. [71, 72] it has been studied the effect of interactions on the classification of topological phases in insulators and superconductors in case of $1D$ systems; moreover, very recently it has been found that the construction of bosonic SPT orders can be generalized to fermionic systems by generalizing the group cohomolgy theory to group supercohomology theory [57].

At the end of this chapter, we would like to point out that, since non-local orders and SPT orders are both beyond the Landau SB theory, some connection may exist between them. In fact, while the parity order is topologically trivial, the string Haldane order signals the presence of degenerate edge modes with fractional charge or spin [73–77]. The linkage is even stronger, since the phases classified according to non-local order parameters, as in Table 2.2, when derived in the context of bosonization, appear to be in one to one correspondence with those obtained from group cohomology theory [78]. Further elucidations will be given in Chapter 3.

Chapter 3

Analytical techniques: the bosonization

The one dimensional Hubbard model (1.16) can be exactly solved by means of the Bethe Ansatz method [8]. However, unfortunately, the integrable models that can be solved by exact techniques as the Bethe Ansatz, are not a very extended class. Most quantum condensed matter systems are described by richer models which cannot be exactly solved. Nevertheless there exist many approximate analytical techniques which allow to get very meaningful insights into the physics of these systems and provide some useful basic information that can be used as the starting point for a subsequent numerical investigation. Among them, the bosonization is a well established method for one dimensional systems. It is a powerful field-theoretical tool that enables to calculate correlation functions. In fact, it gives very reliable results in the weak coupling regime, furnishing the low energy phase diagram of the model.

Here, we do not intend to derive the framework of bosonization, but to give all the tools needed to apply the technique. Therefore we will not follow the usual construction; instead we will provide a schematic treatment of the main concepts and will derive the formula that will be used in the second part of the thesis. For a complete treatment of bosonization, we refer the reader to [79–84].

While most of the chapter is devoted to illustrate the technique, the last two sections contain important information for the full comprehension of this work. In particular, in Section 3.12 we will apply the bosonization to derive an effective weak coupling model for strongly interacting systems, and in Section 3.13 we will show how to

treat the non-local order parameters and the subsequent classification of phases in this context, as well as their connection with symmetry protected topological order.

3.1 General context

The bosonization consists in the representation of fermionic fields $\Psi_\sigma(x)$ in terms of bosonic fields $\phi_\sigma(x)$ through an expression of the form

$$\Psi_\sigma(x) \sim \eta_\sigma e^{-\imath \phi_\sigma(x)} . \tag{3.1}$$

This can be derived in a rigorous way by noticing that the fermionic field operator applied to the N-particle ground state (i.e., the state with lowest energy for fixed N, which is the one with no particle-hole excitations) turns out to be an eigenstate of the bosonic annihilation operator in the momentum space. Thus one can obtain the form (3.1) from a coherent state representation. For the details we refer the reader to [82, 84].

This construction enables to study many problems that appear intractable when formulated in terms of fermions and turn out to become very simple in the language of boson fields.

Since this procedure is dealing with field theory, a preliminary step for our purposes consists in doing the continuum limit of the lattice Hamiltonian. Once the Hamiltonian is written in terms of fermionic fields, one can proceed to substitute their expression in terms of bosonic fields. An important aspect of our treatment relies in the structure of the Fermi surface. In $1D$ systems, this is formed only by the two points $\pm k_F$. Therefore one can classify the excitations as right(R)- and left(L)-moving particles and regard the fermionic field as the sum of two fields, acting on the right and left movers, respectively. In the following, we will start by introducing the continuum limit for fermion operators and then we will define the fermionic and bosonic fields with the correct commutation rules.

3.2   Continuum limit and bosonization

The first step in the standard bosonization approach is to perform the continuum limit of the discrete Hamiltonian. Thus we replace the sums with integrals as

$$\sum_j \longrightarrow \frac{1}{a} \int dx \tag{3.2}$$

and the annihilation operator with the fermionic fields as

$$c_{j,\sigma} \longrightarrow \sqrt{a}\Psi_\sigma(x) = \sqrt{a}\left[e^{\imath k_F x}\Psi_{R\sigma}(x) + e^{-\imath k_F x}\Psi_{L\sigma}(x)\right] \tag{3.3}$$

with $x = ja$ (a being the lattice spacing). At half filling $k_F = \pi/(2a)$ and the fermion operator takes the following expression

$$c_{j,\sigma} \longrightarrow \sqrt{a}\left[(\imath)^j\Psi_{R\sigma}(x) + (-\imath)^j\Psi_{L\sigma}(x)\right] . \tag{3.4}$$

Then, the bosonization amounts to write the fermionic fields $\Psi_{\chi\sigma}$ in terms of the bosonic ones $\phi_{\chi\sigma}$:

$$\begin{aligned}
\Psi_{\chi\sigma}(x) &= \frac{\eta_{\chi\sigma}}{\sqrt{2\pi\alpha}}e^{-\imath\chi\sqrt{4\pi}\phi_{\chi\sigma}(x)} = \\
&= \frac{\eta_{\chi\sigma}}{\sqrt{2\pi\alpha}}e^{\imath\sqrt{\pi}[\chi\phi_\sigma(x)+\theta_\sigma(x)]} = \\
&= \frac{\eta_{\chi\sigma}}{\sqrt{2\pi\alpha}}e^{\imath\sqrt{\frac{\pi}{2}}[\chi\phi_c(x)+\theta_c(x)+\sigma(\chi\phi_s(x)+\theta_s(x))]}
\end{aligned} \tag{3.5}$$

where the generic index χ can denote right (R) or left (L) movers, with the usual convention that it assumes a positive sign in the first case and a negative sign in the second one; while $\alpha \sim a$ is an ultraviolet cutoff. In the second and third lines, the bosonic fields have been rearranged in different combinations, whose meaning will be clear in the following, as well as that of the the Klein factor $\eta_{\chi\sigma}$.

3.3   Definition of the bosonic fields

In our later calculations, we will apply the bosonization at first order in a. In the Hamiltonian, one always deals with products of an even number of fermion operators.

To properly treat the product of exponential operators of the form (3.5), one needs to carefully consider the commutation relations between the bosonic field operators. For that purpose, we provide the expressions of the fields in terms of the lattice operators (in Fourier space) and derive the commutation rules in the continuum space from those in the discrete space. In doing that, for the sake of simplicity, we will neglect the spin index. Thus all the following formula are supposed to hold for bosons of the same species. In fact, bosonic fields describing different species always commute. However, later we will reintegrate the spin indexes and combine them in order to define two new degrees of freedom. Starting from boson creation and annihilation operators, we define the bosonic fields in the following way:

$$\varphi_R(x) \;=\; \frac{\iota}{\sqrt{2L}} \sum_{q>0} \frac{e^{\iota q x}}{\sqrt{q}} e^{-\alpha q/2} b_{qR} \tag{3.6}$$

$$\varphi_R^\dagger(x) \;=\; -\frac{\iota}{\sqrt{2L}} \sum_{q>0} \frac{e^{-\iota q x}}{\sqrt{q}} e^{-\alpha q/2} b_{qR}^\dagger \tag{3.7}$$

$$\varphi_L(x) \;=\; -\frac{\iota}{\sqrt{2L}} \sum_{q>0} \frac{e^{-\iota q x}}{\sqrt{q}} e^{-\alpha q/2} b_{qL} \tag{3.8}$$

$$\varphi_L^\dagger(x) \;=\; \frac{\iota}{\sqrt{2L}} \sum_{q>0} \frac{e^{\iota q x}}{\sqrt{q}} e^{-\alpha q/2} b_{qL}^\dagger \tag{3.9}$$

which can be expressed, in a more compact form, as

$$\varphi_\chi(x) = \frac{\iota \chi}{\sqrt{2L}} \sum_{q>0} \frac{e^{\iota \chi q x}}{\sqrt{q}} e^{-\alpha q/2} b_{q\chi} \tag{3.10}$$

and its hermitian conjugate. We also define the real fields

$$\phi_\chi(x) = \varphi_\chi(x) + \varphi_\chi^\dagger(x) = \frac{\iota \chi}{\sqrt{2L}} \sum_{q>0} \frac{e^{-\alpha q/2}}{\sqrt{q}} \left(e^{\iota \chi q x} b_{q\chi} - e^{-\iota \chi q x} b_{q\chi}^\dagger \right) . \tag{3.11}$$

Now we can write the fermionic fields in terms of the bosonic fields (3.11) as

$$\Psi_\chi(x) = \frac{\eta_\chi}{\sqrt{2\pi\alpha}} e^{-\iota \sqrt{4\pi} \chi \phi_\chi(x)} . \tag{3.12}$$

Explicitly:

$$\Psi_R(x) = \frac{\eta_R}{\sqrt{2\pi\alpha}}e^{-\iota\sqrt{4\pi}\phi_R(x)} = \frac{\eta_R}{\sqrt{2\pi\alpha}}e^{\iota\sqrt{\pi}[\phi(x)+\theta(x)]} \tag{3.13}$$

$$\Psi_L(x) = \frac{\eta_L}{\sqrt{2\pi\alpha}}e^{\iota\sqrt{4\pi}\phi_L(x)} = \frac{\eta_L}{\sqrt{2\pi\alpha}}e^{\iota\sqrt{\pi}[-\phi(x)+\theta(x)]} \tag{3.14}$$

$$\Psi_R^\dagger(x) = \frac{\eta_R^\dagger}{\sqrt{2\pi\alpha}}e^{\iota\sqrt{4\pi}\phi_R(x)} = \frac{\eta_R^\dagger}{\sqrt{2\pi\alpha}}e^{-\iota\sqrt{\pi}[\phi(x)+\theta(x)]} \tag{3.15}$$

$$\Psi_L^\dagger(x) = \frac{\eta_L^\dagger}{\sqrt{2\pi\alpha}}e^{-\iota\sqrt{4\pi}\phi_L(x)} = \frac{\eta_L^\dagger}{\sqrt{2\pi\alpha}}e^{-\iota\sqrt{\pi}[-\phi(x)+\theta(x)]} \tag{3.16}$$

where we have introduced the dual fields $\phi(x)$ and $\theta(x)$:

$$\phi(x) = -(\phi_R(x)+\phi_L(x)) \tag{3.17}$$

$$\theta(x) = -(\phi_R(x)-\phi_L(x)) . \tag{3.18}$$

By inserting eq. (3.11) into (3.17), we obtain the expression of the field ϕ in terms of the boson creation and annihilation operators:

$$\phi(x) = \iota\sum_{q\neq 0}\frac{e^{-\alpha|q|/2-\iota qx}}{q}\left(\frac{|q|}{2L}\right)^{1/2}\left(b_q^\dagger + b_{-q}\right) \tag{3.19}$$

where we have used $b_{qL} = b_{-q}$ (see Appendix B.1). Analogously, its dual field is

$$\theta(x) = \iota\sum_{q\neq 0}\frac{e^{-\alpha|q|/2-\iota qx}}{|q|}\left(\frac{|q|}{2L}\right)^{1/2}\left(b_q^\dagger - b_{-q}\right) . \tag{3.20}$$

Let's focus on $\phi(x)$. As $\phi_\chi(x)$, it is a real field and can be written as the sum of two hermitian conjugate fields, related to annihilation and creation boson operators, respectively:

$$\phi(x) = \varphi(x) + \varphi^\dagger(x) \tag{3.21}$$

with

$$\varphi(x) \quad = \quad \iota \sum_{q \neq 0} \frac{e^{-\alpha|q|/2 - \iota q x}}{q} \left(\frac{|q|}{2L} \right)^{1/2} b_{-q} \tag{3.22}$$

$$\varphi^\dagger(x) \quad = \quad \iota \sum_{q' \neq 0} \frac{e^{-\alpha|q'|/2 - \iota q' x}}{q'} \left(\frac{|q'|}{2L} \right)^{1/2} b_{q'}^\dagger . \tag{3.23}$$

3.4   The $q = 0$ contribution

We observe that in defining the bosonic fields (3.10) and (3.11), as well as (3.19) and (3.20), we neglected the $q = 0$ contribution in the sum. This can be justified when working in the thermodynamic limit $L \to \infty$, since it decays as $1/L$. If we want to reintegrate it, we can take it into account separately, by including it directly inside eq. (3.12) as an extra term added to the bosonic field $\phi_\chi(x)$:

$$\Psi_\chi(x) = \frac{\eta_\chi}{\sqrt{2\pi\alpha}} e^{\iota \chi \frac{2\pi \hat{N}_\chi}{L} x} e^{-\iota \sqrt{4\pi} \chi \phi_\chi(x)} \tag{3.24}$$

where $\hat{N}_\chi$ counts the number of χ-particles added or removed from the system in the excited state. Its meaning will be explained in Section 3.11. Sometimes the $q = 0$ contribution is included into the bosonic field:

$$\phi_\chi(x) \to \phi_\chi(x) - \frac{\sqrt{\pi}\hat{N}_\chi}{L} x . \tag{3.25}$$

Although the number operator $\hat{N}_\chi$ defined for $q = 0$ does not commute with the Klein factors

$$[\hat{N}_\chi, \eta_{\chi'}^\dagger] = \delta_{\chi,\chi'} \eta_\chi^\dagger , \quad [\hat{N}_\chi, \eta_{\chi'}] = -\delta_{\chi,\chi'} \eta_\chi , \tag{3.26}$$

it commutes with the bosonic operators defined for $q \neq 0$

$$[b_{q\chi'}, \hat{N}_\chi] = [b_{q\chi'}^\dagger, \hat{N}_\chi] = 0 . \tag{3.27}$$

Therefore, also if this term was included in the bosonic field, it would not be relevant in the calculation of commutation rules between the bosonic fields and we will continue to neglect it in the following sections.

3.5   Normal ordering

Since the fermionic field depends on the exponential of the field ϕ, in the bosonization procedure the operator $e^{\iota\sqrt{4\pi}\phi(x)}$ is recurrent and sometimes one approximates it by a Taylor expansion. In doing that, one has to pay attention to commutation rules between the two components (3.22) and (3.23). Indeed, the expansion can be done if the operator is normal ordered, which means that all the creation operators are on the left of the annihilation operators in the product. By denoting the normal ordering operation with the symbol ::, we have the following relation:

$$
\begin{aligned}
e^{\iota\sqrt{4\pi}\phi(x)} &= e^{\iota\sqrt{4\pi}\left(\varphi(x)+\varphi^\dagger(x)\right)} = e^{\iota\sqrt{4\pi}\varphi^\dagger(x)}e^{\iota\sqrt{4\pi}\varphi(x)}e^{2\pi\left[\varphi^\dagger(x),\varphi(x)\right]} = \\
&= \, : e^{\iota\sqrt{4\pi}\phi(x)} : e^{-2\pi\left[\varphi(x),\varphi^\dagger(x)\right]} =: e^{\iota\sqrt{4\pi}\phi(x)} : \frac{2\pi\alpha}{L} \, .
\end{aligned}
\tag{3.28}
$$

For the derivation of the last equality, see Appendix B.1. As mentioned before, normal ordering is important when dealing with the expansion of exponential operators. This happens especially when the exponent is the difference of the same field computed in two different points. For example

$$
e^{\iota\sqrt{4\pi}[\phi(x+R)-\phi(x)]} \, .
\tag{3.29}
$$

Since the field varies slowly, we can approximate $\phi(x+R) \simeq \phi(x) + R\nabla\phi(x)$ and then expand $e^{\iota\sqrt{4\pi}R\nabla\phi(x)} \simeq 1 + \iota\sqrt{4\pi}R\nabla\phi(x)$. However, this last expression is wrong, since the field ϕ contains both creation and annihilation operators which do not commute with each other and cannot be treated as simple variables. The correct expansion is

$$
: e^{\iota\sqrt{4\pi}R\nabla\phi(x)} :\simeq 1 + \iota\sqrt{4\pi}R\nabla\phi(x) \, .
\tag{3.30}
$$

The normal ordered exponential is related to (3.29) by

$$
e^{\iota\sqrt{4\pi}[\phi(x+R)-\phi(x)]} =: e^{\iota\sqrt{4\pi}[\phi(x+R)-\phi(x)]} : \left(\frac{\alpha}{R}\right)^2
\tag{3.31}
$$

(see Appendix B.1 for the proof).

3.6 Commutation rules

Here we compute the commutation rules involving the real bosonic fields ϕ and θ:

$$[\phi(x), \phi(y)] = [\theta(x), \theta(y)] = 0$$

$$[\phi(x), \theta(y)] = -\sum_{q,q' \neq 0} \frac{e^{-\frac{\alpha}{2}(|q|+|q'|)} e^{-\iota(qx+q'y)}}{q|q'|} \frac{\sqrt{|qq'|}}{2L} \underbrace{[b_q^\dagger + b_{-q}, b_{q'}^\dagger - b_{-q'}]}_{2\delta_{q',-q}} \rightarrow$$

$$= -\frac{1}{L} \sum_{q \neq 0} \frac{e^{-\alpha|q|+\iota qR}}{q} =$$

$$\xrightarrow{L \to \infty} -\frac{\iota}{\pi} \int_0^\infty \frac{dq}{q} \sin(qR) e^{-\alpha|q|} \rightarrow$$

$$\xrightarrow{\alpha \to 0} \frac{\iota}{2} \mathrm{sgn}(x-y)$$

$$(3.32)$$

(see Appendix B.1 for the complete calculation). From these formula, one can also derive the commutation rules between ϕ_χ's:

$$\phi_R = -\frac{\phi + \theta}{2} \qquad\qquad \phi_L = -\frac{\phi - \theta}{2} \qquad\qquad (3.33)$$

hence

$$[\phi_\chi(x), \phi_\chi(y)] = \frac{1}{4}[\phi(x) + \chi\theta(x), \phi(y) + \chi\theta(y)] =$$
$$= \frac{\chi}{4}([\phi(x), \theta(y)] - [\phi(y), \theta(x)]) =$$
$$= \frac{\chi}{4}\left(\frac{\iota}{2}\mathrm{sgn}(x-y) - \frac{\iota}{2}\mathrm{sgn}(y-x)\right) =$$
$$= \chi\frac{\iota}{4}\mathrm{sgn}(x-y)$$

$$(3.34)$$

whereas

$$[\phi_R(x), \phi_L(y)] = -\frac{1}{4}([\phi(x), \theta(y)] + [\phi(y), \theta(x)]) =$$
$$= -\frac{1}{4}\left(\frac{\iota}{2}\mathrm{sgn}(x-y) + \frac{\iota}{2}\mathrm{sgn}(y-x)\right) = 0 \,.$$

$$(3.35)$$

3.7   Derivatives of the fields

By bosonizing an Hamiltonian at first order, not only the bosonic fields themselves appear, but also their derivatives. Therefore we give their expressions as functions of the creation and annihilation operators and their commutation rules:

$$\nabla\phi(x) = \quad \sum_{q\neq 0} e^{-\alpha|q|/2-\iota qx}\left(\frac{|q|}{2L}\right)^{1/2}\left(b_q^\dagger + b_{-q}\right) \tag{3.36}$$

$$\nabla\theta(x) = \quad \sum_{q\neq 0} e^{-\alpha|q|/2-\iota qx}\frac{q}{|q|}\left(\frac{|q|}{2L}\right)^{1/2}\left(b_q^\dagger - b_{-q}\right). \tag{3.37}$$

The commutation rules are

$$[\nabla\phi(x),\nabla\phi(y)] = [\nabla\theta(x),\nabla\theta(y)] = 0$$

$$[\phi(x),\nabla\phi(y)] = [\theta(x),\nabla\theta(y)] = 0$$

$$[\nabla\phi(x),\nabla\theta(x)] = 0 \tag{3.38}$$

$$[\nabla\phi(x),\theta(y)] = \iota\delta(x-y)$$

$$[\phi(x),\nabla\theta(y)] = -\iota\delta(x-y).$$

These commutation rules can be easily obtained also directly from expressions (3.19), (3.20), (3.36) and (3.37). For example, the last one is

$$[\phi(x),\nabla\theta(y)] = -\iota\sum_{q\neq 0}\frac{e^{-\alpha|q|-\iota q(x-y)}}{q}\frac{q}{|q|}\frac{|q|}{2L}\cdot 2 =$$

$$= -\frac{\iota}{L}\sum_{q\neq 0}e^{-\alpha|q|+\iota qR} \rightarrow$$

$$\xrightarrow{L\to\infty} -\frac{\iota}{2\pi}\int_{-\infty}^{+\infty}dq e^{\iota qR}e^{-\alpha|q|} \rightarrow \tag{3.39}$$

$$\xrightarrow{\alpha\to 0} -\iota\underbrace{\frac{1}{2\pi}\int_{-\infty}^{+\infty}dq e^{\iota qR}}_{\delta(R)}$$

whereas the commutator between the two derivatives is

$$
\begin{aligned}
[\nabla\phi(x),\nabla\theta(x)] &= \frac{1}{2L}\sum_{q,q'\neq 0} e^{-\alpha(|q|+|q'|)/2-\imath x(q+q')y}\frac{q'}{|q'|}\sqrt{|qq'|}[b_q^\dagger+b_{-q},b_{q'}^\dagger-b_{-q'}] = \\
&= \frac{1}{L}\sum_{q,q'\neq 0} e^{-\alpha(|q|+|q'|)/2-\imath x(q+q')y}\frac{q'}{|q'|}\sqrt{|qq'|}\delta_{q',-q} = \\
&= -\frac{1}{L}\sum_{q\neq 0} e^{-\alpha|q|}q = 0\,.
\end{aligned}
$$

$$(3.40)$$

3.8   Spinfull case: charge and spin degrees of freedom

In the previous sections we defined the fields for spinless fermions. The same relations are true for spinfull fermions. In this case we simply add a spin index to all expressions. Indeed one can use the boson representation for each fermionic species separately. Thus we deal with two sets of fields $(\phi_\uparrow,\theta_\uparrow)$ and $(\phi_\downarrow,\theta_\downarrow)$, with the following commutation rules:

$$
[\phi_\sigma(x),\phi_{\sigma'}(y)] = [\theta_\sigma(x),\theta_{\sigma'}(y)] = 0
$$

$$(3.41)$$

$$
[\phi_\sigma(x),\theta_{\sigma'}(y)] = \delta_{\sigma,\sigma'}\tfrac{\imath}{2}\mathrm{sgn}(x-y)\,.
$$

It is useful to combine up- and down-spin fields to get the so-called charge and spin bosonic fields:

$$
\begin{aligned}
\phi_c &= \frac{\phi_\uparrow+\phi_\downarrow}{\sqrt{2}} & \theta_c &= \frac{\theta_\uparrow+\theta_\downarrow}{\sqrt{2}} \\
\phi_s &= \frac{\phi_\uparrow-\phi_\downarrow}{\sqrt{2}} & \theta_s &= \frac{\theta_\uparrow-\theta_\downarrow}{\sqrt{2}}\,.
\end{aligned}
$$

$$(3.42)$$

In fact, Hamiltonian can often be decoupled in two independent Hamiltonians, one depending only on the charge degree of freedom and the other on the spin degree of freedom.

The charge and spin fields commute:

$$[\phi_c(x), \phi_s(y)] = [\theta_c(x), \theta_s(y)] = 0$$

$$[\phi_c(x), \theta_s(y)] = \frac{1}{2}\left\{[\phi_\uparrow(x), \theta_\uparrow(y)] - [\phi_\downarrow(x), \theta_\downarrow(y)] + [\phi_\downarrow(x), \theta_\uparrow(y)] - [\phi_\uparrow(x), \theta_\downarrow(y)]\right\} = 0 \tag{3.43}$$

whereas

$$
\begin{aligned}
[\phi_c(x), \theta_c(y)] &= \frac{1}{2}\left\{[\phi_\uparrow(x), \theta_\uparrow(y)] + [\phi_\downarrow(x), \theta_\downarrow(y)] + [\phi_\downarrow(x), \theta_\uparrow(y)] + [\phi_\uparrow(x), \theta_\downarrow(y)]\right\} = \\
&= \frac{1}{2} \cdot 2[\phi(x), \theta(y)] = \frac{\iota}{2}\mathrm{sgn}(x-y)
\end{aligned}
$$

$$
\begin{aligned}
[\phi_s(x), \theta_s(y)] &= \frac{1}{2}\left\{[\phi_\uparrow(x), \theta_\uparrow(y)] + [\phi_\downarrow(x), \theta_\downarrow(y)] - [\phi_\downarrow(x), \theta_\uparrow(y)] - [\phi_\uparrow(x), \theta_\downarrow(y)]\right\} = \\
&= \frac{1}{2} \cdot 2[\phi(x), \theta(y)] = \frac{\iota}{2}\mathrm{sgn}(x-y) \,.
\end{aligned} \tag{3.44}
$$

As anticipated, the fermionic field (3.5) in terms of charge and spin bosonic fields is

$$\Psi_{\chi\sigma}(x) = \frac{\eta_{\chi\sigma}}{\sqrt{2\pi\alpha}} e^{\iota\sqrt{\frac{\pi}{2}}[\chi\phi_c(x) + \theta_c(x) + \sigma(\chi\phi_s(x) + \theta_s(x))]} \,. \tag{3.45}$$

3.9 Klein factors and fermion anti-commutation rules

In the definition of the fermionic field, eq. (3.5), we have introduced the quantity $\eta_{\chi\sigma}$. It is a unitary operator, called Klein factor, which changes the total number of fermions by one and guarantees the anti-commutation relations between fermionic fields of different species[1] (see, e.g., [84], [85]). They satisfy the following properties:

$$
\begin{aligned}
\eta_\lambda^\dagger \eta_\lambda &= \eta_\lambda \eta_\lambda^\dagger = 1 & \tag{3.46}\\
\{\eta_\lambda, \eta_{\lambda'}^\dagger\} &= 2\delta_{\lambda,\lambda'} & \tag{3.47}\\
\{\eta_\lambda^\dagger, \eta_{\lambda'}^\dagger\} &= \{\eta_\lambda, \eta_{\lambda'}\} = 0 & \text{for } \lambda \neq \lambda' \tag{3.48}
\end{aligned}
$$

---

[1]Here the term species is used in a very general sense. It can denote, for example, the spin or the left/right moving modes.

where we have used the multi-index $\lambda = (\chi, \sigma)$. Moreover we observe that the Klein factors commute with the bosonic operators

$$[b_{q\lambda}, \eta_{\lambda'}^{\dagger}] = [b_{q\lambda}^{\dagger}, \eta_{\lambda'}^{\dagger}] = [b_{q\lambda}, \eta_{\lambda'}] = [b_{q\lambda}^{\dagger}, \eta_{\lambda'}] = 0, \tag{3.49}$$

while, as already argued, do not commute with the number operator

$$[\hat{N}_{\lambda}, \eta_{\lambda'}^{\dagger}] = \delta_{\lambda,\lambda'} \eta_{\lambda}^{\dagger}, \quad [\hat{N}_{\lambda}, \eta_{\lambda'}] = -\delta_{\lambda,\lambda'} \eta_{\lambda}. \tag{3.50}$$

Sometimes the Klein factors are written as $\eta_{\lambda} = e^{-\imath \hat{\theta}_{\lambda}}$, with $\hat{\theta}_{\lambda} = \hat{\theta}_{\lambda}^{\dagger}$ [82]. In this case, equations (3.50) correspond to the following

$$[\hat{N}_{\lambda}, \imath \hat{\theta}_{\lambda'}] = \delta_{\lambda,\lambda'}. \tag{3.51}$$

In the thermodynamic limit one can forget about the fact that the Klein factors change the total number of particles and concentrate on the sign due to these operators. Then, they can be replaced by Majorana fermions, which are hermitian operators $\eta_{\lambda}^{\dagger} = \eta_{\lambda}$ and obey the Clifford algebra

$$\{\eta_{\lambda}, \eta_{\lambda'}\} = 2\delta_{\lambda,\lambda'}. \tag{3.52}$$

The space on which they act has a minimal dimension which depends on the number of fermion species. In case of four species (up/down spins and right/left movers), the minimal dimension is four and the Klein factors have a representation in terms of Kronecker products of Pauli matrices [86], [13]. For instance, we can take

$$\begin{aligned}
\eta_{R\uparrow} &= \sigma^x \otimes \sigma^x, & \eta_{R\downarrow} &= \sigma^z \otimes \sigma^x, \\
\eta_{L\uparrow} &= \sigma^y \otimes \sigma^x, & \eta_{L\downarrow} &= \mathbb{I} \otimes \sigma^y.
\end{aligned} \tag{3.53}$$

Then, the products of four Klein factors appearing in the Hamiltonian are diagonal with eigenvalues ± 1. For a given product, we can choose one of the two eigenvalues. We choose

$$\eta_{L\downarrow} \eta_{L\uparrow} \eta_{R\downarrow} \eta_{R\uparrow} = 1. \tag{3.54}$$

The values of the other products follow from the anticommutation rules of the Clifford algebra.

3.10   Fermion densities and point splitting

We conclude the definition of the operators needed for applying the bosonization by introducing very important quantities, i.e. fermion densities. For right- and left-movers, fermion density operators are defined as

$$
\rho_\chi(x) = : \Psi_\chi^\dagger(x)\Psi_\chi(x) := \lim_{a\to 0}\left[\Psi_\chi^\dagger(x+a)\Psi_\chi(x) - \langle\Psi_\chi^\dagger(x+a)\Psi_\chi(x)\rangle\right] =
$$
$$
= \lim_{a\to 0}\left[\frac{\eta_\chi^\dagger\eta_\chi}{2\pi\alpha}e^{\imath\chi\sqrt{4\pi}\phi_\chi(x+a)}e^{-\imath\chi\sqrt{4\pi}\phi_\chi(x)} - \langle...\rangle\right] = \tag{3.55}
$$
$$
\simeq -\frac{1}{\sqrt{\pi}}\nabla\phi_\chi(x) = \frac{1}{2\sqrt{\pi}}\left(\nabla\phi(x) + \chi\nabla\theta(x)\right)
$$

(see Appendix B.1 for the derivation). We notice that we have denoted the "fermionic" normal ordering :: with the same symbol used to normal order exponentials of the bosonic field. Here it indicates the operation written in the first line that is more properly called "point splitting". It is necessary to avoid divergences when one takes the limit $\alpha\to 0$. Eq. (3.55) implies

$$
\rho_R = \ -\frac{1}{\sqrt{\pi}}\nabla\phi_R = \frac{1}{2\sqrt{\pi}}\left(\nabla\phi + \nabla\theta\right) \tag{3.56}
$$
$$
\rho_L = \ -\frac{1}{\sqrt{\pi}}\nabla\phi_L = \frac{1}{2\sqrt{\pi}}\left(\nabla\phi - \nabla\theta\right) \tag{3.57}
$$

and

$$
\rho = \rho_R + \rho_L = \ \frac{1}{\sqrt{\pi}}\nabla\phi \tag{3.58}
$$
$$
\tilde{\jmath} = \rho_R - \rho_L = \ \frac{1}{\sqrt{\pi}}\nabla\theta\,. \tag{3.59}
$$

These two quantities correspond to the density and the renormalized current $\tilde{\jmath} = \jmath/v_F$, respectively. The same relations hold when the spin label is added:

$$
\rho_{\chi\sigma} \ = \ -\frac{1}{\sqrt{\pi}}\nabla\phi_{\chi\sigma} = \frac{1}{2\sqrt{\pi}}\left(\nabla\phi_\sigma + \chi\nabla\theta_\sigma\right) \tag{3.60}
$$
$$
\rho_\sigma \ = \ \rho_{R\sigma} + \rho_{L\sigma} = \frac{1}{\sqrt{\pi}}\nabla\phi_\sigma \tag{3.61}
$$
$$
\tilde{\jmath}_\sigma \ = \ \rho_{R\sigma} - \rho_{L\sigma} = \frac{1}{\sqrt{\pi}}\nabla\theta_\sigma\,. \tag{3.62}
$$

As for the fields, we can combine up- and down- densities and currents to obtain their expressions in the charge and spin degrees of freedom:

$$\rho_c = \frac{\rho_\uparrow + \rho_\downarrow}{\sqrt{2}} = \frac{1}{\sqrt{\pi}} \nabla \phi_c \qquad \tilde{j}_c = \frac{\tilde{j}_\uparrow + \tilde{j}_\downarrow}{\sqrt{2}} = \frac{1}{\sqrt{\pi}} \nabla \theta_c \qquad (3.63)$$

$$\rho_s = \frac{\rho_\uparrow - \rho_\downarrow}{\sqrt{2}} = \frac{1}{\sqrt{\pi}} \nabla \phi_s \qquad \tilde{j}_s = \frac{\tilde{j}_\uparrow - \tilde{j}_\downarrow}{\sqrt{2}} = \frac{1}{\sqrt{\pi}} \nabla \theta_s \,. \qquad (3.64)$$

At this point we have all the instruments to apply the technique. A summary of the main formula can be found in Appendix C. In the following section we would like to sketch some physical aspects which are at the basis of the procedure.

3.11 On the relation of fields with discrete fermionic operators

So far we have developed a batch of practical rules which enables us to apply bosonization in a very simple way. Here we would like to provide more deep physical justification of the procedure. For this purpose, we go back to the fermionic creation and annihilation operators in the momenta space and explicit the important fields as function of them. In $\mathbb{K}$ space, the vacuum state is defined as the Dirac sea, where all the states below the Fermi level are occupied and all the states above it are empty. The bosonization relies on the assumptions that the energy spectrum is linear around the two Fermi points

$$\varepsilon_k - \mu \sim \begin{cases} v_F(k - k_F) & \text{right moving branch} \\ -v_F(k + k_F) & \text{left moving branch} \end{cases} \qquad (3.65)$$

and that each branch can be extended in order that k runs from $-\infty$ to $+\infty$. For both of them, we can define a particle number operator as

$$\hat{N}_\chi = \sum_k : c_{k\chi}^\dagger c_{k\chi} := \sum_k \left[c_{k\chi}^\dagger c_{k\chi} - {}_0\langle c_{k\chi}^\dagger c_{k\chi} \rangle_0 \right] \qquad (3.66)$$

where ${}_0\langle ... \rangle_0$ denotes the expectation value computed with respect to the vacuum state. Therefore it represents the number of particles added or removed from the Fermi sea in each branch. Moreover, we can define the operators that create particle-

hole excitations of momentum $q \neq 0$ as

$$\rho_\chi(q) = \sum_k c^\dagger_{k+q\chi} c_{k\chi} .$$

(3.67)

Those are called density fluctuation operators and obey the following algebra

$$[\rho_\chi(q), \rho_{\chi'}(q')] = -\chi \frac{qL}{2\pi} \delta_{q,-q'} \delta_{\chi,\chi'}$$

(3.68)

which can be turned into the canonical bosonic algebra by renormalizing the operators in the following way

$$b_{q\chi} = \sqrt{\frac{2\pi}{Lq}} \rho_\chi(-\chi q), \quad b^\dagger_{q\chi} = \sqrt{\frac{2\pi}{Lq}} \rho_\chi(\chi q)$$

(3.69)

with $q > 0$. These bosonic operators create collective excitations involving the coherent superposition of a large number of electron–hole pairs. The non-interacting fermionic Hamiltonian can be rewritten as a non-interacting Hamiltonian in terms of the new bosonic operators. When interactions are included into the model, one needs to distinguish two types of possible processes: particle-hole excitations can be created by scatterings which occur on one branch of the Fermi surface or by scatterings which bring particles from one branch to the other. The first kind of interaction is referred to as forward scattering, while the second kind is called backward scattering. Forward scattering interactions can still be written in terms of the density fluctuation operators. The Hamiltonian involving only the kinetic part and the forward scattering interaction is known as the Tomonaga-Luttinger model and, ones written in terms of bosons, is easily diagonalized by a Bogoliubov transformation. Since the diagonal boson operators are linear combinations of the original ones, the elementary excitations are collective bosonic density fluctuations. This is also true in presence of backward scattering interactions only in case of spinless fermions. Clearly all the previous relations can be rewritten by adding a spin index. In this case, the backward scattering interactions can not be expressed as combinations of the bosonic operators and one needs to bosonize the single fermionic operator, as in (3.12). At half filling, also umklapp processes, which entail momentum transfer between the fermion system and the lattice, can occur and require the bosonization of $\Psi_\chi(x)$.

Finally, we observe that $\Psi_\chi(x)$ in terms of fermion operators in reciprocal space can

be defined as

$$\Psi_\chi(x) = \frac{1}{\sqrt{L}} \sum_k e^{\iota k x} c_{k\chi}, \tag{3.70}$$

its inverse being

$$c_{k\chi} = \frac{1}{\sqrt{L}} \int dx\, e^{-\iota k x} \Psi_\chi(x). \tag{3.71}$$

Thus, the density field in real space (3.55) is given by

$$\rho_\chi(x) = :\Psi_\chi^\dagger(x)\Psi_\chi(x) := \frac{1}{L} \sum_{k,k'} e^{\iota(k-k')x} : c_{k'\chi}^\dagger c_{k\chi} := \frac{1}{L} \sum_{k,q} e^{-\iota q x} : c_{k+q\chi}^\dagger c_{k\chi} :=$$

$$= \frac{1}{L} \sum_k : c_{k\chi}^\dagger c_{k\chi} : + \frac{1}{L} \sum_{q\neq 0} e^{-\iota q x} \sum_k c_{k+q\chi}^\dagger c_{k\chi} =$$

$$= \frac{\hat{N}_\chi}{L} + \frac{1}{L} \sum_{q\neq 0} e^{-\iota q x} \rho_\chi(q). \tag{3.72}$$

The first term here is missing in eq. (3.55), since we used the definition (3.12) in deriving it. It is recovered if instead one uses (3.24). Note that $c_{kR} \equiv c_{k_F+k}$ and $c_{kL} \equiv c_{-k_F+k}$.[2] Therefore the field $\Psi(x)$, which is the continuum limit analogs of c_j, is given by

$$\Psi(x) = \frac{1}{\sqrt{L}} \sum_k e^{\iota k x} c_k = \frac{1}{\sqrt{L}} \sum_k e^{\iota(k_F+k)x} c_{k_F+k} + \frac{1}{\sqrt{L}} \sum_k e^{-\iota(k_F-k)x} c_{-k_F+k}$$

$$= e^{\iota k_F x} \Psi_R(x) + e^{-\iota k_F x} \Psi_L(x), \tag{3.73}$$

and the corresponding density, at half filling, is

$$n(x) =: \Psi^\dagger(x)\Psi(x) := \rho(x) + (-)^j M(x) \tag{3.74}$$

with

$$M(x) = \Psi_R^\dagger(x)\Psi_L(x) + \Psi_L^\dagger(x)\Psi_R(x). \tag{3.75}$$

---

[2]Another possibility is to define $c_{kL} \equiv c_{-k_F-k}$. This would entail a slightly different definition of (3.70), (3.71) and (3.72), as well as (3.68) and (3.69). However, the bosonic operators obtained at the end are the same and the formula of the previous sections are not affected. For more details, see Appendix B.2.

3.12   Application to interacting fermions: the sine-Gordon model

The Hamiltonian of an interacting fermion model with linear spectrum describing the low energy excitations can be written as

$$H \approx H_0 + H_{int} \tag{3.76}$$

with

$$H_0 = v_F \sum_{k,\chi,\sigma} \chi k : c^{\dagger}_{k\chi\sigma} c_{k\chi\sigma} : \tag{3.77}$$

$$
\begin{aligned}
H_{int} = \frac{1}{2L} \sum_{k,k',q} \sum_{\chi} \sum_{\sigma,\sigma'} \Big\{ & g_{1\sigma\sigma'} c^{\dagger}_{k+q\chi\sigma} c_{k\bar\chi\sigma} c^{\dagger}_{k'-q\bar\chi\sigma'} c_{k'\chi\sigma'} + \\
& g_{2\sigma\sigma'} c^{\dagger}_{k+q\chi\sigma} c_{k\chi\sigma} c^{\dagger}_{k'-q\bar\chi\sigma'} c_{k'\bar\chi\sigma'} + \\
& g_{3\sigma\sigma'} c^{\dagger}_{k+q\chi\sigma} c_{k\bar\chi\sigma} c^{\dagger}_{k'-q\chi\sigma'} c_{k'\bar\chi\sigma'} + \\
& g_{4\sigma\sigma'} c^{\dagger}_{k+q\chi\sigma} c_{k\chi\sigma} c^{\dagger}_{k'-q\chi\sigma'} c_{k'\chi\sigma'} \Big\}
\end{aligned}
\tag{3.78}
$$

where $\bar\chi$ denotes the opposite moving branch with respect to χ and the momentum q is assumed to be small enough that k and $k \pm q$ belong to the neighborhood of the same Fermi point. The g_2 and g_4 terms model the forward scattering processes, whereas g_1 describes the backward scattering interactions and g_3 is the umklapp term. By using the relation (3.71), with the spin index included,

$$c_{k\chi\sigma} = \frac{1}{\sqrt{L}} \int dx e^{-\imath kx} \Psi_{\chi\sigma}(x), \tag{3.79}$$

one obtains the Hamiltonians (3.77) and (3.78) in the continuum real space

$$H_0 = v_F \sum_{\chi,\sigma} \int dx : \Psi^{\dagger}_{\chi\sigma}(x)(-\imath\chi\partial_x)\Psi_{\chi\sigma}(x) : \tag{3.80}$$

$$
\begin{aligned}
H_{int} = \frac{1}{2} \sum_{\chi} \sum_{\sigma,\sigma'} \int dx \Big\{ & g_{1\sigma\sigma'} \Psi^{\dagger}_{\chi\sigma}(x)\Psi_{\bar\chi\sigma}(x)\Psi^{\dagger}_{\bar\chi\sigma'}(x)\Psi_{\chi\sigma'}(x) + \\
& g_{2\sigma\sigma'} \Psi^{\dagger}_{\chi\sigma}(x)\Psi_{\chi\sigma}(x)\Psi^{\dagger}_{\bar\chi\sigma'}(x)\Psi_{\bar\chi\sigma'}(x) + \\
& g_{3\sigma\sigma'} \Psi^{\dagger}_{\chi\sigma}(x)\Psi_{\bar\chi\sigma}(x)\Psi^{\dagger}_{\chi\sigma'}(x)\Psi_{\bar\chi\sigma'}(x) + \\
& g_{4\sigma\sigma'} \Psi^{\dagger}_{\chi\sigma}(x)\Psi_{\chi\sigma}(x)\Psi^{\dagger}_{\chi\sigma'}(x)\Psi_{\chi\sigma'}(x) \Big\}.
\end{aligned}
\tag{3.81}
$$

If the system is unpolarized (i.e., it is invariant under time reversal), the interactions depend only on the relative orientation of the spins:

$$g_{i\uparrow\uparrow} = g_{i\downarrow\downarrow} = g_{i\|}, \qquad g_{i\uparrow\downarrow} = g_{i\downarrow\uparrow} = g_{i\perp}, \qquad i = \{1,2,3,4\}. \tag{3.82}$$

By applying the bosonization mapping to this Hamiltonian, after appropriate normal ordering, one gets an Hamiltonian of the form

$$H = \sum_{v=c,s} H_v + H_{cs} \tag{3.83}$$

with

$$H_v = \frac{1}{2}\int dx \left[v_v K_v \left(\nabla \theta_v(x)\right)^2 + \frac{v_v}{K_v}\left(\nabla \phi_v(x)\right)^2 \right] + \frac{2g_v}{(2\pi a)^2}\int dx \cos(\sqrt{8\pi}\phi_v(x)) \tag{3.84}$$

$$H_{cs} = \frac{2g_{cs}}{(2\pi a)^2}\int dx \cos(\sqrt{8\pi}\phi_c(x)) \cos(\sqrt{8\pi}\phi_s(x)), \tag{3.85}$$

being the coefficients given by

$$v_v K_v = v_F \left[1 + \frac{g_{4\|} - g_{2\|} + g_{1\|} + c_v\left(g_{4\perp} - g_{2\perp}\right)}{2\pi v_F} \right] \tag{3.86}$$

$$\frac{v_v}{K_v} = v_F \left[1 + \frac{g_{4\|} + g_{2\|} - g_{1\|} + c_v\left(g_{4\perp} + g_{2\perp}\right)}{2\pi v_F} \right] \tag{3.87}$$

$$g_c = -g_{3\perp}, \quad g_s = g_{1\perp}, \quad g_{cs} = -g_{3\|}, \tag{3.88}$$

where $c_c = +1$ and $c_s = -1$. From equations (3.86) and (3.87), we get the velocities v_v and the Luttinger parameters K_v

$$v_v = v_F \left[(1 + y_{-,v})(1 + y_{+,v})\right]^{1/2} \simeq v_F \left[1 + \frac{y_{-,v}}{2} + \frac{y_{+,v}}{2} \right] \tag{3.89}$$

$$K_v = \left[\frac{1 + y_{-,v}}{1 + y_{+,v}} \right]^{1/2} \simeq 1 + \frac{y_{-,v}}{2} - \frac{y_{+,v}}{2}, \tag{3.90}$$

where $y_{\pm,v} = (g_{4\|} \pm (g_{2\|} - g_{1\|}) + c_v(g_{4\perp} \pm g_{2\perp}))/(2\pi v_F)$, and in the second equality we have done a linear approximation valid for small interaction values. Very often, the Hamiltonian (3.85), which couples the charge and spin degrees of freedom, can be neglected upon resorting to a renormalization group analysis (see, e.g., [81],[18],[87],[88],[89],[90]). So, assuming charge-spin separation, one ends up

with two decoupled Hamiltonians, each one having the form

$$H_{SG} = \frac{1}{2} \int dx \left[vK \left(\nabla \theta(x) \right)^2 + \frac{v}{K} \left(\nabla \phi(x) \right)^2 \right] + \frac{2g}{(2\pi a)^2} \int dx \cos(\sqrt{8\pi}\phi(x)) ,$$

(3.91)

which is known as the sine-Gordon Hamiltonian. This Hamiltonian contains two competing terms. Indeed the quadratic term does not want the field ϕ to be locked and favors its fluctuations. On the other hand, the massive term tries to pin the field in one of the minima of the cosine. In order to know which term wins and to obtain the low-energy physical properties of the model, one has to employ the renormalization group procedure. The basic idea of this procedure is to move towards larger distances (i.e, lower energies) by integrating out the fields with shorter and shorter wavelengths. Technically, one starts with a decomposition of the original field into short-wavelength and long-wavelength parts, then integrates over the short-wavelength component and get an effective model for the long-wavelength field. The structure of the new effective action will be the same as the original one, but with a different set of coupling constants. This procedure is repeated many times and at each RG iteration one obtains to reproduce the form of the starting model (up to irrelevant terms). Relations between the renormalized couplings and the original ones generate the RG equations, which solution provides informations about the low-energy phase diagram. The RG analysis can be performed in several ways. The most standard, based on the Kadanoff-Wilson picture, is to start from the partition function

$$Z = \int \mathscr{D}\phi \, e^{-S}$$

(3.92)

and compute the action. For the sine-Gordon model, the action is

$$S = \underbrace{\frac{1}{2K} \int dx d\tau \left[\frac{1}{v} \left(\partial_\tau \phi(x,\tau) \right)^2 + v \left(\partial_x \phi(x,\tau) \right)^2 \right]}_{S_0} + \underbrace{\frac{2g}{(2\pi a)^2} \int dx d\tau \cos(\sqrt{8\pi}\phi(x,\tau))}_{S_g} .$$

(3.93)

Now the procedure consists in changing the cutoff of the system and at the same time varying the coupling constants in order to keep the low-energy properties unchanged. We denote the original cutoff, which delimits the Brillouin zone, by Λ. Then, the Brillouin zone $|k| < \Lambda$ can be split into two regions: $0 < |k| < \Lambda'$ and $\Lambda' < |k| < \Lambda$, with $\Lambda' = \Lambda - d\Lambda$. If one writes the field in Fourier transform, it can be divided into
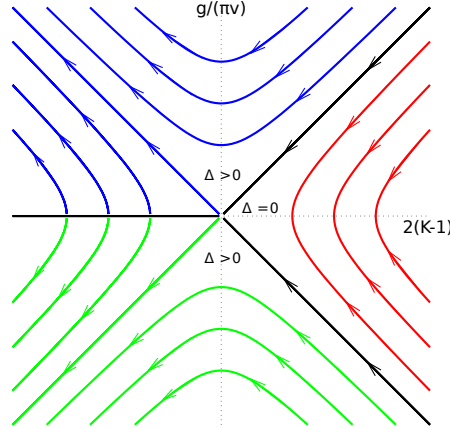
Fig. 3.1 RG flow diagram for the sine-Gordon model (3.91). The arrows indicate the direction of the flow with increasing the length scale. The black lines mark the phase transitions. In the green region $\phi = 0$, while in the blue region $\phi = \sqrt{\pi/8}$.

the sum of slow ($0 < |k| < \Lambda'$) and fast ($\Lambda' < |k| < \Lambda$) components:

$$\phi = \phi^< + \phi^> . \tag{3.94}$$

The same holds for the quadratic part of the action S_0

$$S_0 = S_0^< + S_0^> , \tag{3.95}$$

while it is not possible for S_g. Therefore a perturbative expansion of the partition function in the cosine term is needed. Here we realize that the RG procedure is a perturbative method. Hence it is reliable only if the renormalized couplings remain small. After the expansion in powers of the cosine term, one can average over the fast modes and obtain the partition function expressed in terms of an effective action for the slow fields only, i.e., with a smaller cutoff Λ' with respect to the original one. At this point, if one rescales the momenta as

$$k' = \frac{\Lambda}{\Lambda'}k , \tag{3.96}$$

one recovers the original form for the action, with new coupling constants. The cutoff is usually parametrized by $\Lambda(l) = \Lambda_0 e^{-l}$. Therefore $\Lambda'(l) = \Lambda_0 e^{-l-dl}$ and $\frac{\Lambda}{\Lambda'} = e^{dl} \approx 1 + dl$. With this notation, one gets that the relation between the new

coupling and the old one is

$$g(l+dl) = g(l)e^{(2-2K)dl} \tag{3.97}$$

which leads to the following differential equation

$$\frac{\partial g(l)}{\partial l} = g(l)(2 - 2K(l)). \tag{3.98}$$

Within this RG procedure, one can also obtain another differential equation for $\partial K(l)/\partial l$, coupled to (3.98). The exact form of this equation depends on the precise cutoff procedure used. Therefore here we do not write it. For the details of the RG method, see e.g. [81], [25], [32], [86] or [91]. The RG flow is drawn in Figure 3.1. We see that the system flows to the point $g = 0$ if $|g| \leq 2\pi v(K-1)$, while it flows toward strong coupling if $|g| > 2\pi v(K-1)$. In fact, in the first case the parameter g is irrelevant (i.e., it decreases algebraically under renormalization) and the theory is massless ($\Delta = 0$), while in the second case g becomes relevant (i.e., it grows algebraically) and makes the theory massive ($\Delta \neq 0$), with two possible distinct phases, depending on the sign of g. Finally, if $K = 1$, the cosine term is marginal (i.e., it undergoes logarithmic variations).

We observe that if the original lattice model is invariant under the SU(2) symmetry, the RG flow is restricted to the line $2\pi v(K-1) = g$, implying that the theory is gapless for $K > 1$ and gapped for $K < 1$. For the Hubbard model, this is the case in both charge and spin sectors. However, the presence of adding terms in the Hamiltonian may break the symmetry at least in one of the two sectors, thus expanding the number of possible phases.

3.13   Non-local order parameters in bosonization, classification of phases in the sine-Gordon model and their topological properties

The previous analysis offers an ideal platform to derive, in a systematic way, the classification of phases introduced in Section 2.5.1. Indeed, most Hubbard-like Hamiltonians can be mapped , at first order in the lattice parameter a, into the sum

of two decoupled sine-Gordon models

$$H = \sum_{v=c,s} H_v \, , \qquad (3.99)$$

with H_v given by eq. (3.84). As a result of the competition between the quadratic term and the interaction term, some gapless or gapped phases can appear in each $v-$sector. In particular, the gap is open when the field ϕ_v is pinned at some fixed value. The condition $|g_v| > 2\pi v_v (K_v - 1)$ guarantees the fulfillment of this requirement. In order to minimize the energy, depending on the sign of the mass g_v, the only two possible pinning values are 0 or $\sqrt{\pi/8}$, which correspond to unit values of $\cos(\sqrt{2\pi}\phi_v)$ and $\sin(\sqrt{2\pi}\phi_v)$ respectively. Thus, these two operators can be regarded as detectors for the corresponding gapped phases. In fact, it is easy to verify that they are the continuum version of the parity and Haldane string operators introduced in Section 2.5:

$$O_P^{(v)}(x) \sim \cos(\sqrt{2\pi}\phi_v(x)) \quad ; \quad O_S^{(v)}(x) \sim \sin(\sqrt{2\pi}\phi_v(x)) \qquad (3.100)$$

and the corresponding correlators, which in the asymptotic limit act as order parameters, are expressed as

$$C_P^{(v)}(R) \sim \langle \cos(\sqrt{2\pi}\phi_v(x)) \cos(\sqrt{2\pi}\phi_v(x+R)) \rangle \qquad (3.101)$$

$$C_S^{(v)}(R) \sim \langle \sin(\sqrt{2\pi}\phi_v(x)) \sin(\sqrt{2\pi}\phi_v(x+R)) \rangle \, . \qquad (3.102)$$

As a consequence, the phases of Table 2.2 can be reinterpreted in the bosonization language. According to this picture, eight distinct gapped phases can be induced by the interaction in the gapless Luttinger Liquid regime. In each channel, the two pinning values of the field (i.e., 0 and $\sqrt{\pi/8}$) correspond to two distinct orders (i.e., the parity and the Haldane string). That determines the existence of four distinct partly gapped phases and four fully gapped phases, the latter occurring when both ϕ_c and ϕ_s are pinned. In conclusion, the bosonization provides adding information to the classification of phases given in Table 2.2. A complete description of those phases is reported in Table 3.1. We observe that here the scenario of possible phases is enlarged with respect to that found in the literature. In fact, Hubbard-like models typically have SU(2) spin symmetry, which prevents the case $\phi_s = \sqrt{\pi/8}$ in one-loop bosonization.

We would like to highlight that the partly gapped phases can not be detected by

Table 3.1 Classification of 1D quantum phases and corresponding string orders from bosonization and RG analysis. The letter u has been used to label the unpinned fields and NLOP stands for *non-local order parameter*.

	Φ_c	Φ_s	Δ_c	Δ_s	NLOP
LL	u	u	0	0	none
MI	0	u	$\neq 0$	0	$C_P^{(c)}$
LE	u	0	0	$\neq 0$	$C_P^{(s)}$
HI	$\sqrt{\pi/8}$	u	$\neq 0$	0	$C_S^{(c)}$
HLE	u	$\sqrt{\pi/8}$	0	$\neq 0$	$C_S^{(s)}$
CDW	$\sqrt{\pi/8}$	0	$\neq 0$	$\neq 0$	$C_S^{(c)}, C_P^{(s)}$
SDW	0	$\sqrt{\pi/8}$	$\neq 0$	$\neq 0$	$C_P^{(c)}, C_S^{(s)}$
BOW	0	0	$\neq 0$	$\neq 0$	$C_P^{(c)}, C_P^{(s)}$
BSDW	$\sqrt{\pi/8}$	$\sqrt{\pi/8}$	$\neq 0$	$\neq 0$	$C_S^{(c)}, C_S^{(s)}$

means of local order parameters. By contrast, according to the one loop bosonization presented above, we can always find a local order parameter for the fully gapped phases, where the charge and spin degrees of freedom can be recombined. Nevertheless those phases are also characterized by the simultaneous non-vanishing of two non-local string operators. Thus the string order parameters (2.18) and (2.19), and their continuum version (3.101) and (3.102), are able to capture all the possible gapped phases appearing in the sine-Gordon model.

Finally we stress that also the topological properties associated to the string order find a deeper explanation in the framework of bosonization. In fact, since the cosine term in the sine-Gordon model can pin the field ϕ_v to either the value 0 or $\sqrt{\pi/8}$, at the interface between the two corresponding phases the field experiences a kink. This affects the spin (or pseudo-spin) operator $S_j^{z,(v)}$. Indeed, in the continuum limit $S_j^{z,(v)} \sim \frac{a}{\sqrt{2\pi}}\nabla\phi_v(x)$. In particular, it is found that at the edges of the system (or equivalently at the boundary between the two separated phases) a fractional spin (or charge) is accumulated [76–78]:

$$\lim_{a\to 0}\frac{1}{\sqrt{2\pi}}\int_x^{x+a} dx\nabla\phi_v(x) = \pm\frac{1}{4}\,. \tag{3.103}$$

The evidence of such fractionalization at the edges is a typical signature of an SPT phase. Actually, here the distinction of phases is established under the protection of the particle-hole symmetry. In Ref. [78] the correspondence between the phases

obtained for the sine-Gordon model and those derived from the group cohomology
theory has been made more consistent. Indeed, it has been shown that each (charge
or spin) channel is described by a $U(1) \rtimes \mathbb{Z}_2$ symmetry hosted by the sine-Gordon
Hamiltonian and it has been proven that two inequivalent projective representations
exist, as predicted by the group cohomology classification. Those are associated with
a trivial and a non-trivial SPT phase, the first one being identified with the parity
non-local order and the second one with the Haldane string order. These findings
have confirmed and enforced the previous results about the relation of Haldane string
order with non-trivial SPT phases based on the matrix product formalism [73–75].

Chapter 4

Numerical methods

In this Chapter we present two kinds of numerical techniques, which will be used in the second part of the thesis to investigate Hubbard-like systems. The first one is the density matrix renormalization group (DMRG) method, which is particularly suitable to study one dimensional systems. It relies on the truncation of the Hilbert space based on the eigenvalues of the reduced density matrix. The second one is the quantum Monte Carlo (QMC), which is built on the sampling of the possible configurations of the system. These two methods allow to compute non-local order parameters since the latter can be constructed from the product of local operators with diagonal entries.

4.1 Density matrix renormalization group (DMRG)

The DMRG has been introduced by White in 1992 [92, 93]. It consists in a procedure to progressively enlarge the system size without extending the Hilbert space beyond a given dimension m. In order to obtain this result, the system is embedded in a larger environment and the truncation of the Hilbert space is attained by choosing the eigenvectors of the reduced density matrix with the largest eigenvalues. Indeed, this choice provides the most accurate representation of the state of the entire lattice, i.e., the system plus the universe.

The first step of the algorithm consists in building a portion of the lattice, called block, of size ℓ and described by m_ℓ states. It will be denoted by $\mathscr{B}_\ell(m_\ell)$. At the beginning, the block is composed by just one site: $\mathscr{B}_1(m_1)$, where m_1 is the dimension of the

single site Hilbert space (for the Hubbard model $m_1 = 4$). In the second step, a site is added to the right of the block. The block plus the site constitutes the left enlarged block, which is also referred to as the system. Then the right enlarged block, which represents the environment, is constructed by reflecting the left enlarged block. This global system is called superblock (see Fig. 4.1, *Left panel*) and is described by the following Hamiltonian

$$H_{sB}^n = H_{leB}^n + H_{reB}^n + H_{lS,rS}^n \tag{4.1}$$

where the superscript $n = \ell - 1$ indicates the iteration of the DMRG algorithm, $H_{lS,rS}^n$ is the interaction between the two central sites and $H_{leB(reB)}^n$ is the Hamiltonian of the left (right) enlarged block, given by the sum of the block Hamiltonian, the site Hamiltonian and the interaction between block and site:

$$H_{leB}^n = H_{lB}^n + H_{lS}^n + H_{lB,lS}^n . \tag{4.2}$$

The Hamiltonian of the superblock, H_{sB}^n, is memorized as a sparse matrix and is diagonalized in order to find a particular state (generally the ground state). This is called the target state. If $|i\rangle_n$ and $|j\rangle_n$ are complete sets of states for the system and the environment, respectively, the state of the superblock can be expressed as

$$|\Psi_n\rangle = \sum_{i,j} \psi_{i,j}^n |i\rangle_n |j\rangle_n . \tag{4.3}$$

However, we are interested in finding a representation of $|\Psi_n\rangle$ such that the system is described at most by m states. In particular, we would like to characterize the left enlarged block with $m_{\ell+1} = \min(m_\ell m_1, m)$ states $|u^{\alpha=1,\dots,m_{\ell+1}}\rangle_n = \sum_i u_i^{\alpha,n}|i\rangle_n$. Therefore, we want to find the optimal states $|u^\alpha\rangle_n$ such that the state $|\Psi_n\rangle$ can be approximated as

$$|\Psi_n\rangle \approx |\bar{\Psi}_n\rangle = \sum_{\alpha,j} a_{\alpha,j}^n |u^\alpha\rangle_n |j\rangle_n , \tag{4.4}$$

i.e., we wish to minimize the quantity $||\Psi_n\rangle - |\bar{\Psi}_n\rangle|^2$ by varying both $|u^\alpha\rangle_n$ and $a_{\alpha,j}^n$. It can be proven [93] that this is achieved by taking the eigenstates of the reduced density matrix of the system

$$\rho_{i,i'}^n = \sum_j \psi_{i,j}^n \psi_{i',j}^n \tag{4.5}$$

corresponding to the largest eigenvalues. Thus, the change of basis is performed through a $m_\ell m_1 \times m_{\ell+1}$ rectangular matrix $\hat{O}_n$ which columns are the selected $m_{\ell+1}$ eigenstates of ρ^n. The output is a truncated enlarged block which forms the block $\mathscr{B}_{\ell+1}(m_{\ell+1})$ for the next iteration. Its Hamiltonian is given by

$$H_{lB}^{n+1} = \hat{O}_n^\dagger H_{leB}^n \hat{O}_n \,. \tag{4.6}$$

This procedure is repeated many times, until convergence is reached. At each iteration a truncation error is introduced. It can be estimated by looking at the eigenvalues w_α^n of ρ^n. Indeed each of them represents the probability of being in the state $|u^\alpha\rangle_n$ and the sum of all the eigenvalues is equal to 1: $\sum_\alpha w_\alpha^n = 1$. Therefore, the deviation of $\sum_{\alpha=1}^m w_\alpha^n$ from unity provides a measure of the accuracy of the results.

The procedure described here is called "infinite-system DMRG" and furnishes informations about the ground state of an infinite chain. However, in many cases, it is not sufficiently accurate. A grater precision can be obtained by implementing the so-called "finite-system DMRG", which yields results for a finite chain of length L. The first steps of this algorithm rely on the infinite-system method. In fact this is applied until the superblock reaches the length L, being composed of two blocks $\mathscr{B}_{L/2-1}(m)$ and two sites. At this point, the efficiency is improved by employing the so-called "sweep procedure" (Fig. 4.1, *Right panel*). It consists in enlarging the left block to $\mathscr{B}_{L/2}(m)$ with the usual method, and simultaneously reducing the right block to $\mathscr{B}_{L/2-2}(m)$ by taking it from memory. The procedure is iterated until the left block reaches the size $L-4$. At this point, the new left block $\mathscr{B}_{L-3}(m)$ is given by the renormalization procedure, while the right block $\mathscr{B}_1(m_1)$ is built from scratch. Finally, the algorithm continues by exchanging the role of the two blocks. The sweep procedure can be iterated several times in order to enhance the accuracy of the ground state representation.

We would like to stress that the configuration of the superblock depicted in Fig. 4.1 is optimal for open boundary conditions. If periodic boundary conditions are applied, it is more advisable to modify the configuration in order to not have the two blocks as neighbors, which would reduce the sparseness of H_{sB}. Therefore, the right enlarged block is constructed by switching the positions of block and site.

Some reviews about density matrix renormalization group can be found in [94, 95].
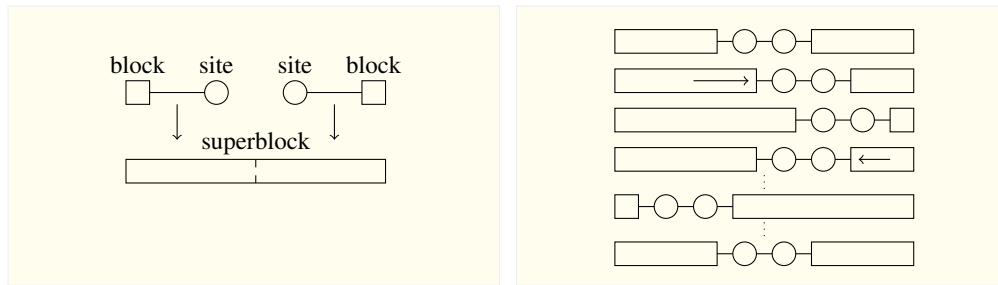
Fig. 4.1 *Left panel:* DMRG construction of blocks and superblock. *Right panel:* Schematic representation of the sweep procedure.

Summary of the DMRG algorithm

In summary, the DMRG algorithm relies on the following steps:

1. Construct the initial block $\mathscr{B}_1(m_1)$.

2. Construct the enlarged left block by adding one site to the block and build the superblock by reflecting the left enlarged block.

3. Diagonalize the superblock Hamiltonian to find the target state (usually the ground state).

4. Use the state to build the reduced density matrix of the left enlarged block (and eventually to compute expectation values of operators).

5. Diagonalize the reduced density matrix.

6. Use the eigenvectors of the reduced density matrix with largest eigenvalues to form the columns of the matrix $\hat{O}$.

7. Use the matrix $\hat{O}$ to redefine the Hamiltonian of the left enlarged block. This will become the left block for the next iteration.

8. Iterate the procedure from point 2 with the new block until the superblock reaches the length L.

9. Continues to iterate the procedure by enlarging the left block and reducing the right block, until the latter is composed by just one sites.

10. Continues to iterate the procedure by switching the role of left and right blocks.

11. Iterate points 9,10 until a satisfactory convergence is reached.

4.2   Quantum Monte Carlo (QMC)

In this section, we will describe two Monte Carlo schemes: the variational quantum Monte Carlo (VQMC) and the Green's function quantum Monte Carlo (GFQMC) [96]. These techniques face the problem of large Hilbert space by sampling the configuration space. In general, we can divide the process of solving a many body problem into two steps: the computation of the ground state wave function $|\Phi_{GS}\rangle$ and the computation of its energy E_{GS}, i.e., the expectation value of the Hamiltonian over $|\Phi_{GS}\rangle$.

In the VQMC the form of the wave function $|\Phi\rangle = |\Phi\rangle_{\{\gamma\}}$ is assumed at the beginning. It depends on some variational parameters $\{\gamma\}$ which have to be optimized[1] in order to minimize the energy. For a given configuration[2] x, the squared norm of the normalized wave function $|\Phi_{NORM}(x)|^2 \equiv |\langle x|\Phi_{NORM}\rangle|^2$, yields the probability for the system of being in the state $|x\rangle$. Then, the Monte Carlo technique is applied to move about in the configuration space and to extract the sample configurations used to compute the expectation value of the Hamiltonian. The move is guided by the ratio between the probability of the new configuration and that of the old one, through an acceptance-rejection method. After the energy converged to its equilibrium value, the algorithm continues to sample the configurations. Indeed all the physical quantities are computed as the average of a given function over many configurations.

The GFQMC is based on the power method, which consists in applying recursively a projector operator to an initial wave function to filter out the high energy components and find the ground state. Therefore, contrary to the VQMC, the GFQMC provides an exact result. This projection procedure is implemented in a stochastic way, by using a Monte Carlo technique where the move from one configuration to another is driven by the matrix elements of the Hamiltonian. Since, in this case, the transfer matrix is not normalized to 1, one has to introduce a weight associated to each configuration and the expectation values will be computed as weighted averages.

---

[1] The optimization is typically performed by a preliminary Monte Carlo simulation.

[2] The set of all the possible configurations is the basis of the space over which the Monte Carlo simulation is performed. For example, in bosonic and fermionic systems, the configuration is specified by the number of particles at each lattice site.

4.2.1 Variational QMC

Given a state $|\Phi\rangle$ and a complete basis $|x\rangle$, the expectation value of an operator $\hat{O}$ on the state $|\Phi\rangle$ can be expressed as

$$\langle\hat{O}\rangle = \frac{\langle\Phi|\hat{O}|\Phi\rangle}{\langle\Phi|\Phi\rangle} = \sum_x \frac{\langle\Phi|x\rangle}{\langle\Phi|\Phi\rangle}\langle x|\hat{O}|\Phi\rangle = \sum_x P(x)O(x) \qquad (4.7)$$

with $P(x)$ and $O(x)$ given by

$$P(x) = \frac{|\langle\Phi|x\rangle|^2}{\langle\Phi|\Phi\rangle} \equiv \frac{|\Phi(x)|^2}{\sum_{x'}|\Phi(x')|^2}\,, \qquad (4.8)$$

$$O(x) = \frac{\langle x|\hat{O}|\Phi\rangle}{\langle x|\Phi\rangle}\,, \qquad (4.9)$$

respectively. We observe that $P(x)$ satisfies the properties of a probability distribution, i.e., $P(x) \geq 0$ and $\sum_x P(x) = 1$. Therefore, the calculation of the expectation value $\langle\hat{O}\rangle$ can be casted as the average of a random variable $O(x)$ over a probability distribution $P(x)$.

The random variable $O(x)$ can be computed as

$$O(x) = \sum_{x'}\langle x|\hat{O}|x'\rangle\frac{\langle x'|\Phi\rangle}{\langle x|\Phi\rangle} \equiv \sum_{x'} O_{x,x'}\frac{\Phi(x')}{\Phi(x)}\,. \qquad (4.10)$$

In particular, we are interested in the case in which $\Phi \equiv \Phi_{GS}$ and $\hat{O} \equiv H$, hence $O(x) \equiv e_L(x)$ is the local energy and $\langle\hat{O}\rangle \equiv E_{GS}$ is the energy of the ground state. Therefore, we are dealing with two problems: 1) finding the form of $|\Phi_{GS}\rangle$; 2) computing the sums. Indeed, since the Hilbert space of a many-body system is typically very large, the number of possible configurations $\{x\}$ is large too and the sum (4.7) cannot be computed exactly.[3] The first issue is solved by choosing a variational wave function, which depends on some variational parameters. Those parameters are optimized by a preliminary Monte Carlo simulation (see the subsection below), which provides the general form of the wave function that will be employed for the calculation of the expectation values. In particular, its normalized squared norm, eq. (4.8), is regarded as a probability distribution and is used in the step 2) to drive the

---

[3]We notice that the sum (4.10), instead, can be easily computed, since the operator $\hat{O}$ typically connects only few configurations x' to a given configuration x, i.e. the matrix element $O_{x,x'}$ is non-zero only for a small number of configurations.

system from an initial configuration x_0 to a configuration x_1, or in general from x_n to x_{n+1}, where the label n indicates the n-th iteration of the Monte Carlo algorithm. Indeed, step 2) consists in extracting the configurations $\{x\}$ over which the sums are computed according to the probability distribution (4.8). That is achieved by means of the Metropolis algorithm (see the subsection below). It allows, after an equilibration time, to converge to the minimum energy. When the convergence is reached, the Metropolis algorithm continues to work to extract the configurations over which the average will be done. In fact, the expectation value will be evaluated after having generated a sequence of configurations $\{x_n | n \geq \bar{n}\}$ distributed according to the equilibrium probability (4.8) as an average of the function $O(x_n)$ over $\{x_n\}$:

$$\langle \hat{O} \rangle = \frac{1}{\bar{N}_{it}} \sum_{n=\bar{n}}^{N_{it}} O(x_n) \,, \tag{4.11}$$

where N_{it} is the number of iterations and $\bar{N}_{it} = N_{it} - \bar{n} + 1$ is the number of iterations after equilibration . In fact we observe that at the beginning the variables x are not distributed according to the equilibrium probability distribution $P(x)$. Only after $\bar{n}$ iterations (i.e., the number of iterations corresponding to the equilibration time) that is achieved. In general, for $n < \bar{n}$, the variable x_n will be distributed according to a different probability $P_n(x_n)$. However, these distributions are not important and are not computed. Whereas $P(x_n)$ is computed (up to a normalization constant) also for $n < \bar{n}$ in order to drive the algorithm towards the convergence, as will be explained in the subsection devoted to the Metropolis algorithm.
In what follows, we will see the details of the Metropolis algorithm and the optimization technique.

Markov chain and Metropolis algorithm

We assume that at each step n, the configuration x_n depends only on the configuration at the step $n-1$. Therefore, this process is a Markov chain and the evolution of the probability distribution can be described by the following master equation

$$P_{n+1}(x_{n+1}) = \sum_{x_n} \omega_{x_{n+1},x_n} P_n(x_n) \,, \tag{4.12}$$

where ω_{x_{n+1},x_n} is the transition probability from the configuration x_n to x_{n+1}. We want to generate a Markov chain such that, for large n, the variables x_n are distributed

according to a stationary probability given by (4.8). This means that after the equilibration time, i.e., for $n \geq \bar{n}$, the variables are distributed according to the desired probability: $P_n(x_n) \equiv P(x_n)$ and the master equation reads

$$P(x_{n+1}) = \sum_{x_n} \omega_{x_{n+1},x_n} P(x_n) . \tag{4.13}$$

A sufficient requirement for reaching a stationary distribution $P(x)$ is the detailed balance condition

$$\omega_{x_{n+1},x_n} P(x_n) = \omega_{x_n,x_{n+1}} P(x_{n+1}) . \tag{4.14}$$

Therefore, we have to define a transition matrix $\omega_{x',x}$ which satisfies this condition. A simple way to do this is to implement the Metropolis scheme. The idea is to split the transition matrix into the product of two elements

$$\omega_{x_{n+1},x_n} = A_{x_{n+1},x_n} T_{x_{n+1},x_n} . \tag{4.15}$$

Then, the configuration x_{n+1} is generated from x_n by T_{x_{n+1},x_n}, which can be chosen with great freedom, as long as ergodicity is ensured. The proposed move is accepted with probability

$$A_{x_{n+1},x_n} = \min\left\{ 1, \frac{P(x_{n+1})T_{x_n,x_{n+1}}}{P(x_n)T_{x_{n+1},x_n}} \right\} \tag{4.16}$$

meaning that a random number $\xi \in [0,1]$ is extracted and the move is accepted if $\xi \leq A_{x_{n+1},x_n}$. In most cases, the matrix T can be taken symmetric, in which case the acceptance rate (4.16) reduces to

$$A_{x_{n+1},x_n} = \min\left\{ 1, \frac{P(x_{n+1})}{P(x_n)} \right\} \equiv \min\left\{ 1, \frac{|\Phi(x_{n+1})|^2}{|\Phi(x_n)|^2} \right\} . \tag{4.17}$$

We finally observe that, in order to implement the Metropolis algorithm, at each iteration n it is sufficient to compute the probability $P(x_n)$ up to a normalization constant, i.e. it is sufficient to compute $|\Phi(x_n)|^2$.

Optimization of the variational parameters

Before performing the actual Monte Carlo simulation, it is necessary to optimize the variational parameters of the wave function, in order to obtain reliable results. There exist different optimization schemes, based both on the variance minimization and

on the energy minimization. Here, we present the stochastic reconfiguration method, which belongs to the second category.

Since the wave function depends on some variational parameters $\{\gamma\}$, also the expectation value (4.7) changes with $\{\gamma\}$. In particular, the expectation value of the Hamiltonian can be written as

$$E_{\{\gamma\}} = \frac{\langle \Phi_{\{\gamma\}} | H | \Phi_{\{\gamma\}} \rangle}{\langle \Phi_{\{\gamma\}} | \Phi_{\{\gamma\}} \rangle} \,, \tag{4.18}$$

where $\{\gamma\}$ denotes a set of p parameters: $\{\gamma\} \equiv \{\gamma_k\}_{k=1,\dots,p}$. The index k will be often omitted in the following. We would like to set up an iterative scheme that allows to find the values of $\{\gamma\}$ for which the energy reaches the minimum possible value. In order to do that, let's consider an initial set of parameters $\{\gamma^0\}$ and run a Monte Carlo simulation to compute $E_{\{\gamma^0\}}$, as described in the previous subsections. Then consider a small variation of the parameters: $\gamma_k^1 = \gamma_k^0 + \delta\gamma_k^0$. If the wave function has the form

$$|\Phi_{\{\gamma\}}\rangle = e^{\sum_{k=1}^p \gamma_k \hat{O}_k} |\phi_0\rangle \,, \tag{4.19}$$

we can linearly expand $|\Phi_{\{\gamma^1\}}\rangle$ with respect to $\delta\gamma^0$:

$$|\Phi_{\{\gamma^1\}}\rangle = e^{\sum_{k=1}^p \gamma_k^1 \hat{O}_k}|\phi_0\rangle = e^{\sum_{k=1}^p (\gamma_k^0 + \delta\gamma_k^0)\hat{O}_k}|\phi_0\rangle \simeq \sum_{k=0}^p \delta\gamma_k^0 \hat{O}_k |\Phi_{\{\gamma^0\}}\rangle \,, \tag{4.20}$$

with $\delta\gamma_0^0 = 1$ and $\hat{O}_0 = \mathbb{I}$. We want that $|\Phi_{\{\gamma^1\}}\rangle$ has a lower energy than $|\Phi_{\{\gamma^0\}}\rangle$. For this to happen, we could use the projection $|\Phi_H\rangle = (\Lambda - H)|\Phi_{\{\gamma^0\}}\rangle$. However, in general, this wave function is not of the form (4.19). In fact, we see from eq. (4.20) that $|\Phi_{\{\gamma^1\}}\rangle$ must lie in the subspace spanned by the basis $\{\hat{O}_k|\Phi_{\{\gamma^0\}}\rangle\}_{k=0,\dots p}$. Therefore, we can project $|\Phi_H\rangle$ over that subspace. In particular, we project it along a basis vector and impose that this projection is equal to the projection of (4.20) along the same vector:

$$\langle \Phi_{\{\gamma^0\}} | \hat{O}_k (\Lambda - H) | \Phi_{\{\gamma^0\}} \rangle = \sum_{k'=0}^p \langle \Phi_{\{\gamma^0\}} | \hat{O}_k \delta\gamma_{k'}^0 \hat{O}_{k'} | \Phi_{\{\gamma^0\}} \rangle \,. \tag{4.21}$$

From eq. (4.21) with $k = 0$ we can obtain $\delta\gamma_0^0$ as a function of Λ and by substituting this value into eq. (4.21) with $k > 0$, we get

$$\sum_{k'=1}^{p} \delta\gamma_{k'}^0 s_{k,k'}^0 = f_k^0 \tag{4.22}$$

with $s_{k,k'}^0 = \langle \hat{O}_k \hat{O}_{k'} \rangle - \langle \hat{O}_k \rangle \langle \hat{O}_{k'} \rangle$ and $f_k^0 = -\left[\langle \hat{O}_k H \rangle - \langle \hat{O}_k \rangle \langle H \rangle \right]$, where the expectation values are computed over $|\Phi_{\{\gamma^0\}}\rangle$. Therefore, during the Monte Carlo simulation in which $E_{\{\gamma^0\}}$ is computed, also those quantities should be evaluated, in a stochastic way. Then, one can evaluate the variation of the parameters by inverting eq. (4.22):

$$\delta\gamma^0 = (s^0)^{-1} \cdot f^0 \tag{4.23}$$

and the procedure is iterated with the new parameters $\{\gamma^1 = \gamma^0 + \delta\gamma^0\}$ and the corresponding wave function $|\Phi_{\{\gamma^1\}}\rangle$. The scheme is repeated until the variational parameters converge to a stationary value.

Summary of the VQMC algorithm

In summary, the VQMC algorithm relies on the following steps:

1. Choose a variational wave function $\Phi \equiv \Phi_{\{\gamma\}}$.

2. Optimize the parameters $\{\gamma\}$ by preliminary QMC simulations, i.e., follow points 3-10, evaluating for each configuration, not only the local energy, but also the quantities needed to compute the expectation values involved in eq. (4.22); at the end of point 10, solve eq. (4.23) to find the new parameters and repeat the entire procedure until the parameters reach a stationary value.

3. Choose the matrix T, i.e. the rule to propose a move in the configuration space.

4. Choose an initial configuration x_0.

5. Compute the local energy $e_L(x_0)$ (i.e., compute the ratio $RA(x'|x_0) = \frac{\Phi(x')}{\Phi(x_0)}$ and the matrix element $H_{x_0,x'}$, for all the configurations x' connected to x_0).

6. Propose a move from x_0 to a new configuration x_1, according to T.

7. Compute the square norm $|RA(x_1|x_0)|^2$ and accept or reject the move, according to the acceptance rate A_{x_1,x_0}.

8. If the move has been rejected, set $x_1 = x_0$.

9. Iterate points 5-8 with the new configuration, i.e., with the subscript of x increased by 1.

10. Compute the ground state energy as the average of the local energies $e_L(x_n)$ by discarding the values with $n < \bar{n}$.

11. Notice that the points 5,10 can be extended to compute any other observable with the same procedure used for the energy; however, in most cases it is convenient to memorize the configurations x_n and to compute the desired observables *a posteriori*.

4.2.2 Green's function QMC

Contrary to the VQMC, the goal of the GFQMC [97] is to find the exact ground state $|\Phi_{GS}\rangle$ of a quantum system. In the VQMC, the ground state is approximated and its form is known after the optimization process. Therefore, the stationary probability distribution $P(x) \sim |\langle x|\Phi_{GS}\rangle|^2$ in the master equation (4.13) is known *a priori* and the strength of the method consists in determining the transition matrix $\omega_{x',x}$ that drives the move in configuration space in such a way that the probability distribution of the extracted configurations converges to $P(x)$. If, instead, knowing the ground state wave function only approximately through the variational optimization of an initial guess is not satisfactory and the target is to get it exactly, $P(x)$ can not be determined *a priori*. Therefore, in the GFQMC the Markov chain described by eq. (4.12) is realized thanks to the knowledge of the particular transition matrix (the Green function) that enables the initial probability distribution $P_0(x)$ (i.e., the initial wave function $\Phi_0(x)$) to evolve towards the probability distribution $P(x)$ corresponding to the exact ground state of the system $\Phi_{GS}(x)$. In fact, the sampling in the configuration space is leaded by the Hamiltonian of the system.
As a matter of fact, the ground state of a system can be found through the power method, which consists in applying iteratively the operator[4] $\Lambda\mathbb{I} - H$ to an initial trial wave function $|\Phi_0\rangle$:

$$|\Phi_{n+1}\rangle = (\Lambda\mathbb{I} - H)|\Phi_n\rangle = (\Lambda\mathbb{I} - H)^{n+1}|\Phi_0\rangle. \qquad (4.24)$$

---

[4]Another operator that is able to project an initial state onto the ground state is $e^{-\beta H}$.

Indeed, the operator $(\Lambda\mathbb{I} - H)^n$ filters out the excited states from $|\Phi_0\rangle$, thus projecting it onto the ground state, for large n:

$$|\Phi_{GS}\rangle = \lim_{n\to\infty} (\Lambda\mathbb{I} - H)^n |\Phi_0\rangle . \tag{4.25}$$

The power method can be implemented stochastically. Indeed by projecting eq. (4.24) onto a basis vector $\langle x|$, it reads

$$\Phi_{n+1}(x) = \sum_{x'} G_{x,x'}\Phi_n(x') \tag{4.26}$$

with $G_{x,x'} \equiv \left(\Lambda\delta_{x,x'} - H_{x,x'}\right)$. We can recognize that this has the same form of the master equation (4.12) and the property (4.25) implies that for large enough n a stationary wave function $\Phi_{GS}(x)$ is achieved, as in (4.13). Therefore, it should be possible to solve the equation for $\Phi_{GS}(x)$ stochastically by sampling the configuration space according to the transition matrix G. However $G_{x,x'}$ does not have the characteristics of a transition probability, since in general it is not normalized to 1 and it is not always positive. This issue is solved by decomposing this matrix element into three factors:

$$G_{x,x'} = s_{x,x'}\omega_{x,x'}b_{x'} \tag{4.27}$$

where $\omega_{x,x'}$ fulfills the conditions $\omega_{x,x'} \geq 0$ and $\sum_{x'} \omega_{x,x'} = 1$, $b_{x'} = \sum_x G_{x,x'}$ is a normalization factor, and $s_{x,x'}$ is a sign. This last factor can be taken always equal to one in case of bosonic systems. Indeed, the interchanging of bosonic operators does not introduce a negative sign and the positiveness of $G_{x,x}$ can be guaranteed by taking a sufficiently large Λ. We will do this assumption hereinafter.

Thus, equation (4.26) can be written as

$$\Phi_{n+1}(x_{n+1}) = \sum_{x_n} \omega_{x_{n+1},x_n}b_{x_n}\Phi_n(x_n) . \tag{4.28}$$

Here the transition probability ω_{x_{n+1},x_n} determines the evolution of the configuration x_n. However the full matrix contains also the diagonal factor b_{x_n}. It can be taken into account in the stochastic process by introducing another variable, the so called weight w_n. Therefore, the basic element of the Markov chain is now the so called *walker*, i.e. the pair (x_n, w_n). At each Monte Carlo step, the new configuration x_{n+1} is extracted according to the probability ω_{x_{n+1},x_n}, whereas the weight is obtained from the deterministic rule $w_{n+1} = b_{x_n}w_n$ (with $w_0 = 1$). That can be thought as an

evolution under a transition probability having the form of a Dirac delta function $\delta(w_{n+1} - b_{x_n} w_n)$ (notice that w_n is a continuous variable).

The walker moves about in the Hilbert space of the matrix G and assumes a configuration (x_n, w_n) according to a given probability $P_n(x_n, w_n)$. The Master equation corresponding to such a probability is

$$P_{n+1}(x_{n+1}, w_{n+1}) = \sum_{x_n} \int dw_n \omega_{x_{n+1}, x_n} \delta(w_{n+1} - b_{x_n} w_n) P_n(x_n, w_n) . \qquad (4.29)$$

Indeed, if we require that

$$\Phi_n(x) = \int dw_n w_n P_n(x, w_n) = \sum_{x_n} \int dw_n (w_n \delta_{x, x_n}) P_n(x_n, w_n) , \qquad (4.30)$$

it is easy to recover eq. (4.28) from (4.29). On the other hand, one can also verify from eq. (4.29) that the probability $P_n(x_n) = \int dw_n P_n(x_n, w_n)$ of the configuration x_n evolves as

$$P_{n+1}(x_{n+1}) = \sum_{x_n} \omega_{x_{n+1}, x_n} P_n(x_n) , \qquad (4.31)$$

which is identical to (4.12).

From the GFQMC technique it would be possible, in principle, to obtain the amplitude of the ground state wave function for a given configuration x. Indeed, eq. (4.30) corresponds to the stochastic average of the weights over many realizations of the Markov chain, i.e., over the possible paths[5] to reach the configuration x, namely $\langle w_n \delta_{x, x_n} \rangle$.[6] However, it is rarely pursued in actual practice, since it is computationally demanding and the information contained in $\Phi_{GS}(x)$ for a fixed x is too large for being physically relevant.

The most important information about the ground state of the system are, instead, obtained from the energy and the correlation functions over the state $|\Phi_{GS}\rangle$. The ground state energy $E_{GS} = H|\Phi_{GS}\rangle$ can be written as

$$E_{GS} = \frac{\sum_x \langle x|H|\Phi_{GS}\rangle}{\sum_x \langle x|\Phi_{GS}\rangle} , \qquad (4.32)$$

---

[5]Notice that the weight w_n associated to the configuration $x \equiv x_n$ strongly depends on the pathway followed to reach x via $w_n = \prod_{i=0}^{n-1} b_{x_i}$.

[6]In order to obtain the amplitude of the ground state, the walkers (x_n, w_n) must be distributed according to the equilibrium probability $P(x_n, w_n)$, i.e., $n \geq \bar{n}$, $\bar{n}$ being the equilibration time.

which can be computed as the following statistical average

$$E_{GS} = \frac{\langle(\Lambda - b_x)w\rangle}{\langle w\rangle} \equiv \frac{\frac{1}{\#I}\sum_{(x,w)\in I}(\Lambda - b_x)w}{\frac{1}{\#I}\sum_{(x,w)\in I} w} , \tag{4.33}$$

where I is a set of walkers (x, w) which are distributed according to the equilibrium probability $P(x, w)$ and $\#I$ is its cardinality. For the demonstration of the formula (4.33), see Appendix D. However, we notice that this calculation of the energy does not satisfy the zero variance property as in the VQMC, i.e., the average (4.33) is always affected by large statistical fluctuation, regardless of the initial trial wave function. The zero variance property would allow to reduce the statistical fluctuations by using a trial wave function close to the ground state wave function. In particular, if the trial wave function coincides with the ground state wave function, then the energy is free of statistical fluctuations. This property can be recovered by introducing the so called *importance sampling* Green'function

$$\tilde{G}_{x,x'} = G_{x,x'}\frac{\Phi_G(x)}{\Phi_G(x')} , \tag{4.34}$$

where Φ_G is named *guiding wave function* and is a guess of the ground state wave function, typically obtained via the optimization scheme of the VQMC. The importance sampling allows to reduce the statistical fluctuations when Φ_G is close to Φ_{GS}. With this definition of the Green's function, the master equation (4.26) reads

$$\tilde{\Phi}_{n+1}(x) = \sum_{x'} \tilde{G}_{x,x'}\tilde{\Phi}_n(x') , \tag{4.35}$$

with $\tilde{\Phi}_n(x) = \Phi_G(x)\Phi_n(x) = \int dw\, w\tilde{P}(x, w)$. Therefore, if the GFQMC scheme reproduces eq. (4.35) instead of (4.26), ones the convergence is reached, the walkers will be distributed according to the probability $\tilde{P}(x, w)$, corresponding to the wave function $\tilde{\Phi}_{GS}(x)$. In this case, the ground state energy can be evaluated as

$$E_{GS} = \frac{\langle\Phi_G|H|\Phi_{GS}\rangle}{\langle\Phi_G|\Phi_{GS}\rangle} = \frac{\sum_x e_L(x)\tilde{\Phi}_{GS}(x)}{\sum_x \tilde{\Phi}_{GS}(x)} = \frac{\langle e_L(x)w\rangle}{\langle w\rangle} = \frac{\langle(\Lambda - \tilde{b}_x)w\rangle}{\langle w\rangle} . \tag{4.36}$$

Here, $e_L(x)$ is the local energy on the guiding wave function, defined as in (4.9)[7] and $\tilde{b}_x = \sum_{x'} \tilde{G}_{x',x}$. The details of the calculation can be found in Appendix D. Notice

---

[7]We are assuming that the wave function is real.

that eq. (4.36) is similar to eq. (4.33), but now the averages are computed over the walkers $(x, w) \in \tilde{I}$ distributed according to $\tilde{P}(x, w)$, and $\tilde{b}_x$ depends on the guiding wave function. That allows to reduce the statistical fluctuations by improving Φ_G. The stochastic averages in eq. (4.36) could be evaluated upon several Markov chains, namely

$$
\frac{\langle e_L(x)w \rangle}{\langle w \rangle} = \frac{\langle e_L(x_n)w_n \rangle}{\langle w_n \rangle} = \frac{\frac{1}{N_{MC}} \sum_{i=1}^{N_{MC}} e_L(x_n^{(i)})w_n^{(i)}}{\frac{1}{N_{MC}} \sum_{i=1}^{N_{MC}} w_n^{(i)}} \, , \tag{4.37}
$$

where N_{MC} is the number of Markov chains used to accumulate statistics in the calculation of the average, i labels the different Markov chains and n, labeling a particular iteration of each Markov process, is large enough that all the Markov chains have reached the convergence. An alternative to this, would be to develop a long Markov chain (with $N_{it} >> \bar{n}$). In this case, we have

$$
\frac{\langle e_L(x)w \rangle}{\langle w \rangle} = \frac{\frac{1}{N_{it}-l} \sum_{n=\bar{n}+l}^{N_{it}} e_L(x_n)w_n^l}{\frac{1}{N_{it}-l} \sum_{n=\bar{n}+l}^{N_{it}} w_n^l} \, , \tag{4.38}
$$

where the weight $w_n = \prod_{i=0}^{n-1} b_{x_i}$, which would increase exponentially with n, has been replaced by $w_n^l = \prod_{i=1}^{l} b_{x_{n-1}}$. This is allowed by the following argument: after the equilibration time, the configurations x_n are distributed according to the probability $\tilde{P}(x_n) = \int dw_n \tilde{P}(x_n, w_n)$, which differs from $\tilde{\Phi}_{GS}(x_n)$ by the weights that weight differently the various configurations; therefore, we may consider the equilibrium state $\tilde{\Phi}_{GS}(x_n)$ as being obtained from the power method (4.25) with an initial trial state $\tilde{P}(x_{n-l})$. That would imply that the initial walker (x_{n-l}, w'_{n-l}), with weight $w'_{n-l} = 1$, distributed according to $\tilde{P}(x_{n-l})$, evolves into the walker (x_n, w'_n), with weight $w'_n = \prod_{i=1}^{l} b_{x_{n-i}}$, distributed according to $\tilde{\Phi}_{GS}(x_n)$, in l steps. Then, we can recognize that $w'_n \equiv w_n^l$. In summary, this procedure consists in doing many Markov chains, starting from the configurations $\{x_{\bar{n}}, x_{\bar{n}+1}, x_{\bar{n}+2}, ...\}$ and ending in the configurations $\{x_{\bar{n}+l}, x_{\bar{n}+1+l}, x_{\bar{n}+2+l}, ...\}$. This is advantageous because their convergence is much faster than the initial thermalization (requiring $\bar{n}$ iterations). In Figure 4.2, we show the behavior of the ground state energy as a function of the number l of correcting factors.
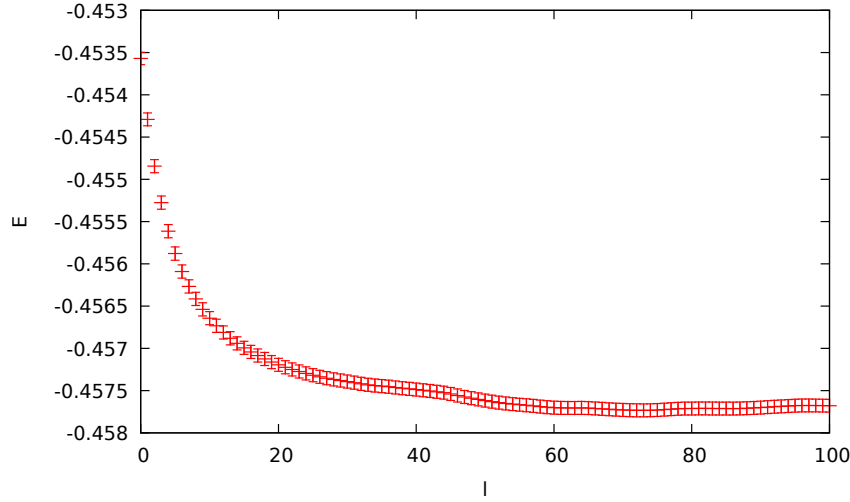
Fig. 4.2 Example of ground state energy as a function of the numbel l of correcting factors. The computation refers to the superfluid phase of the one-dimensional Bose-Hubbard model.

Many walkers formulation and branching

In the scheme presented above, for large l the variance of w_n^l diverges exponentially. In order to overcome this problem, one can consider a scheme where many walkers evolve simultaneously and every n_B iterations a reconfiguration scheme that redefines the walkers is applied. During this process, the walkers with negligible weights are suppressed and those with high weights are duplicated. Equations (4.29) and (4.30) are easily generalized to the case of many independent walkers. Within the importance sampling scheme, they read

$$\tilde{P}(\vec{x}_{n+1}, \vec{w}_{n+1}) = \sum_{x_n^{(1)}, \dots, x_n^{(N_W)}} \int dw_n^{(1)} \dots dw_n^{(N_W)} \left(\prod_{j=1}^{N_W} \tilde{\omega}_{x_{n+1}^{(j)}, x_n^{(j)}} \delta(w_{n+1}^{(j)} - \tilde{b}_{x_n^{(j)}} w_n^{(j)}) \right) \tilde{P}_n(\vec{x}_n, \vec{w}_n)$$

(4.39)

and

$$\tilde{\Phi}_n(x) = \sum_{x_n^{(1)}, \dots, x_n^{(N_W)}} \int dw_n^{(1)} \dots dw_n^{(N_W)} \left(\frac{1}{N_W} \sum_{j=1}^{N_W} w_n^{(j)} \delta_{x, x_n^{(j)}} \right) \tilde{P}_n(\vec{x}_n, \vec{w}_n) = \langle \frac{1}{N_W} \sum_{j=1}^{N_W} w_n^{(j)} \delta_{x, x_n^{(j)}} \rangle,$$

(4.40)

respectively, where the couple of vectors $(\vec{x}_n, \vec{w}_n)$ denote the set of N_W simultaneous walkers $(\{x_n^{(j)}\}, \{w_n^{(j)}\})$ at iteration n, with the superscript (j) labeling the j-th walker. Moreover, since the walkers are uncorrelated from each other, the probability

$\tilde{P}_n(\vec{x}_n, \vec{w}_n)$ is given by

$$\tilde{P}_n(\vec{x}_n, \vec{w}_n) \equiv \tilde{P}_n(x_n^{(1)}, ..., x_n^{(N_W)}, w_n^{(1)}, ...w_n^{(N_W)}) = \prod_{j=1}^{N_W} \tilde{P}_n(x_n^{(j)}, w_n^{(j)}). \qquad (4.41)$$

The reconfiguration process consists in defining new walkers $(\vec{x}_n', \vec{w}_n')$ that are distributed according to a new probability $\tilde{P}_n'(\vec{x}_n', \vec{w}_n')$, without changing the wave function given by the statistical average in (4.40), namely $\tilde{\Phi}_n(x) = \tilde{\Phi}_n'(x)$. This can be achieved through a particular Markov process which, starting from the old walkers $(\vec{x}_n, \vec{w}_n)$, generate the new ones $(\vec{x}_n', \vec{w}_n')$. It is described by the following Master equation

$$\tilde{P}_n'(\vec{x}_n', \vec{w}_n') = \sum_{x_n^{(1)}, ..., x_n^{(N_W)}} \int dw_n^{(1)} ... dw_n^{(N_W)} K(\vec{x}_n', \vec{w}_n' | \vec{x}_n, \vec{w}_n) \tilde{P}_n(\vec{x}_n, \vec{w}_n) \qquad (4.42)$$

with $K(\vec{x}_n', \vec{w}_n' | \vec{x}_n, \vec{w}_n) = \prod_{j=1}^{N_W} \frac{\sum_i w_n^{(i)} \delta_{x_n'^{(j)}, x_n^{(i)}}}{\sum_i w_n^{(i)}} \delta(w_n'^{(j)} - \frac{\sum_i w_n^{(i)}}{N_W})$, implying that all the new walkers are generated with the same weight $w_n'^{(j)} = \bar{w}_n = \sum_i w_n^{(i)}/N_W$ and a configuration $x_n'^{(j)}$ chosen among the N_W old configurations $\{x_n^{(i)}\}_{i=1,...,N_W}$ with a probability proportional to their weights: $w_n^{(i)}/\sum_k w_n^{(k)}$. This reconfiguration process is called *branching* and is applied repeatedly every n_B steps of independent walker propagation. Within this scheme, we can generalize formula (4.38) to the many-walker case. After or before each reconfiguration process, the local energy is averaged over all the walkers and this average is used to calculate the ground state energy as in eq. (4.38):

$$E_{GS} = \frac{\frac{1}{\bar{N}_B - l} \sum_{n=\bar{n}+l}^{N_B} \bar{e}_L(x_n) w_n^l}{\frac{1}{\bar{N}_B - l} \sum_{n=\bar{n}+l}^{N_B} w_n^l}, \qquad (4.43)$$

where now n labels the reconfiguration process, N_B is the number of times it is applied, $\bar{n}$ is the first reconfiguration process at equilibrium, and $\bar{N}_B = N_B - \bar{n} + 1$. If the local energy $\bar{e}_L$ is computed immediately after the branching, when all the walkers have the same weights, it is obtained as $\bar{e}_L(x_n) = \frac{1}{N_W} \sum_{j=1}^{N_W} e_L(x_n^{(j)})$; whereas, if it is computed just before the branching, it is given by $\bar{e}_L(x_n) = \frac{\sum_{j=1}^{N_W} w_n^{(j)} e_L(x_n^{(j)})}{\sum_{j=1}^{N_W} w_n^{(j)}}$. In the second case, the statistical error is reduced. Obviously, also the coefficients w_n^l

change. Indeed now they have the form $w_n^l = \prod_{i=0}^{l-1} \bar{w}_{n-i}$[8], thus corresponding to the application of $l \times n_B$ iterations of the power method [98].

Computation of the correlations: forward walking technique

The GFQMC also allows to efficiently compute the expectation values of operators that are diagonal in the chosen basis. The procedure is similar to that followed for the energy. However, in this case it is not sufficient to apply the power method to the right state in $\langle \Phi_G | \hat{O} | \Phi_G \rangle$, since in general $| \Phi_{GS} \rangle$ is not an eigenstate of $\hat{O}$. In order to get convergence also for the left state $\langle \Phi_G |$, the so called forward walking technique is applied. It amounts to calculate the weight factor w_n^l corresponding to an equilibrated configuration x_n considering not only the l iterations backward but also m iterations forward, namely

$$\langle \hat{O} \rangle = \frac{\sum_n \bar{O}(x_n) w_n^{(l,m)}}{\sum_n w_n^{(l,m)}} , \qquad (4.44)$$

with $\bar{O}(x_n) = \frac{1}{N_W} \sum_{j=1}^{N_W} \langle x_n^{(j)} | \hat{O} | x_n^{(j)} \rangle$ [9], and $w_n^{(l,m)} = \prod_{i=-m}^{l-1} \bar{w}_{n-i}$. For further details, see [98].

Summary of the GFQMC algorithm

In summary, the GFQMC algorithm relies on the following steps:

1. Choose a variational wave function $\Phi \equiv \Phi_{\{\gamma\}}$.

2. Optimize the parameters through the optimization scheme of the VQMC and define the guiding wave function Φ_G as the optimized variational wave function.

3. Choose an initial set of N_W configurations $\vec{x}_0 = \{x_0^{(i)}\}_{i=1,...,N_W}$, with associated weights $w_0^{(i)} = 1$, i.e., define the initial walkers $(\vec{x}_0, \vec{w}_0)$.

---

[8]Usually the mean weight $\bar{w}_n$ is stored after each reconfiguration process and the weights of all the walkers are reset equal to 1 instead than $\bar{w}_n$.

[9]This follows from the fact that the operator $\hat{O}$ is diagonal in the basis $|x\rangle$, so that $O(x_n^{(j)}) \equiv \frac{\langle \Phi_G | \hat{O} | x \rangle}{\langle \Phi_G | x \rangle} = \langle x | \hat{O} | x \rangle$.

For each walker:

4. Compute the matrix elements $\tilde{G}_{x',x_0} = G_{x',x_0} \frac{\Phi_G(x')}{\Phi_G(x_0)}$ for all the configurations x' connected to x_0; hence compute $\tilde{b}_{x_0} = \sum_{x'} \tilde{G}_{x',x_0}$ and the probabilities $\tilde{\omega}_{x',x_0} = \frac{\tilde{G}_{x',x_0}}{\tilde{b}_{x_0}}$.

5. Extract the new configuration $x' = x_1$ according to the probability $\tilde{\omega}_{x',x_0}$.

6. Calculate the associated weight as $w_1 = \tilde{b}_{x_0} w_0$.

7. Iterate points 4-6 with the new walker, i.e, with the subscripts of x and w increased by 1.

8. If $n = a n_B - 1$ (with $a \in \mathbb{N}$), compute the local energy $\bar{e}_L(x_n)$ as a weighted average over the N_W walkers. Memorize the local energy and the average weight.[10]

9. If $n = a n_B$, apply the reconfiguration scheme to redefine the walkers.

10. For each redefined walker, repeat points 4-7.

11. Iterate points 8-10.

12. After many reconfiguration processes, compute the GS energy E_{GS} as in (4.43).

13. Compute the wanted observables as in (4.44).[11]

4.2.3 Estimation of error bars: the binning technique

At the end of this section, we would like to mention how the errors on the computed quantities can be estimated. In particular, let's focus on the energy. In the VQMC and GFQMC it is computed respectively as

$$E_{GS}^{VQMC} = \frac{1}{\bar{N}_{it}} \sum_{n=\bar{n}}^{N_{it}} e_L(x_n) \tag{4.45}$$

---

[10]Alternatively, it is possible to memorize the configurations and weights of the N_W walkers and compute the local energy successively.

[11]Notice that the computation of the observables require that the configurations and the weights have been memorized.

and

$$E_{GS}^{GFQMC} = \frac{\sum_{n=\bar{n}+l}^{N_B} \bar{e}_L(x_n) w_n^l}{\sum_{n=\bar{n}+l}^{N_B} w_n^l} \, . \tag{4.46}$$

The standard error of the energy could be estimated through the variance. However, we observe that the variables involved in the calculation of these averages are correlated to each other. Therefore, the variance would underestimate the error bars. This issue can be solved by reducing the correlations in two different ways:

a) computing the local energy every n_A iterations instead then at each $n \geq \bar{n}$;

b) using the binning technique.

While the point a) is computationally much expensive, since it requires a number of iterations much larger than that effectively used to accumulate statistics for the computation of the averages, the point b) is very efficient. It consists in dividing the number of iterations at which the local energy is computed, N_{comp}, into N_{bin} bins of length $L_{bin} = N_{comp}/(N_{bin})$.[12] Then, on each bin j one can compute the average energy E_j^{bin}. For example, in the case of VQMC, it reads

$$E_j^{bin} = \frac{1}{L_{bin}} \sum_{n=(j-1)L_{bin}+1}^{jL_{bin}} e_L(x_n) \, . \tag{4.47}$$

Hence, the ground state energy will be calculated as the average of E_j^{bin} over many bins, by discarding the first $\bar{n} - 1$ bins corresponding to the equilibration time:

$$E_{GS} = \frac{1}{\bar{N}_{bin}} \sum_{j=\bar{n}}^{N_{bin}} E_j^{bin} \, , \tag{4.48}$$

with $\bar{N}_{bin} = N_{bin} - \bar{n} + 1$. The random variables E_j^{bin} are more and more uncorrelated with increasing the bin length L_{bin}. Therefore now the variance of the ground state energy (4.48) can be estimated as

$$\sigma_{E_{GS}}^2 = \frac{1}{\bar{N}_{bin}(\bar{N}_{bin} - 1)} \sum_{j=\bar{n}}^{N_{bin}} \left(E_j^{bin} - E_{GS} \right)^2 \, , \tag{4.49}$$

provided that both L_{bin} and $\bar{N}_{bin}$ are sufficiently large.

---

[12] $N_{comp} = N_{it}/n_A$ in VQMC and $N_{comp} = N_B/n_A$ in GFQMC.

Chapter 5

Experimental techniques and applications: cold atom systems

This brief chapter is devoted to illustrate the relevance of Hubbard-like models and non-local order parameters in the context of cold atoms and possible future applications. In this regard, we touch upon experimental techniques and measurements. Ultracold atom experiments allow to mimic condensed matter systems with high control and tunability of the parameters involved and to reach even new regimes, for instance, in low dimensions. They rely on the possibility of slowing atoms to very low temperature, where phase transitions are driven by quantum fluctuations, and trapping them into optical lattices, where their motion is highly controllable.
In the following we will provide an elementary explanation of how experiments are carried on and their main achievements.

5.1   Atom cooling and traps

Cold atom experiments exploit laser light to both cool down and trap atoms. That is typically combined with the application of external magnetic fields, which can be used either to favor the laser cooling and to produce spatial confinement. Indeed the most common laser cooling techniques are based on the radiation pressure force, which is responsible for the transfer of momentum from light to atoms in a resonant scattering process. When an atom is hit by an incident laser beam, it absorbs photons and emits them in random directions when decaying back to the ground state. As
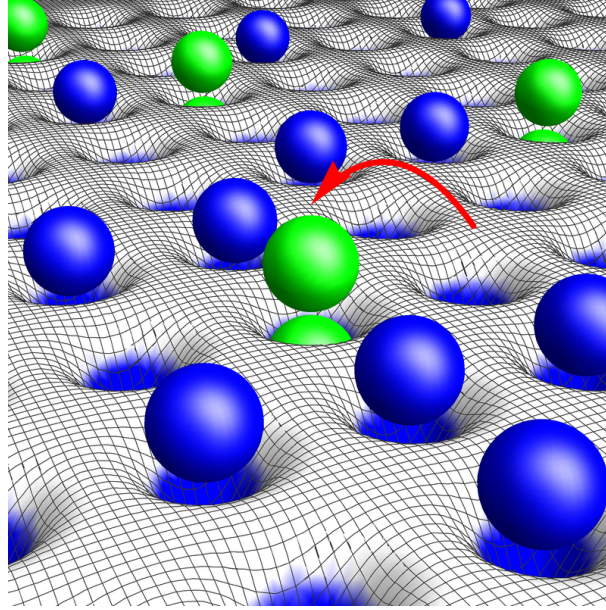
Fig. 5.1 Atoms in a periodic lattice.

a consequence, an average momentum $\hbar k$ is transfered (k being the wavevector of the laser). The application of a spatially varying magnetic field allows to shift the atomic levels, thus neutralizing the Doppler shift that would accompany the slowing down of atoms and bring them out of resonance with the laser. On the other hand, the interaction of an inhomogeneous magnetic field with the atomic magnetic dipole moment can be used to create magnetic traps for atoms. When the atoms are confined with both optical and magnetic traps, they are further cooled down by the so-called evaporative cooling, based on removing the most energetic atoms. In fact, then the atom-atom collisions cause a thermalization of the remaining atoms at lower temperature.

One of the main application of the aforementioned techniques is the engineering of model Hamiltonians to simulate the physics of condensed matter systems. This is primarily achieved by mimicking the periodic potential generated by the ions of a crystalline solid that acts upon the motion of electrons (Fig. 5.1). In experiments, the latter are replaced by cold neutral atoms, while the periodic potential is produced by the standing waves generating from the interference of two counterpropagating laser beams in each of the three spatial directions. It is described by the following expression

$$V_{lat}(x,y,z) = V_{0x}\sin^2(kx) + V_{0y}\sin^2(ky) + V_{0z}\sin^2(kz) \tag{5.1}$$
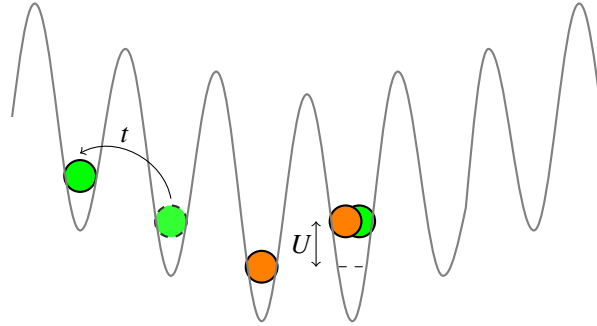
Fig. 5.2 System of cold atoms in an optical lattice described by the Hubbard model plus the term (5.4) accounting for the harmonic confinement.

where $k = 2\pi/\lambda$ is the wave vector of the laser and the wavelength λ determines the spatial periodicity $a = \lambda/2$ of the generated optical lattice. In the optical lattice atoms experience a potential of the form (5.1) due to the interaction between their induced electric dipole moment and the laser light. Typically the atomic gas is transfered into the optical lattice after having been laser cooled and magnetically trapped. Therefore it is subject to the combined effect of magnetic and optical potentials. Moreover an adding harmonic confinement is superimposed. It may be provided by the optical beams themselves or by other magnetic or optical traps. The parameters of the optical lattice can be tuned. In particular, the height of its barrier in a given direction $V_{0\alpha}$ (with $\alpha = x, y, z$) is proportional to the intensity of the corresponding pair of laser beams, which can be controlled in an experiment. Therefore that allows to guide the kinetics of atoms. Indeed, an increase of the potential depth results in a reduction of the atom tunneling. As a consequence, this tool can be exploited to realize $1D$ and $2D$ geometries by suppressing the tunneling in the orthogonal direction(s).

5.2   Tuning and control of parameters

The experimental setup previously described can be implemented to simulate Hubbard-like systems (Fig. 5.2). In this case, the hopping term can be controlled through the intensity of the standing laser waves, as explained above. On the other hand, due to the low kinetic energy, two atoms lying in the same potential well interact via s-wave scattering. This process, modeled by the contact interaction of the Hubbard Hamiltonian, is governed by the scattering length a_s, which can be tuned by varying an

external magnetic field through Feshbach resonances. In particular, for a $1D$ system, the hopping amplitude and the on-site interaction can be estimated, respectively, as [99, 100]

$$
\begin{aligned}
\frac{t}{E_R} &= \frac{4}{\sqrt{\pi}} \left(\frac{V_0}{E_R} \right)^{3/4} e^{-2\sqrt{V_0/E_R}} \\
\frac{U}{E_R} &= \frac{2\pi}{\lambda} a_s \sqrt{\frac{8}{\pi}} \left(\frac{V_0}{E_R} \right)^{1/4} \left(\frac{V_\perp}{E_R} \right)^{1/2}
\end{aligned}
\tag{5.2}
$$

in units of the recoil energy

$$
E_R = \frac{\hbar^2}{2m} \left(\frac{2\pi}{\lambda} \right)^2
\tag{5.3}
$$

with m the mass of atoms, V_0 the maximum amplitude of the potential in the direction of motion and $V_\perp$ the maximum amplitude of the potential in each of the two transverse directions. Finally the effect of the confining harmonic potential can be accounted for by adding a term of the form

$$
\sum_i \varepsilon_i n_i
\tag{5.4}
$$

to the Hamiltonian. Here $\varepsilon_i \approx V_T(x_i)$ is the energy offset experienced by an atom in the lattice site i due to the harmonic trapping potential [101].

The Hubbard model has first been realized with ^{87}Rb bosonic atoms loaded in a three dimensional optical lattice [102]. Here the transition has been observed by tuning the height of the potential barrier and analysing the interference pattern of the atomic wave functions during free expansion occurring when the combined trapping potentials are suddenly turned off. Subsequently also fermionic atoms have been employed to realize ultracold atom systems [103]. In this case, the fermionic atoms are cooled by thermal contact with an auxiliary bosonic species, which is evaporated and later removed from the trap. Then, the two spin species are realized by preparing the atoms in two different magnetic Zeeman sublevels. In the first experiment a mixture of potassium ^{40}K atoms was used, with either $|F = -9/2, m_F = -9/2\rangle$ and $|F = -9.2, m_F = -7/2\rangle$ or $|F = -9/2, m_F = -9/2\rangle$ and $|F = -9.2, m_F = -5/2\rangle$($F$ being the total angular momentum and m_F the magnetic quantum number). A similar mixture was handled to reach, some years later, the strongly interacting MI regime [104]. Here, informations on the state of the system have been inferred by measuring the number of double occupancies. Other types of fermionic atoms typically used

in recent experiments are ^{6}Li and ^{173}Yb. Instead, ^{168}Er bosonic dipolar atoms or ^{167}Er fermionic dipolar atoms can be employed to realize long-range dipole-dipole interactions [105, 106].

In the context of Hubbard-like models, the relevance of cold atom systems with respect to solid state materials relies on the fact that they provide a pure realization of model Hamiltonians, thus motivating the intense theoretical research of hidden phases. In the next section we will review the latest developments of experimental techniques to probe (non-local) correlation functions.

5.3 Measurement of correlation functions

In most experiments information about the state of the system has been inferred by time-of-flight images, where the momentum distribution of the atomic gas is measured by absorption when it is released from the trap. Recently the detection techniques have been greatly improved by the possibility of revealing individual atoms via high-resolution fluorescence imaging [107]. Single-site and single-atom resolved detection of ultracold quantum gases enables to directly observe all particle fluctuations in the system, thus giving access to the measurement of non-local correlation functions. In [108] this technique has been applied to get experimental observation of parity non-local correlators in a one-dimensional Bose-Hubbard system. Furthermore, in ref. [109] spin and charge degrees of freedom have been detected simultaneously in fermionic Hubbard chains. Thus the system has been fully characterized reconstructing the position of all spins, doublons and holons. Advancements in this field are very rapid. In fact a particular kind of non-local Haldane-like correlator has also been measured [110] in hole-doped fermionic Hubbard chains. It contains a charge operator in the middle of the string and two spin operators at the edges. The experiment has provided an evidence for the spin-charge separation and has unveiled the presence of a hidden magnetic order. The ability to measure multi-point correlations opens the path to the detection of many non-local string-like order parameters.

Part II

Our original contributions

Chapter 6

Using NLOPs as a probe for phase transitions

In the first part of this thesis, we have described in detail all the ingredients needed for our purposes. Here we start to apply them to develop some original contribution. Since this thesis mostly concerns with non-local orders, our first aim is to test the efficiency of non-local order parameters in detecting phase transitions. Therefore, in this chapter we prove that all the phases encoded in the one dimensional extended Hubbard model (EHM) can be probed via non-local operators related to charge and spin fluctuations. The great advantage in using them with respect to usual local operators consists in the fact that their average value is non-zero in the asymptotic limit only in the appropriate gapped phases. That makes them powerful and accurate probes to reveal different quantum phases. Indeed, the results that will be presented in the following confirm that they capture both the nature and the location of the phase transitions. Relevantly, this holds also for conducting phases with a spin gap, thus being able to identify superconducting and paired superfluid regimes.
The content of this chapter has been published in Ref. [111].

6.1   Introduction and motivation

The one-dimensional extended Hubbard model, already introduced in Section 1.3, presents a rich phase diagram, with a wide spectrum of applications. Indeed, it properly describes conducting polymers [112] and organic charge-transfer salts [113], as

well as copper-oxide materials related to the high-T_c cuprate superconductors [114]. Its full phase diagram has been investigated for specific fillings by means of different techniques [15, 115–118, 25, 24].

In particular, great attention has been devoted to the repulsive interaction regime due to the presence of a phase with bond-order waves [118, 25], which is not predicted by single loop bosonization [18–21, 23, 119, 120]. In recent years it has been shown that this phase is accurately described by non-local order parameters [53].

Relevantly, the bosonic EHM [121] with dipolar interaction has been experimentally realized by using ultracold quantum gases of Er magnetic atoms [105]. Furthermore many kinds of fermionic particles with strong dipolar momentum [122, 106, 123] are currently available, thus making just matter of time the simulation of the extended Hubbard Hamiltonian in cold atom experiments. Motivated by the aformentioned reasons, theorists have considered the EHM with long-range dipole-dipole interaction [26]. Their results show that the main feature of the phase diagram are captured also if the dipolar interaction is truncated to nearest neighbors. On the other hand, in-situ imaging has allowed to measure the non-local parity in the charge degree of freedom [108], while the others are in principle detectable with the advancing experimental techniques [124, 109].

These experimental achievements motivated us to show that non-local order parameters are able to detect all the phase transitions occurring in the EHM. In fact, they provide some crucial information about the system. In particular, they are able to detect the non-local long-range orders that respect the continuous symmetry of the Hamiltonian; therefore they recognize the appearance of different phases in one dimension that do not violate the Mermin-Wagner theorem [47]. Moreover, they can reveal the presence of topological phases [78], as well as hidden orders which are not easily distinguishable by looking at the ordinary two-point correlation functions [49].

In this chapter, we will first review the model and its phase diagram and then we will discuss the behavior of NLOPs across the phase transitions by means of DMRG analysis. Our numerical results are in agreement with the previous studies in predicting both the location and the nature of transitions. That reveals the non-local character of all phases at zero temperature, with both trivial and exotic [48] orders.

6.2   Model and phase diagram

We consider a 1D unit density balanced two-component Fermi mixture of N fermions trapped in L lattice sites. It is described by the Hamiltonian (1.47):

$$H = -t \sum_{j,\sigma} \left(c_{j,\sigma}^{\dagger} c_{j+1,\sigma} + h.c. \right) + U \sum_j n_{j,\uparrow} n_{j,\downarrow} + V \sum_j n_j n_{j+1} \,. \qquad (6.1)$$

The three terms with coefficients t, U, V describe the tunneling processes, on-site and nearest-neighbor interactions, respectively. This model shows a very rich phase diagram. A qualitative picture is drawn in Fig. 6.1. Depending on the strength of the interactions, we observe the appearance of six different phases. This variety is due to the charge-spin separation, which allows the charge and the spin gaps to open at different values of the Hamiltonian parameters. We remind that they are defined respectively as

$$\Delta_c = \frac{E(N = L + 2, \mathrm{S}^{(s),z} = 0) + E(N = L - 2, \mathrm{S}^{(s),z} = 0) - 2E(N = L, \mathrm{S}^{(s),z} = 0)}{2} \qquad (6.2)$$

$$\Delta_s = E(N = L, \mathrm{S}^{(s),z} = 1) - E(N = L, \mathrm{S}^{(s),z} = 0) \,, \qquad (6.3)$$

where $E(N, \mathrm{S}^{(s),z})$ is the energy of a system with N fermions and total unbalance $\mathrm{S}^{(s),z} = (N_\uparrow - N_\downarrow)/2$. The phase diagram shows both fully gapped and partly gapped phases, as well as gapless phases. The strong repulsive nearest-neighbor interaction favors the alternation of empty and doubly occupied sites. In fact, this kind of phase takes place for strong $V > 0$. It is a fully gapped charge density wave (CDW). When the strength of the interaction is reduced, it survives but is affected by fluctuations which consist in the appearance of pairs of singly occupied sites with fermions of opposite spins. On the other hand, the strong repulsive on-site interaction supports the presence of the Mott insulator (MI) phase, with one particle per site (without a preferred arrangement of the two species). As the value of U is reduced, fluctuations produce the formation of holon/doublon pairs. Between the CDW and MI phases, at intermediate couplings, a thin region characterized by bond ordered wave (BOW) appears. Here, holon/doublon and and up/down spin pairs localized on bonds coexist. The fermionic pairing is also present in the strong $U < 0$ regime, where a phase separation (PS) or a Luther Emery (LE) phase with dominant singlet superconducting (SS) correlations occurs, depending on the strength of V. In particular, the last one appears in the presence of a weak attractive nearest-neighbor interaction, where

single fermions with opposite spins are coupled in correlated pairs in a background of holons and doublons. Instead, for strong attractive nearest-neighbor interactions, holons and doublons coexist in separated regions. Finally, a gapless phase with dominant triplet superconducting (TS) correlations takes place at small U and $V < 0$. An intuitive scheme of all the aformentioned phases can be found in the bottom right panel of Fig. 6.1.

Most of these phases are predicted by the bosonization approximation at low energies. Following the procedure described in Chapter 3, one finds that the extended Hubbard Hamiltonian (6.1) in the weak coupling limit is equivalent to two decoupled sine-Gordon models, each one entirely expressed by the charge or the spin degree of freedom :

$$H = H_c + H_s \tag{6.4}$$

with

$$H_v = \frac{1}{2} \int dx \left[v_v K_v \left(\nabla \theta_v(x) \right)^2 + \frac{v_v}{K_v} \left(\nabla \phi_v(x) \right)^2 \right] + \frac{2 g_v}{(2\pi\alpha)^2} \int dx \cos(\sqrt{8\pi}\phi_v(x)) \tag{6.5}$$

and $v = c, s$. The Luttinger parameters K_v, the velocities v_v and the masses $g_v = m_v v_v$ contain the physical parameters t, U, V. Their expression are explicitly written as

$$
\begin{aligned}
v_v K_v &= 2ta \\
\frac{v_c}{K_c} &= 2ta \left[1 + \frac{1}{2\pi t} (U + 6V) \right] \\
\frac{v_s}{K_s} &= 2ta \left[1 - \frac{1}{2\pi t} (U - 2V) \right] \\
g_v &= -ac_v(U - 2V)
\end{aligned}
\tag{6.6}
$$

where a is the lattice spacing and $c_v = \pm 1$ for $v = c, s$, respectively. These results can be found in [81] and in [54] (see also Chapter 7 for the details of the calculation in a slightly different model). In each of the two sine-Gordon models, the competition between the kinetic and mass terms establishes the limits in which the interaction becomes relevant, giving rise to a gapped regime in the corresponding channel. Within the same sector, different gapped phases can be distinguished, depending on the sign of g_v, which determines the pinning value of the field $\phi_v = 0, \sqrt{\pi/8}$. In fact, due to the presence of the SU(2) symmetry in the spin channel, the value $\sqrt{\pi/8}$ for the field ϕ_s is inhibited. The properties of the different phases are summarized in the

first four columns of the table in Fig. 6.1. This framework is able to capture all the ordered phases of Fig. 6.1, except for the BOW and the PS. For weak interactions, the prediction of bosonization are in agreement with the transition lines obtained from numerical methods.

	$\tilde{\phi}_c$	$\tilde{\phi}_s$	Δ_c	Δ_s	LRO
LL(TS)	u	u	0	0	none
LE(SS)	u	0	0	$\neq 0$	$O_P^{(s)}$
PS	-	-	0	$\neq 0$	$O_P^{(s)}$
MI	0	u	$\neq 0$	0	$O_P^{(c)}$
BOW	0	0	$\neq 0$	$\neq 0$	$O_P^{(c)}, O_P^{(s)}$
CDW	$\frac{\pi}{2}$	0	$\neq 0$	$\neq 0$	$O_S^{(c)}, O_P^{(s)}$
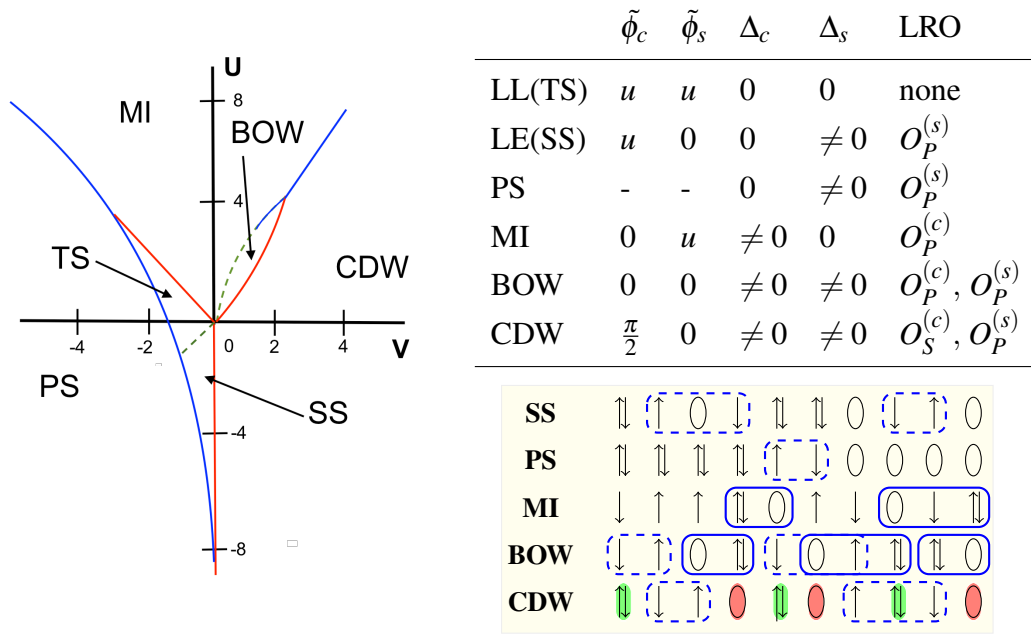
Fig. 6.1 *Left panel:* Phase diagram of the model (6.1) with U and V expressed in unit of t. Dashed green lines denote KT transitions, blue lines are first order transitions and red lines indicate continuous Gaussian transitions. *Right upper panel:* Correspondence between ground state quantum phases, bosonic fields and non-local operators. The fields have been expressed as $\tilde{\phi}_\nu = \sqrt{2\pi}\phi_\nu$. Here the letter u means *unlocked*. *Right lower panel:* Schematic representation of the gapped phases of the model. The blue solid (dashed) lines signal the presence of the parity order in the form of correlated holon-doublon (up-down spin) pairs. The green and red circles highlight the charge Haldane string order consisting in the alternation of diluted holons and doublons.

6.3 Non-Local Order Parameters

Following [49, 51–53], we now use the parity and Haldane string non-local operators introduced in eqs. (2.15) and (2.16):

$$O_P^{(\nu)}(j) = \prod_{k=0}^{j-1} e^{i2\pi S_k^{(\nu),z}} \quad , \quad O_S^{(\nu)}(j) = \left(\prod_{k=0}^{j-1} e^{i2\pi S_k^{(\nu),z}}\right) 2S_j^{(\nu),z} \quad , \tag{6.7}$$

with $S_j^{(c),z} = (n_j - 1)/2$, $S_j^{(s),z} = (n_{j,\uparrow} - n_{j,\downarrow})/2$. In Ref. [53] it has been claimed that the asymptotic limit of their correlation functions

$$C_A^{(v)} = \lim_{r \to \infty} < [O_A^{(v)}(j)]^\dagger O_A^{(v)}(j+r) > \quad , A = P, S \tag{6.8}$$

should remain finite in the presence of a specific gapped phase in the v channel. In particular, according to bosonization, if $\Delta_v \neq 0$, the parity correlator

$$C_P^{(v)} \propto < (\cos \sqrt{2\pi}\phi_v)^2 > \tag{6.9}$$

is non-zero when the field ϕ_v pins to the value 0, whereas the Haldane string correlator

$$C_S^{(v)} \propto < (\sin \sqrt{2\pi}\phi_v)^2 > \tag{6.10}$$

is finite if $\phi_v = \sqrt{\pi/8}$. Therefore, the expectation value of $O_A^{(v)}$ acts as an order parameter for a given gapped phase, as reported in the last column of the table in Fig. 6.1. Among the listed phases, those characterized by a non-vanishing $C_S^{(v)}$ can be recognized as being non-trivial symmetry protected topological phases [78]. On the contrary, a finite value of $C_P^{(v)}$ signals the presence of a trivial SPT order.

In addition to the topological properties, NLOPs are able to unveil the microscopic structure of the ground state. Indeed, a non-zero Haldane string parameter signals an antiferromagnetic order of diluted holons and doublons or up and down spins, in the charge and spin sectors, respectively. Instead, the parity order entails the presence of virtual excitations in the form of holon/doublon or up/down spin pairs. The bottom right panel of Fig. 6.1 depicts the microscopic structure of the different gapped phases.

6.4   Phase Transitions

As seen, the EHM presents a very rich phase diagram, with KT, Gaussian and first order phase transitions. Approximated methods are not able to capture some of them. In particular, first order phase transitions are usually not observed within standard bosonization approaches. Therefore, we investigate the model with quasi-exact DMRG simulations which can efficiently reveal any type of phase transition. The regime of repulsive interactions, for weak and intermediate couplings U and V, has already been studied by employing NLOPs [53]. Here, it has been shown that

the non-local order parameters describe very accurately the ground state quantum phases. However, it remains an open question whether NLOPs can capture the entire phase diagram. In this section, we tackle this problem. In our analysis we use both periodic boundary conditions (PBC) and open boundary conditions (OBC). In particular, OBC are used to detect the phase transitions that involve the PS phase. Indeed, it is characterized by an high degeneracy, which can be reduced by OBC. For all the other phase transitions, we employ PBC, which allow to remove the boundary effects. That is a quite relevant aspect in the computation of non-local order parameters; thus the adoption of PBC provide a great numerical accuracy in the extrapolation of the thermodynamic limit also keeping the system sizes relatively small. More precisely, we extrapolate the thermodynamic limit of the NLOPs from the finite size values $C_S^{(v)}(L/2)$ in case of Haldane strings, and from the averages $(C_P^{(v)}(L/2) + C_P^{(v)}(L/2+1))/2$ in case of parities. These were obtained for periodic chains with maximum length $L = 32$, keeping up to 1200 DMRG states and performing 6 sweeps, or for open chains with up to $L = 56$ sites and a number of DMRG states ranging from 768 to 1024 with 5 sweeps. In the latter case, we cut out the first three sites in the evaluation of finite size NLOPs, in order to minimize boundary effects.

6.4.1   Attractive U Regime

As typical of lattice models with a Fermi-Dirac statistics, the regime of attractive on-site interactions is dominated by a trivial singlet-like spin gap associated with the parity order. Therefore, here we expect a non-zero value of $C_P^{(s)}$. In one dimension, this kind of pairing is usually related to fermionic quasi-condensation (q-BEC) or superconducting (SC) order revealed by a power-law decay of the pair-pair correlation function. Here we show that $C_P^{(s)}$ behaves as an order parameter for both the SS and the PS regimes, in the second case unveiling the presence of a metallic phase without any kind of q-BEC or SC character. Fig. 6.2a shows the behavior of $C_P^{(s)}$ across the PS-SS transition. Although it remains finite everywhere, thus signaling the presence of a spin gap, its sudden jump at the transition point allows to locate the phase transition and to classify it as first order. This is, in fact, a common feature in transitions involving a PS regime, as confirmed also by the PS-TS transition occurring at weaker attractive U, where the competition between nearest-neighbor and on-site interactions makes possible a fully gapless regime. As
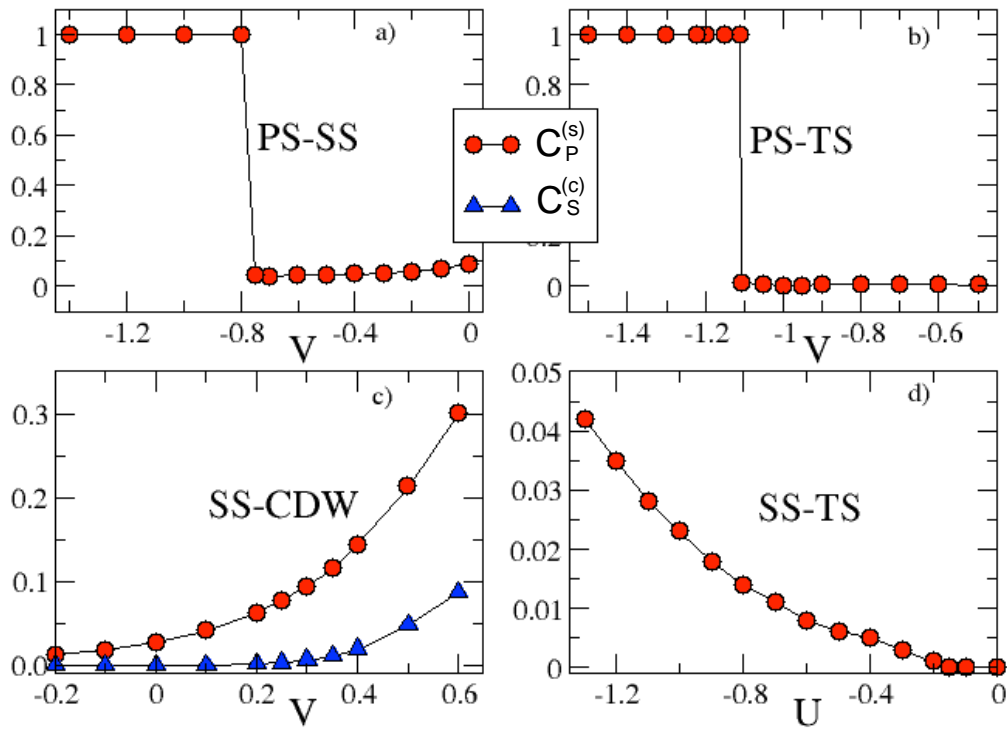
Fig. 6.2 TDL of the NLOPs for: a) $U = -1.5$; b) $U = -0.1$; c) $U = -0.9$; d) $V = -0.1$. The hopping amplitude is set to $t = 1$.

clearly visible from Fig. 6.2b, the first order phase transition associated to the phase separation is signaled by an abrupt jump of $C_P^{(s)}$ from zero in the TS to almost one in the PS.

On the other hand, transitions between gapless and gapped phases not involving the PS can usually be recognized as KT transitions. In this case, the order parameter grows slowly from zero to non-zero values, in conjunction with the exponential opening of the gap [25]. Indeed, that happens also in the TS-SS transition, which is ones again captured by the spin parity, as shown in Fig. 6.2d.

Finally, in Fig. 6.2c, we plot the behavior of both the spin parity and the charge Haldane string going from attractive to repulsive nearest-neighbor interactions. Here $C_P^{(s)}$ remains finite and the transition is signaled by $C_S^{(c)}$, which shows the features typical of a Gaussian continuous transition. Indeed, in the positive V region, a fully gapped phase with singlet-like pairing and charge antiferromagnetic order takes place.

6.4.2 Repulsive U Regime
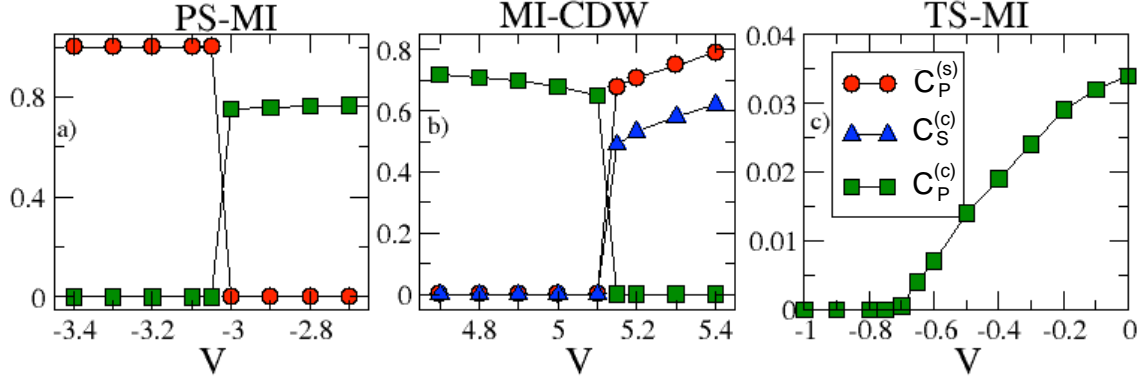
Fig. 6.3 TDL of the NLOPs for: a) $U = 5.0$; b) $U = 10$; c) $U = 1$. The hopping amplitude is set to $t = 1$.

While the behavior of NLOPs in the weak $U, V > 0$ case has already been studied [53], it has not been verified in the $U > 0$, $V < 0$ and the strong $U, V > 0$ regimes. Here, we take under consideration these regions.

For large U and strongly attractive V the system shows two partly gapped phases: the MI, with finite charge gap, and the PS, with finite spin gap, both of them characterized by parity order. Therefore, the transition is detected by two different order parameters, one in the charge sector and the other in the spin sector. This is shown in Fig. 6.3a, where it is evident that both $C_P^{(c)}$ and $C_P^{(s)}$ present the typical features of a first order phase transition.

Similar discontinuities can be observed in the opposite strong coupling limit, i.e. in the repulsive V regime, where the MI is replaced by a CDW. Indeed here, although the PS does not appear, the strong values of on-site and nearest-neighbor interactions drive the system well inside the atomic limit, thus inducing a sort of classical behavior. As before, this phase transition occurs in both the charge and spin sectors. However, in this case a fully gapped phase is involved and, as a consequence, three different order parameters can be identified: $C_P^{(s)}$ for the spin channel and both $C_P^{(c)}$ and $C_S^{(c)}$ for the charge channel (see Fig. 6.3b).

A rather different situation is established for weak couplings. Indeed, for small $V < 0$, we observe a Gaussian transition from MI to TS, as U decreases. This manifests in the behavior of the charge parity $C_P^{(c)}$, which is shown in Fig. 6.3c, as a function of V, for fixed $U = 1$.

6.5 Conclusions

In conclusion, we have shown by means of DMRG analysis that all phase transitions appearing in the extended Hubbard model can be properly described by non-local order parameters.

While it was already observed that NLOPs behave as expected in transitions involving insulating states, our results prove that they are able to identify also partly gapped conducting regimes. That provides a new tool for the detection of superconductivity and fermionic quasi-condensation.

In particular, the employment of NLOPs could have an important impact on the experimental detection of phase transitions in $1D$ systems. Indeed, our numerical analysis shows that they can be only zero or finite in a given phase, thus providing a very efficient way of distinguishing different regimes with respect to the local two-point correlation functions, which only manifest a change of the decay law.

Finally we stress that, since both our probes, i.e. parities and Haldane strings, have already been measured [108] or are measurable [124] and the EHM can be simulated with the ongoing experimental technologies, our findings could be tested in experiments with cold atoms.

Chapter 7

Study of dipolar fermions subject to correlated hopping processes

After having verified in the previous chapter that non-local order parameters detect all quantum phases, including those that do not break any symmetry, here we use them to study an Hubbard-like Hamiltonian with further terms in order to observe a possible reacher structure of the phase diagram. In particular, we are interested in finding a model that can be realized in experiments and that is able to reproduce hidden magnetic phases, i.e. those showing an Haldane string non-local order, which is typically associated with the presence of protected edge modes. To this purpose, we consider the effects of correlated hopping processes as well as dipole-dipole interaction, both in its long-range and truncated forms. Indeed, experiments with cold atoms allow to simulate this kind of models by using magnetic atoms. However, as we will see, sometimes the effect of long-range interaction is negligible since the crucial features are already captured by a truncated Hamiltonian. On the other hand, the density dependent hopping is a fundamental element to observe hidden magnetism in the extended Hubbard model. As we will see, it can be induced by periodically modulated on-site interaction, which is experimentally realizable [125]. The most general Hamiltonian that we will consider is the following

$$
\begin{aligned}
H = -t \sum_{j,\sigma} Q_{j,j+1,\sigma} & \left[1 - \frac{X}{t} \left(n_{j,\bar{\sigma}} + n_{j+1,\bar{\sigma}} \right) + \frac{\tilde{X}}{t} n_{j,\bar{\sigma}} n_{j+1,\bar{\sigma}} \right] \\
& + U \sum_j n_{j,\uparrow} n_{j,\downarrow} + V \sum_{j,r>0} \frac{n_j n_{j+r}}{r^3} ,
\end{aligned}
\tag{7.1}
$$

where $Q_{j,j+1,\sigma} = c_{j,\sigma}^{\dagger} c_{j,\sigma} + h.c.$ and the coefficients are assumed to be non-negative. We also provide its expression in terms of Hubbard operators, which will be useful in the following:

$$
H = -\sum_{j,\sigma} \left[t_{AA} X_j^{\sigma 0} X_{j+1}^{0\sigma} + t_{AB} \sigma \left(X_j^{\sigma 0} X_{j+1}^{\bar{\sigma} 2} + X_j^{2\bar{\sigma}} X_{j+1}^{0\sigma} \right) + t_{BB} X_j^{2\bar{\sigma}} X_{j+1}^{\bar{\sigma} 2} \right] + h.c.
$$
$$
+ \sum_j U X_j^{22} + \sum_{j,r} \frac{V}{r^3} \left(1 + X_j^{22} - X_j^{00} \right) \left(1 + X_{j+r}^{22} - X_{j+r}^{00} \right) ,
$$

$$(7.2)$$

with $t_{AA} = t$, $t_{AB} = 1 - X$ and $t_{BB} = (1 - 2X + \tilde{X})$.

In Section 7.1 we will present the solution for the two-body system with the dipolar interaction truncated to nearest-neighbors, and we will derive the Yang-Baxter relations, in order to eventually find the presence of integrability points in the model. In the following sections we will focus on the particle-hole symmetric case $\tilde{X} = 2X$ and we will present first an analytical study, by investigating the weak and strong coupling limits, and then the numerical results. In particular, in Section 7.2 we will study the weak coupling phase diagram by means of bosonization. Besides the standard approach, we will explore another route, by including part of the interaction non-perturbatively in the single species Hamiltonian. In Section 7.3 we will calculate and compare the energies of the competing phases in the strong coupling limit. In Section 7.4 we will show the DMRG results for NLOPs and we will derive a numerical phase diagram. Finally, in Section 7.5 we will use the Floquet analysis to show that the correlated hopping processes can be induced by a periodically modulated time-dependent on-site interaction. Therefore, we will regard the static Hamiltonian as an effective model for the time-dependent Hamiltonian. To validate this result, we will also compare the NLOPs obtained for the two models.
Most of the contents of this chapter can be found in Refs. [126] and [127].

7.1   Computation of the two-particle scattering matrix and Yang-Baxter relations

In this section we evaluate the integrability of the model by studying the two-body problem in the case of interactions truncated to nearest neighbors. Moreover we observe that, since we are dealing with only two particles, the three-body term with

coefficient $\tilde{X}$ does not act.[1] Therefore, we consider the following Hamiltonian

$$H = -\sum_{j,\sigma} Q_{j,j+1,\sigma}[1 - X(n_{j,\bar{\sigma}} + n_{j+1,\bar{\sigma}})] + U\sum_j n_{j,\uparrow}n_{j,\downarrow} + V\sum_j n_j n_{j+1} \qquad (7.3)$$

where we have assumed $t = 1$.

The two-particle state can be expressed as

$$|\Psi\rangle = \frac{1}{2}\sum_{x_1,x_2}\sum_{\sigma_1,\sigma_2}\psi_{\sigma_1,\sigma_2}(x_1,x_2)\underbrace{|x_2\sigma_2,x_1\sigma_1\rangle}_{c^\dagger_{x_2\sigma_2}c^\dagger_{x_1\sigma_1}|0\rangle}, \qquad (7.4)$$

where x_n and σ_n, with $n = \{1,2\}$ denote the position and the spin of the first or the second particle. The problem consists first of all in solving the eigenvalue equation

$$H|\Psi\rangle = E|\Psi\rangle. \qquad (7.5)$$

Applying the Hamiltonian (7.3) to the state (7.4), we get the following eigenvalue equation in first quantization

$$(X\delta_{x_1,x_2} - 1)[\psi_{\sigma_1,\sigma_2}(x_1,x_2+1) + \psi_{\sigma_1,\sigma_2}(x_1,x_2-1) + \psi_{\sigma_1,\sigma_2}(x_1+1,x_2) + \psi_{\sigma_1,\sigma_2}(x_1-1,x_2)] +$$
$$+ X\delta_{x_1,x_2-1}[\psi_{\sigma_1,\sigma_2}(x_1,x_2-1) + \psi_{\sigma_1,\sigma_2}(x_1+1,x_2)] +$$
$$+ X\delta_{x_1,x_2+1}[\psi_{\sigma_1,\sigma_2}(x_1,x_2+1) + \psi_{\sigma_1,\sigma_2}(x_1-1,x_2)] +$$
$$+ [U\delta_{x_1,x_2} + V(\delta_{x_1,x_2+1} + \delta_{x_1,x_2-1}) - E]\psi_{\sigma_1,\sigma_2}(x_1,x_2) = 0. \qquad (7.6)$$

We now observe that the wave function can be factorized into a part depending on the spin and a part depending on the spatial coordinates

$$\psi_{\sigma_1,\sigma_2}(x_1,x_2) = \psi(\sigma_1,\sigma_2)\psi(x_1,x_2), \qquad (7.7)$$

and make the following ansatz for the spatial wave function

$$\psi(x_1,x_2) = [A_2 e^{\iota(k_1 x_1 + k_2 x_2)} + A_1 e^{\iota(k_2 x_1 + k_1 x_2)}]\Theta(x_1 - x_2) +$$
$$+ [\Pi A_2 e^{\iota(k_2 x_1 + k_1 x_2)}] + \Pi A_1 e^{\iota(k_1 x_1 + k_2 x_2)}]\Theta(x_2 - x_1) + \qquad (7.8)$$
$$+ [A_0 - \frac{1}{2}((A_1 + A_2) + \Pi(A_1 + A_2))]e^{\iota(k_1 + k_2)x_1}\delta_{x_1,x_2},$$

---

[1]We will account for this term after having derived the Yang-Baxter relations.

where $\Theta(x)$ is the Heaviside function defined as

$$\Theta(r) = \begin{cases} 0 & \text{if } x < 0 \\ \frac{1}{2} & \text{if } x = 0 \\ 1 & \text{if } x > 0 \end{cases} , \tag{7.9}$$

and $A_1, A_2, \Pi A_1, \Pi A_2$ are complex amplitudes; in particular, the symbol Π is a permutation operator which interchanges the positions of the two particles. Thus, we insert this expression into the eigenvalue equation (7.6) and consider four different cases:

  1) $|x_1 - x_2| > 1$

  2) $x_1 = x_2$

  3) $x_1 = x_2 + 1$

  4) $x_1 = x_2 - 1$.

For each of them we should impose that the eigenvalue equation is satisfied. These conditions will provide the unknown informations. In particular, the case 1) will give us the expression for the energy eigenvalues, while the others will give the relations between the coefficients of the wave function. In the following we write the eigenvalue equation for each of the four aforementioned cases:

  1) $|x_1 - x_2| > 1$

$$-[\psi(x_1, x_2+1) + \psi(x_1, x_2-1) + \psi(x_1+1, x_2) + \psi(x_1-1, x_2)] - E\psi(x_1, x_2) = 0$$

$$\Rightarrow \quad E = -2[\cos k_1 + \cos k_2] \tag{7.10}$$

  2) $x_1 = x_2 = x$

$$(X-1)[\psi(x+1,x) + \psi(x-1,x) + \psi(x,x+1) + \psi(x,x-1)] + [U-E]\psi(x,x) = 0$$

$$(X-1)[(A_2 + \Pi A_2)(e^{\imath k_1} + e^{-\imath k_2}) + (A_1 + \Pi A_1)(e^{\imath k_2} + e^{-\imath k_1})] +$$
$$[U + 2(\cos k_1 + \cos k_2)]A_0 = 0$$

$$\Rightarrow \quad A_0 = -\frac{(X-1)[(A_2 + \Pi A_2)(e^{\imath k_1} + e^{-\imath k_2}) + (A_1 + \Pi A_1)(e^{\imath k_2} + e^{-\imath k_1})]}{U + 2(\cos k_1 + \cos k_2)}$$

$$\tag{7.11}$$

3) $x_1 = x_2 + 1$

$$- [\psi(x_2+2,x_2) + \psi(x_2,x_2) + \psi(x_2+1,x_2+1) + \psi(x_2+1,x_2-1)] +$$
$$+ X[\psi(x_2+1,x_2+1) + \psi(x_2,x_2)] + (V-E)\psi(x_2+1,x_2) = 0$$

$$\Rightarrow \quad A_1(1+e^{\iota(k_1+k_2)}+Ve^{\iota k_2}) + A_2(1+e^{\iota(k_1+k_2)}+Ve^{\iota k_1}) +$$
$$+ (X-1)(1+e^{\iota(k_1+k_2)})A_0 = 0 \tag{7.12}$$

4) $x_1 = x_2 - 1$

$$- [\psi(x_2,x_2) + \psi(x_2-2,x_2) + \psi(x_2-1,x_2+1) + \psi(x_2-1,x_2-1)] +$$
$$+ X[\psi(x_2-1,x_2-1) + \psi(x_2,x_2)] + (V-E)\psi(x_2-1,x_2) = 0$$

$$\Rightarrow \quad \Pi A_1(1+e^{-\iota(k_1+k_2)}+Ve^{-\iota k_1}) + \Pi A_2(1+e^{-\iota(k_1+k_2)}+Ve^{-\iota k_2}) +$$
$$+ (X-1)(1+e^{-\iota(k_1+k_2)})A_0 = 0. \tag{7.13}$$

Finally, inserting the expression of A_0 (7.11) into equations (7.12) and (7.13), we get the following system of equations

$$\begin{cases} (1+e^{\iota(k_1+k_2)})[A_1 + A_2 - (X-1)^2\xi] + V[A_2 e^{\iota k_1} + A_1 e^{\iota k_2}] = 0 \\ (1+e^{-\iota(k_1+k_2)})[\Pi A_1 + \Pi A_2 - (X-1)^2\xi] + V[\Pi A_2 e^{-\iota k_2} + \Pi A_1 e^{-\iota k_1}] = 0 \end{cases} \tag{7.14}$$

with

$$\xi = \frac{(A_2 + \Pi A_2)(e^{\iota k_1} + e^{-\iota k_2}) + (A_1 + \Pi A_1)(e^{\iota k_2} + e^{-\iota k_1})}{U + 2(\cos k_1 + \cos k_2)}. \tag{7.15}$$

Before facing the most general case, in the following subsections we solve the system in the two cases with $V = 0$ and $X = 0$.

7.1.1   The case $V = 0$

In absence of nearest-neighbor interaction ($V = 0$) the previous two equations simplify into the following:

$$\begin{cases} A_1 + A_2 - (X-1)^2\xi = 0 \\ \Pi A_1 + \Pi A_2 - (X-1)^2\xi = 0, \end{cases} \tag{7.16}$$

from which we get the simple relation

$$\Pi A_2 = A_1 + A_2 - \Pi A_1 \,. \tag{7.17}$$

Eliminating ΠA_2 from the first equation of (7.16), we obtain

$$
\begin{aligned}
&[U + 2(c_1 + c_2)](A_1 + A_2) \\
&- (X-1)^2 [2A_2(e^{\iota k_1} + e^{-\iota k_2}) + 2A_1(c_1 + c_2) - 2\iota \Pi A_1(s_1 - s_2)] = 0
\end{aligned}
\tag{7.18}
$$

where $c_i = \cos k_i$ and $s_i = \sin k_i$.

Before going on, we observe that by setting $X = 0$ we recover the Hubbard model. In this case we find

$$A_2 = -\frac{\frac{1}{2}\iota U}{\frac{1}{2}\iota U + s_1 - s_2} A_1 + \frac{s_1 - s_2}{\frac{1}{2}\iota U + s_1 - s_2} \Pi A_1 \,, \tag{7.19}$$

which, after having defined the operator

$$Y_{12} = \frac{-\frac{1}{2}\iota U + (s_1 - s_2)\Pi}{\frac{1}{2}\iota U + s_1 - s_2} = (u_{12} - 1) + u_{12}\Pi \,, \tag{7.20}$$

yields the following relation between the coefficients

$$A_2 = Y_{12} A_1 \,. \tag{7.21}$$

This relation holds also when $X \neq 0$; however in this case the quantity u_{12} is expressed as

$$u_{12} = \frac{(X-1)^2(s_1 - s_2)}{\frac{1}{2}\iota[U - 2X(X-2)(c_1 + c_2)] + (X-1)^2(s_1 - s_2)} \,, \tag{7.22}$$

and consequently

$$u_{12} - 1 = \frac{-\frac{1}{2}\iota[U - 2X(X-2)(c_1 + c_2)]}{\frac{1}{2}\iota[U - 2X(X-2)(c_1 + c_2)] + (X-1)^2(s_1 - s_2)} \,. \tag{7.23}$$

In general, we can define the operator Y_{ij}^{ab} as

$$Y_{ij}^{ab} = (u_{ij} - 1)I + u_{ij}\Pi_{ab} \,, \tag{7.24}$$

where Π_{ab} interchanges the positions of particles a and b. The operator (7.24) represents the two-particle scattering matrix and can be used to establish whether the model is integrable. Indeed, a sufficient (but not necessary) condition for the integrability consists in the two-particle scattering matrix satisfying the Yang-Baxter relation, which reads

$$Y_{23}^{12}Y_{13}^{23}Y_{12}^{12} = Y_{12}^{23}Y_{13}^{12}Y_{23}^{23} \qquad (7.25)$$

or, equivalently,

$$Y_{jk}^{ab}Y_{ik}^{bc}Y_{ij}^{ab} = Y_{ij}^{bc}Y_{ik}^{ab}Y_{jk}^{bc} \; . \qquad (7.26)$$

The latter is satisfied if

$$(u_{ij} - 1)(u_{ik} - 1)u_{jk} + u_{ij}(u_{ik} - 1)(u_{jk} - 1) = (u_{ij} - 1)u_{ik}(u_{jk} - 1) \qquad (7.27)$$

that is

$$
\begin{aligned}
&(X-1)^2(s_j - s_k)\left[\frac{U}{2} - X(X-2)(c_i + c_j)\right]\left[\frac{U}{2} - X(X-2)(c_i + c_k)\right] \\
&+(X-1)^2(s_i - s_j)\left[\frac{U}{2} - X(X-2)(c_i + c_k)\right]\left[\frac{U}{2} - X(X-2)(c_j + c_k)\right] \\
&=(X-1)^2(s_i - s_k)\left[\frac{U}{2} - X(X-2)(c_i + c_j)\right]\left[\frac{U}{2} - X(X-2)(c_j + c_k)\right] \; .
\end{aligned}
\qquad (7.28)
$$

It can be easily seen that this is verified in the three cases $X = 0$, $X = 1$ and $X = 2$. We observe that the first one corresponds to the Hubbard model. Regarding the other two cases, instead, from symmetry considerations we may deduce that they are integrable points also in the presence of three-body bond-charge interaction $\tilde{X} = 2X$. In particular, when this term is added to the Hamiltonian, the case $X = 2$ can be mapped into the case $X = 0$. That is achieved through the transformation $c_{j,\sigma} \rightarrow (1 - 2n_{j,\bar{\sigma}})c_{j,\sigma}$, which changes the sign of the amplitude t_{AB}: $t_{AB} \rightarrow -t_{AB}$, and consequently $X \rightarrow 2 - X$, $\tilde{X} \rightarrow \tilde{X} - 4X + 4$ [128, 129]. On the other hand, when $X = 1$, the amplitude of hopping processes that alter the number of doublons vanishes ($t_{AB} = 0$). In this case, the two conditions $\tilde{X} = 0$ and $\tilde{X} = 2X$ are obtained for $t_{BB} = \mp 1$, respectively. They can be mapped into each other by the canonical transformation $c_{j,\sigma} \rightarrow [1 - (1 - (-)^j)n_{j,\bar{\sigma}}]c_{j,\sigma}$, which instead preserves the sign of t_{AA}. Therefore, after the mapping, we get $\tilde{X} \rightarrow 2 - \tilde{X}$, while X is still equal to 1 [130, 31].

We would like to mention that the scattering matrix is sometimes written in the

following alternative form:

$$Y_{ij}^{ab} \equiv R_{ab}(k_i, k_j) = \frac{f(k_i, k_j)\Pi_{ab} + \iota}{f(k_i, k_j) - \iota} \qquad (7.29)$$

with

$$f(k_i, k_j) = \frac{(s_i - s_j)(X - 1)^2}{X(X - 2)(c_i + c_j) - U/2} . \qquad (7.30)$$

With this notation, the Yang-Baxter relation reads

$$R_{23}(k_1, k_2)R_{12}(k_1, k_3)R_{23}(k_2, k_3) = R_{12}(k_2, k_3)R_{23}(k_1, k_3)R_{12}(k_1, k_2) \qquad (7.31)$$

that is

$$[f(k_1, k_2)\Pi_{23} + \iota][f(k_1, k_3)\Pi_{12} + \iota][f(k_2, k_3)\Pi_{23} + \iota]$$
$$= [f(k_2, k_3)\Pi_{12} + \iota][f(k_1, k_3)\Pi_{23} + \iota][f(k_1, k_2)\Pi_{12} + \iota] . \qquad (7.32)$$

This is satisfied if

$$f(k_1, k_2) + f(k_2, k_3) - f(k_1, k_3) = 0 . \qquad (7.33)$$

The explicit form of equation (7.33) is

$$\frac{(s_1 - s_2)(X - 1)^2}{X(X - 2)(c_1 + c_2) - U/2} + \frac{(s_2 - s_3)(X - 1)^2}{X(X - 2)(c_2 + c_3) - U/2}$$
$$- \frac{(s_1 - s_3)(X - 1)^2}{X(X - 2)(c_1 + c_3) - U/2} = 0 \qquad (7.34)$$

that is satisfied for $X = 1$ and for $X = 0$ (as well as $X = 2$). Finally, we observe that, if $X \neq 0, 1, 2$, the equation reduces to

$$-\frac{U}{2}\underbrace{[s_1(c_3 - c_2) + s_2(c_1 - c_3) + s_3(c_2 - c_1)]}_{b}$$
$$+ X(X - 2)\underbrace{[s_1(c_3^2 - c_2^2) + s_2(c_1^2 - c_3^2) + s_3(c_2^2 - c_1^2)]}_{a} = 0 . \qquad (7.35)$$

This is a second degree equation of the form

$$aX^2 - 2aX - \frac{U}{2}b = 0 \qquad (7.36)$$

whose roots are

$$X = 1 \pm \sqrt{1 + \frac{Ub}{2a}}, \tag{7.37}$$

which depend on the momenta k_1, k_2, k_3 through the parameters a and b; therefore they are not acceptable solutions for our problem.

We conclude that the only integrable points emerging from the Yang-Baxter relations are $X = 0$ and $X = 1$.

7.1.2 The case $X = 0$

In the case $X = 0$ the system of equations (7.14) becomes

$$\begin{cases} (1 + e^{\iota(k_1+k_2)})[A_1 + A_2 - \xi] + V[A_2 e^{\iota k_1} + A_1 e^{\iota k_2}] = 0 \\ (1 + e^{-\iota(k_1+k_2)})[\Pi A_1 + \Pi A_2 - \xi] + V[\Pi A_2 e^{-\iota k_2} + \Pi A_1 e^{-\iota k_1}] = 0 \end{cases} \tag{7.38}$$

and the problem is much more complicated with respect to the previous case. Indeed we have

$$\Pi A_2 = A_2 + \underbrace{\frac{1 + e^{\iota(k_1+k_2)} + V e^{\iota k_2}}{1 + e^{\iota(k_1+k_2)} + V e^{\iota k_1}}}_{-\left(\frac{A_2}{A_1}\right)^{triplet} := -R^{tr}} (A_1 - \Pi A_1) \tag{7.39}$$

instead of (7.17).

Let us insert expression (7.39) into ξ (formula (7.15)) and hence into the first equation of the system. We obtain

$$(1 + e^{\iota(k_1+k_2)}) \left\{ A_1 + A_2 - \frac{2(e^{\iota k_1} + e^{-\iota k_2})}{U + 2(\cos k_1 + \cos k_2)} A_2 \right.$$
$$\left. - \frac{(e^{\iota k_2} + e^{-\iota k_1} - (e^{\iota k_1} + e^{-\iota k_2})R^{tr})}{U + 2(\cos k_1 + \cos k_2)} A_1 - \frac{(e^{\iota k_2} + e^{-\iota k_1} + (e^{\iota k_1} + e^{-\iota k_2})R^{tr})}{U + 2(\cos k_1 + \cos k_2)} \Pi A_1 \right\}$$
$$+ V(A_2 e^{\iota k_1} + A_1 e^{\iota k_2}) = 0$$
$$\tag{7.40}$$

which can be reordered as

$$
\left\{ 1 + e^{\iota(k_1+k_2)} + V e^{\iota k_1} - \frac{2(1+e^{\iota(k_1+k_2)})(e^{\iota k_1}+e^{-\iota k_2})}{U + 2(\cos k_1 + \cos k_2)} \right\} A_2
$$
$$
+ \left\{ 1 + e^{\iota(k_1+k_2)} + V e^{\iota k_2} - \frac{(1+e^{\iota(k_1+k_2)})(e^{\iota k_2}+e^{-\iota k_1}-(e^{\iota k_1}+e^{-\iota k_2})R^{tr})}{U + 2(\cos k_1 + \cos k_2)} \right\} A_1
$$
$$
- \frac{(1+e^{\iota(k_1+k_2)})(e^{\iota k_2}+e^{-\iota k_1}+(e^{\iota k_1}+e^{-\iota k_2})R^{tr})}{U + 2(\cos k_1 + \cos k_2)} \Pi A_1 = 0 \,.
$$

$$(7.41)$$

In order to have a more symmetric form, we multiply this equation by $e^{-\iota k_1}$:

$$
\left\{ e^{-\iota k_1} + e^{\iota k_2} + V - \frac{2(e^{-\iota k_1}+e^{\iota k_2})(e^{\iota k_1}+e^{-\iota k_2})}{U + 2(\cos k_1 + \cos k_2)} \right\} A_2
$$
$$
+ \left\{ e^{-\iota k_1} + e^{\iota k_2} + V e^{\iota(k_2-k_1)} - \frac{(e^{-\iota k_1}+e^{\iota k_2})^2 - (e^{\iota k_2}+e^{-\iota k_1})(e^{\iota k_1}+e^{-\iota k_2})R^{tr}}{U + 2(\cos k_1 + \cos k_2)} \right\} A_1
$$
$$
- \frac{(e^{-\iota k_1}+e^{\iota k_2})^2 + (e^{\iota k_2}+e^{-\iota k_1})(e^{\iota k_1}+e^{-\iota k_2})R^{tr}}{U + 2(\cos k_1 + \cos k_2)} \Pi A_1 = 0 \,.
$$

$$(7.42)$$

If now we define

$$
z := e^{-\iota k_1} + e^{\iota k_2}
$$

$$(7.43)$$

the previous equation becomes

$$
\left\{ z + V - \frac{2|z|^2}{U + 2(\cos k_1 + \cos k_2)} \right\} A_2 + \left\{ z + V e^{-\iota(k_1-k_2)} - \frac{z^2 - |z|^2 R^{tr}}{U + 2(\cos k_1 + \cos k_2)} \right\} A_1
$$
$$
- \frac{z^2 + |z|^2 R^{tr}}{U + 2(\cos k_1 + \cos k_2)} \Pi A_1 = 0
$$

$$(7.44)$$

where

$$
\begin{aligned}
|z|^2 = zz^* &= (e^{-\iota k_1}+e^{\iota k_2})(e^{\iota k_1}+e^{-\iota k_2}) = 2 + e^{\iota(k_1+k_2)} + e^{-\iota(k_1+k_2)} = \\
&= (1+e^{-\iota(k_1+k_2)})(1+e^{\iota(k_1+k_2)}) = (2\cos(K/2))^2 = J_K^2 \,.
\end{aligned}
$$

$$(7.45)$$

From (7.44) we obtain the following ratio

$$Y_{12} = \frac{A_2}{A_1} = -\frac{z + Ve^{-\iota(k_1 - k_2)} - \frac{z^2 - |z|^2 R^{tr}}{U + 2(\cos k_1 + \cos k_2)} - \frac{z^2 + |z|^2 R^{tr}}{U + 2(\cos k_1 + \cos k_2)}\Pi}{z + V - \frac{2|z|^2}{U + 2(\cos k_1 + \cos k_2)}} . \qquad (7.46)$$

It can be easily verified that for the triplet state ($\Pi A = -A$), one recovers the formula

$$Y_{12}^{triplet} = R^{tr} \qquad (7.47)$$

while for the singlet state ($\Pi A = A$) one obtains

$$\begin{aligned}
Y_{12}^{singlet} &= -\frac{z + Ve^{-\iota(k_1 - k_2)} - \frac{2z^2}{U + 2(\cos k_1 + \cos k_2)}}{z + V - \frac{2|z|^2}{U + 2(\cos k_1 + \cos k_2)}} \\
&= \frac{R^{tr} + \frac{2z^2}{E'}}{1 - \frac{2|z|^2}{E'}} \\
&= -\frac{J_K + Ve^{-\iota k/2} - \frac{2J_K^2 e^{-\iota k/2}}{U + 2J_K \cos k/2}}{J_K + Ve^{\iota k/2} - \frac{2J_K^2 e^{\iota k/2}}{U + 2J_K \cos k/2}}
\end{aligned} \qquad (7.48)$$

where $E' = -[z + V]E = [z + V][U + 2(\cos k_1 + \cos k_2)]$, $J_K = 2\cos K/2$, $K = k_1 + k_2$, $k = k_1 - k_2$.

Expression (7.46) can be rewritten in a more compact way as

$$\frac{1}{2}(R^{si} + R^{tr}) + \frac{z^2 + |z|^2 R^{tr}}{E' - 2|z|^2}\Pi \qquad (7.49)$$

with $R^{si} = (A_2/A_1)^{singlet}$.

In order to verify the Yang-Baxter relation, we observe that for the Hubbard model with $V = 0$, the two-particle scattering matrix takes the form

$$Y_{12} = \frac{-\iota\frac{U}{2} + (s_1 - s_2)\Pi}{\iota\frac{U}{2} + (s_1 - s_2)} . \qquad (7.50)$$

Thus we expect the following form for the extended Hubbard model with $V \neq 0$

$$Y_{12} = \frac{-\iota(\frac{U}{2} + f_1(V)) + (s_1 - s_2 + f_2(V))\Pi}{\iota(\frac{U}{2} + f_3(V)) + (s_1 - s_2 + f_4(V))} \qquad (7.51)$$

with $f_i(V=0) = 0$.

If we rewrite (7.46) in order to obtain this expression, we obtain

$$
\begin{aligned}
f_2(V) &= -V\frac{s_1 - s_2}{e^{-\iota k_1} + e^{\iota k_2} + V}\\
f_3(V) &= V(c_1 + c_2)\frac{U + 2(c_1 + c_2)}{4(1 + \cos(k_1 + k_2))}\\
f_4(V) &= -V(s_1 - s_2)\frac{U + 2(c_1 + c_2)}{4(1 + \cos(k_1 + k_2))}\\
f_1(V) &= f_3(V) + \iota(f_4(V) - f_2(V)).
\end{aligned}
\tag{7.52}
$$

Hence

$$
\begin{aligned}
Y_{12} &= \frac{-\iota(\frac{U}{2} + f_3(V) + \iota(f_4(V) - f_2(V))) + (s_1 - s_2 + f_2(V))\Pi}{\iota(\frac{U}{2} + f_3(V)) + (s_1 - s_2 + f_4(V))}\\
&= \frac{-\iota(\frac{U}{2} + f_3(V)) + f_4(V) - f_2(V) + (s_1 - s_2 + f_2(V))\Pi}{\iota(\frac{U}{2} + f_3(V)) + f_4(V) - f_2(V) + (s_1 - s_2 + f_2(V))}\\
&= \frac{F(k_1, k_2)\Pi + a_1 - a_2}{F(k_1, k_2) + a_1 + a_2}, \qquad \left.\begin{aligned}a_1 &= a_1(k_1, k_2)\\ a_2 &= a_2(k_1, k_2)\end{aligned}\right\} \in C\\
&= \frac{F(k_1, k_2)\Pi + a(k_1, k_2)}{F(k_1, k_2) + a'(k_1, k_2)}, \qquad a = a_1 - a_2, a' = a_1 + a_2\\
&= \frac{F'(k_1, k_2)\Pi + 1}{F'(k_1, k_2) + a''(k_1, k_2)}, \qquad a'' = a'/a.
\end{aligned}
\tag{7.53}
$$

Finally we write the Yang-Baxter equation and obtain

$$
[F'(k_1, k_2) + F'(k_2, k_3) - F'(k_1, k_3)](\Pi_{23} - \Pi_{12}) = 0
\tag{7.54}
$$

with

$$
F'(k_1, k_2) = \frac{F(k_1, k_2)}{a(k_1, k_2)}.
\tag{7.55}
$$

Thus we recover the relation (7.33). The only solution of this equation that is independent of k_1, k_2 and k_3 is $V = 0$, which corresponds to the Hubbard model.

7.1.3   The general case

In this section, we finally review the general case, with both $X \neq 0$ and $V \neq 0$. Here the two-particle scattering matrix is given by

$$
\begin{aligned}
Y_{12} &= -\frac{z + Ve^{-\iota(k_1-k_2)} - \frac{(X-1)^2(z^2-|z|^2R^{tr})}{U+2(\cos k_1+\cos k_2)} - \frac{(X-1)^2(z^2+|z|^2R^{tr})}{U+2(\cos k_1+\cos k_2)}\Pi}{z + V - \frac{2(X-1)^2|z|^2}{U+2(\cos k_1+\cos k_2)}} \\[2mm]
&= \frac{-\iota(\frac{U}{2} + g_2(X,V)) + g_1(X,V) + G(k_1,k_2)\Pi}{\iota(\frac{U}{2} + g_2(X,V)) + g_1(X,V) + G(k_1,k_2)} \\[2mm]
&= \frac{G(k_1,k_2)\Pi + b(k_1,k_2)}{G(k_1,k_2) + b'(k_1,k_2)} \\[2mm]
&= \frac{G'(k_1,k_2)\Pi + 1}{G'(k_1,k_2) + b''(k_1,k_2)}
\end{aligned}
\tag{7.56}
$$

with

$$
\begin{aligned}
&g_1(X,V) = f_4(V) - g_0(X,V) = f_4(V) - (X-1)^2 f_2(V) \\[1mm]
&g_2(X,V) = f_3(V) - X(X-2)(c_1+c_2) \\[1mm]
&G(k_1,k_2) = (X-1)^2 F(k_1,k_2) = (X-1)^2[s_1 - s_2 + f_2(V)] = (X-1)^2(s_1-s_2) + g_0(X,V) \\[1mm]
&b(k_1,k_2) = g_1(X,V) - \iota\left(\frac{U}{2} + g_2(X,V)\right) \\[1mm]
&b'(k_1,k_2) = g_1(X,V) + \iota\left(\frac{U}{2} + g_2(X,V)\right) \\[1mm]
&b''(k_1,k_2) = \frac{b'(k_1,k_2)}{b(k_1,k_2)} \\[1mm]
&G'(k_1,k_2) = \frac{G(k_1,k_2)}{b(k_1,k_2)}\,.
\end{aligned}
\tag{7.57}
$$

Clearly all these quantities depend on the momenta and on the parameters X, U, V. However we have explicitly written only the dependence on X and V in g_1 and g_2 to point out that $g_1(X=0,V=0) = g_2(X=0,V=0) = 0$; and the dependence on the momenta in G and b because it is important for the Yang-Baxter relations. The Yang-Baxter relation takes the usual form:

$$
[G'(k_1,k_2) + G'(k_2,k_3) - G'(k_1,k_3)](\Pi_{23} - \Pi_{12}) = 0\,.
\tag{7.58}
$$

Explicitly, we have

$$G(k_1, k_2) = (X-1)^2 (s_1 - s_2) \left\{ 1 - \frac{V}{e^{-\iota k_1} + e^{\iota k_2} + V} \right\}$$

$$b(k_1, k_2) = -\iota \left\{ \frac{U}{2} + \frac{V(c_1 + c_2 - \iota(s_1 - s_2))(U + 2(c_1 + c_2))}{4(1 + \cos(k_1 + k_2))} - X(X-2)(c_1 + c_2) \right\} +$$

$$+ \frac{V(X-1)^2 (s_1 - s_2)}{e^{-\iota k_1} + e^{\iota k_2} + V} ,$$

$$(7.59)$$

from which we conclude that the case $X = 1$ is integrable also if $V \neq 0$. The considerations done in Section 7.1.1 about the three-body term $\tilde{X}$ are still valid in the presence of finite V.

7.2   Weak coupling limit: two bosonization approaches

Established that, except for the case $X = 1$, the model is not integrable, in this section we give some insights into the ground state phase diagram by exploring the weak coupling regime with the bosonization technique.

In addition to the standard approach, we also derive the low energy phase diagram by embodying part of the interaction non-perturbatively in the single species Hamiltonians. In this case we find that the Luttinger liquid regime becomes unstable with respect to some gapped phases, such as the bond ordered wave and the Haldane insulator, the latter with degenerate edge modes.

As we have seen in Chapter 3, the standard bosonization description for spinfull fermions relies on the existence of two non-interacting single species Luttinger liquids that serve as starting points for the discovery of possible gapped phases promoted by the interaction, which effect is included in a perturbative way.

In fact, in Ref. [81] it has been noticed that in some cases part of the interaction can be embodied non-perturbatively in the single species Hamiltonian, as long as it remains in a Luttinger liquid regime. This alternative approach has been applied, for instance, in [26] to show that the dipolar interaction can stabilize a bond ordered wave phase, which existence is predicted already within one-loop bosonization.

Here we compare the zero-temperature phase diagram obtained from the latter method with that derived from the standard bosonization for the model (7.1) with

particle-hole invariance ($\tilde{X} = 2X$), i.e.,

$$H = -\sum_{j,\sigma} Q_{j,j+1,\sigma}\left[1 - X(n_{j,\bar{\sigma}} - n_{j+1,\bar{\sigma}})^2\right] + U\sum_{j} n_{j,\uparrow}n_{j,\downarrow} + V\sum_{j,r>0} \frac{n_j n_{j+r}}{r^3},$$

$$(7.60)$$

where we have set $t = 1$. Upon normal ordering of the operators,

$$Q_{j,j+1,\sigma} =: Q_{j,j+1,\sigma} : +\langle Q_{j,j+1,\sigma}\rangle =: Q_{j,j+1,\sigma} : +\frac{2}{\pi} \qquad (7.61)$$

$$n_{j,\sigma} =: n_{j,\sigma} : +\langle n_{j,\sigma}\rangle =: n_{j,\sigma} : +\frac{1}{2}, \qquad (7.62)$$

and omitting the constant terms, the Hamiltonian reads

$$H = -\left(1 - \frac{X}{2}\right)\sum_{j,\sigma} : Q_{j,j+1,\sigma} : + \sum_{j,\sigma}\sum_{r} V_{\parallel}(r) : n_{j,\sigma} :: n_{j+r,\sigma} : +$$

$$+ \sum_{j,\sigma}\sum_{r} V_{\perp}(r) : n_{j,\sigma} :: n_{j+r,\bar{\sigma}} : + U\sum_{j} : n_{j,\uparrow} :: n_{j,\downarrow} : \qquad (7.63)$$

$$- 2X\sum_{j,\sigma} : Q_{j,j+1,\sigma} :: n_{j,\bar{\sigma}} :: n_{j+1,\bar{\sigma}} :$$

where we have defined

$$V_{\parallel}(r) = \frac{V}{r^3} - \frac{4X}{\pi}\delta_{r,1} \quad \text{and} \quad V_{\perp}(r) = \frac{V}{r^3}. \qquad (7.64)$$

7.2.1   Standard approach

Within the standard procedure of bosonization, the starting point is given by the non-interacting Hamiltonian, upon which the effect of interactions is considered in a perturbative manner. As explained in Chapter 3, after having done the continuum limit

$$\sum_{j} \longrightarrow \frac{1}{a}\int dx \quad, \quad c_{j,\sigma} \longrightarrow \sqrt{a}\left[e^{ik_F x}\Psi_{R\sigma}(x) + e^{-ik_F x}\Psi_{L\sigma}(x)\right], \qquad (7.65)$$

with $k_F = \pi/(2a)$ for $n = 1$, one can express the fermionic fields $\Psi_{\chi\sigma}$ for left ($\chi = L$) and right ($\chi = R$) movers in terms of the bosonic ones ϕ_σ and θ_σ:

$$\Psi_{\chi\sigma}(x) = \frac{\eta_{\chi\sigma}}{\sqrt{2\pi\alpha}}e^{i\sqrt{\pi}[\chi\phi_\sigma(x) + \theta_\sigma(x)]}. \qquad (7.66)$$

Within this framework, the kinetic operator $: Q_{j,j+1,\sigma} :$ and the density operator $: n_{j,\sigma} :$ appearing in Hamiltonian (7.63) are expressed in the following way

$$: Q_{j,j+1,\sigma} := -\frac{2}{\pi}(-1)^j \cos\left(2\sqrt{\pi}\phi_\sigma(x)\right) - a^2 \left[(\nabla\phi_\sigma(x))^2 + (\nabla\theta_\sigma(x))^2\right] + ...$$
(7.67)

$$: n_{j,\sigma} := a\left[\frac{1}{\sqrt{\pi}}\nabla\phi_\sigma(x) - \frac{(-1)^j}{\pi a}\sin\left(2\sqrt{\pi}\phi_\sigma(x)\right)\right] + ...$$
(7.68)

where dots denote the higher order terms in expansion with respect to a, which will be neglected in the derivation of the bosonized Hamiltonian. For the demonstration of formula (7.67) and (7.68) see Appendix E. The two- and three-body terms in the Hamiltonian (7.63) are constructed by the product of operators of the form (7.67) and (7.68). The calculation of such a product is straightforward when this is given by two factors acting on different fermionic species. Instead, when operators acting on the same species are involved, the operator product expansion is needed. In particular, we make use of the following fusion rules

$$\sin\left(2\sqrt{\pi}\phi_\sigma(x)\right)\sin\left(2\sqrt{\pi}\phi_\sigma(x+R)\right) =$$
$$= \frac{a^2}{2R^2} - \frac{1}{2}\cos\left(4\sqrt{\pi}\phi_\sigma(x)\right) - \pi a^2 \left(\nabla\phi_\sigma(x)\right)^2 + ... \quad , \quad R = ra$$
(7.69)

$$\nabla\phi_\sigma(x)\sin\left(2\sqrt{\pi}\phi_\sigma(x+a)\right) = -\sin\left(2\sqrt{\pi}\phi_\sigma(x)\right)\nabla\phi_\sigma(x+a) =$$
$$= \frac{1}{\sqrt{\pi}a}\cos\left(2\sqrt{\pi}\phi_\sigma(x)\right) + ...$$
(7.70)

in deriving the bosonized expression for the product of two density operators. Thus we get

$$: n_{j,\sigma} :: n_{j+r,\sigma} : \simeq a^2\left\{\frac{1-(-1)^r}{\pi}\left(\nabla\phi_\sigma(x)\right)^2 - \frac{(-1)^r}{2\pi^2 a^2}\cos\left(4\sqrt{\pi}\phi_\sigma(x)\right)\right.$$
$$\left. + \frac{(-1)^r}{2\pi^2 R^2} + (-1)^j...\right\}$$
(7.71)

and

$$: n_{j,\sigma} :: n_{j+1,\sigma} : \simeq a^2 \left\{ \frac{2}{\pi} \left(\nabla \phi_\sigma(x) \right)^2 + \frac{1}{2\pi^2 a^2} \cos \left(4\sqrt{\pi} \phi_\sigma(x) \right) \right.$$
$$\left. - \frac{1}{2\pi^2 \alpha^2} + (-1)^j \frac{2}{\pi^2 a^2} \cos \left(2\sqrt{\pi} \phi_\sigma(x) \right) \right\} \tag{7.72}$$

where, in the last case, we have evaluated also the oscillating part since it contributes in the three-body term. The derivation of the previous formula is reported in Appendix E. Now we can proceed to calculate the bosonized expression of the various terms of the Hamiltonian.

The kinetic term

$$- \left(1 - \frac{X}{2} \right) \sum_{j,\sigma} : Q_{j,j+1,\sigma} : \tag{7.73}$$

By using eq. (7.67) and eliminating the oscillating part which vanishes after integration, we immediately get

$$\left(1 - \frac{X}{2} \right) a \int dx \left[(\nabla \phi_\uparrow)^2 + (\nabla \phi_\downarrow)^2 + (\nabla \theta_\uparrow)^2 + (\nabla \theta_\downarrow)^2 \right] =$$
$$= \left(1 - \frac{X}{2} \right) a \int dx \left\{ \left[(\nabla \phi_c)^2 + (\nabla \theta_c)^2 \right] + \left[(\nabla \phi_s)^2 + (\nabla \theta_s)^2 \right] \right\} . \tag{7.74}$$

The three-body term

$$- 2X \sum_{j,\sigma} : Q_{j,j+1,\sigma} :: n_{j\bar{\sigma}} :: n_{j+1\bar{\sigma}} : \tag{7.75}$$

By multiplying the right hand sides of equations (7.67) and (7.72) and retaining only the non-oscillating lower-order contributions, we get the following two terms:

a)

$$- 2X \frac{a^2}{2\pi^2 \alpha^2} \frac{a^2}{a} \int dx \sum_\sigma \left[(\nabla \phi_\sigma(x))^2 + (\nabla \theta_\sigma(x))^2 \right] =$$
$$= - \frac{X}{\pi^2} a \int dx \left\{ \left[(\nabla \phi_c)^2 + (\nabla \theta_c)^2 \right] + \left[(\nabla \phi_s)^2 + (\nabla \theta_s)^2 \right] \right\} \tag{7.76}$$

b)

$$
-2X\left(-\frac{4}{\pi^3}\right)\frac{1}{a}\int dx \sum_{\sigma}\cos\left(2\sqrt{\pi}\phi_\sigma(x)\right)\cos\left(2\sqrt{\pi}\phi_{\bar{\sigma}}(x)\right) =
$$

$$
= \frac{-2X}{a}\left(\frac{-8}{\pi^3}\right)\int dx\cos\left(2\sqrt{\pi}\phi_\uparrow(x)\right)\cos\left(2\sqrt{\pi}\phi_\downarrow(x)\right) =
$$

$$
= \frac{-2X}{a}\left(\frac{-2}{\pi^3}\right)\int dx\left[e^{\imath 2\sqrt{\pi}(\phi_\uparrow+\phi_\downarrow)} + e^{-\imath 2\sqrt{\pi}(\phi_\uparrow+\phi_\downarrow)} + e^{\imath 2\sqrt{\pi}(\phi_\uparrow-\phi_\downarrow)} + e^{-\imath 2\sqrt{\pi}(\phi_\uparrow-\phi_\downarrow)}\right] =
$$

$$
= \frac{-2X}{a}\left(\frac{-4}{\pi^3}\right)\int dx\left[\cos\left(\sqrt{8\pi}\phi_c(x)\right) + \cos\left(\sqrt{8\pi}\phi_s(x)\right)\right] =
$$

$$
= \frac{8X}{\pi^3 a}\int dx\left[\cos\left(\sqrt{8\pi}\phi_c(x)\right) + \cos\left(\sqrt{8\pi}\phi_s(x)\right)\right] .
$$

$$(7.77)$$

The on-site interaction

$$
U\sum_j :n_{j,\uparrow}::n_{j,\downarrow}: \tag{7.78}
$$

The double occupation number operator can be bosonized in the following way

$$
:n_{j,\uparrow}::n_{j,\downarrow}: = a^2\left[\frac{1}{\pi}\nabla\phi_\uparrow(x)\nabla\phi_\downarrow(x) + \frac{1}{\pi^2\alpha^2}\sin\left(2\sqrt{\pi}\phi_\uparrow(x)\right)\sin\left(2\sqrt{\pi}\phi_\downarrow(x)\right) + (-1)^j...\right] . \tag{7.79}
$$

Therefore, the on-site interaction generates the following two contributions in the bosonized Hamiltonian:

a)

$$
U\frac{a^2}{\pi}\frac{1}{a}\int dx\nabla\phi_\uparrow(x)\nabla\phi_\downarrow(x) =
$$

$$
= U\frac{a^2}{\pi}\frac{1}{a}\int dx\frac{1}{2}\nabla(\phi_c(x) + \phi_s(x))\nabla(\phi_c(x) - \phi_s(x)) = \tag{7.80}
$$

$$
= \frac{Ua}{2\pi}\int dx\left[(\nabla\phi_c(x))^2 - (\nabla\phi_s(x))^2\right]
$$

b)

$$U\frac{a^2}{\pi^2\alpha^2}\frac{1}{a}\int dx\sin\left(2\sqrt{\pi}\phi_\uparrow(x)\right)\sin\left(2\sqrt{\pi}\phi_\downarrow(x)\right) =$$

$$= U\frac{a^2}{\pi^2\alpha^2}\frac{1}{a}\int dx\left(-\frac{1}{4}\right)\left(e^{\imath 2\sqrt{\pi}\phi_\uparrow} - e^{-\imath 2\sqrt{\pi}\phi_\uparrow}\right)\cdot\left(e^{\imath 2\sqrt{\pi}\phi_\downarrow} - e^{-\imath 2\sqrt{\pi}\phi_\downarrow}\right) =$$

$$= U\frac{a^2}{\pi^2\alpha^2}\frac{1}{a}\int dx\left(-\frac{1}{4}\right)\left[e^{\imath 2\sqrt{\pi}(\phi_\uparrow+\phi_\downarrow)} + e^{-\imath 2\sqrt{\pi}(\phi_\uparrow+\phi_\downarrow)} - e^{\imath 2\sqrt{\pi}(\phi_\uparrow-\phi_\downarrow)} - e^{-\imath 2\sqrt{\pi}(\phi_\uparrow-\phi_\downarrow)}\right] =$$

$$= -\frac{U}{2\pi^2 a}\int dx\left[\cos\left(\sqrt{8\pi}\phi_c(x)\right) - \cos\left(\sqrt{8\pi}\phi_s(x)\right)\right] .$$

$$(7.81)$$

The parallel-spin-nearest-neighbor interaction

$$\sum_{j,\sigma}\sum_r V_\|(r) : n_{j,\sigma} :: n_{j+r,\sigma} :$$

$$(7.82)$$

Neglecting the constant term in eq. (7.71), this interaction gives rise to the following two contributions:

a)

$$a^2\sum_r\left(V_\|(r)\frac{1-(-1)^r}{\pi}\right)\frac{1}{a}\int dx\sum_\sigma(\nabla\phi_\sigma)^2 =$$

$$= \frac{a}{\pi}\sum_r\left(\frac{V}{r^3} - \frac{V(-1)^r}{r^3} - \frac{4X}{\pi}(1-(-1)^r)\,\delta_{r,1}\right)\int dx\sum_\sigma(\nabla\phi_\sigma)^2 =$$

$$= \frac{a}{\pi}\left(\zeta(3)V + \frac{3}{4}\zeta(3)V - \frac{8X}{\pi}\right)\int dx\sum_\sigma(\nabla\phi_\sigma)^2 =$$

$$= \left(\frac{7}{4}\zeta(3)\frac{V}{\pi} - \frac{8X}{\pi^2}\right)a\int dx\sum_\sigma(\nabla\phi_\sigma)^2 =$$

$$= \left(\frac{7}{4}\zeta(3)\frac{V}{\pi} - \frac{8X}{\pi^2}\right)a\int dx\left[(\nabla\phi_\uparrow)^2 + (\nabla\phi_\downarrow)^2\right] =$$

$$= \left(\frac{7}{4}\zeta(3)\frac{V}{\pi} - \frac{8X}{\pi^2}\right)a\int dx\left[(\nabla\phi_c)^2 + (\nabla\phi_s)^2\right]$$

$$(7.83)$$

where $\zeta(n) = \sum_r\frac{1}{r^n}$ is the Zeta Riemann function and $\eta(n) = -\sum_r\frac{(-1)^r}{r^n} = \sum_r\frac{(-1)^{r-1}}{r^n}$ is the Dirichlet eta function, related to the zeta function by $\eta(n) = (1-2^{1-n})\zeta(n)$;

b)

$$
-\frac{a^2}{2\pi^2\alpha^2}\left(\sum_r V_\parallel(r)(-1)^r\right)\frac{1}{a}\int dx \sum_\sigma \cos\left(4\sqrt{\pi}\phi_\sigma(x)\right) =
$$

$$
= \frac{1}{2\pi^2 a}\sum_r \left(-\frac{V(-1)^r}{r^3}+\frac{4X}{\pi}(-1)^r\delta_{r,1}\right)\int dx \sum_\sigma \cos\left(4\sqrt{\pi}\phi_\sigma(x)\right) =
$$

$$
= \frac{1}{2\pi^2 a}\left(\frac{3}{4}\zeta(3)V-\frac{4X}{\pi}\right)\int dx\left[\cos\left(4\sqrt{\pi}\phi_\uparrow\right)+\cos\left(4\sqrt{\pi}\phi_\downarrow\right)\right] =
$$

$$
= \frac{1}{2\pi^2 a}\left(\frac{3}{4}\zeta(3)V-\frac{4X}{\pi}\right)\int dx\left[\cos\left(\sqrt{8\pi}(\phi_c+\phi_s)\right)+\cos\left(\sqrt{8\pi}(\phi_c-\phi_s)\right)\right] =
$$

$$
= \left(\frac{3}{4}\zeta(3)\frac{V}{\pi^2 a}-\frac{4X}{\pi^3 a}\right)\int dx\cos\left(\sqrt{8\pi}\phi_c\right)\cos\left(\sqrt{8\pi}\phi_s\right).
$$

(7.84)

The opposite-spin-nearest-neighbor interaction

$$
\sum_{j,\sigma}\sum_r V_\perp(r):n_{j,\sigma}::n_{j+r,\bar\sigma}:
$$

(7.85)

In this case, the product of the two density operators is given by

$$
:n_{j,\sigma}::n_{j+r,\bar\sigma}:=
$$

$$
= a^2\left[\frac{1}{\pi}\nabla\phi_\sigma(x)\nabla\phi_{\bar\sigma}(x+R)+\frac{(-1)^r}{\pi^2\alpha^2}\sin\left(2\sqrt{\pi}\phi_\sigma(x)\right)\sin\left(2\sqrt{\pi}\phi_{\bar\sigma}(x+R)\right)+(-1)^j...\right] =
$$

$$
\simeq a^2\left[\frac{1}{\pi}\nabla\phi_\sigma(x)\nabla\phi_{\bar\sigma}(x)+\frac{(-1)^r}{\pi^2\alpha^2}\sin\left(2\sqrt{\pi}\phi_\sigma(x)\right)\sin\left(2\sqrt{\pi}\phi_{\bar\sigma}(x)\right)+(-1)^j...\right].
$$

(7.86)

Notice that, unlike the case of parallel spins (eq. (7.71)), here we can replace $\phi_{\bar\sigma}(x+R)$ with $\phi_{\bar\sigma}(x)$ in the product of the two sine functions since, using the exponential notation, we get $\phi_\sigma\pm\phi_{\bar\sigma}$ in the exponent, which does not vanish at lowest order. The two terms in eq. (7.86) can be rewritten as

a)

$$\frac{a^2}{\pi} \sum_r V_\perp(r) \frac{1}{a} \int dx \sum_\sigma \nabla \phi_\sigma \nabla \phi_{\bar\sigma} =$$
$$= \frac{2Va}{\pi} \sum_r \frac{1}{r^3} \int dx \nabla \phi_\uparrow \nabla \phi_\downarrow =$$
$$= 2\zeta(3) \frac{Va}{\pi} \int dx \nabla \phi_\uparrow \nabla \phi_\downarrow =$$
$$= \zeta(3) \frac{Va}{\pi} \int dx \left[(\nabla \phi_c)^2 - (\nabla \phi_s)^2 \right]$$

(7.87)

b)

$$\frac{a^2}{\pi^2 \alpha^2} \sum_r V_\perp(r)(-1)^r \frac{1}{a} \int dx \sum_\sigma \sin(2\sqrt{\pi}\phi_\sigma) \sin(2\sqrt{\pi}\phi_{\bar\sigma}) =$$
$$= \frac{V}{\pi^2 a} \sum_r \frac{(-1)^r}{r^3} \int dx \sum_\sigma \sin(2\sqrt{\pi}\phi_\sigma) \sin(2\sqrt{\pi}\phi_{\bar\sigma}) =$$
$$= -\frac{3}{4}\zeta(3) \frac{V}{\pi^2 a} \int dx \sum_\sigma \sin(2\sqrt{\pi}\phi_\sigma) \sin(2\sqrt{\pi}\phi_{\bar\sigma}) =$$
$$= \frac{3}{8}\zeta(3) \frac{V}{\pi^2 a} \int dx \sum_\sigma \left[\cos(2\sqrt{\pi}(\phi_\sigma + \phi_{\bar\sigma})) - \cos(2\sqrt{\pi}(\phi_\sigma - \phi_{\bar\sigma})) \right] =$$
$$= \frac{3}{4}\zeta(3) \frac{V}{\pi^2 a} \int dx \left[\cos(2\sqrt{\pi}(\phi_\sigma + \phi_{\bar\sigma})) - \cos(2\sqrt{\pi}(\phi_\sigma - \phi_{\bar\sigma})) \right] =$$
$$= \frac{3}{4}\zeta(3) \frac{V}{\pi^2 a} \int dx \left[\cos(\sqrt{8\pi}\phi_c) - \cos(\sqrt{8\pi}\phi_s) \right] .$$

(7.88)

The full Hamiltonian and RG flow

Now, by summing all the previous contributions, we obtain the following bosonized form of Hamiltonian (7.63)

$$
\begin{aligned}
H = {} & \left(1 - \frac{X}{2} - \frac{X}{\pi^2}\right) a \int dx \left[(\nabla\theta_c)^2 + (\nabla\theta_s)^2\right] + \\
& + \left(1 - \frac{X}{2} - \frac{X}{\pi^2} - \frac{8X}{\pi^2} + \frac{U}{2\pi} + \frac{11\zeta(3)V}{4\pi}\right) a \int dx\,(\nabla\phi_c)^2 + \\
& + \left(1 - \frac{X}{2} - \frac{X}{\pi^2} - \frac{8X}{\pi^2} - \frac{U}{2\pi} + \frac{3\zeta(3)V}{4\pi}\right) a \int dx\,(\nabla\phi_s)^2 + \\
& + \left(\frac{8X}{\pi^3 a} - \frac{U}{2\pi^2 a} + \frac{3\zeta(3)V}{4\pi^2 a}\right) \int dx \cos\left(\sqrt{8\pi}\phi_c\right) + \\
& + \left(\frac{8X}{\pi^3 a} + \frac{U}{2\pi^2 a} - \frac{3\zeta(3)V}{4\pi^2 a}\right) \int dx \cos\left(\sqrt{8\pi}\phi_s\right) + \\
& + \left(-\frac{4X}{\pi^3 a} + \frac{3\zeta(3)V}{4\pi^2 a}\right) \int \cos\left(\sqrt{8\pi}\phi_c\right) \cos\left(\sqrt{8\pi}\phi_s\right).
\end{aligned}
\tag{7.89}
$$

We can easily notice that, as expected, it has the form (3.83), i.e., it is the sum of two independent sine-Gordon models plus a coupling Hamiltonian. Here the coefficients are given by

$$
v_\nu K_\nu = \left(1 - \frac{X}{2} - \frac{X}{\pi^2}\right) 2a
\tag{7.90}
$$

$$
\frac{v_c}{K_c} = \left(1 - \frac{X}{2} - \frac{X}{\pi^2} - \frac{8X}{\pi^2} + \frac{U}{2\pi} + \frac{11\zeta(3)V}{4\pi}\right) 2a
\tag{7.91}
$$

$$
\frac{v_s}{K_s} = \left(1 - \frac{X}{2} - \frac{X}{\pi^2} - \frac{8X}{\pi^2} - \frac{U}{2\pi} + \frac{3\zeta(3)V}{4\pi}\right) 2a
\tag{7.92}
$$

$$
g_c = m_c v_c = \left(\frac{16X}{\pi} - U + \frac{3}{2}\zeta(3)V\right) a
\tag{7.93}
$$

$$
g_s = m_s v_s = \left(\frac{16X}{\pi} + U - \frac{3}{2}\zeta(3)V\right) a
\tag{7.94}
$$

$$
g_{cs} = \left(-\frac{8X}{\pi} + \frac{3}{2}\zeta(3)V\right) a,
\tag{7.95}
$$

from which we can extrapolate the Luttinger parameters and the velocities. At first order in the interaction parameters they read

$$K_\nu = 1 + \frac{1}{4\pi}\left[\frac{16X}{\pi} - c_\nu U - \frac{3\zeta(3)V}{2} - 4\zeta(3)V\delta_{\nu,c}\right] \qquad (7.96)$$

$$v_\nu = 2a\left[2 - \frac{X}{2} - \frac{X}{\pi^2} - K_\nu\right] \qquad (7.97)$$

where $c_c = 1$ and $c_s = -1$. We also notice that, as a consequence of the SU(2) symmetry in the spin channel, the Luttinger parameter is related to the mass by

$$K_s = 1 + \frac{g_s}{4\pi a} = 1 + \frac{m_s}{2\pi}. \qquad (7.98)$$

As mentioned in Chapter 3, if the charge-spin coupling is neglected, the RG analysis of the sine-Gordon model in the ν sector predicts the presence of a gapped phase when

$$2\pi(K_\nu - 1) < |m_\nu|. \qquad (7.99)$$

In the spin sector, since the relation (7.98) holds, the condition for obtaining a non-zero gap reduces to $m_s < |m_s|$, which implies $m_s < 0$ or, equivalently, $K_s < 1$. Therefore, we get the following critical line:

$$U_s = \frac{3}{2}\zeta(3)V - \frac{16}{\pi}X. \qquad (7.100)$$

For $U < U_s$, the spin field ϕ_s is pinned to 0 and $\Delta_s \neq 0$; whereas for $U > U_s$, ϕ_s is unpinned and $\Delta_s = 0$. We stress that here the case $m_s > 0$, which corresponds to $\phi_s = \sqrt{\pi/8}$ is forbidden by the SU(2) symmetry.

In the charge sector, the solution of equation (7.99) provides the following transition line

$$U_c = \frac{3}{2}\zeta(3)V + \frac{16}{\pi}X, \qquad (7.101)$$

corresponding to $g_c = 0$. It separates two insulating regimes ($\Delta_c \neq 0$ everywhere), characterized by $\phi_c = 0$ for $U > U_c$ and $\phi_c = \sqrt{\pi/8}$ for $U < U_c$.

Therefore, according to the classification furnished in Chapter 3 (Tab. 3.1), the ground state of Hamiltonian (7.63) in the weak coupling approximation presents three different phases in the repulsive regime: a Mott insulator with localized holon-doublon fluctuations in a uniform unit-density background for $U > U_c$; an Haldane insulator with "dilute" hidden antiferromagnetic order of holons and doublons for

Table 7.1 Correspondence between ground state quantum phases, bosonic fields and non-local order parameters from one-loop bosonization for a model with SU(2) spin symmetry. We have indicated the unpinned fields with the letter u.

	$\sqrt{2\pi}\Phi_c$	$\sqrt{2\pi}\Phi_s$	Δ_c	Δ_s	LRO
LL	u	u	0	0	none
LE	u	0	0	open	$C_P^{(s)}$
MI	0	u	open	0	$C_P^{(c)}$
HI	$\pi/2$	u	open	0	$C_S^{(c)}$
BOW	0	0	open	open	$C_P^{(c)}, C_P^{(s)}$
CDW	$\pi/2$	0	open	open	$C_S^{(c)}, C_P^{(s)}$

$U_s < U < U_c$; and a charge density wave for $U < U_s$ (see Fig. 7.1). In general, further phases are possible. For example, when the dipolar interaction vanishes, the $\eta-$symmetry is restored and the relation (7.98) holds also in the charge sector, preventing the pinning of the field to the value $\phi_c = \sqrt{\pi/8}$ and the subsequent formation of antiferromagnetic order of holons and doublons. Therefore the Haldane insulator is replaced by a Luttinger liquid phase and the charge density wave is reduced to a metallic Luther Emery phase. Finally, in case both fields are locked to the value 0, a bond ordered wave takes place. A summary of the possible phases allowed by the sine-Gordon model and the symmetries of the original fermionic Hamiltonian is reported in Table 7.1. In the last column, each phase is characterized by means of non-local order parameters, signaling the presence of a parity order when $\phi_v = 0$ and an Haldane string order when $\phi_v = \sqrt{\pi/8}$.

7.2.2   Including interaction non-perturbatively

In this section, we present an alternative approach to bosonization. To this purpose, we split the Hamiltonian (7.63) into the sum of two single-species Hamiltonians, already containing part of the interaction non perturbatively, plus an inter-species contribution:

$$H = \sum_\sigma H_\sigma + H_{\uparrow\downarrow}, \qquad (7.102)$$

where $\sum_\sigma H_\sigma$ contains the first row of (7.63). Up to the coefficient $(1 - \frac{X}{2})$, each of the two single-species Hamiltonians, H_σ, is a long-range "t-V" model, which is known to show a gapless Luttinger liquid behavior for small enough interaction
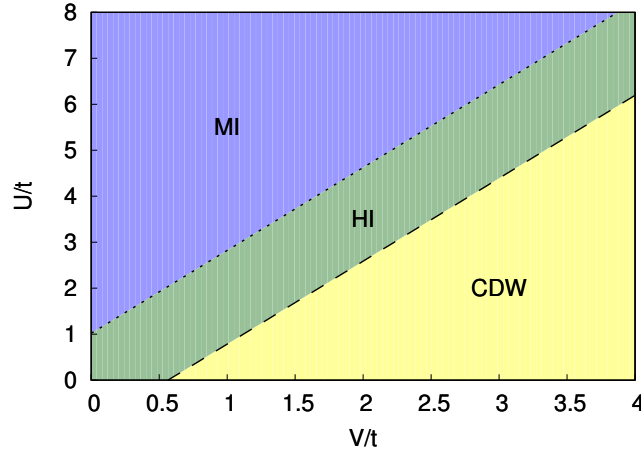
Fig. 7.1 Weak coupling phase diagram of Hamiltonian (7.63) from standard bosonization analysis. The dotted line signals the transition in the charge sector, while the dashed line signals the transition in the spin sector.

strength. Its Luttinger parameter $K(X,V)$ can be estimated numerically with high precision [131, 132]; whereas the two limits for $X = 0$ and $V = 0$ can be derived analytically (see [133] and [81], respectively). In this case, one obtains:

$$K(0,V) = \left[1 + \frac{6\zeta(3)V}{\pi^2} \right]^{-1/2} \quad , \quad K(X,0) = \left[\frac{2}{\pi} \arccos \frac{2X}{\pi \left(1 - \frac{X}{2} \right)} \right]^{-1} . \quad (7.103)$$

Obviously, K can also be calculated within the standard bosonization approximation [134], obtaining

$$K(X,V) \simeq 1 + \frac{1}{4\pi} \left[\frac{16X}{\pi} - \frac{7\zeta(3)V}{2} \right] . \quad (7.104)$$

At this point, we proceed to bosonize the inter-species Hamiltonian $H_{\uparrow\downarrow}$. This procedure produces a fully decoupling between the charge and spin channels:

$$H = H'_c + H'_s \quad (7.105)$$

with

$$H'_\nu = \frac{v'_\nu}{2} \int dx \left[K'_\nu (\nabla \theta_\nu)^2 + \frac{1}{K'_\nu} (\nabla \phi_\nu)^2 \right] + \frac{m_\nu v_\nu}{2\pi^2 a^2} \int dx \cos \left(\sqrt{8\pi} \phi_\nu \right) \quad (7.106)$$

and

$$\begin{cases} \frac{v'_\nu K'_\nu}{2} = \frac{vK}{2} - \frac{Xa}{\pi^2} \\ \frac{v'_\nu}{2K'_\nu} = \frac{v}{2K} + \left[-\frac{X}{\pi^2} + \frac{c_\nu}{2\pi} (U + 2\zeta(3)V) \right] a . \end{cases} \quad (7.107)$$
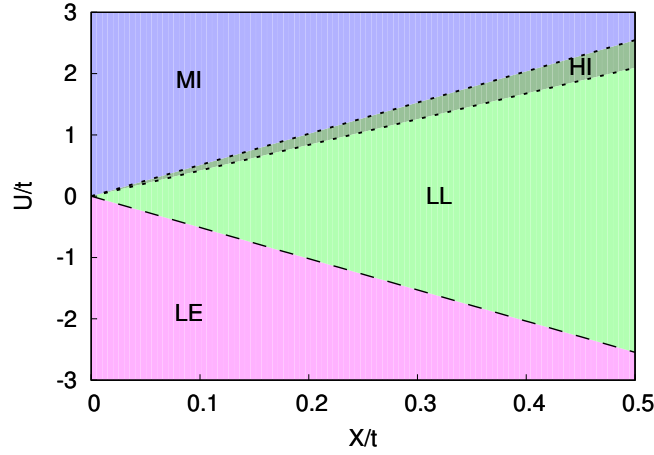
Fig. 7.2 Phase diagram at $V = 0$ from bosonization analysis of Section 7.2.2. The dashed line signals the transition in the spin sector, while the dotted lines indicate transitions in the charge sector. In case of standard bosonization, the Haldane insulator phase HI would still be a LL.

Now, using the relation $vK = (1 - \frac{X}{2})2a$, one gets

$$(K'_\nu)^2 = \frac{1 - \frac{X}{2} - \frac{X}{\pi^2}}{\left(1 - \frac{X}{2}\right)\frac{1}{K^2} - \frac{X}{\pi^2} + \frac{c_\nu}{2\pi}(U + 2\zeta(3)V)} \quad , \quad v'_\nu = v_\nu \frac{K_\nu}{K'_\nu} \qquad (7.108)$$

which, upon linearization, gives

$$K'_\nu = K\left\{1 - \frac{X}{2\pi^2} + \frac{K^2}{4\pi}\left[\frac{2X}{\pi} - c_\nu(U + 2\zeta(3)V)\right]\right\} \qquad (7.109)$$

where $c_c = 1$, $c_s = -1$.

Now the renormalization group analysis can be done by considering the expression of K with non-perturbative dependence on V (or X), and approximating to first order the remaining interaction in K, K'_ν and m_ν. This approach has already been applied to the case $X = 0$ in [26], where it has been shown that a BOW phase, not predicted within the standard bosonization, can appear. As an application of our results at generic X and V, here we derive the phase diagram in the case $V = 0$, where $K \equiv K(X,0)$ is given by eq. (7.103). The outcome is plotted in Fig. 7.2. From the comparison with the result of the standard approach, we observe the appearance of a non-trivial HI phase in the range $\frac{4\pi}{3}X \leq U \leq \frac{16}{\pi}X$. As described in Table 7.1, this corresponds to the presence of an Haldane string order in the charge sector, with degenerate edge modes [78].

7.3 Strong coupling limit

The bosonization approach is known to work for small values of interaction strengths. Here we want to study the opposite limit. Let's start by considering the model with short-range interaction, described by the Hamiltonian

$$H = -\sum_{j,\sigma} Q_{j,j+1,\sigma} \left[1 - X(n_{j,\bar{\sigma}} - n_{j+1,\bar{\sigma}})^2 \right] + U \sum_j n_{j,\uparrow} n_{j,\downarrow} + V \sum_j n_j n_{j+1} . \quad (7.110)$$

If the interactions are strong enough, we can neglect the kinetic term and the phase diagram reduces to just two phases, the MI and the CDW, emerging from the competition between the on-site and the nearest-neighbor interactions. The contact interaction is minimized when there are no double occupations. Since we are working at half-filling, this means that a situation in which all the sites are singly occupied is favoured. Hence the system behaves as a Mott insulator and its energy is

$$\frac{E^{MI}}{L} = V . \quad (7.111)$$

Meanwhile the nearest-neighbor interaction is minimized by a CDW configuration in which empty sites alternate with doubly occupied sites:

$$\frac{E^{CDW}}{L} = \frac{U}{2} . \quad (7.112)$$

Requiring the condition $E^{MI} = E^{CDW}$, one obtains the transition line between the two phases:

$$U = 2V. \quad (7.113)$$

In the case in which the nearest-neighbor interaction is replaced by the dipolar interaction (as in Hamiltonian (7.60)), the energies of these two phases change into

$$\frac{E^{MI}}{L} = \frac{V}{L} \sum_{i,j>i} \frac{1}{|i-j|^3} = V\zeta(3) \quad (7.114)$$

and

$$\frac{E^{CDW}}{L} = \frac{U}{2} + \frac{4V}{2} \sum_k \frac{1}{(2k)^3} = \frac{U}{2} + \frac{V}{4}\zeta(3) , \quad (7.115)$$

respectively. Requiring the condition $E^{MI} = E^{CDW}$, one gets

$$U = \frac{3}{2}\zeta(3)V \, . \tag{7.116}$$

Since the numerical analysis shows the appearance of a further BOW phase for $X = 0$ [26], here we also consider the possibility of its existence in our model. In fact, it seems to disappear at least in the strong coupling limit. In the following we calculate the energy of the particular BOW configuration shown in figure 7.3 and verify that it is always grater than the energy of the MI or that of the CDW considered above.
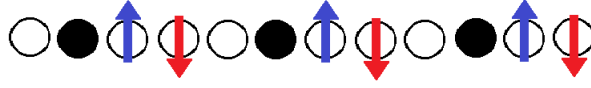
Fig. 7.3 A particular BOW configuration, which has both charge and spin parity orders.

Its energy is given by

$$\frac{E^{BOW}}{L} = \frac{1}{4}\left\{ U + V\left(3\sum_n \frac{1}{(4n-3)^3} + 4\sum_n \frac{1}{(4n-2)^3} + 3\sum_n \frac{1}{(4n-1)^3} + 6\sum_n \frac{1}{(4n)^3} \right) \right\}$$
$$= \frac{U}{4} + \frac{101}{128}\zeta(3)V \, .$$
$$\tag{7.117}$$

It is easily verified that the condition $E^{BOW} < E^{MI} \wedge E^{BOW} < E^{CDW}$ is never satisfied. Thus a direct MI-CDW phase transition is expected in the strong coupling limit also in the presence of dipolar interaction.

7.4   Numerical analysis

Here we study the phase diagram of Hamiltonian (7.60) by using DMRG simulations. In fact, for appropriate range of parameters we find the evidence of a further underlying order in the spin channel with respect to the bosonization predictions. This is revealed by the Haldane string non-local order parameter, thus showing the presence of protected edge modes.

As a first step we investigate the charge sector by evaluating the thermodynamic limit of the charge gap

$$\Delta_c = \frac{E(L+2) + E(L-2) - 2E(L)}{2} \, , \tag{7.118}$$

where $E(N)$ is the ground state energy of the system with N particles. Our results are reported in Fig. 7.4, as a function of the interaction parameter U, for fixed $X = 0.2$ and $V = 0.5$. Although Δ_c is very small in the intermediate region, our results show
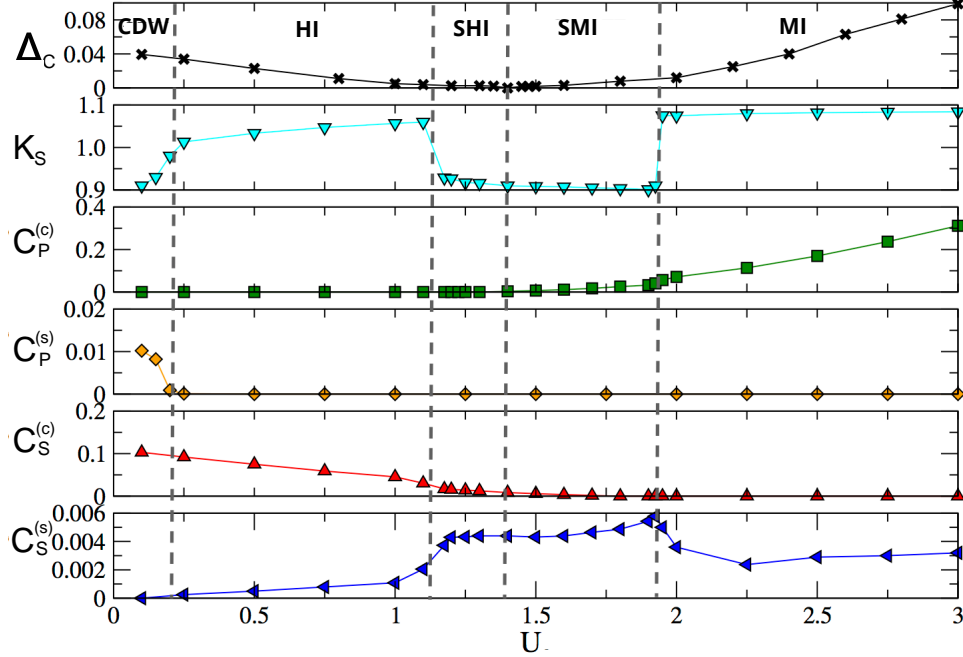
Fig. 7.4 Thermodynamic limit of charge gap, spin Luttinger constant and NLOPs of Hamiltonian (7.60) for $t = 1$, $V = 0.5$ and $X = 0.2$ as a function of U. Δ_c is extrapolated from finite size values up to $L = 44$ obtained with OBC. K_s and the NLOPs are extrapolated from finite size values up to $L = 36$ obtained with PBC. The value of the Haldane strings is extrapolated from the finite size values $C_S^{(v)}(L/2)$, while the value of the parities is extrapolated from $(C_P^{(v)}(L/2) + C_P^{(v)}(L/2 + 1))/2$. In our DMRG simulations we cut r to three nearest-neighbors keeping up to 1600 DMRG states and performing up to 6 finite size sweeps.

that it vanishes only in one point. Therefore, the system is always insulating; however the nature of the insulating behavior changes at the transition point, where $\Delta_c = 0$. The numerical analysis becomes more crucial when analyzing the behavior in the spin degree of freedom, where the presence of correlated hopping processes is known to make bosonization less predictive [29, 135]. In this case, as a fist step we evaluate the thermodynamic limit of the Luttinger parameter

$$K_s = \lim_{q \to 0} \pi \frac{S^s(q)}{q} \tag{7.119}$$

where

$$S^s(q) = \frac{1}{L} \sum_{k,l} e^{iq(k-l)} \left(\langle S_k^{(s),z} S_l^{(s),z} \rangle - \langle S_k^{(s),z} \rangle \langle S_l^{(s),z} \rangle \right) \qquad (7.120)$$

is the spin structure factor. Luttinger liquid theory predicts $K_s = 1$ or $K_s = 0$ depending on whether the spin gap is closed ($\Delta_s = 0$) or open ($\Delta_s \neq 0$), where Δ_s is defined as the energy variation in flipping one spin. When the Luttinger constant is computed numerically, both logarithmic corrections and finite size effects make very hard to get sharp $0, 1$ values. Nevertheless a well established and accurate method for distinguishing gapless and gapped phases, based on K_s, is to recognize a gapless phase in case $K_s > 1$ and a gapped phase when $K_s < 1$ [20, 23]; consequently the point $K_s = 1$ can be identified as the transition point. As shown in Fig. 7.4, the analysis based on the TDL of K_s surprisingly finds two different spin gapped phases, the first one close to $U = 0$ and the second one around the point $\Delta_c = 0$. In particular, the latter is not predicted within the bosonization approximation.

After having identified the gapped and gapless regions in the two sectors, we observe the behavior of NLOPs, in order to characterize the different phases. Based on their values, we find a charge density wave order (with $C_S^{(c)}, C_P^{(s)} \neq 0$) for large V, in analogy with the extended Hubbard model described in the previous chapter. The similarities extend also to the strong U region where the system behaves as a Mott insulator, characterized by the presence of a finite $C_P^{(c)}$. Instead, for intermediate values of the parameters, we find three different phases characterized by the presence of hidden magnetism. In particular, as U increases from very small values, the spin gap closes and the CDW order is replaced by an Haldane insulator, characterized solely by the charge Haldane string order parameter $C_S^{(c)}$, as predicted by bosonization. This partly gapped phase reproduces in a two-species fermionic system the charge hidden antiferromagnetic order that characterizes the well known topological Haldane insulator found in the context of spin-1 chains [48] and extended Bose-Hubbard model [136, 137, 121]. Finally, according to our DMRG analysis, the two remaining phases are fully gapped and share the same antiferromagnetic order in the spin channel (signaled by finite $C_S^{(s)}$), while the charge order changes from hidden antiferromagnetism ($C_S^{(c)} \neq 0$) to the formation of localized holons/doublons pairs ($C_P^{(c)} \neq 0$). These two phases have been called spin Haldane insulator (SHI) and spin Mott insulator (SMI), respectively. Figure 7.4 shows the identification of phase transitions based on the observation of Δ_c, K_s and the NLOPs for fixed $X = 0.2$, $V = 0.5$ and with varying U. In addition, we show the finite size scaling of

the Haldane string operators in Figure 7.5 for the three intermediate regions, i.e, the HI, SHI and SMI phases.
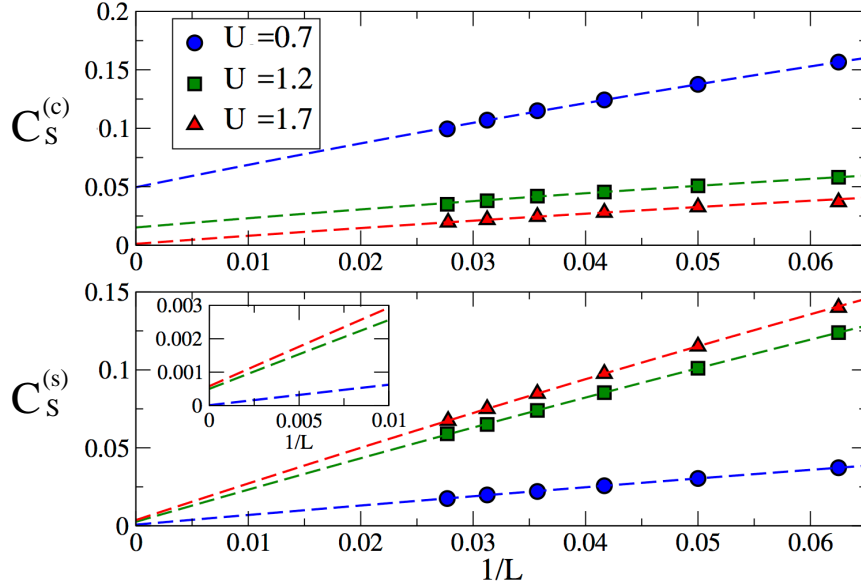
Fig. 7.5 Scaling of Haldane string correlators at $X = 0.2$ and $V = 0.5$ for different values of U, namely in the HI, SHI and SMI phases.

In Figure 7.6 we draw the full phase diagram of Hamiltonian (7.60) at fixed $X = 0.2$, by comparing the results obtained from DMRG simulations (points and dotted/dashed lines) with the predictions of bosonization (solid lines). In this regard, we observe that the one-loop bosonization is not able to capture the presence of the spin Haldane string order, since the spin SU(2) symmetry prevents the mass m_s from assuming a positive value and consequently the field ϕ_s from pinning to $\sqrt{\pi/8}$. Moreover we would like to highlight the fact that both SHI and SMI regimes cannot be detected by means of a local order, although they are fully gapped, as would suggest the one-loop bosonization. Indeed a non-zero local parameter would entail the presence of a long-range order that breaks a continuous symmetry of the Hamiltonian, thus violating the Mermin-Wagner theorem. Therefore, SHI and SMI phases cannot be identified with BSDW and SDW of Table 3.1. In fact, these phases go beyond the one-loop bosonization treatment. Nevertheless, the bosonization approach could be corrected by releasing the requirement of spin-charge separation and/or by including the effect of higher order harmonics, as done in [135]. In particular, an approximative method to take into account the effect of spin-charge coupling consists in considering an effective spin sine-Gordon model with renormalized mass
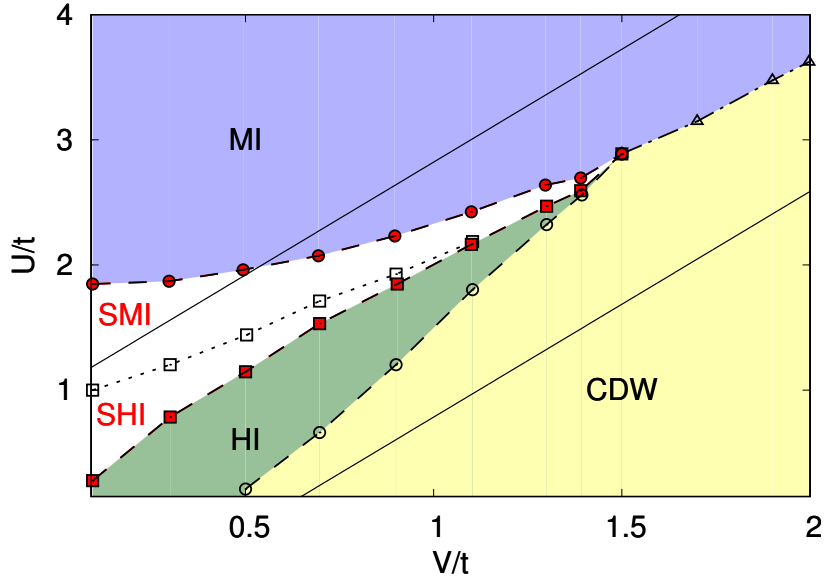
Fig. 7.6 DMRG (symbols) and bosonization (solid lines) phase diagram of (7.60) as a function of U and V with $t = 1$ and $X = 0.2$. The dotted line signals the transition in the charge sector, while the dashed lines indicate transitions in the spin sector. The dotted-dashed line is a transition involving both channels. The red points mark the new transition lines with respect to the previous results.

$m_s^* = m_s + M_{cs} < \cos\sqrt{8\pi}\phi_c >$, where $\phi_c = 0$ or $\phi_c = \sqrt{\pi/8}$. Hence, depending on the sign of M_{cs}, one can find $m_s^* > 0$ even for a negative m_s. That happens for $M_{cs} > 0$ if $\phi_c = 0$, thus generating a SMI phase, and for $M_{cs} < 0$ if $\phi_c = \sqrt{\pi/8}$, thus producing a SHI phase. The same approach could also be applied to justify the deviation of the CDW-HI transition line from the one-loop bosonization predictions, exploring the case $m_s^* < 0$.

Finally, we checked the stability and robustness of the phase diagram with respect to varying X. In particular, as X is increased, the shape of the entire region with spin Haldane string order (finite $C_S^{(s)}$) is preserved, whereas the region with charge Haldane string order (finite $C_S^{(c)}$) expands, thus increasing the size of the SHI phase. The crucial point is that the spin Haldane order persists also for very weak X, as shown in Figure 7.7. This fact suggests that hidden spin orders are generated by the only presence of correlated hopping terms, thus producing a new scenario. Indeed, previous discoveries of (metallic) phases with spin Haldane string orders [76, 77] were induced by explicitly breaking the full rotational spin symmetry. Instead, our results support the presence of insulating regimes with hidden spin magnetic orders generated by interaction.
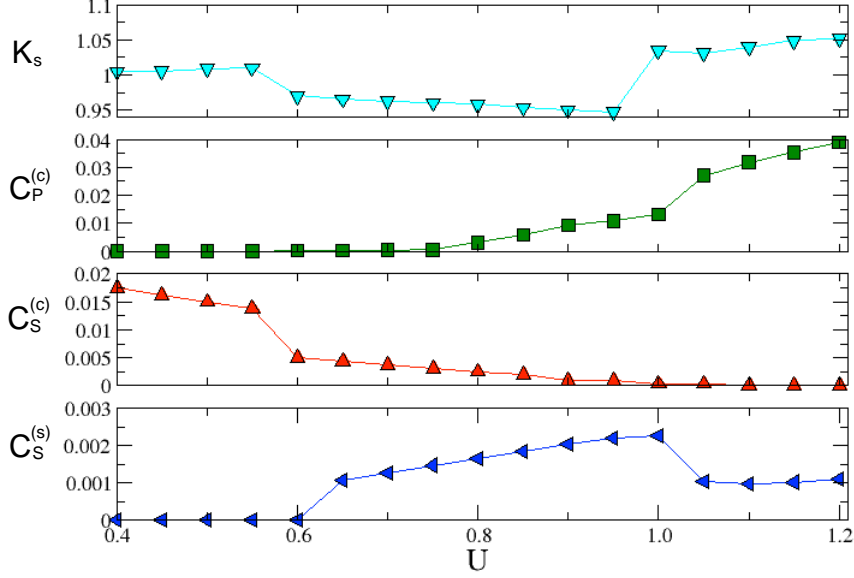
Fig. 7.7 Thermodynamic limit of spin Luttinger constant K_s and NLOPs for $t = 1$, $V = 0.3$ and $X = 0.05$ as a function of U. Data are extrapolated from finite size values up to $L = 24$ with PBC. The Haldane string is extrapolated from $C_S^{(v)}(L/2)$ with varying L while the the parity is extrapolated as $(C_P^{(v)}(L/2) + C_P^{(v)}(L/2 + 1))/2$. In our DMRG simulations we cut r to three nearest-neighbors keeping up to 1200 DMRG states and performing up to 6 finite size sweeps.

7.5   Correspondence with a time-dependent model: Floquet analysis

In this last section we show the equivalence between the model (7.60) and the effective static model corresponding to a time-periodic extended Hubbard model of the form

$$H = -\sum_{j,\sigma}(c_{j,\sigma}^{\dagger}c_{j+1,\sigma} + h.c.) + \bar{U}(\mathtt{t})\sum_{j}n_{j,\uparrow}n_{j,\downarrow} + V\sum_{j,r\geq 1}\frac{n_j n_{j+r}}{r^3}. \qquad (7.121)$$

The study of time-dependent models is of great interest to understand how equilibrium states can be reached through local dynamics and related phenomena like transport or many-body localization. Besides that, periodically driven systems open

the way to the observation of topologically non-trivial orders. In particular, they can be described by an effective Hamiltonian. That is achieved by means of the Floquet analysis, which plays an important role for quantum simulation. Indeed in cold-atom experiments all the couplings, i.e., the hopping amplitude t, the short range interaction U and the long-range dipolar repulsion V can be independently controlled. On the other hand, the time dependence in $\bar{U}(t)$ can be induced by a rapid variation of the scattering length [138]. In fact, this can generate a periodic modulation of the form $\bar{U}(t) = U + U_1 \cos(\omega t)$, which consequently makes the Hamiltonian time-periodic $H(t) = H(t + t_P)$ with period $t_P = 2\pi/\omega$. Therefore, in the regime of high frequencies $\omega >> V/\hbar, U/\hbar, t/\hbar$, Floquet theory can be applied [139] to reduce Hamiltonian (7.121) to an effective static model with the hopping processes renormalized by the density, namely eq. (7.60), with the rate X determined by the strength of the interaction U_1 and the frequency ω. In the following, we provide the details of the calculation, by starting from the case $V = 0$ [100].
Let us consider the Hamiltonian

$$H = - \sum_{\langle i,j\rangle,\sigma} \left(c_{i,\sigma}^{\dagger} c_{j,\sigma} + h.c. \right) + \bar{U}(t) \sum_i n_{i,\uparrow} n_{i,\downarrow}, \qquad (7.122)$$

with

$$\bar{U}(t) = U + U_1 \cos(\omega t). \qquad (7.123)$$

Following the Floquet theory, we observe that solutions of the Schroedinger problem have the form

$$|\psi_n(t)\rangle = e^{-\iota E_n t/\hbar} |u_n(t)\rangle, \qquad (7.124)$$

where $|u_n(t)\rangle$ are the so-called Floquet modes and are periodic with the same period t_P of the driving force [100, 140, 141]. They can be regarded as the eigenstates of the so-called Floquet Hamiltonian

$$\tilde{H}(t) = H(t) - i\hbar\partial_t, \qquad (7.125)$$

while E_n are the corresponding eigenvalues:

$$\tilde{H}(t)|u_n(t)\rangle = E_n|u_n(t)\rangle. \qquad (7.126)$$

The solutions $|\psi_n(t)\rangle$ are unique up to a shift of the quasienergies E_n by an integer multiple m of $\hbar\omega$. Thus this system, being periodically time-dependent, possesses a

Brillouin zone-like structure.

The eigenvalue problem (7.126) is defined in the Hilbert space $\mathcal{H}' = \mathcal{H} \otimes \mathcal{H}_T$, where $\mathcal{H}$ is the standard Fock space and $\mathcal{H}_T$ is the Hilbert space of time-periodic functions. Hence, if we indicate the Fock states with $|n_{j,\sigma}\rangle$ and label the basis of the periodic functions with m, we can define the following Floquet basis

$$|n_{j,\sigma},m\rangle = |n_{j,\sigma}\rangle e^{-\alpha(t)\hat{D}+\imath m\omega t} \tag{7.127}$$

with

$$\alpha(t) = \imath K \sin(\omega t) = \imath \frac{U_1}{\hbar\omega} \sin(\omega t) \tag{7.128}$$

and $\hat{D} = \sum_j n_{j,\uparrow} n_{j,\downarrow}$ is the double-occupation operator.

We can obtain the quasienergies by computing the matrix elements

$$\langle\langle n_{j,\sigma},m|\tilde{H}(t)|n'_{j,\sigma},m'\rangle\rangle_{t_P} = \langle\langle n_{j,\sigma}|e^{\alpha(t)\hat{D}}e^{-\imath m\omega t}\tilde{H}(t)e^{\imath m'\omega t}e^{-\alpha(t)\hat{D}}|n'_{j,\sigma}\rangle\rangle_{t_P} \tag{7.129}$$

where the symbol $\langle\langle...\rangle\rangle_{t_P}$ means that the scalar product is time-averaged:

$$\langle\langle...\rangle\rangle_{t_P} = \frac{1}{t_P}\int_0^{t_P} dt\langle...\rangle . \tag{7.130}$$

Let us compute this expectation value

$$\langle\langle n_{j,\sigma}|e^{\alpha(\mathtt{t})\hat{D}}e^{-\imath m\omega\mathtt{t}}(-\imath\hbar\partial_{\mathtt{t}})e^{\imath m'\omega\mathtt{t}}e^{-\alpha(\mathtt{t})\hat{D}}|n'_{j,\sigma}\rangle\rangle_{\mathtt{t_P}} =$$

$$=m'\hbar\omega\underbrace{\frac{1}{\mathtt{t_P}}\int_0^{\mathtt{t_P}}e^{-\imath(m-m')\omega\mathtt{t}}}_{\delta_{m,m'}}\underbrace{\langle n_{j,\sigma}|n'_{j,\sigma}\rangle}_{\delta_{n,n'}}$$

$$-\imath\hbar\langle\langle n_{j,\sigma}|e^{\alpha(\mathtt{t})\hat{D}}e^{-\imath(m-m')\omega\mathtt{t}}\left(-\imath\frac{U_1}{\hbar}\cos(\omega\mathtt{t})\hat{D}\right)e^{-\alpha(\mathtt{t})\hat{D}}|n'_{j,\sigma}\rangle\rangle_{\mathtt{t_P}}$$

$$=m\hbar\omega\delta_{m,m'}\delta_{n,n'}-U_1\langle\langle n_{j,\sigma}|e^{-\imath(m-m')\omega\mathtt{t}}\cos(\omega\mathtt{t})\hat{D}|n'_{j,\sigma}\rangle\rangle_{\mathtt{t_P}}$$

$$\langle\langle n_{j,\sigma}|e^{\alpha(\mathtt{t})\hat{D}}e^{-\imath m\omega\mathtt{t}}H(\mathtt{t})e^{\imath m'\omega\mathtt{t}}e^{-\alpha(\mathtt{t})\hat{D}}|n'_{j,\sigma}\rangle\rangle_{\mathtt{t_P}} =$$

$$=\langle\langle n_{j,\sigma}|e^{-\imath(m-m')\omega\mathtt{t}}e^{\alpha(\mathtt{t})\hat{D}}\hat{T}e^{-\alpha(\mathtt{t})\hat{D}}|n'_{j,\sigma}\rangle\rangle_{\mathtt{t_P}}$$

$$+\langle\langle n_{j,\sigma}|e^{-\imath(m-m')\omega\mathtt{t}}e^{\alpha(\mathtt{t})\hat{D}}U\hat{D}e^{-\alpha(\mathtt{t})\hat{D}}|n'_{j,\sigma}\rangle\rangle_{\mathtt{t_P}}$$

$$+\langle\langle n_{j,\sigma}|e^{-\imath(m-m')\omega\mathtt{t}}e^{\alpha(\mathtt{t})\hat{D}}U_1\cos(\omega\mathtt{t})\hat{D}e^{-\alpha(\mathtt{t})\hat{D}}|n'_{j,\sigma}\rangle\rangle_{\mathtt{t_P}}$$

$$=\langle\langle n_{j,\sigma}|e^{-\imath(m-m')\omega\mathtt{t}}e^{\alpha(\mathtt{t})\hat{D}}(\hat{T}+\hat{U})e^{-\alpha(\mathtt{t})\hat{D}}|n'_{j,\sigma}\rangle\rangle_{\mathtt{t_P}}$$

$$+U_1\langle\langle n_{j,\sigma}|e^{-\imath(m-m')\omega\mathtt{t}}\cos(\omega\mathtt{t})\hat{D}|n'_{j,\sigma}\rangle\rangle_{\mathtt{t_P}}.$$

$$(7.131)$$

Hence

$$\langle\langle n_{j,\sigma},m|\tilde{H}(\mathtt{t})|n'_{j,\sigma},m'\rangle\rangle_{\mathtt{t_P}} =$$

$$=m\hbar\omega\delta_{m,m'}\delta_{n,n'}+\frac{1}{\mathtt{t_P}}\int_0^{\mathtt{t_P}}d\mathtt{t}e^{-\imath(m-m')\omega\mathtt{t}}\langle n_{j,\sigma}|e^{\alpha(\mathtt{t})\hat{D}}H_{Hubbard}e^{-\alpha(\mathtt{t})\hat{D}}|n'_{j,\sigma}\rangle$$

$$(7.132)$$

with $H_{Hubbard}=\hat{T}+U\hat{D}$. Clearly $\hat{D}$ commutes with the exponential operator. Thus, this term gives $\delta_{m,m'}\langle n_{j,\sigma}|U\hat{D}|n'_{j,\sigma}\rangle$. Let us compute the expectation value of $\hat{T}$. To do this, we use the formula

$$e^B A e^{-B}=\sum_{n=0}^{\infty}\frac{1}{n!}[B,A]_n \tag{7.133}$$

which entails

$$e^{\alpha(\mathtt{t})\hat{D}}\hat{T}e^{-\alpha(\mathtt{t})\hat{D}}=\sum_{n=0}^{\infty}\frac{\alpha(\mathtt{t})^n}{n!}[\hat{D},\hat{T}]_n. \tag{7.134}$$

The commutator gives

$$[\hat{D}, \hat{T}] = -\sum_{\langle i,j \rangle \sigma} (c^{\dagger}_{i,\sigma} c_{j,\sigma} - h.c.)(n_{i,\bar{\sigma}} - n_{j,\bar{\sigma}}) \tag{7.135}$$

and in terms of the *X*-operators it is

$$-\sum_{\langle i,j \rangle \sigma} (X_i^{2\bar{\sigma}} X_j^{0\sigma} - X_i^{\sigma 0} X_j^{\bar{\sigma}2}) + h.c. = T_+ - T_- \tag{7.136}$$

where we have indicated with T_+ the first term and with T_- the second one. Then, we have

$$\begin{aligned} [\hat{D}, \hat{T}]_2 &= T_+ + T_- \\ [\hat{D}, \hat{T}]_3 &= T_+ - T_- \end{aligned} \tag{7.137}$$

and so on. Consequently

$$\sum_n \frac{\alpha(\mathtt{t})^n}{n!} [\hat{D}, \hat{T}]_n =$$

$$= \hat{T} + (T_+ + T_-) \sum_{n=1}^{\infty} \frac{\alpha(\mathtt{t})^{2n}}{(2n)!} + (T_+ - T_-) \sum_{n=0}^{\infty} \frac{\alpha(\mathtt{t})^{2n+1}}{(2n+1)!}$$

$$= \hat{T} + (T_+ + T_-) \left(\sum_{n=0}^{\infty} \frac{(-1)^n (K \sin(\omega \mathtt{t}))^{2n}}{(2n)!} - 1 \right) + \iota(T_+ - T_-) \sum_{n=0}^{\infty} \frac{(-1)^n (K \sin(\omega \mathtt{t}))^{2n+1}}{(2n+1)!}$$

$$= \hat{T} + (T_+ + T_-) (\cos(K \sin(\omega \mathtt{t})) - 1) + \iota(T_+ - T_-) \sin(K \sin(\omega \mathtt{t})). \tag{7.138}$$

Finally we average these quantities on time. If we assume that the frequency is sufficiently high, we can neglect the non-diagonal blocks and consider only $m = m'$. Thus, we have

$$\begin{aligned} \frac{1}{T} \int_0^T \cos(K \sin(\omega \mathtt{t})) d\mathtt{t} &= \frac{1}{\pi} \int_0^{\pi} \cos(K \sin x) dx = \mathscr{J}_0(K) \\ \frac{1}{T} \int_0^T \sin(K \sin(\omega \mathtt{t})) d\mathtt{t} &= \frac{1}{2\pi} \int_0^{2\pi} \sin(K \sin x) dx = 0 \end{aligned} \tag{7.139}$$

where $\mathscr{J}_0$ is the first kind Bessel function. Hence, our result is the following

$$\langle\langle n_{j,\sigma}, m | \tilde{H}(\mathtt{t}) | n'_{j,\sigma}, m' \rangle\rangle_{\mathtt{tp}} = \delta_{m,m'} \left(\langle n_{j,\sigma} | H_{eff} | n'_{j,\sigma} \rangle + m\hbar\omega\delta_{n,n'} \right). \tag{7.140}$$

where

$$H_{eff} = \hat{T} - (1 - \mathscr{J}_0(K))(T_+ + T_-) + \hat{U} \tag{7.141}$$

is an effective time-independent Hamiltonian. Thus we have reduced the original time-dependent Hamiltonian to an effective static Hamiltonian. We observe that

$$T_+ + T_- = - \sum_{\langle i,j \rangle \sigma} (c^\dagger_{i,\sigma} c_{j,\sigma} + h.c.)(n_{i,\bar\sigma} + n_{j,\bar\sigma} - 2n_{i,\bar\sigma} n_{j,\bar\sigma}) \tag{7.142}$$

and the effective Hamiltonian can be written in the following form

$$H_{eff} = - \sum_{\langle i,j \rangle \sigma} (c^\dagger_{i,\sigma} c_{j,\sigma} + h.c.)[1 - X(n_{i,\bar\sigma} + n_{j,\bar\sigma} - 2n_{i,\bar\sigma} n_{j,\bar\sigma})] + U \sum_i n_{i,\uparrow} n_{i,\downarrow}. \tag{7.143}$$

with $X = 1 - \mathscr{J}_0(K)$. This can be easily recognized as the particle-hole invariant correlated-hopping model (7.60), at $V = 0$.

Now suppose to add a (time-independent) dipolar interaction to Hamiltonian (7.122). Since this extra-term commutes with $\hat{D}$, we can repeat the same procedure and obtain

$$\begin{aligned}
H_{eff} = &- \sum_{\langle i,j \rangle \sigma} (c^\dagger_{i,\sigma} c_{j,\sigma} + h.c.)[1 - X(n_{i,\bar\sigma} + n_{j,\bar\sigma} - 2n_{i,\bar\sigma} n_{j,\bar\sigma})] + \\
&+ U \sum_i n_{i,\uparrow} n_{i,\downarrow} + V \sum_{\langle i,r \rangle} \frac{n_i n_{i+r}}{r^3},
\end{aligned} \tag{7.144}$$

which coincides with Hamiltonian (7.60).

In order to check the validity of the Floquet theory we compute with numerical simulations the finite size NLOPs for both the time dependent model (7.121) and the effective one (7.144). In the first case, the simulations are performed by means of Exact Diagonalization starting from an initial state with given parameters t, U, V; while at $\mathtt{t} > 0$ a time periodic interaction $\bar{U}(\mathtt{t})$ is applied in order to get correlated hopping processes with amplitude $X = 0.2$. Then, we monitor the time evolution and we evaluate the time-averages of the NLOPs. The results are shown in Figure 7.8. Here the red-dashed lines represent the time averaged values of NLOPs, while black-dotted lines are the NLOPs computed in the ground state of the effective model, with couplings t, U, V, X. The comparison shows a perfect agreement, thus validating the possibility of investigating the model (7.144) in order to get information about the system described by Hamiltonian (7.121).
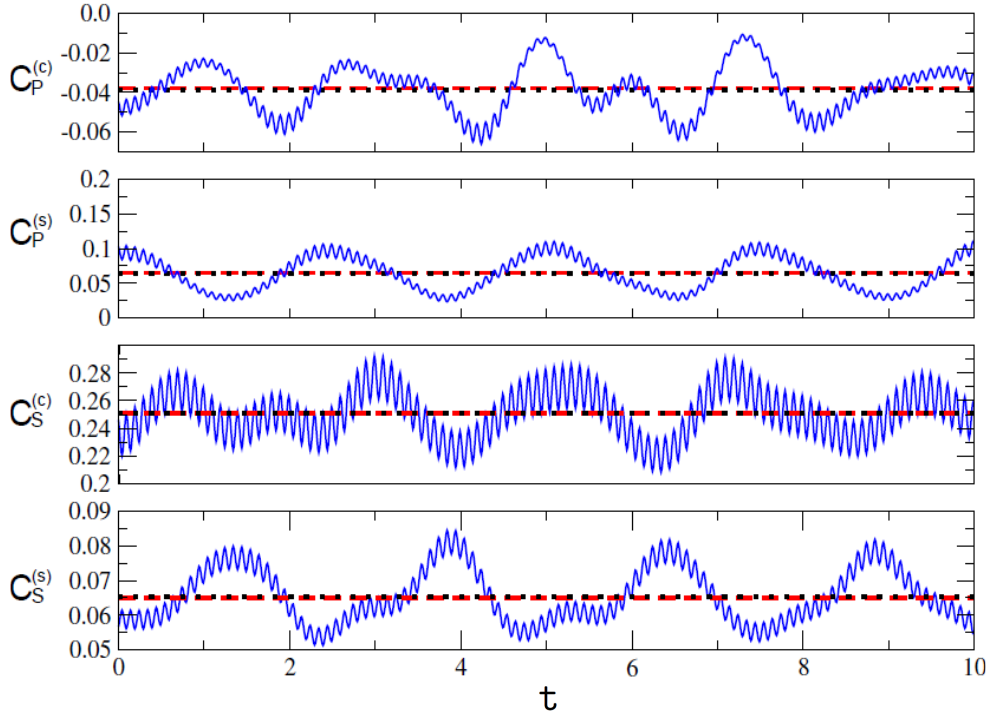
Fig. 7.8 Blue continuous lines are the time evolution of NLOPs in Hamiltonian (7.121), red dashed lines are their time-averaged values and black dotted lines are the NLOPs given by the effective Hamiltonian (7.144). The Haldane strings are computed as $C_S^{(v)}(L/2)$ while the parities are computed as $(C_P^{(v)}(L/2)+C_P^{(v)}(L/2+1))/2$ for a system of $L=8$ sites, with couplings $U=0.6$, $V=0.6$ and $U_1/(\hbar\omega)=0.918$ (the latter corresponding to an amplitude of the correlated hopping processes $X=0.2$).

We finally would like to highlight that the regimes characterized by the presence of hidden magnetism can be reached by means of the currently available experimental setups and probes. In fact proposals for the observation of hidden charge magnetism [50, 142–145] have been carried out. At the same time, investigations of periodically modulated quantum systems [146] have stimulated the realization of particle-hole symmetric Hubbard-like Hamiltonians with correlated hopping processes [125].

Our results could be verified by using a mixture of Erbium isotopes. In particular fermionic ^{167}Er [106] and bosonic ^{168}Er [105] isotopes are currently available in laboratories. In the second case, the scattering length can be tuned in order to reach an hard-core regime. That would allow to get an effective two-component Fermi mixture. An appropriate lattice depth should allow to easily obtain the regime $0.5 \lesssim V/t \lesssim 2$, where hidden magnetism is predicted. On the other hand, Feshbach

resonance to tune the on-site interaction between the two *Er* isotopes should become available [147]. Finally, the correlated hopping processes can be realized by applying a rapid time dependent modulation, as described in [125]. Doing measurements in a dynamical environment is very challenging. Nevertheless, recently local correlations have been probed for a system of periodically modulated fermions [148]. The technique is based on a sudden freeze of the system and subsequent application of procedures used in static configurations.

7.6   Conclusions

In this Chapter we have studied both the effect of correlated hopping processes and long-range interaction on the phase diagram of the Hubbard model. We have used both analytical and numerical techniques. In particular, by comparing the ground state phase diagrams obtained from one-loop bosonization in the weak coupling limit and DMRG simulations, we have found good agreement for the charge sector, while numerical data support the presence of a further hidden order in the spin channel, which is not predicted by bosonization. In fact, although this hidden magnetism emerges inside fully gapped phases, it can be solely detected by the non-vanishing of Haldane string-like non-local order parameters.

Finally we have shown that the phases found could be observed also in a periodically modulated two-component fermionic system and experimentally detected in cold-atom gases.

Chapter 8

Two-dimensional non-local parity operator

Our next task is to generalize the non-local order parameters defined in $1D$ to higher dimensions. In particular, we focus on the $2D$ charge parity order, which we expect to characterize the Mott insulator. The latter has a number of particles in each site equal to the (integer) filling n, with small deviations, i.e., pairs of sites with $n-1$ and $n+1$ particles forming bound states. In $1D$ this effect is captured by a non-zero value of the non-local string of parities given in eq. (2.15), with $v = c$. Here we explore the behavior of generalized brane parity operators from $1D$ to $2D$ in the superfluid-Mott insulator transition occurring in the Bose-Hubbard model at $n = 1$. Indeed, the parity order parameter is expected to be zero in the superfluid (SF) and finite in the Mott insulator. In fact, in ref. [149] it has been conjectured that in two dimensions the average of the parity operator should decay to zero also in the MI, if defined in a way similar to that adopted in the one dimensional lattice. We confirm this prediction by means of GFQMC simulations and show that the introduction of a further phase makes the parameter non-zero in the MI while still vanishing in the SF. The content of this chapter has been published in Ref. [150].

8.1   The SF-MI transition in the Bose-Hubbard model

A non-vanishing value of the charge parity order parameter introduced in Chapter 2, eq. (2.15), signals the presence of a MI phase, in both fermionic and bosonic models.

Indeed, this phase, which is induced by interaction, is a paradigmatic example of a quantum phase that has no classical counterparts and cannot be detected by a local order parameter. The general picture of the MI is described by a state with a uniform distribution of particles (n per site), with quantum fluctuations consisting of bound pairs of holons and doublons, i.e., sites with $n-1$ and $n+1$ particles, respectively (see Fig. 8.1). The correlation length of these pairs is finite, so that their presence
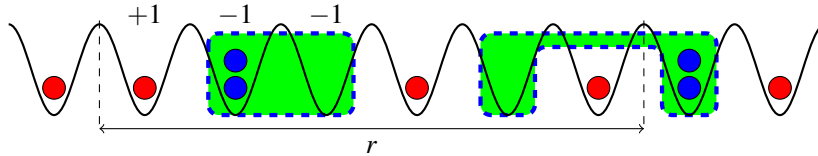
Fig. 8.1 Picture of the MI phase in the case $n = 1$. The on-site parity $\mathscr{P}_R$ (eq. 8.2) is equal to $+1$ for single occupations and to -1 for fluctuations (i.e., doublons and holons). The order parameter for the one-dimensional MI phase is given by the product of on-site parities on a string of length r (eq. (8.3)).

does not affect the overall parity of a string of sites unless for those straddling its boundary, which amount to a zero-measure set. As the correlation length of the pairs grows to infinity, the system transits from the MI phase to a gapless one. In order to check the validity of generalized parity operators in higher dimensions, here we analyze their behavior in the SF-MI transition occurring in the Bose-Hubbard model on M-leg ladders, with M ranging from 1 (corresponding to the $1D$ case) to ∞ (corresponding to the $2D$ case). The Bose-Hubbard model, introduced in equation (1.55), on ladders with $L \times M$ sites, reads

$$H = -\frac{t}{2}\sum_{\langle R,R'\rangle} b_R^\dagger b_{R'} + \text{h.c.} + \frac{U}{2}\sum_R n_R(n_R - 1) \tag{8.1}$$
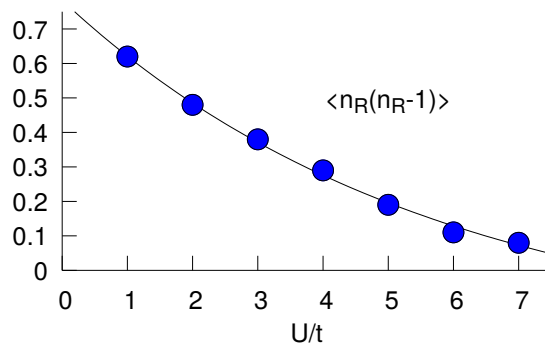
Fig. 8.2 Formation of doublons through the MI-SF transition. The data have been computed on a 2-leg ladder with $L = 30$.

where we have renormalized the amplitude of the hopping term and have relabeled each site i with its coordinates $R = (x,y)$ on the rectangular lattice. As always, $\langle R, R' \rangle$ indicates nearest-neighbor sites, $b_R^\dagger$ (b_R) creates (destroys) a boson on the site R, and $n_R = b_R^\dagger b_R$ is the density on the site R. The density per site is fixed to be $n = N/(L \times M)$, where N is the number of bosons and $L \times M$ is the number of lattice sites. In the following, we concentrate on the case with $n = 1$. We first consider finite systems. As an example, in Figure 8.2, we show the formation of doublons as the interaction strength U/t decreases, for a ladder with $M = 2$ and $L = 30$. Then we study the properties of the ladders with M legs by extrapolating the $L \to \infty$ limit of the parity operators computed on lattices with finite number of sites and periodic-boundary conditions in both directions. Finally, in order to assess the properties of the two-dimensional lattice, we vary the number of legs M and extrapolate the $M \to \infty$ limit, which provides insights into the two-dimensional case.

8.2   Brane parities

In order to achieve the goal of finding a proper order parameter for the MI, we consider the density fluctuations with respect to the average value $n = 1$ on a single site R, namely $\delta n_R = n_R - 1$. They can be described through an on-site parity operator $\mathscr{P}_R$ defined as

$$\mathscr{P}_R = \mathrm{e}^{\iota \pi \delta n_R} . \tag{8.2}$$

Depending on the parity of the boson density n_R this operator assumes one of the two possible values $\mathscr{P}_R = \pm 1$. Then, the $1D$ non-local parity introduced in equation (2.15) can be regarded as a string of on-site parity operators (from $x = 0$ to $x = r$):

$$O_P(r, M = 1) = \prod_{0 \leq x < r} \mathscr{P}_{x,0} \tag{8.3}$$

(see Fig. 8.1). With respect to the notation used in the previous chapters, here we omit the index ν (since it is always referred to the charge), and explicit the dependence on M. In case $M = 1$ we recover the definition given for the one-dimensional case. This definition can be extended to the case with $M > 1$ in different ways. The most natural generalization consists in introducing a *brane* of on-site parity operators, or

equivalently, a string of rung parity operators, in the following way:

$$O_P(r,M) = \prod_{0 \le x < r} \prod_{0 \le y < M} \mathscr{P}_{x,y} = \prod_{0 \le x < r} \mathscr{P}_x^{\text{rung}}(M) \,, \tag{8.4}$$

where the role of the single site in the $1D$ chain is replaced by the entire rung (see Fig. 8.3). Therefore, $\mathscr{P}_x^{\text{rung}}$ is defined in terms of the rung density fluctuations $\delta n_x^{\text{rung}} = n_x^{\text{rung}} - M = \sum_{y=0}^{M-1} n_{x,y} - M$, namely

$$\mathscr{P}_x^{\text{rung}}(M) = e^{i\pi \delta n_x^{\text{rung}}} \,. \tag{8.5}$$

In one dimension ($M = 1$), the MI phase can be distinguished from the SF by looking
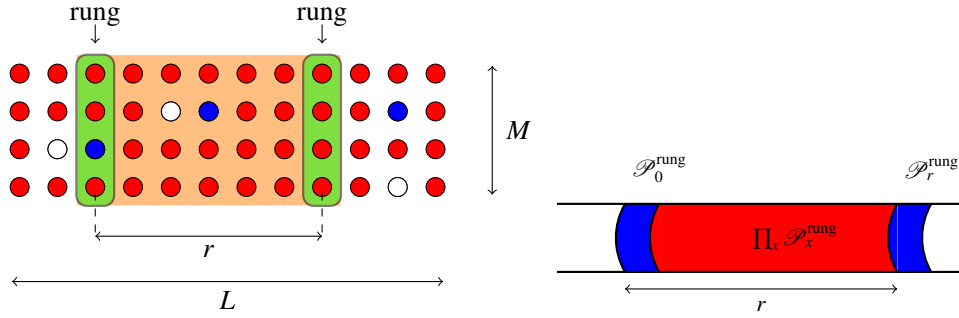
Fig. 8.3 *Left:* Schematic representation of the 2D lattice with single occupations (red circles) and holons/doublons pairs (white and blue circles). The orange area represents a brane enclosed between two delimiting rungs. *Right:* Schematic representation of the brane parity operator (8.4).

at the ground-state expectation value of $O_P(r,M)$:

$$C_P(r,M) \equiv \langle O_P(r,M) \rangle = \langle \Phi_{GS} | O_P(r,M) | \Phi_{GS} \rangle \,, \tag{8.6}$$

which coincides with the correlation function $\langle O_P^\dagger(0,M)O_P(r,M) \rangle$. Indeed, $C_P(r,1)$, in the limit $r \to \infty$, is known to stay finite in the MI, while it is vanishing in the SF phase [51], thus playing the role of an order parameter for the MI phase. For higher spatial dimensions, that is less obvious. In fact, it has been argued [149] that $C_P(r,M)$ should decay to zero with $M, r \to \infty$ (i.e., in the two dimensional case) in both the SF and the MI, even though a different asymptotic behavior should appear in the two phases (see below). Recently it has been suggested [151] to generalize the brane parity operator (8.4) by normalizing the phase in $P_x^{\text{rung}}(M)$ with the number of legs M, in order to obtain a non-vanishing expectation value in the MI also for $M \to \infty$.

In this regard, we observe that, if we consider only small density fluctuations on each site, namely $\delta n_R = \pm 1$, we get that the rung density fluctuates between 0 and $2M$, implying that δn_x^{rung} can assume the $2M + 1$ integer values ranging from $-M$ and $+M$. Thus, the density fluctuation on a rung of length M can be associated with the z-component of a spin-M and the Hamiltonian on the M-leg ladder with a spin-M model on a chain. Hence, in analogy with the choice made in the latter case for the Haldane string operator, [152, 153] we redefine the brane parity operator by introducing an arbitrary phase θ:

$$O_P^{(\theta)}(r,M) \equiv [O_P(r,M)]^{\frac{\theta}{\pi}}, \tag{8.7}$$

where θ may depend on M and on the model Hamiltonian. In particular, in case of the Heisenberg model, one obtains that $\theta = (\pi/M)$ maximizes the average value of the non-local operator. The same result is found in [151] for the MI on a fermionic ladder.

More generally, we suggest that, for convenient values of θ, the expectation value of the generalized parity operator

$$C_P^{(\theta)}(M) = \lim_{r\to\infty} \langle O_P^{(\theta)}(r,M) \rangle \tag{8.8}$$

could work as an order parameter for the SF-MI transition also in the $2D$-limit (i.e., for $M \to \infty$), decaying to zero only in the superfluid phase. In order to test this conjecture, first we investigate the behavior of $C_P^{(\theta)}(M)$ for the Bose-Hubbard model within a Gaussian approximation. That gives

$$\langle O_P^{(\theta)}(r,M) \rangle \approx e^{-\frac{\theta^2}{2}\langle(\delta n^{\text{brane}})^2\rangle}, \tag{8.9}$$

with $\delta n^{\text{brane}} = \sum_{x=0}^{r-1} \delta n_x^{\text{rung}}$. This quantity represents the fluctuation of bosonic density on the brane of size $r \times M$ and can be evaluated by following the procedure used in Ref. [149]. Then, one obtains

$$C_P^{(\theta)}(M) \approx \begin{cases} \lim_{r\to\infty} r^{-aM\theta^2} & \text{SF,} \\ e^{-bM\theta^2} & \text{MI,} \end{cases} \tag{8.10}$$

where a and b are positive constants depending on the physical parameters. At this point, if we assume $\theta \propto M^{-\alpha}$, in order to get a finite value of $C_P^{(\theta)} = \lim_{M\to\infty} C_P^{(\theta)}(M)$

in the MI we should claim $\alpha \geq \frac{1}{2}$. This calculation also shows that, by contrast, the standard parity operator (i.e., $\theta = \pi$, or $\alpha = 0$), decays with a "perimeter-law", as found in Ref. [149]. In any case, the SF phase is characterized by a zero value of $C_P^{(\theta)}(M)$ for arbitrary θ at any finite M, and thus in the $2D$ limit. However, we observe that, if the two limits $M \to \infty$ and $r \to \infty$ (i.e., $L \to \infty$) are inverted, $C_P^{(\theta)}$ vanishes only for $\alpha \leq \frac{1}{2}$.

8.3   Numerical results

In the following we test the behavior of the generalized parity operator with $\theta = \pi M^{-\alpha}$ and $\alpha = 0, 1, 1/2$ through the SF-MI transition in the Bose-Hubbard model by means of Monte Carlo simulations on ladders with different values of M. For the sake of simplicity, hereinafter we adopt the following notation

$$C_\alpha(r,M) \equiv \langle O_P^{(\pi/M^\alpha)}(r,M) \rangle \,, \tag{8.11}$$

for the expectation value of the parity operator at finite values of r and M, and

$$C_\alpha(M) \equiv \lim_{r \to \infty} C_\alpha(r,M) \,, \quad C_\alpha \equiv \lim_{M \to \infty} C_\alpha(M) \tag{8.12}$$

for its limiting values.

The ground state properties of the Hamiltonian are extracted by employing the GFQMC technique, with the following optimized Jastrow function used as the guiding wave function:

$$|\Phi_G\rangle = e^{-\frac{1}{2} \sum_{R,R'} v_{R,R'} n_R n_{R'}} |\Phi\rangle_{U=0} \,, \tag{8.13}$$

where $v_{R,R'}$ are the optimized variational parameters and

$$|\Phi\rangle_{U=0} = \frac{1}{\sqrt{N!}} \left(b_{k=0}^\dagger \right)^N |0\rangle \tag{8.14}$$
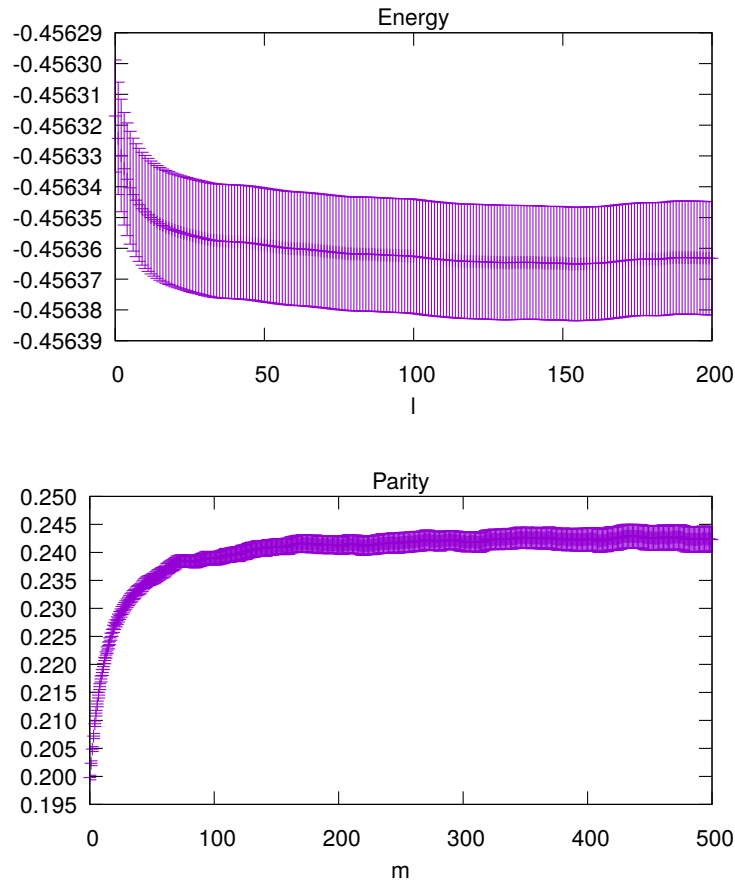
Fig. 8.4 Ground state energy and standard parity $C_0(L/2 = 15, M = 1)$ as a function of the number of correcting weight factors used respectively in the backward- and forward-walking reconfiguration processes of GFQMC. The calculation refers to the point $U/t = 2$.

is the BEC[1] state introduced in Section 1.6. The basis used for simulating the Markov chain is the following

$$|x\rangle = \prod_{\{R\}} \frac{\left(b_R^\dagger\right)^{n_R}}{\sqrt{n_R!}} |0\rangle . \tag{8.15}$$

The observables, such as generalized brane parities, are computed by implementing the forward-walking technique. As an example, in Figure 8.4 we show the convergence of the energy and the standard parity $C_0(L/2, M)$ for $L = 30$ and $M = 1$ at $U/t = 2$ as a function of the number of correcting weight factors used in the backward- and forward-walking reconfiguration processes, respectively.

---

[1] Bose-Einstein condensate

We start by analyzing the behavior of the standard parity, i.e., the case $\alpha = 0$. In Figure 8.5a, we show its behavior as a function of the interaction strength U/t for a rectangular lattice with a finite number of sites. In particular, the graph refers to a ladder with two legs ($M = 2$) of length $L = 120$. Since periodic boundary conditions are applied, we evaluate the expectation value between two rungs separated by a distance $r = L/2$. We observe that $C_0(L/2 = 60, M = 2)$ is vanishing for small values of the interaction parameter and becomes non-zero when increasing U/t. That signals the transition from the gapless SF phase to the gapped MI phase. We notice that $L = 120$ is great enough to give a zero value of the parity operator in the superfluid; however the transition point marked in the figure has been located after having performed the asymptotic limit $L \to \infty$, i.e., after having computed $C_0(M = 2)$. In fact, $C_0(M)$ is zero in the superfluid and remains finite in the MI. We have evaluated this quantity for different values of M. Then, based on the results for $C_0(M)$, we located the transition point U_c/t with increasing M. The outcome is displayed in the phase diagram of Figure 8.5b. We would like to point out that the transition point increases monotonically with M and converges quite rapidly to the value obtained in two dimensions [154, 155]. Indeed, we find $U_c/t = 1.8(1)$ for $M = 1$, while it is already $U_c/t = 8.1(1)$ for $M = 4$, thus approaching the value of $U_c/t = 8.5(1)$ that has been obtained in two dimensions. These results would suggest that $C_0(M)$ is a good order parameter for the MI on a ladder with M legs. However, that holds only for finite values of M. In fact, we find that $C_0(M)$ decreases with growing M and decays exponentially to zero for $M \to \infty$, as shown in Figure 8.5c for $U/t = 12$, deep inside the MI. Those data have been obtained for fixed $L = 30$, after having verified that the calculations do not change sensibly for larger values of L. Our findings are in agreement with the predictions of Ref. [149]. In particular, we can recognize that our data lie on the exponential curve given in eq. (8.10), with $b = t^2/(2U^2)$.

Therefore, we conclude that C_0 is not an order parameter for the two-dimensional MI. A totally different scenario appears in the case of the brane parity C_1.

The trend of $C_1(r, M)$ as a function of U is similar to that obtained for $C_0(r, M)$, for any finite value of M. As an example, in the upper panel of Figure (8.6), we show the behavior of $C_1(r = L/2, M = 2)$ for different values of L. We observe that, within the SF phase, it shows very large size effects with varying L. In fact, they are much larger than those observed in the case $\alpha = 0$. That is clearly visible by comparing Figs 8.5a and 8.6 (upper panel). On the other hand, our observations are in agreement with the prediction of eq. (8.10). The finite size scaling with increasing L shows that $C_1(M)$
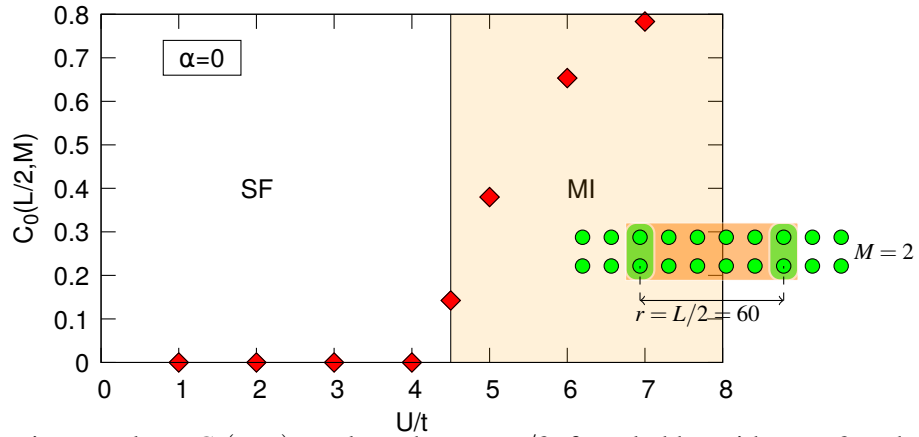
(a) Brane parity correlator $C_0(r,M)$, evaluated at $r = L/2$, for a ladder with $M = 2$ and $L = 120$ as a function of U/t.
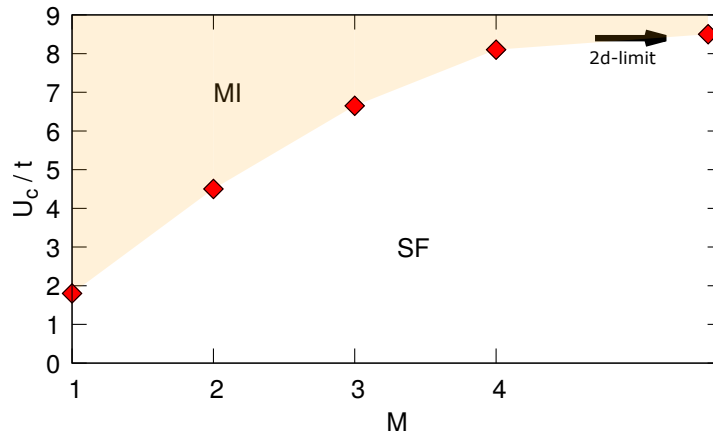
(b) Phase diagram of the Bose-Hubbard model (8.1) for $n = 1$ with increasing the number of legs M of the ladder.
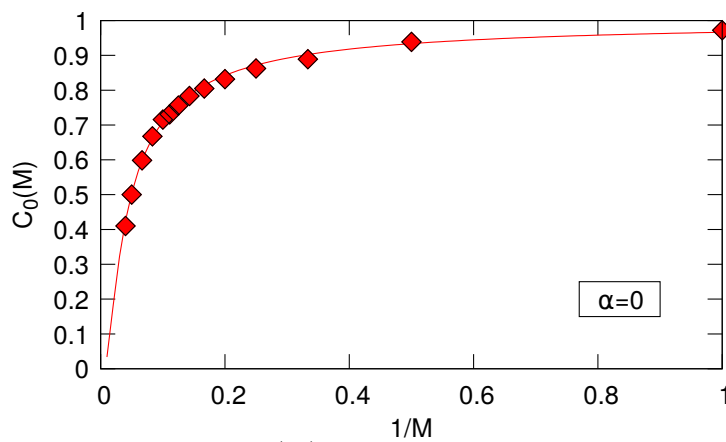
(c) Size scaling of brane parity $C_0(M)$ (i.e., $\theta = \pi$) with M in the MI phase ($U/t = 12$). Data are fitted by Eq. (8.10) with $b = t^2/(2U^2)$. The simulations have been performed for systems with $L = 30$, after having verified that the results do not change sensibly for larger values of L.

Fig. 8.5 Numerical results for the generalized brane parity operator with $\alpha = 0$ and the derived phase diagram.
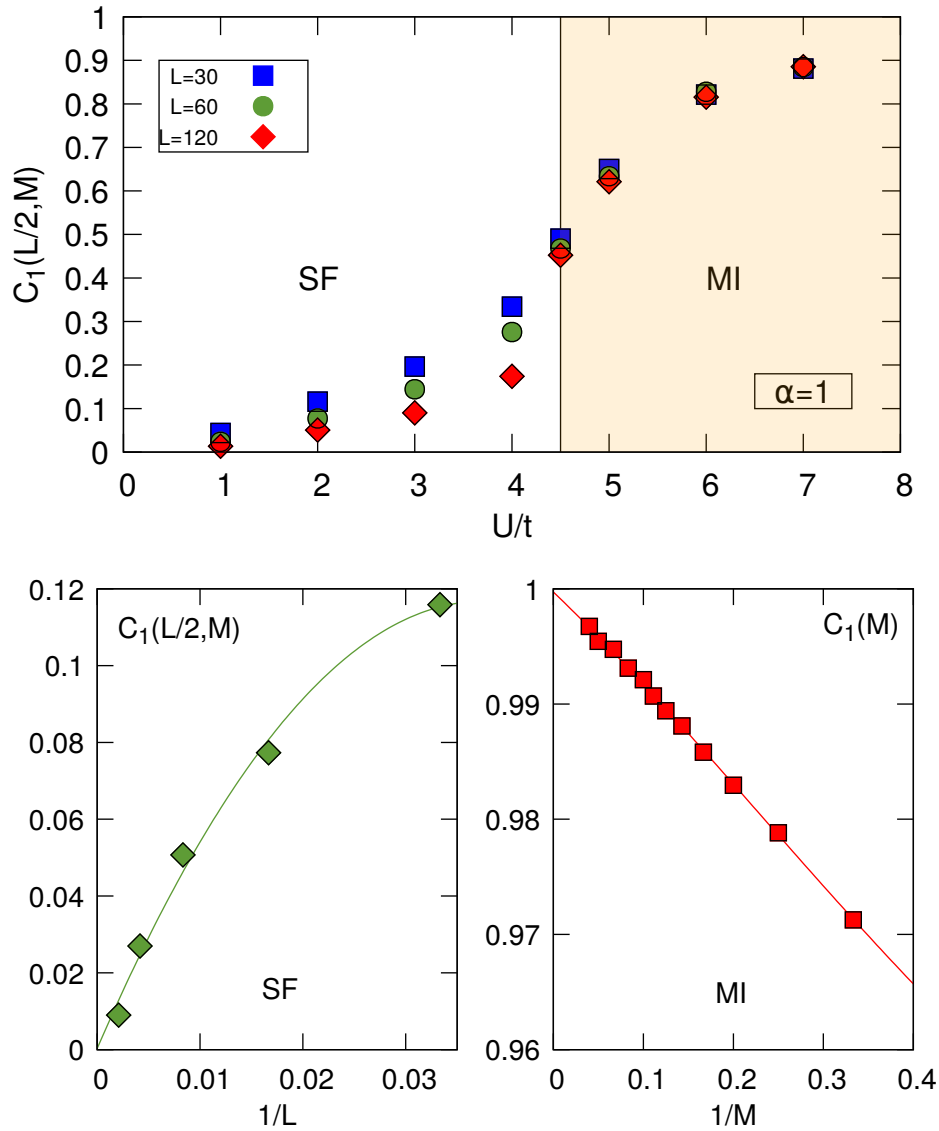
Fig. 8.6 Numerical results for the generalized brane parity operator with $\alpha = 1$. *Upper panel:* Brane parity correlator $C_1(r, M)$ (i.e. $\theta = \pi/M$), evaluated at $r = L/2$, for a ladder with $M = 2$ and different lengths L, as a function of U/t. *Left lower panel:* Finite-size scaling of $C_1(L/2, M = 2)$ with increasing L, in the SF phase (i.e., $U/t = 2$). *Right lower panel:* Finite size-scaling of $C_1(M)$ with increasing M, in the MI phase (i.e., $U/t = 12$). Here, the simulations have been performed for systems with $L = 30$, after having verified that the results do not change sensibly for larger values of L.
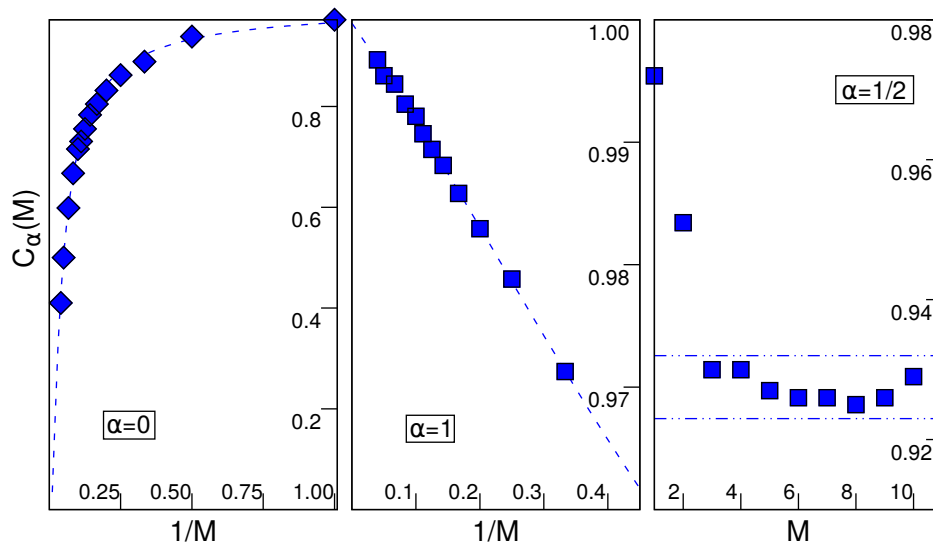
Fig. 8.7 Scaling of the brane parity $C_\alpha(M)$ with increasing M to the two dimensional limit $M \to \infty$, for $\alpha = 0$ (left panel), $\alpha = 1$ (central panel) and $\alpha = 1/2$ (right panel), at $U/t = 12$, deep inside the MI. The extrapolated values are: $C_0 = 0$, $C_1 = 1$ and $C_{1/2} = e^{-(\pi t/U)^2}$.

is zero in the superfluid (see left lower panel of Fig. 8.6), while it is non-zero in the MI phase. Therefore, $C_1(M)$, as well as $C_0(M)$, is an order parameter for the MI on a ladder. Moreover, contrary to the previous case, it remains an order parameter also in the 2D limiting case $M \to \infty$, as shown in the right lower panel of Fig. 8.6, where C_1 is extrapolated. In fact, our numerical results confirm that $C_1 = 1$ for each value of $U > U_c$, as suggested again by the Gaussian approximation. Finally, for $\alpha = 1/2$, the latter predicts that the brane parity behaves again as an order parameter for the two-dimensional MI, in this case with a non-trivial dependence on U through the parameter b: $C_{1/2} = e^{-\pi^2 b}$. Our numerical simulations support this guess. In Figure 8.7, we report the main results about the behavior of $C_\alpha(M)$ in the MI as M is increased to the two-dimensional limit, for the three cases $\alpha = 0, 1, 1/2$. In all the cases, our results agree with the prediction of the Gaussian approximation. Indeed, the numerical data of Fig. 8.7 can be fitted by the curve

$$C_\alpha(M) = e^{-b_\alpha \pi^2 M^{1-2\alpha}}, \tag{8.16}$$

with the fitting coefficient b_α depending, in general, on the specific case. In particular, for the case $\alpha = 1$, the exponential curve can be linearized at large M: $C_1(M) \approx$

$1 - b_1 \pi^2 \frac{1}{M}$. We find the following values for the fitting parameter:

$$b_0 = \frac{t^2}{2U^2}, \quad b_1 = 2.5b_0, \quad b_{1/2} = 2b_0. \tag{8.17}$$

In Figure 8.8 we show the behavior of the two order parameters C_1 and $C_{1/2}$ for the two-dimensional MI, as a function of U/t.

We finally checked the robustness of our results when the microscopic details of the band structure change. In particular, we have performed few calculations in the presence of a second-neighbor hopping t' (with $t'/t = 0.8$) and found similar qualitative results. Those are shown in Figure 8.9: although the transition to the MI phase is moved to higher U values, we observe that at $U/t = 20$, hence within the MI phase, C_1 is already 1 whereas $C_{1/2} \approx 0.9$. Therefore, we expect that C_α, with appropriate values of α, is a good order parameter for many different 2D Mott insulators, independently on the microscopic details of the band structure.

8.4 Conclusions

In conclusion, in this chapter we have addressed the issue of characterizing the MI in more than one-dimensional systems. In particular, we probed the efficiency of
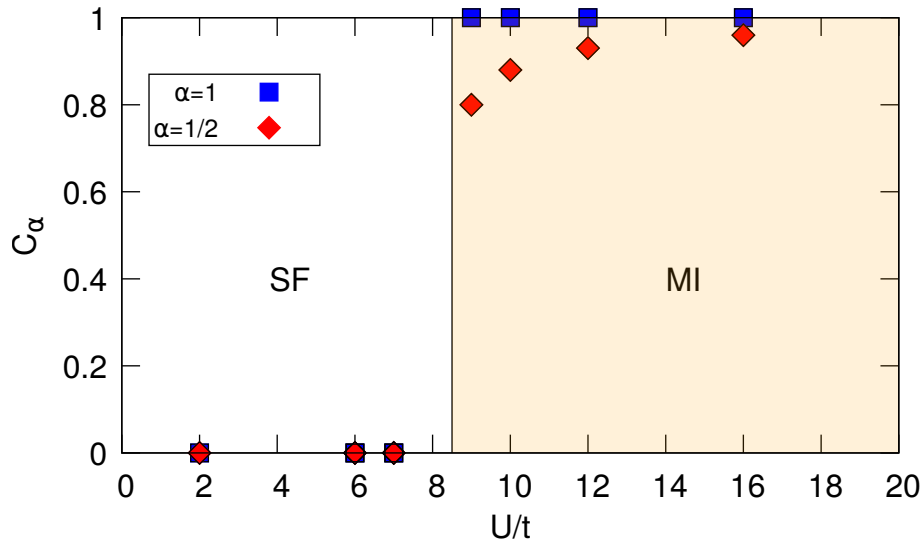
Fig. 8.8 Two-dimensional brane parity C_α for $\alpha = 1$ (i.e., $\theta = \pi/M$) and $\alpha = 1/2$ (i.e., $\theta = \pi/\sqrt{M}$) as a function of U/t.

generalized brane parity operators in capturing the order underlying the MI phase. By means of GFQMC simulations, we have studied the SF-MI transition in the Bose-Hubbard model on ladders with L rungs and M legs. In particular, we have investigated the asymptotic limit $L \to \infty$, when passing from one dimension ($M = 1$) to two dimensions ($M \to \infty$). Our results have shown that the average value of the standard brane parity operator $C_0(M)$ behaves as an order parameter for the MI at any finite M. However, it decays to zero with a "perimeter law" in the two-dimensional limit, thus being hardly detectable in experiments. By contrast, exploiting the fact
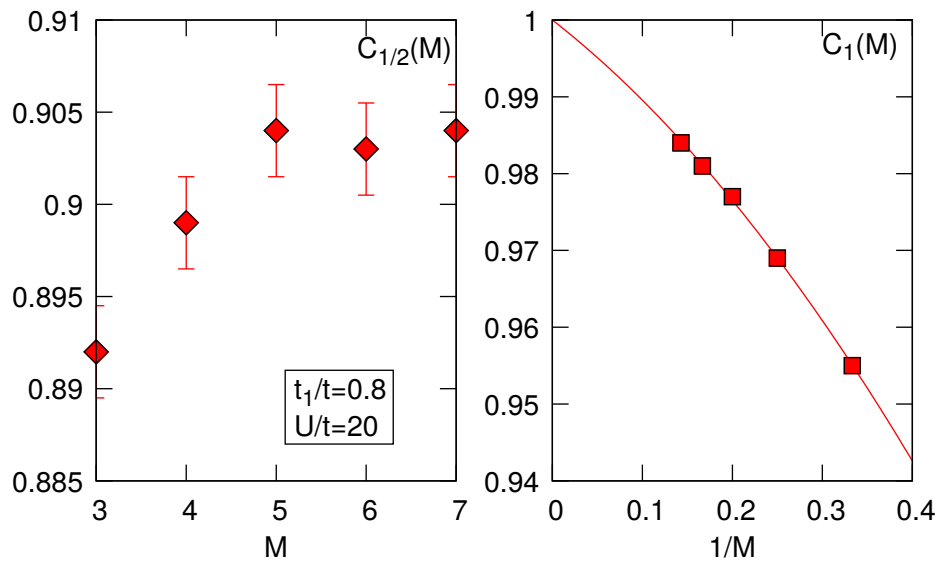
Fig. 8.9 Behavior of $C_\alpha(M)$ for $\alpha = 1/2$ (left panel) and $\alpha = 1$ (right panel) with varying M, in the MI phase of the Bose-Hubbard model with second-neighbor hopping. The evaluation has been done at $t'/t = 0.8$ and $U/t = 20$.

that in the MI the boson density undergoes only small fluctuations around its average value n, we have argued that a generalized brane parity operator C_α is non-zero in the 2D-Mott insulator for any $\alpha \geq 1/2$. In fact, the Gaussian approximation suggests that $C_\alpha = 1$ in the MI for $\alpha > 1/2$; whereas $C_{1/2}$ assumes a finite value depending on the Hamiltonian parameter U/t, thus enlightening the role of interaction in driving the transition. Moreover, in the SF, $C_{1/2} = 0$, regardless of which of the two limits $L \to \infty$ and $M \to \infty$ is considered first. These predictions, which have been confirmed by our numerical calculations, suggest that the proper order parameter to describe the MI-SF transition could be $C_{1/2}$. Our findings supply a unique tool to probe the appearance of the MI phase in cold atom systems. Indeed, with the currently available experimental setups, it is possible to measure in-situ density fluctuations

by means of high-resolution imaging [108].

In conclusion of this chapter, we would like to suggest as a near future perspective the application of generalized brane parity - and possibly *brane string* - operators for the investigation of two dimensional fermionic phases, in both density and spin channels. In fact, we expect they will help to detect many different phases, including magnetic states, spin liquids, and superconductors.

Conclusions and outlook

We have approached the problem of detection of hidden and symmetry-breaking phases in strongly correlated systems, focusing on Hubbard-type models. As found in recent years [49–53], the solution of this issue deals with non-local order parameters. Here, we have studied their behavior in the ground state phase diagram of different Hamiltonians. After having introduced, in the first part of the thesis, the fundamental concepts for the development of our research activity, in Chapter 6 we have shown the results of our DMRG simulations to compute the non-local order parameters across all the ground state phase transitions of the one-dimensional extended Hubbard model. Our results have shown that they are able to capture all of them, including those that involve partly gapped conducting phases, thus establishing themselves as efficient probes for the detection of many - known and novel - quantum regimes. Their strength relies especially on two main points: on one hand, they allow to characterize each quantum phase in its microscopic picture and topological nature, and locate it inside an unambiguous classification; on the other hand, they are observables which would enable experimentalists to distinguish clearly different phases. In light of our first results, in Chapter 7 we have used this powerful tool to investigate a more complex model, with bond-charge interaction. This was particularly interesting since, from bosonization predictions and previous literature, we expected to observe a charge Haldane insulator, which is known to have non-trivial topological order. With respect to the model studied in previous works, we also considered the effect of long-range dipolar interaction which can be implemented in cold atom experiments. Besides the expected non-trivial charge Haldane insulator, our numerical analysis supports the evidence of further two phases with non-trivial behavior in the spin channel. Interestingly, the correlated hopping processes we considered can be generated dynamically through the Floquet mapping, starting from a time-periodic on-site interaction. Our simulations also show a perfect agreement

between the values of the order parameters computed in the static model and those, time-averaged, obtained for the time-dependent model. Finally, our interest was to find a proper generalization of non-local order parameters to the two-dimensional case. In this regard, we considered one of them: the charge parity. In Chapter 8 we illustrated how to attain such generalization by redefining the phase of the operator in order to take into account the growth of the system in the transverse direction. Then, we tested our conjectures in the well-known SF-MI transition occurring in the Bose-Hubbard model, by exploiting the quantum Monte Carlo technique. The generalization of the parity operator was a remarkable result, since it opens the way to the investigation of two-dimensional hidden phases with a unique tool.

At this point, the next natural step will be to extend to higher dimensions the definition of the spin parity and, most notably, that of the Haldane strings, which should provide a deeper understanding of non-trivial topological phases. Indeed, as we have seen, non-local orders are strictly connected to topological phases, specifically the symmetry protected topological phases. In this context, we think that a key element to deepen the comprehension of such systems is the mapping between fermion and spin models, expressed in terms of spin and pseudo-spin operators, i.e., the generators of symmetries. That should enable us to depict non-local orders in terms of triplets and singlets [156], at least in the strong coupling limit, thus providing a simple and intuitive picture of exotic orders to be exported in the fermionic language. In particular, we expect that the Hubbard Hamiltonian with adding exchange interactions is the natural context in which the presence of a metallic phase with spin Haldane order could be observed [157].

Another possible route for future investigations might be to explore the possible presence of other types of non-local orders, at first in one dimension. In particular, as we have seen that the parity and Haldane string in the bosonization approximation are related to the field ϕ_v, it would be interesting to study the emergence of possible new non-local orders due to the locking of the dual field θ_v. The latter may take place in different physical scenarios in which spin/charge conservation does not hold [158].

In summary, in this thesis we have shown new results on both hidden phases in strongly correlated systems and non-local order parameters, that should be considered an essential tool to investigate the arising novel quantum physics in low dimensionality, and offer a fascinating and still widely unexplored field of research.

References

[1] M. C. Gutzwiller. Effect of correlation on the ferromagnetism of transition metals. *Phys. Rev. Lett.*, 10:159–162, 1963.

[2] J. Hubbard. Electron Correlations in Narrow Energy Bands. *Proc. of the Royal Soc. A*, 276:238–257, 1963.

[3] J. Hubbard. Electron Correlations in Narrow Energy Bands. II. The Degenerate Band Case. *Proc. of the Royal Soc. A*, 277:237–259, 1964.

[4] J. Hubbard. Electron Correlations in Narrow Energy Bands. III. An Improved Solution. *Proc. of the Royal Soc. A*, 281:401–419, 1964.

[5] J. Hubbard. Electron Correlations in Narrow Energy Bands. IV. The Atomic Representation. *Proc. of the Royal Soc. A*, 285:542–560, 1965.

[6] J. Hubbard. Electron Correlations in Narrow Energy Bands. V. a Perturbation Expansion About the Atomic Limit. *Proc. of the Royal Soc. A*, 296:82–99, 1967.

[7] J. Hubbard. Electron Correlations in Narrow Energy Bands. VI. the Connection with Many-Body Perturbation Theory. *Proc. of the Royal Soc. A*, 296:100–112, 1967.

[8] F. H. L. Essler, H-Frahm, F. Göhmann, A. Klümper, and V. E. Korepin. *The One-Dimensional Hubbard Model*. Cambridge University Press, 2005.

[9] J. E. Hirsch. Two-dimensional Hubbard model: Numerical simulation study. *Phys. Rev. B*, 31:4403–4419, 1985.

[10] J. E. Hirsch. Simulations of the three-dimensional hubbard model: Half-filled band sector. *Phys. Rev. B*, 35:1851–1859, 1987.

[11] A. Montorsi. *The Hubbard Model: A Reprint Volume*. World Scientific Pub Co Inc, 1992.

[12] D. Baeriswyl, D. K. Campbell, J. M. P. Carmelo, F. Guinea, and E. Louis. *The Hubbard Model: Its Physics and Mathematical Physics*. Springer Science+Business Media, LLC, 1995.

[13] A. M. Tsvelik. *Quantum Field Theory in Condensed Matter Physics*. Cambridge University Press, 2003.

[14] M. Mancini. Fermionization of Spin Systems. Master's thesis, Università degli studi di Perugia, Facoltà di Scienze Matematiche, Fisiche e Naurali, 2008.

[15] J. E. Hirsch. Charge-Density-Wave to Spin-Density-Wave Transition in the Extended Hubbard Model. *Phys. Rev. Lett.*, 53:2327–2330, 1984.

[16] P. G. J. van Dongen. Extended Hubbard model at strong coupling. *Phys. Rev. B*, 49:7904–7915, 1993.

[17] R. T. Clay, A. W. Sandvik, and D. K. Campbell. Possible exotic phases in the one-dimensional extended Hubbard model. *Phys. Rev. B*, 59:4665–4679, 1999.

[18] M. Tsuchiizu and A. Furusaki. Phase Diagram of the One-Dimensional Extended Hubbard Model at Half Filling. *Phys. Rev. Lett*, 88:056402, 2002.

[19] E. Jeckelmann. Ground-State Phase Diagram of a Half-Filled One-Dimensional Extended Hubbard Model. *Phys. Rev. Lett*, 89:236401, 2002.

[20] P. Sengupta, A. W. Sandvik, and D. K. Campbell. Bond-order-wave phase and quantum phase transitions in the one-dimensional extended Hubbard model. *Phys. Rev. B*, 65:155113, 2002.

[21] A. W. Sandvik, L. Balents, and D. K. Campbell. Ground State Phases of the Half-Filled One-Dimensional Extended Hubbard Model. *Phys. Rev. Lett.*, 92:236401, 2004.

[22] S.-J. Gu, S.-S. Deng, Y.-Q. Li, and H.-Q. Lin. Entanglement and Quantum Phase Transition in the Extended Hubbard Model. *Phys. Rev. Lett.*, 93:086402, 2004.

[23] S. Ejima and S. Nishimoto. Phase Diagram of the One-Dimensional Half-Filled Extended Hubbard Model. *Phys. Rev. Lett.*, 99:216403, 2007.

[24] F. Iemini, T. O. Maciel, and R. O. Vianna. Entanglement of indistinguishable particles as a probe for quantum phase transitions in the extended Hubbard model. *Phys. Rev. B*, 92:075423, 2015.

[25] M. Nakamura. Tricritical Behavior in the Extended Hubbard Chains. *Phys. Rev. B*, 61:16377–16392, 2000.

[26] M. Di Dio, L. Barbiero, A. Recati, and M. Dalmonte. Spontaneous Peierls dimerization and emergent bond order in one-dimensional dipolar gases. *Phys. Rev. A*, 90:063608, 2014.

[27] L. Arrachea and A. A. Aligia. Exact Solution of a Hubbard Chain with Bond-Charge Interaction. *Phys. Rev. Lett.*, 73:2240–2243, 1994.

[28] A. Schadschneider. Superconductivity in an exactly solvable hubbard model with bond-charge interaction. *Phys. Rev. B*, 51:10386–10391, 1995.

[29] A. A. Aligia, A. Anfossi, L. Arrachea, C. Degli Esposti Boschi, A. O. Dobry, C. Gazza, A. Montorsi, F. Ortolani, and M. E. Torio. Incommensurability and Unconventional Superconductor to Insulator Transition in the Hubbard Model with Bond-Charge Interaction. *Phys. Rev. Lett.*, 99:206401, 2007.

[30] M. E. Simón and A. A. Aligia. Brinkman-Rice transition in layered perovskites. *Phys. Rev. B*, 48:7471–7477, 1993.

[31] A. A. Aligia, L. Arrachea, and E. R. Gagliano. Phase diagram of an extended hubbard model with correlated hopping at half filling. *Phys. Rev. B*, 51:13774–13777, 1995.

[32] J. I. Japaridze and A. P. Kampf. Weak-coupling phase diagram of the extended hubbard model with correlated-hopping interaction. *Phys. Rev. B*, 59:12822–12829, 1999.

[33] G. Japaridze and E. Müller-Hartmann. Electrons with correlated hopping interaction in one dimension. *Ann. Phys. (Berlin)*, 3:163–180, 1994.

[34] D. Rossini, V. Lante, A. Parola, and F. Becca. Phase diagram of hard-core bosons on a zigzag ladder. *Phys. Rev. B*, 83:155106, 2011.

[35] M. Capello, F. Becca, M. Fabrizio, and S. Sorella. Superfluid to Mott-Insulator Transition in Bose-Hubbard Models. *Phys. Rev. Lett.*, 99:056402, 2007.

[36] B. Capogrosso-Sansone, Ş. G. Söyler, N. Prokof'ev, and B. Svistunov. Monte Carlo study of the two-dimensional Bose-Hubbard model. *Phys. Rev. A*, 77:015602, 2008.

[37] B. Capogrosso-Sansone, N. V. Prokof'ev, and B. V. Svistunov. Phase diagram and thermodynamics of the three-dimensional Bose-Hubbard model. *Phys. Rev. B*, 75:134302, 2007.

[38] K. G. Wilson. Renormalization Group and Critical Phenomena. I. Renormalization Group and the Kadanoff Scaling Picture. *Phys. Rev. B*, 4:3174–3183, 1971.

[39] K. G. Wilson. Renormalization Group and Critical Phenomena. II. Phase-Space Cell Analysis of Critical Behavior. *Phys. Rev. B*, 4:3184–3205, 1971.

[40] L. D. Landau and E. M. Lifshitz. *Statistical Physics*. Pergamon Press, 3 edition, 1980.

[41] B. Simons. Phase Transitions and Collective Phenomena. Lecture Notes, University of Cambridge, 1997.

[42] G. Morandi, F. Napoli, and E. Ercolessi. *Statistical Mechanics: An Intermediate Course*. World Scientific, 2 edition, 2001.

[43] C. Di Castro and R. Rimondi. *Statistical Mechanics and Applications in Condensed Matter*. Cambridge University Press, 2015.

[44] M. Vojta. Quantum phase transitions. *Rep. Prog. Phys.*, 66:2069–2110, 2003.

[45] S. Sachdev. *Quantum Phase Transitions*. Cambridge University Press, 2 edition, 2011.

[46] J. Tsuda, Y. Yamanaka, and H. Nishimori. Energy Gap at First-Order Quantum Phase Transitions: An Anomalous Case. *J. Phys. Soc. Jpn*, 82:114004, 2013.

[47] N. Mermin and H. Wagner. Absence of Ferromagnetism or Antiferromagnetism in One- or Two-Dimensional Isotropic Heisenberg Models. *Phys Rev. Lett.*, 17:1133–1136, 1966.

[48] F. D. M. Haldane. Nonlinear Field Theory of Large-Spin Heisenberg Antiferromagnets: Semiclassically Quantized Solitons of the One-Dimensional Easy-Axis Néel State. *Phys Rev. Lett.*, 50:1153–1156, 1983.

[49] M. den Nijs and K. Rommelse. Preroughening transitions in crystal surfaces and valence-bond phases in quantum spin chains. *Phys Rev. B*, 40:4709–4734, 1989.

[50] E. G. Dalla Torre, E. Berg, and E. Altman. Hidden Order in 1D Bose Insulators. *Phys. Rev. Lett.*, 97:260401, 2006.

[51] E. Berg, E. G. Dalla Torre, T. Giamarchi, and E. Altman. Rise and fall of hidden string order of lattice bosons. *Phys. Rev. B*, 77:245119, 2008.

[52] A. Montorsi and M. Roncaglia. Nonlocal Order Parameters for the 1D Hubbard Model. *Phys. Rev. Lett.*, 109:236404, 2012.

[53] L. Barbiero, A. Montorsi, and M. Roncaglia. How hidden orders generate gaps in one-dimensional fermionic systems. *Phys. Rev. B*, 88:035109, 2013.

[54] F. Dolcini and A. Montorsi. Quantum phases of one-dimensional Hubbard models with three- and four-body couplings. *Phys. Rev. B*, 88:115115, 2013.

[55] X. Chen, Z.-C. Gu, and X.-G. Wen. Classification of gapped symmetric phases in one-dimensional spin systems. *Phys. Rev. B*, 83:035107, 2011.

[56] X. Chen, Z.-C. Gu, and X.-G. Wen. Complete classification of one-dimensional gapped quantum phases in interacting spin systems. *Phys. Rev. B*, 84:235128, 2011.

[57] Z.-C. Gu and X.-G. Wen. Symmetry-protected topological orders for interacting fermions: Fermionic topological nonlinear σ models and a special group supercohomology theory. *Phys. Rev. B*, 90:115141, 2014.

[58] F. D. M. Haldane. Continuum dynamics of the 1-D Heisenberg antiferromagnet: Identification with the O(3) nonlinear sigma model. *Phys. Lett. A*, 93:464–468, 1983.

[59] I. Affleck, T. Kennedy, E. H. Lieb, and H. Tasaki. Rigorous results on valence-bond ground states in antiferromagnets. *Phys. Rev. Lett.*, 59:799–802, 1987.

[60] C. L. Kane and E. J. Mele. Quantum Spin Hall Effect in Graphene. *Phys. Rev. Lett.*, 95:226801, 2005.

[61] C. L. Kane and E. J. Mele. Z_2 Topological Order and the Quantum Spin Hall Effect. *Phys. Rev. Lett.*, 95:146802, 2005.

[62] B. A. Bernevig and S.-C. Zhang. Quantum Spin Hall Effect. *Phys. Rev. Lett.*, 96:106802, 2006.

[63] L. Fu, C. L. Kane, and E. J. Mele. Topological Insulators in Three Dimensions. *Phys. Rev. Lett.*, 98:106803, 2007.

[64] J. E. Moore and L. Balents. Topological invariants of time-reversal-invariant band structures. *Phys. Rev. B*, 75:121306, 2007.

[65] X.-L. Qi, T. Hughes, and S.-C. Zhang. Topological field theory of time-reversal invariant insulators. *Phys. Rev. B*, 78:195424, 2008.

[66] A. Altland and M. R. Zirnbauer. Nonstandard symmetry classes in mesoscopic normal-superconducting hybrid structures. *Phys. Rev. B*, 55:1142–1161, 1997.

[67] A. P. Schnyder, S. Ryu, A. Furusaki, , and A. W. W. Ludwig. Classification of topological insulators and superconductors in three spatial dimensions. *Phys. Rev. B*, 78:195125, 2008.

[68] A. Kitaev. Periodic table for topological insulators and superconductors. *AIP Conf. Proc.*, 1134:22–30, 2009.

[69] X.-G. Wen. Symmetry-protected topological phases in noninteracting fermion systems. *Phys. Rev. B*, 85:085103, 2012.

[70] F. Verstraete, J. I. Cirac, J. I. Latorre, E. Rico, and M. M. Wolf. Renormalization-Group Transformations on Quantum States. *Phys. Rev. Lett.*, 94:140601, 2005.

[71] L. Fidkowski and A. Kitaev. Effects of interactions on the topological classification of free fermion systems. *Phys. Rev. B*, 81:134509, 2010.

[72] L. Fidkowski and A. Kitaev. Topological phases of fermions in one dimension. *Phys. Rev. B*, 83:075103, 2011.

[73] D. Pérez-García, M. Wolf, M. Sanz, F. Verstraete, and J. I. Cirac. String Order and Symmetries in Quantum Spin Lattices. *Phys. Rev. Lett.*, 100:167202, 2008.

[74] J. Haegeman, D. Pérez-García, I. Cirac, and N. Schuch. Order Parameter for Symmetry-Protected Phases in One Dimension. *Phys. Rev. Lett.*, 109:050402, 2012.

[75] F. Pollmann and A. M. Turner. Detection of symmetry-protected topological phases in 1D. *Phys. Rev. B*, 86:125441, 2012.

[76] A. Keselman and E. Berg. Gapless symmetry-protected topological phase of fermions in one dimension. *Phys. Rev. B*, 91:235309, 2015.

[77] N. Kainaris and Sam T. Carr. Emergent topological properties in interacting one-dimensional systems with spin-orbit coupling. *Phys. Rev. B*, 92:035139, 2015.

[78] A. Montorsi, F. Dolcini, R. Iotti, and F. Rossi. Symmetry protected topological phases of 1D interacting fermions with spin-charge separation. *Phys Rev. B*, 95:245108, 2017.

[79] J. Sólyom. *Fundamentals of the Physics of Solids. Volume 3 - Normal, Broken-Symmetry, and Correlated Systems*. Springer, 2010.

[80] A. O. Gogolin, A. A. Nersesyan, and A. M. Tsvelik. *Bosonization and Strongly Correlated Systems*. Cambridge University Press, 1998.

[81] T. Giamarchi. *Quantum Physics in One Dimension*. Oxford University Press, 2003.

[82] J. von Delft and H. Schoeller. Bosonization for Beginners — Refermionization for Experts. *Annalen Phys.*, 7:225–305, 1998.

[83] S. Rao and D. Sen. An Introduction To Bosonization And Some Of Its Applications. In S. Rao, editor, *Field Theories in Condensed Matter Physics. Texts and Readings in Physical Sciences*, pages 239–333. Hindustan Book Agency, 2001.

[84] E. Miranda. Introductin to Bosonization. *Braz. J. Phys.*, 33:3–35, 2003.

[85] C. Mocanu. Bosonization of dimerized spinless-fermion and Hubbard chains. Master's thesis, Universität Augsburg, arXiv:cond-mat/0505238, 2005.

[86] D. Sénćhal. An introduction to bosonization. In D. Sénćhal, A. M. S. Tremblay, and C. Bourbonnais, editors, *Theoretical Methods for Strongly Correlated Electrons*, pages 139–186. Springer, 2004.

[87] J. Dai, X. Feng, T. Xiang, and Y. Yu. Gapped spin-liquid states in a one-dimensional Hubbard model with antiferromagnetic exchange interaction. *Phy. Rev. B*, 70:064518, 2004.

[88] X. Huang, E. Szirmai, F. Gebhard, J. Sólyom, , and R. M. Noack. Phase diagram of the t-U-J_1-J_2 chain at half filling. *Phys. Rev. B*, 78:085128, 2008.

[89] H. Ding and Y. Wang. Effect of correlated-hopping interaction on a one-dimensional extended Hubbard model with spin-exchange interaction. *Mod. Phys. Lett. B*, 26:1150044, 2012.

[90] H. Ding and J. Zhang. Phase diagram of one-dimensional *t*-*U*-*J* model with anisotropic antiferromagnetic exchange. *Mod. Phys. Lett. B*, 24:2769–2783, 2010.

[91] M. Malard. Sine-Gordon Model: Renormalization Group Solution and Applications. *Braz. J. Phys.*, 43:182–198, 2013.

[92] S. R. White. Density Matrix Formulation for Quantum Renormalization Groups. *Phys. Rev. Lett.*, 69:2863–2866, 1992.

[93] S. R. White. Density-matrix algorithms for quantum renormalization groups. *Phys. Rev. B*, 48:10345–10356, 1993.

[94] U. Schollwöck. The density-matrix renormalization group. *Rev. Mod. Phys.*, 77:259–315, 2005.

[95] G. De Chiara, M. Rizzi, D. Rossini, and S. Montangero. Density Matrix Renormalization Group for Dummies. *J. Comput. Theor. Nanos.*, 5:1277–1288, 2008.

[96] F. Becca and S. Sorella. *Quantum Monte Carlo Approaches for Correlated Systems*. Cambridge University Press, 2017.

[97] N. Trivedi and D. M. Ceperley. Ground-state correlations of quantum antiferromagnets: A Green-function Monte Carlo study. *Phys. Rev. B*, 41:4552–4569, 1990.

[98] M. Calandra Buonaura and Sandro Sorella. Numerical study of the two-dimensional heisenberg model using a Green function Monte Carlo technique with a fixed number of walkers. *Phys. Rev. B*, 57:11446–11456, 1998.

[99] I. Bloch, J. Dalibard, and W. Zwerger. Many-body physics with ultracold gases. *Rev. Mod. Phys.*, 80:885–964, 2008.

[100] M. Di Liberto, C. E. Creffield, G. I. Japaridze, and C. Morais Smith. Quantum simulation of correlated-hopping models with fermions in optical lattices. *Phys. Rev. A*, 89:013624, 2014.

[101] D. Jaksch, C. Bruder, J. I. Cirac, C. W. Gardiner, and P. Zoller. Cold Bosonic Atoms in Optical Lattices. *Phys. Rev. Lett.*, 81:3108–3111, 1998.

[102] M. Greiner, O. Mandel, T. Esslinger, T. W. Hänsch, and I. Bloch. Quantum phase transition from a superfluid to a mott insulator in a gas of ultracold atoms. *Nature*, 415:39–44, 2002.

[103] Michael Köhl, Henning Moritz, Thilo Stöferle, Kenneth Günter, , and Tilman Esslinger. Fermionic Atoms in a Three Dimensional Optical Lattice: Observing Fermi Surfaces, Dynamics, and Interactions. *Phys. Rev. Lett.*, 94:080403, 2005.

[104] Robert Jördens, Niels Strohmaier, Kenneth Günter, Henning Moritz, and Tilman Esslinger. A Mott insulator of fermionic atoms in an optical lattice. *Nature*, 455:2014–207, 2008.

[105] S. Baier, M. J. Mark, D. Petter, K. Aikawa, L. Chomaz, Zi Cai, M. Baranov, P. Zoller, , and F. Ferlaino. Extended Bose-Hubbard models with ultracold magnetic atoms. *Science*, 352:201–205, 2016.

[106] K. Aikawa, A. Frisch, M. Mark, S. Baier, R. Grimm, and F. Ferlaino. Reaching fermi degeneracy via universal dipolar scattering. *Phys. Rev. Lett.*, 112:010404, 2014.

[107] M. Endres. *Probing Correlated Quantum Many-Body Systems at the Single-Particle Level.* PhD thesis, Ludwig Maximilian University of Munich, Germany, 2013.

[108] M. Endres, M. Cheneau, T. Fukuhara, C. Weitenberg, P. Schauß, C. Gross, L. Mazza, M. C. Banuls, L. Pollet, I. Bloch, and S. Kuhr. Observation of Correlated Particle-Hole Pairs and String Order in Low-Dimensional Mott Insulators. *Science*, 334:200–203, 2011.

[109] M. Boll, T. A. Hilker, G. Salomon, A. Omran, I. Bloch, and C. Gross. Spin- and density-resolved microscopy of antiferromagnetic correlations in Fermi-Hubbard chains. *Science*, 353:1257–1260, 2016.

[110] T. A. Hilker, G. Salomon, F. Grusdt, A. Omran, M. Boll, E. Demler, I. Bloch, and C. Gross. Revealing hidden antiferromagnetic correlations in doped Hubbard chains via string correlators. *Science*, 357:484–487, 2017.

[111] L. Barbiero, S. Fazzini, and A. Montorsi. Non-local order parameters as a probe for phase transitions in the extended Fermi-Hubbard model. *Eur. Phys. J. Special Topics*, 226:2697–2704, 2017.

[112] H. G. Keiss. *Conjugated Conducting Polymers.* Springer-Verlag, 1992.

[113] T. Ishiguro and K. Yamaji. *Organic Superconductors.* Springer-Verlag, 1990.

[114] V. J. Emery, S. A. Kivelson, and O. Zachar. Spin-gap proximity effect mechanism of high-temperature superconductivity. *Phys. Rev. B*, 56:6120–6147, 1997.

[115] H. Q. Lin and J. E. Hirsch. Condensation transition in the one-dimensional extended Hubbard model. *Phys. Rev. B*, 33:8155–8163, 1986.

[116] J. W. Cannon and E. Fradkin. Phase diagram of the extended Hubbard model in one spatial dimension. *Phys. Rev. B*, 41:9435–9443, 1990.

[117] K. Penc and F. Mila. Phase diagram of the one-dimensional extended Hubbard model with attractive and/or repulsive interactions at quarter filling. *Phys. Rev. B*, 49:9670–9678, 1994.

[118] M. Nakamura. Mechanism of CDW-SDW Transition in One Dimension. *J. Phys. Soc. Jpn.*, 68:3123–3126, 1999.

[119] M. Tsuchiizu and A. Furusaki. Ground-state phase diagram of the one-dimensional half-filled extended Hubbard model. *Phys. Rev. B*, 69:035103, 2004.

[120] M. Dalmonte, J. Carrasquilla, L. Taddia, E. Ercolessi, and M. Rigol. Gap scaling at Berezinskii-Kosterlitz-Thouless quantum critical points in one-dimensional Hubbard and Heisenberg models. *Phys. Rev. B*, 91:165136, 2015.

[121] G.G. Batrouni, R.T. Scalettar, V. G. Rousseau, and B. Grémaud. Competing Supersolid and Haldane Insulator Phases in the Extended One-Dimensional Bosonic Hubbard Model. *Phys. Rev. Lett.*, 110:265303, 2013.

[122] M. Lu, N. Q. Burdick, S. H. Youn, and B.L. Lev. Strongly dipolar Bose-Einstein condensate of dysprosium. *Phys. Rev. Lett.*, 107:190401, 2011.

[123] J. W. Park, S. A. Will, and M. W. Zwierlein. Ultracold dipolar gas of fermionic ^{23}Na^{40}K molecules in their absolute ground state. *Phys. Rev. Lett.*, 114:205302, 2015.

[124] M. F. Parsons, A. Mazurenko, C.S. Chiu, G. Ji, D. Greif, and M. Greiner. Site-resolved measurement of the spin-correlation function in the fermi-hubbard model. *Science*, 353:1253–1256, 2016.

[125] F. Meinert, M. J. Mark, K. Lauber, A. J. Daley, and H.-C. Nägerl. Floquet Engineering of Correlated Tunneling in the Bose-Hubbard Model with Ultracold Atoms. *Phys. Rev. Lett.*, 116:205301, 2016.

[126] S. Fazzini, L. Barbiero, and A. Montorsi. Low energy quantum regimes of 1D dipolar Hubbard model with correlated hopping. *J. Phys.: Conf. Ser.*, 841:012016, 2017.

[127] S. Fazzini, A. Montorsi, M. Roncaglia, and L. Barbiero. Hidden Magnetism in Periodically Modulated One Dimensional Dipolar Fermions. *New J. Phys.*, 19:123008, 2017.

[128] L. Arrachea, A. A. Aligia, E. Gagliano, K. Hallberg, and C. Balseiro. Superconducting correlations in Hubbard chains with correlated hopping. *Phys. Rev. B*, 50:16044–16051, 1994.

[129] L. Arrachea, E. R. Gagliano, and A. A. Aligia. Ground-state phase diagram of an extended Hubbard chain with correlated hopping at half-filling. *Phys. Rev. B*, 55:1173–1184, 1997.

[130] F. Dolcini and A. Montorsi. Integrable extended Hubbard hamiltonians from symmetric group equations. *Int. J. Mod. Phys. B*, 14:1719–1728, 2000.

[131] R. Citro, E. Orignac, S. De Palo, and M. L. Chiofalo. Evidence of Luttinger liquid behavior in one-dimensional dipolar quantum gases. *Phys. Rev. A*, 75:051602(R), 2007.

[132] J. Otterbach, M. Moos, D. Muth, and M. Fleischhauer. Wigner Crystallization of Single Photons in Cold Rydberg Ensembles. *Phys. Rev. Lett.*, 110:156402, 2013.

[133] M. Dalmonte, G. Pupillo, and P. Zoller. One-dimensional quantum liquids with power-law interactions: The Luttinger staircase. *Phys. Rev. Lett.*, 105:140401, 2010.

[134] S. Capponi, D. Poilblanc, and T. Giamarchi. Effects of long-range electronic interactions on a one-dimensional electron system. *Phys. Rev. B*, 61:13410, 2000.

[135] A.O. Dobry and A.A. Aligia. Quantum phase diagram of the half filled hubbard model with bond-charge interaction. *Nucl. Phys. B*, 843:767, 2011.

[136] D. Rossini and R. Fazio. Phase diagram of the extended Bose–Hubbard model. *New J. Phys.*, 14:065012, 2012.

[137] X. Deng, R. Citro, E. Orignac, A. Minguzzi, , and L. Santos. Polar bosons in one-dimensional disordered optical lattices. *Phys. Rev. B*, 87:195101, 2013.

[138] X. Deng A. Rapp and L. Santos. Ultracold lattice gases with periodically modulated interactions. *Phys. Rev. Lett*, 109:203005, 2012.

[139] M. Grifoni and P. Hanggi. Driven quantum tunneling. *Phys. Rep.*, 304:229–, 1998.

[140] A. Eckardt, C. Weiss, and M. Holthaus. Superfluid-insulator transition in a periodically driven optical lattice. *Phys. Rev. Lett*, 95:260404, 2005.

[141] H. Sambe. Steady states and quasienergies of a quantum-mechanical system in an oscillating field. *Phys. Rev. A*, 7:2203, 1973.

[142] M. Dalmonte, M. Di Dio, L. Barbiero, and F. Ortolani. Homogeneous and inhomogeneous magnetic phases of constrained dipolar bosons. *Phys. Rev. B*, 83:155110, 2011.

[143] K. Kobayashi, M. Okumura, Y. Ota, S. Yamada, and M. Machida. Nontrivial Haldane Phase of an Atomic Two-Component Fermi Gas Trapped in a 1D Optical Lattice. *Phys. Rev. Lett.*, 109:235302, 2012.

[144] I. Cohen and A. Retzker. Proposal for Verification of the Haldane Phase Using Trapped Ions. *Phys. Rev. Lett.*, 112:040503, 2014.

[145] R. M. W. van Bijnen and T. Pohl. Quantum Magnetism and Topological Ordering via Rydberg Dressing near Förster Resonances. *Phys. Rev. Lett.*, 114:243002, 2015.

[146] A. Eckardt. Colloquium: Atomic quantum gases in periodically driven optical lattices. *Rev. Mod. Phys.*, 89:011004, 2017.

[147] A. Frisch, M. Mark, K. Aikawa, F. Ferlaino, J. L. Bohn, C. Makrides, A. Petrov, and S. Kotochigova. Quantum chaos in ultracold collisions of gas-phase erbium atoms. *Nature*, 507:475–479, 2014.

[148] P. Bordia, H. Lüschen, U. Schneider, M. Knap, and Immanuel Bloch. Periodically Driving a Many-Body Localized Quantum System. *Nat. Phys.*, 13:460–464, 2017.

[149] S. P. Rath, W. Simeth, M. Endres, and W. Zwerger. Non-local order in Mott insulators, Duality and Wilson loops. *Ann. Phys.*, 334:256–271, 2013.

[150] S. Fazzini, F. Becca, and A. Montorsi. Nonlocal Parity Order in the Two-Dimensional Mott Insulator. *Phys. Rev. Lett.*, 118:157602, 2017.

[151] C. Degli Esposti Boschi, A. Montorsi, and M. Roncaglia. Brane parity orders in the insulating state of Hubbard ladders. *Phys. Rev. B*, 94:085119, 2016.

[152] M. Oshikawa. Hidden $Z_2 * Z_2$ symmetry in quantum spin chains with arbitrary integer spin. *J. Phys. Condens. Matter*, 4:7469–7488, 1992.

[153] S. Qin, J. Lou, L. Sun, and C. Chen. Nonlocal Topological Order in Antiferromagnetic Heisenberg Chains. *Phys. Rev. Lett.*, 90:067202, 2003.

[154] M. Capello, F. Becca, M. Fabrizio, and S. Sorella. Superfluid to Mott-Insulator Transition in Bose-Hubbard models. *Phys. Rev. Lett.*, 99:056402, 2007.

[155] B. Capogrosso-Sansone, S. G. Söyler, N. Prokof'ev, and B. Svistunov. Monte Carlo study of the two-dimensional Bose-Hubbard model. *Phys. Rev. A*, 77:015602, 2008.

[156] B. Zeng, X. Chen, D.-L-Zhou, and X.-G. Wen. Quantum Information Meets Quantum Matter. From Quantum Entanglement to Topological Phase in Many-Body Systems. *arXiv:1508.02595v3*, 2016.

[157] G. I. Japaridze and E. Müller-Hartmann. Triplet superconductivity in a one-dimensional ferromagnetic $t - J$ model. *Phys. Rev. B*, 61:9019–9027, 2000.

[158] V. Gritsev, G. Japaridze, M. Pletyukhov, and D. Baeriswyl. Competing Effects of Interactions and Spin-Orbit Coupling in a Quantum Wire. *Phys. Rev. Lett.*, 94:137207, 2005.

Appendix A

Fermionic and (pseudo)spin operators under different formalisms

Here we introduce different formalisms to express the states (1.22) and the creation and annihilation operators in order to better understand the properties of the local Hilbert space and the relation with spin formalism. In this part we will deal with local operators only and we will omit the site index.

A.1 Matrix expressions for local states and fermion operators

The four states (1.22) that form a basis for the local Hilbert space can be expressed as 4-dimensional vectors

$$
|0\rangle = \begin{pmatrix} 1 \\ 0 \\ 0 \\ 0 \end{pmatrix}, \quad |\uparrow\rangle = \begin{pmatrix} 0 \\ 1 \\ 0 \\ 0 \end{pmatrix}, \quad |\downarrow\rangle = \begin{pmatrix} 0 \\ 0 \\ 1 \\ 0 \end{pmatrix}, \quad |\uparrow\downarrow\rangle = \begin{pmatrix} 0 \\ 0 \\ 0 \\ 1 \end{pmatrix}. \quad \text{(A.1)}
$$

Then the operators acting on these states can be written as 4×4 matrices. In particular, the creation and annihilation operators for each species read

$$c_\uparrow^\dagger = \begin{pmatrix} 0 & 0 & 0 & 0 \\ 1 & 0 & 0 & 0 \\ 0 & 0 & 0 & 0 \\ 0 & 0 & 1 & 0 \end{pmatrix}, \quad c_\uparrow = \begin{pmatrix} 0 & 1 & 0 & 0 \\ 0 & 0 & 0 & 0 \\ 0 & 0 & 0 & 1 \\ 0 & 0 & 0 & 0 \end{pmatrix} \qquad (A.2)$$

$$c_\downarrow^\dagger = \begin{pmatrix} 0 & 0 & 0 & 0 \\ 0 & 0 & 0 & 0 \\ 1 & 0 & 0 & 0 \\ 0 & -1 & 0 & 0 \end{pmatrix}, \quad c_\downarrow = \begin{pmatrix} 0 & 0 & 1 & 0 \\ 0 & 0 & 0 & -1 \\ 0 & 0 & 0 & 0 \\ 0 & 0 & 0 & 0 \end{pmatrix} \qquad (A.3)$$

and the particle number operators are

$$n_\uparrow = c_\uparrow^\dagger c_\uparrow = \begin{pmatrix} 0 & 0 & 0 & 0 \\ 0 & 1 & 0 & 0 \\ 0 & 0 & 0 & 0 \\ 0 & 0 & 0 & 1 \end{pmatrix}, \quad n_\downarrow = c_\downarrow^\dagger c_\downarrow = \begin{pmatrix} 0 & 0 & 0 & 0 \\ 0 & 0 & 0 & 0 \\ 0 & 0 & 1 & 0 \\ 0 & 0 & 0 & 1 \end{pmatrix}. \qquad (A.4)$$

A.1.1 Matrix expressions for spins and pseudospins

This formalism can be used to clarify the action of the spin operators (1.30). One can easily see that the following expressions are valid

$$S^{(s),+} = c_\uparrow^\dagger c_\downarrow = \begin{pmatrix} 0 & 0 & 0 & 0 \\ 0 & 0 & 1 & 0 \\ 0 & 0 & 0 & 0 \\ 0 & 0 & 0 & 0 \end{pmatrix}, \quad S^{(s),-} = c_\downarrow^\dagger c_\uparrow = \begin{pmatrix} 0 & 0 & 0 & 0 \\ 0 & 0 & 0 & 0 \\ 0 & 1 & 0 & 0 \\ 0 & 0 & 0 & 0 \end{pmatrix} \qquad (A.5)$$

$$S^{(s),x} = \frac{S^{(s),+} + S^{(s),-}}{2} = \frac{1}{2}\begin{pmatrix} 0 & 0 & 0 & 0 \\ 0 & 0 & 1 & 0 \\ 0 & 1 & 0 & 0 \\ 0 & 0 & 0 & 0 \end{pmatrix} \qquad (A.6)$$

$$S^{(s),y} = \frac{S^{(s),+} - S^{(s),-}}{2\iota} = \frac{1}{2}\begin{pmatrix} 0 & 0 & 0 & 0 \\ 0 & 0 & -\iota & 0 \\ 0 & \iota & 0 & 0 \\ 0 & 0 & 0 & 0 \end{pmatrix} \tag{A.7}$$

$$S^{(s),z} = \frac{1}{2}(n_\uparrow - n_\downarrow) = \frac{1}{2}\begin{pmatrix} 0 & 0 & 0 & 0 \\ 0 & 1 & 0 & 0 \\ 0 & 0 & -1 & 0 \\ 0 & 0 & 0 & 0 \end{pmatrix}. \tag{A.8}$$

Now it is clear that these spin operators act with non-zero entries only on the subspace spanned by the two states $|\uparrow\rangle$ and $|\downarrow\rangle$. Indeed the first and the last columns/rows are null vectors. We also observe that the 2×2 central blocks of these matrices turn out to be the Pauli matrices.

While the spin representation of $SU(2)$ acts only on the spin degrees of freedom, we analogously expect that the pseudospin representation of $SU(2)$ (1.37) acts only on the charge degrees of freedom, i.e. on the subspace spanned by the two states $|0\rangle$ and $|\uparrow\downarrow\rangle$. In fact, the matrix representations of the charge operators are the following

$$S^{(c),+} = (-)^j \begin{pmatrix} 0 & 0 & 0 & 0 \\ 0 & 0 & 0 & 0 \\ 0 & 0 & 0 & 0 \\ 1 & 0 & 0 & 0 \end{pmatrix}, \quad S^{(c),-} = (-)^j \begin{pmatrix} 0 & 0 & 0 & 1 \\ 0 & 0 & 0 & 0 \\ 0 & 0 & 0 & 0 \\ 0 & 0 & 0 & 0 \end{pmatrix} \tag{A.9}$$

$$S^{(c),x} = \frac{S^{(c),+} + S^{(c),-}}{2} = \frac{(-)^j}{2}\begin{pmatrix} 0 & 0 & 0 & 1 \\ 0 & 0 & 0 & 0 \\ 0 & 0 & 0 & 0 \\ 1 & 0 & 0 & 0 \end{pmatrix} \tag{A.10}$$

$$S^{(c),y} = \frac{S^{(c),+} - S^{(c),-}}{2\iota} = \frac{(-)^j}{2}\begin{pmatrix} 0 & 0 & 0 & \iota \\ 0 & 0 & 0 & 0 \\ 0 & 0 & 0 & 0 \\ -\iota & 0 & 0 & 0 \end{pmatrix} \tag{A.11}$$

$$S^{(c),z} = \frac{1}{2}(n_\uparrow + n_\downarrow - 1) = \frac{1}{2}\begin{pmatrix} -1 & 0 & 0 & 0 \\ 0 & 0 & 0 & 0 \\ 0 & 0 & 0 & 0 \\ 0 & 0 & 0 & 1 \end{pmatrix} \tag{A.12}$$

and we can see that they have non-zero elements only on the first and the last columns/rows.

A.2   Hubbard operators

Sometimes it is useful to write the fermion operators in terms of projectors onto the local basis states. These are the Hubbard operators. The local projector from a state $|\beta\rangle$ to a state $|\alpha\rangle$ can be represented as

$$X^{\alpha\beta} = |\alpha\rangle\langle\beta| \, . \tag{A.13}$$

Then the creation and annihilation operators can be rewritten in the following way

$$
\begin{aligned}
c_\sigma^\dagger &= X^{\sigma 0} + \sigma X^{2\bar{\sigma}} = |\sigma\rangle\langle 0| + \sigma|\uparrow\downarrow\rangle\langle\bar{\sigma}| \\
c_\sigma &= X^{0\sigma} + \sigma X^{\bar{\sigma}2} = |0\rangle\langle\sigma| + \sigma|\bar{\sigma}\rangle\langle\uparrow\downarrow|
\end{aligned} \tag{A.14}
$$

where the label 2 at the exponent indicates the state with two fermions and the coefficient σ assumes the value $+1$ for the up spin and the value -1 for the down spin.

We notice that in general the projector operators have the following property

$$X^{\alpha\beta}X^{\gamma\delta} = |\alpha\rangle\langle\beta|\gamma\rangle\langle\delta| = \delta_{\beta,\gamma}X^{\alpha\delta} \, . \tag{A.15}$$

When the states involved are those spanning the local Hilbert space of the Hubbard Hamiltonian, another important property holds:

$$X^{\uparrow\uparrow} + X^{\downarrow\downarrow} + X^{22} + X^{00} = 1 \, . \tag{A.16}$$

By using these properties, one can see that the local number operators are

$$
\begin{aligned}
n_\uparrow &= X^{\uparrow\uparrow} + X^{22} \\
n_\downarrow &= X^{\downarrow\downarrow} + X^{22} \\
n &= X^{\uparrow\uparrow} + X^{\downarrow\downarrow} + 2X^{22} = 1 + X^{22} - X^{00} \, .
\end{aligned} \tag{A.17}
$$

We finally give the inverse relations of (A.14) and (A.17)

$$
\begin{aligned}
X^{\sigma 0} &= (1 - n_{\bar{\sigma}}) c_{\sigma}^{\dagger} \\
X^{2\sigma} &= \bar{\sigma} n_{\sigma} c_{\bar{\sigma}}^{\dagger} \\
X^{\sigma\sigma} &= (1 - n_{\bar{\sigma}}) n_{\sigma} \\
X^{00} &= (1 - n_{\uparrow})(1 - n_{\downarrow}) \\
X^{22} &= n_{\uparrow} n_{\downarrow}
\end{aligned}
\tag{A.18}
$$

and observe that the Hubbard operators obey the following commutation rules

$$
[X^{ab}, X^{cd}]_{\pm} = X^{ad}\delta_{bc} \pm X^{cb}\delta_{ad}
\tag{A.19}
$$

where the plus sign denotes the anticommutator and has to be taken when both operators are fermionic, i.e. change the particle number by 1 (e.g. $X^{\sigma 0}$ or $X^{2\sigma}$). When acting on different lattice sites, the right hand side is zero.

A.2.1   Spin operators in terms of Hubbard operators

Using Hubbard operators is another way to identify immediately the subspace on which the spin (and pseudospin) operators act. Let's start with the spin sector. Here we get

$$
S^{(s),\alpha} = \frac{1}{2} \sum_{\sigma,\sigma'} \left(X^{\sigma 0} + \sigma X^{2\bar{\sigma}} \right) (\sigma^{\alpha})_{\sigma\sigma'} \left(X^{0\sigma'} + \sigma' X^{\bar{\sigma}'2} \right)
\tag{A.20}
$$

which implies

$$
\begin{aligned}
S^{(s),x} &= \frac{1}{2} \left[\left(X^{\uparrow 0} + X^{2\downarrow} \right) \left(X^{0\downarrow} - X^{\uparrow 2} \right) + \left(X^{\downarrow 0} - X^{2\uparrow} \right) \left(X^{0\uparrow} + X^{\downarrow 2} \right) \right] \\
&= \frac{1}{2} \left(X^{\uparrow\downarrow} + X^{\downarrow\uparrow} \right) \\
S^{(s),y} &= \frac{1}{2} \left[\left(X^{\uparrow 0} + X^{2\downarrow} \right) (-\imath) \left(X^{0\downarrow} - X^{\uparrow 2} \right) + \left(X^{\downarrow 0} - X^{2\uparrow} \right) (\imath) \left(X^{0\uparrow} + X^{\downarrow 2} \right) \right] \\
&= \frac{1}{2\imath} \left(X^{\uparrow\downarrow} - X^{\downarrow\uparrow} \right) \\
S^{(s),z} &= \frac{1}{2} \left[\left(X^{\uparrow 0} + X^{2\downarrow} \right) \left(X^{0\uparrow} + X^{\downarrow 2} \right) - \left(X^{\downarrow 0} - X^{2\uparrow} \right) \left(X^{0\downarrow} - X^{\uparrow 2} \right) \right] \\
&= \frac{1}{2} \left(X^{\uparrow\uparrow} - X^{\downarrow\downarrow} \right) .
\end{aligned}
\tag{A.21}
$$

From eqs. (A.21) we see that the spin operators depend only on the projectors on the states $|\uparrow\rangle$ and $|\downarrow\rangle$. For completeness we also give the expressions for $S^{(s),+}$ and $S^{(s),-}$

$$S^{(s),+} = X^{\uparrow\downarrow}, \quad S^{(s),-} = X^{\downarrow\uparrow} \tag{A.22}$$

In a similar manner we can verify that the charge (or pseudospin) operators can be expressed in terms of projectors on the states $|0\rangle$ and $|\uparrow\downarrow\rangle$ only:

$$
\begin{aligned}
S^{(c),+} &= \pm X^{20}, \quad S^{(c),-} = \pm X^{02} \\
S^{(c),x} &= \pm \frac{1}{2}\left(X^{20} + X^{02}\right) \\
S^{(c),y} &= \pm \frac{1}{2\iota}\left(X^{20} - X^{02}\right) \\
S^{(c),z} &= \frac{1}{2}\left(X^{22} - X^{00}\right)
\end{aligned}
\tag{A.23}
$$

where the plus sign refers to even sites and the minus sign refers to odd sites.

Appendix B

Derivation of bosonization formula and adding details to Chapter 3

B.1 Derivation of bosonization formula

Formula (3.19):

$$
\begin{aligned}
\phi(x) &= \frac{\iota}{\sqrt{2L}} \sum_{q>0} \frac{e^{-\alpha q/2}}{\sqrt{q}} \left(e^{-\iota qx} b_{qL} - e^{\iota qx} b_{qR} - e^{\iota qx} b_{qL}^{\dagger} + e^{-\iota qx} b_{qR}^{\dagger} \right) = \\
&= \iota \sum_{q>0} \frac{e^{-\alpha q/2}}{\sqrt{2qL}} \left[e^{-\iota qx} \left(b_{q}^{\dagger} + b_{-q} \right) - e^{\iota qx} \left(b_{-q}^{\dagger} + b_{q} \right) \right] = \\
&= \iota \left\{ \sum_{q>0} \frac{e^{-\alpha|q|/2}}{\sqrt{2|q|L}} e^{-\iota qx} \left(b_{q}^{\dagger} + b_{-q} \right) - \sum_{q<0} \frac{e^{-\alpha|q|/2}}{\sqrt{2|q|L}} e^{-\iota qx} \left(b_{q}^{\dagger} + b_{-q} \right) \right\} = \\
&= \iota \left\{ \sum_{q>0} \frac{e^{-\alpha|q|/2}}{\sqrt{2L}} \frac{\sqrt{|q|}}{q} e^{-\iota qx} \left(b_{q}^{\dagger} + b_{-q} \right) + \sum_{q<0} \frac{e^{-\alpha|q|/2}}{\sqrt{2L}} \frac{\sqrt{|q|}}{q} e^{-\iota qx} \left(b_{q}^{\dagger} + b_{-q} \right) \right\} = \\
&= \iota \sum_{q\neq0} \frac{e^{-\alpha|q|/2-\iota qx}}{q} \left(\frac{|q|}{2L} \right)^{1/2} \left(b_{q}^{\dagger} + b_{-q} \right)
\end{aligned}
$$

(B.1)

where in the second line we have used $b_{qL} = b_{-q}$.

Formula (3.28):

In order to derive the last equality in eq. (3.28), let us calculate the commutator:

$$[\varphi(x), \varphi^\dagger(y)] = -\sum_{qq'} \frac{e^{-\frac{\alpha}{2}(|q|+|q'|)-\imath qx - \imath q'y}}{2Lqq'} \sqrt{|qq'|} \underbrace{[b_{-q}, b_{q'}^\dagger]}_{\delta_{-q,q'}} =$$

$$= \frac{1}{2L} \sum_{q\neq 0} \frac{e^{-\alpha|q|-\imath q(x-y)}}{|q|} =$$

$$= \frac{1}{2L} \left\{ \sum_{q>0} \frac{e^{-\alpha q - \imath q(x-y)}}{q} + \sum_{q<0} \frac{e^{\alpha q - \imath q(x-y)}}{-q} \right\} = \tag{B.2}$$

$$= \frac{1}{2L} \sum_{q>0} \frac{e^{-\imath q(x-y-\imath\alpha)} + e^{\imath q(x-y+\imath\alpha)}}{q} =$$

$$= \frac{1}{4\pi} \left\{ \sum_n \frac{\left(e^{\imath\frac{2\pi}{L}(\imath\alpha+R)}\right)^n}{n} + \sum_n \frac{\left(e^{\imath\frac{2\pi}{L}(\imath\alpha-R)}\right)^n}{n} \right\} =$$

$$= \frac{1}{4\pi} \left\{ \sum_n \frac{z^n}{n} + \sum_n \frac{(z^\dagger)^n}{n} \right\}$$

where, in the last two lines, we have used $q = \frac{2\pi n}{L}$, $R = y - x$ and $z = e^{\imath\frac{2\pi}{L}(\imath\alpha+R)}$.
The series in eq. (B.2) converges to the logarithmic function

$$\sum_{n=1}^\infty \frac{z^n}{n} = -\ln(1-z) = \ln\frac{1}{1-z} \qquad \text{if } |z| = 1 \text{ and } z \neq 1. \tag{B.3}$$

Thus

$$[\varphi(x), \varphi^\dagger(y)] = -\frac{1}{4\pi} \ln\left(1 - e^{\imath\frac{2\pi}{L}(\imath\alpha+R)}\right) - \frac{1}{4\pi} \ln\left(1 - e^{\imath\frac{2\pi}{L}(\imath\alpha-R)}\right) =$$

$$\stackrel{L\to\infty}{=} -\frac{1}{4\pi} \ln\left(1 - 1 - \imath\frac{2\pi}{L}(\imath\alpha+R)\right) - \frac{1}{4\pi} \ln\left(1 - 1 - \imath\frac{2\pi}{L}(\imath\alpha-R)\right) =$$

$$= -\frac{1}{4\pi} \ln\left(-\imath\frac{2\pi}{L}(\imath\alpha+R)\right)\left(-\imath\frac{2\pi}{L}(\imath\alpha-R)\right) =$$

$$= -\frac{1}{4\pi} \ln\left(\left(\frac{2\pi}{L}\right)^2 (\alpha^2 + R^2)\right)$$

$$\tag{B.4}$$

and

$$e^{2\pi[\varphi(x),\varphi^\dagger(y)]} = e^{-\frac{1}{2}\ln\left[\left(\frac{2\pi}{L}\right)^2(\alpha^2+R^2)\right]} =$$

$$= \left[\left(\frac{2\pi}{L}\right)^2(\alpha^2+R^2)\right]^{-1/2} = \qquad\qquad (B.5)$$

$$= \frac{L}{2\pi}\frac{1}{\sqrt{\alpha^2+R^2}} \xrightarrow{\alpha\to 0} \frac{L}{2\pi R}.$$

In the special case $R=0$, eq. (B.2) becomes

$$[\varphi(x),\varphi^\dagger(x)] = \frac{1}{4\pi}\cdot 2\sum_n \frac{\left(e^{-\frac{2\pi\alpha}{L}}\right)^n}{n} =$$

$$= -\frac{1}{2\pi}\ln\left(1-e^{-\frac{2\pi\alpha}{L}}\right) \to \qquad\qquad (B.6)$$

$$\xrightarrow{L\to\infty} -\frac{1}{2\pi}\ln\left(\frac{2\pi\alpha}{L}\right)$$

and

$$e^{-2\pi[\varphi(x),\varphi^\dagger(x)]} = e^{\ln\left(\frac{2\pi\alpha}{L}\right)} = \frac{2\pi\alpha}{L} \qquad\qquad (B.7)$$

so that eq. (3.28) yields

$$e^{\imath\sqrt{4\pi}\phi(x)} =: e^{\imath\sqrt{4\pi}\phi(x)} : \frac{2\pi\alpha}{L} . \qquad\qquad (B.8)$$

Formula (3.31):

$$e^{\imath\sqrt{4\pi}[\phi(x+R)-\phi(x)]} = e^{\imath\sqrt{4\pi}[\phi(y)-\phi(x)]} =$$

$$= e^{\imath\sqrt{4\pi}[\varphi^\dagger(y)+\varphi(y)-\varphi^\dagger(x)-\varphi(x)]} =$$

$$= e^{\imath\sqrt{4\pi}[\varphi^\dagger(y)-\varphi^\dagger(x)]+\imath\sqrt{4\pi}[\varphi(y)-\varphi(x)]} =$$

$$= e^{\imath\sqrt{4\pi}[\varphi^\dagger(y)-\varphi^\dagger(x)]} e^{\imath\sqrt{4\pi}[\varphi(y)-\varphi(x)]} e^{2\pi[\varphi^\dagger(y)-\varphi^\dagger(x),\varphi(y)-\varphi(x)]} =$$

$$= : e^{\imath\sqrt{4\pi}[\phi(x+R)-\phi(x)]} : \underbrace{e^{-2\pi[\varphi(y)-\varphi(x),\varphi^\dagger(y)-\varphi^\dagger(x)]}}_{\downarrow}$$

$$\underbrace{e^{-2\pi[\varphi(y),\varphi^\dagger(y)]} e^{-2\pi[\varphi(x),\varphi^\dagger(x)]} e^{2\pi[\varphi(x),\varphi^\dagger(y)]} e^{2\pi[\varphi(y),\varphi^\dagger(x)]}}_{\frac{2\pi\alpha}{L}\frac{2\pi\alpha}{L}\frac{L}{2\pi R}\frac{L}{2\pi R}=\left(\frac{\alpha}{R}\right)^2} .$$

$$\qquad\qquad (B.9)$$

Formula (3.32):

$$[\phi(x), \theta(y)] = -\sum_{q,q'\neq 0} \frac{e^{-\frac{\alpha}{2}(|q|+|q'|)}e^{-\iota(qx+q'y)}}{q|q'|}\frac{\sqrt{|qq'|}}{2L}\underbrace{[b_q^\dagger + b_{-q}, b_{q'}^\dagger - b_{-q'}]}_{2\delta_{q',-q}} =$$

$$= -\frac{1}{L}\sum_{q\neq 0}\frac{e^{-\alpha|q|-\iota q(x-y)}}{q|q|}|q| =$$

$$= -\frac{1}{L}\sum_{q\neq 0}\frac{e^{-\alpha|q|+\iota qR}}{q} =$$

$$= -\frac{1}{L}\sum_{q>0}\frac{e^{-\alpha|q|+\iota qR}}{q} - \frac{1}{L}\sum_{q<0}\frac{e^{-\alpha|q|+\iota qR}}{q} =$$

$$= -\frac{1}{L}\sum_{q>0}\frac{e^{-\alpha|q|+\iota qR}}{q} + \frac{1}{L}\sum_{q>0}\frac{e^{-\alpha|q|-\iota qR}}{q} =$$

$$= -\frac{2\iota}{L}\sum_{q>0}\frac{e^{-\alpha|q|}}{q}\frac{e^{\iota qR}-e^{-\iota qR}}{2\iota} \rightarrow$$

$$\xrightarrow{L\to\infty} -\frac{2\iota}{L\Delta q}\int_0^\infty \frac{dq}{q}\sin(qR)e^{-\alpha|q|} = \qquad \left[q = \frac{2\pi n}{L} \implies \Delta q = \frac{2\pi}{L}\right]$$

$$= -\frac{\iota}{\pi}\int_0^\infty \frac{dq}{q}\sin(qR)e^{-\alpha|q|} \rightarrow$$

$$\xrightarrow{\alpha\to 0} -\frac{\iota}{\pi}\int_0^\infty \frac{dq}{q}\sin(qR) =$$

$$= -\frac{\iota}{2}\mathrm{sgn}(R) =$$

$$= \frac{\iota}{2}\mathrm{sgn}(x-y) .$$

$$(B.10)$$

Formula (3.55):

$$\rho_\chi(x) = \,: \Psi_\chi^\dagger(x)\Psi_\chi(x) :\, := \lim_{a\to 0}\left[\Psi_\chi^\dagger(x+a)\Psi_\chi(x) - \langle\Psi_\chi^\dagger(x+a)\Psi_\chi(x)\rangle\right] =$$

$$= \lim_{a\to 0}\left[\frac{\eta_\chi^\dagger\eta_\chi}{2\pi\alpha}e^{\iota\chi\sqrt{4\pi}\phi_\chi(x+a)}e^{-\iota\chi\sqrt{4\pi}\phi_\chi(x)} - \langle...\rangle\right] =$$

$$= \lim_{a\to 0}\left[\frac{1}{2\pi\alpha}e^{\iota\chi\sqrt{4\pi}\left(\phi_\chi(x+a)-\phi_\chi(x)\right)}\underbrace{e^{\frac{4\pi}{2}\left[\phi_\chi(x+a),\phi_\chi(x)\right]}}_{\iota\chi} - \langle...\rangle\right] =$$

$$= \lim_{a\to 0}\left[\frac{1}{2\pi\alpha}:e^{\iota\chi\sqrt{4\pi}\left(\phi_\chi(x+a)-\phi_\chi(x)\right)}:\iota\chi - \langle...\rangle\right] =$$

$$\simeq \lim_{a\to 0}\left[\frac{\iota\chi}{2\pi\alpha}:e^{\iota\chi\sqrt{4\pi}a\nabla\phi_\chi(x)}: - \langle...\rangle\right] =$$

$$\simeq \lim_{a\to 0}\left[\frac{\iota\chi}{2\pi\alpha}\left(1+\iota\chi\sqrt{4\pi}a\nabla\phi_\chi(x)\right) - \langle...\rangle\right] =$$

$$= \frac{\iota\chi}{2\pi\alpha}\iota\chi\sqrt{4\pi}a\nabla\phi_\chi(x) =$$

$$\simeq -\frac{1}{\sqrt{\pi}}\nabla\phi_\chi(x) =$$

$$= \frac{1}{2\sqrt{\pi}}\left(\nabla\phi(x)+\chi\nabla\theta(x)\right)$$

(B.11)

where we have used equations (B.9) and (3.34).

B.2   Consistency of notation

Here we would like to clarify some technical aspects of bosonization. In particular, we show the consistency of the formula expressed in Section 3.11 with those of the previous sections. We notice that we have two equivalent ways of defining the fermionic operator acting on the left branch:

A) $c_{kL} = c_{-k_F+k}$

B) $c_{kL} = c_{-k_F-k}$.

In Section 3.11 we used the notation A). The definition B) would change formula (3.70) and (3.71), expressing the fermionic field in terms of the discrete fermionic

operators, into the following ones

$$\Psi^B_\chi(x) = \frac{1}{\sqrt{L}}\sum_k e^{\imath \chi kx}c^B_{k\chi}, \qquad c^B_{k\chi} = \frac{1}{\sqrt{L}}\int dx\, e^{-\imath \chi kx}\Psi^B_\chi(x), \qquad (B.12)$$

where we have used the letter B to distinguish this notation from that used in the rest of the thesis (corresponding to the case A)). Consequently, the density operator (3.72), neglecting the $q = 0$ contribution, becomes

$$\rho^B_\chi(x) =: \Psi^{\dagger B}_\chi(x)\Psi^B_\chi(x) : \frac{1}{L}\sum_{q\neq 0}e^{-\imath \chi qx}\rho^B_\chi(q) = \frac{1}{L}\sum_{q\neq 0}e^{-\imath qx}\rho^B_\chi(\chi q). \qquad (B.13)$$

However, this notation would also be possible and consistent with the definition of the fermionic field in terms of the discrete bosonic operators (equations (3.12) and (3.11)). In fact, the difference in the sign of k, affects the density operator $\rho_L(q)$ and its commutation rules (3.68), implying different relation between $b_{\chi q}$ and $\rho_\chi(q)$ with respect to (3.69). In the case B), $\rho_L(q)$ is given by

$$\rho^B_L(q) = \sum_k c^\dagger_{-k_F-k-q}c_{-k_F-k} = \sum_k c^\dagger_{-k_F+k-q}c_{-k_F+k} = \rho_L(-q). \qquad (B.14)$$

From this relation we can already see the consistency of the two notations in equation (B.13), which has been obtained from (B.12). It also implies that now the density operators satisfy the following commutation rules

$$[\rho^B_\chi(q),\rho^B_{\chi'}(q')] = [\rho_\chi(\chi q),\rho_{\chi'}(\chi q')] = -\frac{qL}{2\pi}\delta_{q,-q'}\delta_{\chi,\chi'} \qquad (B.15)$$

and, therefore, in order to obtain $[b_{q\chi},b^\dagger_{q'\chi'}] = \delta_{q,q'}\delta_{\chi,\chi'}$, one has to define

$$b_{q\chi} = \sqrt{\frac{2\pi}{Lq}}\rho^B_\chi(-q), \quad b^\dagger_{q\chi} = \sqrt{\frac{2\pi}{Lq}}\rho^B_\chi(q). \qquad (B.16)$$

Finally, we check that the choice of notation A) rather than B) does not affect the definition of $\Psi_\chi(x)$ in terms of $b_{\chi q}$, given in equations (3.12), (3.11), and that this definition is consistent with (3.70) or with (B.12), as long as the proper relations between $b_{q\chi}$ and $\rho_\chi(q)$ are taken. To this extent, we compare the definition of $\rho_\chi(x)$ obtained in terms of bosonic operators from (3.12), (3.11) and (3.55) with that obtained in terms of fermionic operators from (3.70) and (3.72) or from (B.12) and

(B.13). From equations (3.12), (3.11) and (3.55), we get

$$\rho_\chi(x) = -\frac{1}{\sqrt{\pi}} \nabla \phi_\chi(x) = \frac{1}{\sqrt{2\pi L}} \sum_{q>0} e^{-\alpha q/2} \sqrt{q} \left[e^{-\imath \chi q x} b_{q\chi}^\dagger + e^{\imath \chi q x} b_{q\chi} \right] . \quad \text{(B.17)}$$

In the case A), this should be equaled to (3.72), which can be rearranged as

$$\rho_\chi(x) = \frac{1}{L} \sum_{k,q \neq 0} e^{-\imath q x} c_{k+q\chi}^\dagger c_{k\chi} =$$

$$= \frac{1}{\sqrt{2\pi L}} \sum_k \sum_{q>0} \sqrt{q} \sqrt{\frac{2\pi}{Lq}} \left[e^{-\imath q x} c_{k+q\chi}^\dagger c_{k\chi} + e^{\imath q x} c_{k-q\chi}^\dagger c_{k\chi} \right] = \quad \text{(B.18)}$$

$$= \frac{1}{\sqrt{2\pi L}} \sum_{q>0} \sqrt{q} \sqrt{\frac{2\pi}{Lq}} \left[e^{-\imath q x} \rho_\chi(q) + e^{\imath q x} \rho_\chi(-q) \right] .$$

The two expressions are equivalent if the relations (3.69) hold.

In the case B), equation (B.17) must be equal to (B.13)

$$\rho_\chi^B(x) = \frac{1}{L} \sum_k \sum_{q \neq 0} e^{-\imath \chi q x} c_{k+q\chi}^{\dagger B} c_{k\chi}^B =$$

$$= \frac{1}{\sqrt{2\pi L}} \sum_k \sum_{q>0} \sqrt{q} \sqrt{\frac{2\pi}{Lq}} \left[e^{-\imath \chi q x} c_{k+q\chi}^{\dagger B} c_{k\chi}^B + e^{\imath \chi q x} c_{k-q\chi}^{\dagger B} c_{k\chi}^B \right] = \quad \text{(B.19)}$$

$$= \frac{1}{\sqrt{2\pi L}} \sum_{q>0} \sqrt{q} \sqrt{\frac{2\pi}{Lq}} \left[e^{-\imath \chi q x} \rho_\chi^B(q) + e^{\imath \chi q x} \rho_\chi^B(-q) \right] ,$$

thus reproducing the relations (B.16).

Appendix C

Bosonization dictionary

$\sum_j \longrightarrow \frac{1}{a} \int dx$

$c_{j,\sigma} \longrightarrow \sqrt{a} \left[e^{\iota k_F x} \Psi_{R\sigma}(x) + e^{-\iota k_F x} \Psi_{L\sigma}(x) \right] = \sqrt{a} \left[(\iota)^j \Psi_{R\sigma}(x) + (-\iota)^j \Psi_{L\sigma}(x) \right]$

$\Psi_{\chi\sigma}(x) = \frac{\eta_{\chi\sigma}}{\sqrt{2\pi\alpha}} e^{-\iota\chi\sqrt{4\pi}\Phi_{\chi\sigma}(x)} = \frac{\eta_{\chi\sigma}}{\sqrt{2\pi\alpha}} e^{\iota\sqrt{\pi}[\chi\phi_\sigma(x)+\theta_\sigma(x)]} = \frac{\eta_{\chi\sigma}}{\sqrt{2\pi\alpha}} e^{\iota\sqrt{\frac{\pi}{2}}[\chi\phi_c(x)+\theta_c(x)+\sigma(\chi\phi_s(x)+\theta_s(x))]}$

$\varphi_\chi(x) = \frac{\iota\chi}{\sqrt{2L}} \sum_{k>0} \frac{e^{\iota\chi kx}}{\sqrt{k}} e^{-\alpha k/2} b_{k\chi}$

$\phi_\chi(x) = \varphi_\chi(x) + \varphi_\chi^\dagger(x) = \frac{\iota\chi}{\sqrt{2L}} \sum_{k>0} \frac{e^{-\alpha k/2}}{\sqrt{k}} \left(e^{\iota\chi kx} b_{k\chi} - e^{-\iota\chi kx} b_{k\chi}^\dagger \right).$

$\varphi(x) = \iota \sum_{k\neq 0} \frac{e^{-\alpha|k|/2-\iota kx}}{k} \left(\frac{|k|}{2L} \right)^{1/2} b_{-k}$

$\phi(x) = \varphi(x) + \varphi^\dagger(x) = -\left[\phi_R(x) + \phi_L(x) \right] = \iota \sum_{k\neq 0} \frac{e^{-\alpha|k|/2-\iota kx}}{k} \left(\frac{|k|}{2L} \right)^{1/2} \left(b_k^\dagger + b_{-k} \right)$

$\theta(x) = -\left[\phi_R(x) - \phi_L(x) \right] = \iota \sum_{k\neq 0} \frac{e^{-\alpha|k|/2-\iota kx}}{|k|} \left(\frac{|k|}{2L} \right)^{1/2} \left(b_k^\dagger - b_{-k} \right)$

$\nabla\phi(x) = \sum_{k\neq 0} e^{-\alpha|k|/2-\iota kx} \left(\frac{|k|}{2L} \right)^{1/2} \left(b_k^\dagger + b_{-k} \right)$

$\nabla\theta(x) = \sum_{k\neq 0} e^{-\alpha|k|/2-\iota kx} \frac{k}{|k|} \left(\frac{|k|}{2L} \right)^{1/2} \left(b_k^\dagger - b_{-k} \right)$

$\phi_c = (\phi_\uparrow + \phi_\downarrow)/\sqrt{2} \qquad\qquad \theta_c = (\theta_\uparrow + \theta_\downarrow)/\sqrt{2}$

$\phi_s = (\phi_\uparrow - \phi_\downarrow)/\sqrt{2} \qquad\qquad \theta_s = (\theta_\uparrow - \theta_\downarrow)/\sqrt{2}$

$\rho_\chi(x) = \frac{1}{2\sqrt{\pi}} \left(\nabla\phi(x) + \chi\nabla\theta(x) \right)$

$\rho = \rho_R + \rho_L = \frac{1}{\sqrt{\pi}} \nabla\phi$

$\tilde{\jmath} = \rho_R - \rho_L = \frac{1}{\sqrt{\pi}} \nabla\theta$

$\rho_{\chi\sigma} = -\frac{1}{\sqrt{\pi}} \nabla\phi_{\chi\sigma} = \frac{1}{2\sqrt{\pi}} \left(\nabla\phi_\sigma + \chi\nabla\theta_\sigma \right)$

$\rho_\sigma = \rho_{R\sigma} + \rho_{L\sigma} = \frac{1}{\sqrt{\pi}} \nabla\phi_\sigma$

$$\tilde{j}_\sigma = \rho_{R\sigma} - \rho_{L\sigma} = \frac{1}{\sqrt{\pi}} \nabla \theta_\sigma$$

$$\rho_c = \frac{\rho_\uparrow + \rho_\downarrow}{\sqrt{2}} = \frac{1}{\sqrt{\pi}} \nabla \phi_c \qquad \tilde{j}_c = \frac{\tilde{j}_\uparrow + \tilde{j}_\downarrow}{\sqrt{2}} = \frac{1}{\sqrt{\pi}} \nabla \theta_c$$

$$\rho_s = \frac{\rho_\uparrow - \rho_\downarrow}{\sqrt{2}} = \frac{1}{\sqrt{\pi}} \nabla \phi_s \qquad \tilde{j}_s = \frac{\tilde{j}_\uparrow - \tilde{j}_\downarrow}{\sqrt{2}} = \frac{1}{\sqrt{\pi}} \nabla \theta_s$$

$$[\varphi(x), \varphi^\dagger(y)] = -\frac{1}{4\pi} \ln \left(\left(\frac{2\pi}{L} \right)^2 \left(\alpha^2 + R^2 \right) \right) \xrightarrow{\alpha \to 0} -\frac{1}{4\pi} \ln \left(\frac{2\pi R}{L} \right)^2$$

$$[\varphi(x), \varphi^\dagger(x)] = -\frac{1}{2\pi} \ln \left(1 - e^{-\frac{2\pi\alpha}{L}} \right) \xrightarrow{L \to \infty} -\frac{1}{2\pi} \ln \left(\frac{2\pi\alpha}{L} \right)$$

$$[\phi(x), \phi(y)] = [\theta(x), \theta(y)] = 0$$

$$[\phi(x), \theta(y)] = \frac{\iota}{2} \mathrm{sgn}(x - y)$$

$$[\phi_\chi(x), \phi_\chi(y)] = \chi \frac{\iota}{4} \mathrm{sgn}(x - y)$$

$$[\phi_R(x), \phi_L(y)] = 0$$

$$[\nabla \phi(x), \nabla \phi(y)] = [\nabla \theta(x), \nabla \theta(y)] = 0$$

$$[\phi(x), \nabla \phi(y)] = [\theta(x), \nabla \theta(y)] = 0$$

$$[\nabla \phi(x), \theta(y)] = \iota \delta(x - y)$$

$$[\phi(x), \nabla \theta(y)] = -\iota \delta(x - y)$$

$$[\phi_\sigma(x), \phi_{\sigma'}(y)] = [\theta_\sigma(x), \theta_{\sigma'}(y)] = 0$$

$$[\phi_\sigma(x), \theta_{\sigma'}(y)] = \delta_{\sigma,\sigma'} \frac{\iota}{2} \mathrm{sgn}(x - y)$$

$$[\phi_c(x), \phi_s(y)] = [\theta_c(x), \theta_s(y)] = [\phi_c(x), \theta_s(y)] = 0$$

$$[\phi_c(x), \theta_c(y)] = [\phi_s(x), \theta_s(y)] = \frac{\iota}{2} \mathrm{sgn}(x - y)$$

$$e^{2\pi[\varphi(x),\varphi^\dagger(y)]} = \frac{L}{2\pi} \frac{1}{\sqrt{\alpha^2 + R^2}} \xrightarrow{\alpha \to 0} \frac{L}{2\pi R}$$

$$e^{-2\pi[\varphi(x),\varphi^\dagger(x)]} = \frac{2\pi\alpha}{L}$$

$$e^{\iota 2\sqrt{\pi}\phi(x)} =: e^{\iota 2\sqrt{\pi}\phi(x)} : \frac{2\pi\alpha}{L}$$

$$: e^{\iota\sqrt{4\pi}R\nabla\phi(x)} : \simeq 1 + \iota\sqrt{4\pi}R\nabla\phi(x)$$

$$e^{\iota\sqrt{4\pi}[\phi(x+R)-\phi(x)]} =: e^{\iota\sqrt{4\pi}[\phi(x+R)-\phi(x)]} : \left(\frac{\alpha}{R} \right)^2$$

Appendix D

Computation of the ground state energy in the GFQMC

Here we show the proof of some formula used in Chapter 4. In particular the ground state energy in equation (4.33) is obtained in the following way:

$$
\begin{aligned}
E_{GS} = H|\Phi_{GS}\rangle &= \frac{\sum_x \langle x|H|\Phi_{GS}\rangle}{\sum_x \langle x|\Phi_{GS}\rangle} = \frac{\sum_{x,x'} \langle x|Hx'\rangle \langle x'|\Phi_{GS}\rangle}{\sum_x \langle x|\Phi_{GS}\rangle} = \\
&= \frac{\sum_{x'} \left(\sum_x H_{x,x'}\right) \Phi_{GS}(x')}{\sum_x \Phi_{GS}(x)} = \frac{\sum_{x'} (\Lambda - b_{x'}) \Phi_{GS}(x')}{\sum_x \Phi_{GS}(x)} = \\
&= \frac{\sum_x \int dw \, (\Lambda - b_x) \, wP(x,w)}{\sum_x \int dw \, wP(x,w)} = \frac{\frac{1}{\#I}\sum_{(x,w)\in I}(\Lambda - b_x)w}{\frac{1}{\#I}\sum_{(x,w)\in I} w} = \\
&= \frac{\langle (\Lambda - b_x) \, w\rangle}{\langle w\rangle} \, .
\end{aligned} \tag{D.1}
$$

If the importance sampling is applied and the guiding wave function is real, the energy can be computed as in equation (4.36). Here we provide the proof:

$$
\begin{aligned}
E_{GS} &= \frac{\langle \Phi_{GS}|H|\Phi_{GS}\rangle}{\langle \Phi_{GS}|\Phi_{GS}\rangle} = \frac{\langle \Phi_{G}|H|\Phi_{GS}\rangle}{\langle \Phi_{G}|\Phi_{GS}\rangle} = \\
&= \frac{\sum_x \langle \Phi_G|H|x\rangle \langle x|\Phi_{GS}\rangle}{\sum_x \langle \Phi_G|x\rangle \langle x|\Phi_{GS}\rangle} = \frac{\sum_x \frac{\langle \Phi_G|H|x\rangle}{\langle \Phi_G|x\rangle} \langle \Phi_G|x\rangle \langle x|\Phi_{GS}\rangle}{\sum_x \Phi_G(x)\Phi_{GS}(x)} = \\
&= \frac{\sum_x e_L(x)\Phi_G(x)\Phi_{GS}(x)}{\sum_x \Phi_G(x)\Phi_{GS}(x)} = \frac{\sum_x e_L(x)\tilde{\Phi}_{GS}(x)}{\sum_x \tilde{\Phi}_{GS}(x)} = \\
&= \frac{\sum_x \int dw e_L(x)w\tilde{P}(x,w)}{\sum \int dw w\tilde{P}(x,w)} = \frac{\frac{1}{\#\tilde{I}}\sum_{(x,w)\in\tilde{I}} e_L(x)w}{\frac{1}{\#\tilde{I}}\sum_{(x,w)\in\tilde{I}} w} = \\
&= \frac{\frac{1}{\#\tilde{I}}\sum_{(x,w)\in\tilde{I}} (\Lambda - \tilde{b}_x)w}{\frac{1}{\#\tilde{I}}\sum_{(x,w)\in\tilde{I}} w} = \frac{\langle (\Lambda - \tilde{b}_x)\, w\rangle}{\langle w\rangle}
\end{aligned}
\tag{D.2}
$$

where the second to last equality follows from

$$
\begin{aligned}
e_L(x) &= \frac{\langle \Phi_G|H|x\rangle}{\langle \Phi_G|x\rangle} = \sum_{x'} \frac{\langle \Phi_G|x'\rangle \langle x'|H|x\rangle}{\langle \Phi_G|x\rangle} = \sum_{x'} \frac{\Phi_G(x')H_{x',x}}{\Phi_G(x)} = \\
&= \sum_{x'} (\Lambda \delta_{x,x'} - G_{x,x'})\frac{\Phi_G(x')}{\Phi_G(x)} = \Lambda - \sum_{x'} \tilde{G}_{x,x'} = \Lambda - \tilde{b}_x
\end{aligned}
\tag{D.3}
$$

Appendix E

Derivation of the bosonization formula of Chapter 7

This Appendix is devoted to the derivation of some formula used in Section 7.2.

Formula (7.67):

$$
\begin{aligned}
: Q_{j,j+1,\sigma} := \; &: c^\dagger_{j,\sigma} c_{j+1,\sigma} + h.c. := \\
&= a : \left[(-\iota)^j \Psi^\dagger_{R\sigma}(x) + (\iota)^j \Psi^\dagger_{L\sigma}(x) \right] \left[(\iota)^{j+1} \Psi_{R\sigma}(x+a) + (-\iota)^{j+1} \Psi_{L\sigma}(x+a) \right] : + h.c. = \\
&= a\iota \left[: \Psi^\dagger_{R\sigma}(x) \Psi_{R\sigma}(x+a) : - : \Psi^\dagger_{L\sigma}(x) \Psi_{L\sigma}(x+a) : + \right. \\
&\quad \left. - (-1)^j \left(\Psi^\dagger_{R\sigma}(x) \Psi_{L\sigma}(x+a) - \Psi^\dagger_{L\sigma}(x) \Psi_{R\sigma}(x+a) \right) \right] + h.c.
\end{aligned}
$$

$$(\text{E.1})$$

At first order

$$
: \Psi^\dagger_{R\sigma}(x) \Psi_{R\sigma}(x+a) :=: \Psi^\dagger_{R\sigma}(x) \Psi_{R\sigma}(x) := \rho_{R\sigma}(x) = \frac{1}{2\sqrt{\pi}} \left(\nabla \phi_\sigma(x) + \nabla \theta_\sigma(x) \right)
$$

$$(\text{E.2})$$

(see eq. (3.55)). In fact

$$: \Psi^\dagger_{R\sigma}(x)\Psi_{R\sigma}(x+a) :=$$

$$= \frac{\eta^\dagger_{R\sigma}\eta_{R\sigma}}{2\pi\alpha}e^{-\iota\sqrt{\pi}[\phi_\sigma(x)+\theta_\sigma(x)]}e^{\iota\sqrt{\pi}[\phi_\sigma(x+a)+\theta_\sigma(x+a)]} - \langle...\rangle =$$

$$= \frac{1}{2\pi\alpha}e^{\iota\sqrt{\pi}([\phi_\sigma(x+a)-\phi_\sigma(x)]+[\theta_\sigma(x+a)-\theta_\sigma(x)])}e^{\frac{\pi}{2}C} - \langle...\rangle$$

$$(E.3)$$

where C is the commutator

$$[\phi_\sigma(x)+\theta_\sigma(x), \phi_\sigma(x+a)+\theta_\sigma(x+a)] = -\iota. \qquad (E.4)$$

By replacing $\phi_\sigma(x+a) - \phi_\sigma(x)$ with $a\nabla\phi_\sigma(x)$ and $\theta_\sigma(x+a) - \theta_\sigma(x)$ with $a\nabla\theta_\sigma(x)$ in eq. (E.3), and approximating the exponential by a first-order Taylor expansion, we get

$$(E.3) = -\frac{\iota}{2\pi\alpha}\left[\cancel{1} + \iota\sqrt{\pi}a\nabla\phi_\sigma(x) + \iota\sqrt{\pi}a\nabla\theta_\sigma(x)\right] - \cancel{\langle...\rangle}$$

$$= \frac{1}{2\sqrt{\pi}}[\nabla\phi_\sigma(x) + \nabla\theta_\sigma(x)] = \qquad (E.5)$$

$$= \rho_{R\sigma(x)} =: \Psi^\dagger_{R\sigma}(x+a)\Psi_{R\sigma}(x) :=: \Psi^\dagger_{R\sigma}(x)\Psi_{R\sigma}(x) :$$

Analogously

$$: \Psi^\dagger_{L\sigma}(x)\Psi_{L\sigma}(x+a) := \rho_{L\sigma} = \frac{1}{2\sqrt{\pi}}[\nabla\phi_\sigma(x) - \nabla\theta_\sigma(x)]. \qquad (E.6)$$

Thus

$$: \Psi^\dagger_{R\sigma}(x)\Psi_{R\sigma}(x+a) - \Psi^\dagger_{L\sigma}(x)\Psi_{L\sigma}(x+a) := \rho_{R\sigma} - \rho_{L\sigma} = \frac{1}{\sqrt{\pi}}\nabla\theta_\sigma(x) \qquad (E.7)$$

which is the current (see Section 3.10), and it vanishes when adding its hermitian conjiugate.

At second order, we obtain

$$(E.3) = -\frac{\iota}{2\pi\alpha}\left[\not{1} + \iota\sqrt{\pi}a\left(\nabla\phi_\sigma(x) + \nabla\theta_\sigma(x)\right) - \frac{\pi a^2}{2}\left(\nabla\phi_\sigma(x) + \nabla\theta_\sigma(x)\right)^2\right] - \langle\not{\ldots}\rangle$$

$$= \frac{1}{2\sqrt{\pi}}\left[\nabla\phi_\sigma(x) + \nabla\theta_\sigma(x)\right] + \frac{\iota a}{4}\left[\nabla\phi_\sigma(x) + \nabla\theta_\sigma(x)\right]^2$$

$$\tag{E.8}$$

and

$$: \Psi_{L\sigma}^\dagger(x)\Psi_{L\sigma}(x+a) := \frac{\iota}{2\pi\alpha}e^{\iota\sqrt{\pi}a(-\nabla\phi_\sigma(x) + \nabla\theta_\sigma(x))} - \langle\ldots\rangle =$$

$$= \frac{\iota}{2\pi\alpha}\left[\not{1} + \iota\sqrt{\pi}a\left(-\nabla\phi_\sigma(x) + \nabla\theta_\sigma(x)\right)\right.$$

$$\left. - \frac{\pi a^2}{2}\left(-\nabla\phi_\sigma(x) + \nabla\theta_\sigma(x)\right)^2\right] - \langle\not{\ldots}\rangle =$$

$$= \frac{1}{2\sqrt{\pi}}\left[\nabla\phi_\sigma(x) - \nabla\theta_\sigma(x)\right] - \frac{\iota a}{4}\left[-\nabla\phi_\sigma(x) + \nabla\theta_\sigma(x)\right]^2$$

$$\tag{E.9}$$

so that

$$: \Psi_{R\sigma}^\dagger(x)\Psi_{R\sigma}(x+a) - \Psi_{L\sigma}^\dagger(x)\Psi_{L\sigma}(x+a) :=$$

$$\frac{1}{\sqrt{\pi}}\nabla\theta_\sigma(x) + \frac{\iota a}{2}\left[(\nabla\phi_\sigma(x))^2 + (\nabla\theta_\sigma(x))^2\right] \tag{E.10}$$

and

$$a\iota\left(: \Psi_{R\sigma}^\dagger(x)\Psi_{R\sigma}(x+a) - \Psi_{L\sigma}^\dagger(x)\Psi_{L\sigma}(x+a)\right) : + h.c. =$$

$$- a^2\left[(\nabla\phi_\sigma(x))^2 + (\nabla\theta_\sigma(x))^2\right] . \tag{E.11}$$

Now let's calculate the oscillating part in eq. (E.1). We obtain

$$\Psi_{R\sigma}^\dagger(x)\Psi_{L\sigma}(x+a) = \frac{\eta_{R\sigma}^\dagger\eta_{L\sigma}}{2\pi\alpha}e^{-\iota\sqrt{\pi}[\phi_\sigma(x) + \theta_\sigma(x)]}e^{\iota\sqrt{\pi}[-\phi_\sigma(x+a) + \theta_\sigma(x+a)]} =$$

$$= \frac{-\iota}{2\pi\alpha}e^{-\iota\sqrt{\pi}[\phi_\sigma(x) + \phi_\sigma(x+a) - \theta_\sigma(x+a) + \theta_\sigma(x)]}e^{\frac{\pi}{2}C} \tag{E.12}$$

with

$$C = [\phi_\sigma(x) + \theta_\sigma(x), -\phi_\sigma(x+a) + \theta_\sigma(x+a)] = 0 . \tag{E.13}$$

Thus

$$(E.12) \simeq -\frac{\iota}{2\pi\alpha} e^{-\iota 2\sqrt{\pi}\phi_\sigma(x)} = \frac{1}{\pi\alpha} \frac{e^{-\iota 2\sqrt{\pi}\phi_\sigma(x)}}{2\iota} . \qquad (E.14)$$

Analogously, its hermitian conjugate is

$$\Psi^\dagger_{L\sigma}(x)\Psi_{R\sigma}(x+a) = \frac{\eta^\dagger_{L\sigma}\eta_{R\sigma}}{2\pi\alpha} e^{-\iota\sqrt{\pi}[-\phi_\sigma(x)+\theta_\sigma(x)]} e^{\iota\sqrt{\pi}[\phi_\sigma(x+a)+\theta_\sigma(x+a)]} =$$
$$\simeq -\frac{1}{\pi\alpha} \frac{e^{\iota 2\sqrt{\pi}\phi_\sigma(x)}}{2\iota} . \qquad (E.15)$$

Hence

$$\Psi^\dagger_{R\sigma}(x)\Psi_{L\sigma}(x+a) - \Psi^\dagger_{L\sigma}(x)\Psi_{R\sigma}(x+a) = \frac{1}{\pi\alpha\iota} \cos(2\sqrt{\pi}\phi_\sigma(x)) \qquad (E.16)$$

and

$$-a\iota(-1)^j \left[\Psi^\dagger_{R\sigma}(x)\Psi_{L\sigma}(x+a) - \Psi^\dagger_{L\sigma}(x)\ \Psi_{R\sigma}(x+a)\right] + h.c. =$$
$$-\frac{2(-1)^j}{\pi} \cos(2\sqrt{\pi}\phi_\sigma(x)) . \qquad (E.17)$$

Summing (E.11) and (E.17), we finally get

$$: Q_{j,j+1,\sigma} :\simeq -\frac{2}{\pi}(-1)^j \cos(2\sqrt{\pi}\phi_\sigma(x)) - a^2 \left[(\nabla\phi_\sigma(x))^2 + (\nabla\theta_\sigma(x))^2\right] \qquad (E.18)$$

where the last contribution is second order and we include it only when the oscillating one is vanishing (*i.e.*, in the kinetic-like terms).

Formula (7.68):

$$: n_{j,\sigma} := : c^\dagger_{j,\sigma} c_{j,\sigma} :=$$
$$= a : \left[(-\iota)^j \Psi^\dagger_{R\sigma}(x) + (+\iota)^j \Psi^\dagger_{L\sigma}(x)\right] \left[(+\iota)^j \Psi_{R\sigma}(x) + (-\iota)^j \Psi_{L\sigma}(x)\right] :=$$
$$= a \left[: \Psi^\dagger_{R\sigma}(x)\Psi_{R\sigma}(x) : + : \Psi^\dagger_{L\sigma}(x)\Psi_{L\sigma}(x) : +\right.$$
$$\left. + (-)^j \left(\Psi^\dagger_{R\sigma}(x)\Psi_{L\sigma}(x) + \Psi^\dagger_{L\sigma}(x)\Psi_{R\sigma}(x)\right)\right] =$$
$$= a \left[\rho_{R\sigma}(x) + \rho_{L\sigma}(x) + (-)^j \left(\Psi^\dagger_{R\sigma}(x)\Psi_{L\sigma}(x) + \Psi^\dagger_{L\sigma}(x)\Psi_{R\sigma}(x)\right)\right] .$$
$$(E.19)$$

We know that $\rho_{R\sigma} + \rho_{L\sigma} = \frac{1}{\sqrt{\pi}}\nabla\phi_\sigma$ (see Section 3.10); whereas

$$
\begin{aligned}
\Psi_{R\sigma}^\dagger(x)\Psi_{L\sigma}(x) &= \frac{\eta_{R\sigma}^\dagger \eta_{L\sigma}}{2\pi\alpha} e^{-\iota\sqrt{\pi}[\phi_\sigma(x)+\theta_\sigma(x)]} e^{\iota\sqrt{\pi}[-\phi_\sigma(x)+\theta_\sigma(x)]} \\
&= \frac{-\iota}{2\pi\alpha} e^{-\iota 2\sqrt{\pi}\phi_\sigma(x)}
\end{aligned}
\tag{E.20}
$$

and its hermitian conjugate is

$$
\Psi_{L\sigma}^\dagger(x)\Psi_{R\sigma}(x) = \frac{\iota}{2\pi\alpha} e^{\iota 2\sqrt{\pi}\phi_\sigma(x)}
\tag{E.21}
$$

hence

$$
\Psi_{R\sigma}^\dagger(x)\Psi_{L\sigma}(x) + \Psi_{L\sigma}^\dagger(x)\Psi_{R\sigma}(x) = -\frac{1}{\pi\alpha}\sin(2\sqrt{\pi}\phi_\sigma(x))
\tag{E.22}
$$

and

$$
: n_{j,\sigma} := a\left[\frac{1}{\sqrt{\pi}}\nabla\phi_\sigma(x) - \frac{(-1)^j}{\pi\alpha}\sin(2\sqrt{\pi}\phi_\sigma(x))\right].
\tag{E.23}
$$

Formula (7.71):

$$
\begin{aligned}
: n_{j,\sigma} :: n_{j+r,\sigma} = a^2 \Bigg[&\frac{1}{\pi}\nabla\phi_\sigma(x)\nabla\phi_\sigma(x+R) + \\
&\frac{(-1)^r}{(\pi\alpha)^2}\sin(2\sqrt{\pi}\phi_\sigma(x))\sin(2\sqrt{\pi}\phi_\sigma(x+R)) + (-1)^j... \Bigg].
\end{aligned}
\tag{E.24}
$$

We approximate $\nabla\phi_\sigma(x)\nabla\phi_\sigma(x+R) \simeq (\nabla\phi_\sigma(x))^2$ and $\sin(2\sqrt{\pi}\phi_\sigma(x))\sin(2\sqrt{\pi}\phi_\sigma(x+R))$ by using formula (7.69). So we get

$$
\begin{aligned}
(E.24) &= \frac{a^2}{\pi}(\nabla\phi_\sigma(x))^2 + \frac{(-1)^r}{\pi^2}\left[-\frac{1}{2}\cos(4\sqrt{\pi}\phi_\sigma(x)) - \pi\alpha^2(\nabla\phi_\sigma(x))^2\right] = \\
&= \frac{a^2}{\pi}(1-(-1)^r)(\nabla\phi_\sigma(x))^2 - \frac{(-1)^r}{2\pi^2}\cos(4\sqrt{\pi}\phi_\sigma(x)).
\end{aligned}
\tag{E.25}
$$

Formula (7.72):

By using eq. (7.68), we get

$$
\begin{aligned}
: n_{j,\sigma} :: n_{j+1,\sigma} : \simeq a^2 \Bigg\{ &\frac{1}{\pi} \nabla\phi_\sigma(x)\nabla\phi_\sigma(x+a) + \\
&- \frac{1}{(\pi\alpha)^2} \sin(2\sqrt{\pi}\phi_\sigma(x))\sin(2\sqrt{\pi}\phi_\sigma(x+a)) + \\
&+ \frac{(-1)^j}{\pi\sqrt{\pi\alpha}} \Big[\nabla\phi_\sigma(x)\sin(2\sqrt{\pi}\phi_\sigma(x+a)) + \\
&\qquad - \sin(2\sqrt{\pi}\phi_\sigma(x))\nabla\phi_\sigma(x+a) \Big] \Bigg\} \, .
\end{aligned}
\tag{E.26}
$$

The single terms appearing in the previous expression can be approximated in the following way

$$
\nabla\phi_\sigma(x)\nabla\phi_\sigma(x+a) \simeq (\nabla\phi_\sigma(x))^2
$$

$$
\sin(2\sqrt{\pi}\phi_\sigma(x))\sin(2\sqrt{\pi}\phi_\sigma(x+a)) \simeq \tfrac{1}{2} - \tfrac{1}{2}\cos(4\sqrt{\pi}\phi_\sigma(x)) - \pi a^2 (\nabla\phi_\sigma(x))^2
$$
$$
\text{[see eq. (7.69)]}
$$

$$
\nabla\phi_\sigma(x)\sin(2\sqrt{\pi}\phi(x+a)) - \sin(2\sqrt{\pi}\phi_\sigma(x))\nabla\phi_\sigma(x+a) \simeq \tfrac{2}{\sqrt{\pi}a}\cos(2\sqrt{\pi}\phi_\sigma(x))
$$
$$
\text{[see eq. (7.70)]} \, ;
$$

thus

$$
(E.26) \simeq a^2 \frac{2}{\pi}(\nabla\phi_\sigma(x))^2 - \frac{1}{2\pi^2} + \frac{1}{2\pi^2}\cos(4\sqrt{\pi}\phi_\sigma(x)) + (-)^j \frac{2}{\pi^2}\cos(2\sqrt{\pi}\phi_\sigma(x)) \, .
\tag{E.27}
$$